Centre Énergie Matériaux Télécommunications

TIP-ENHANCED RAMAN MAPPING OF THE SUPERPARALECTRIC TRANSITION AND SITE-SPECIFIC CHEMISORPTION ON PEROVSKITE NANOSTRUCTURES

Par

Mohammad Bakhtbidar

Thèse présentée pour l'obtention du grade de

Philosophiae Doctor (Ph.D.)

en sciences de l'énergie et des matériaux

Jury d'évaluation

Président du jury et examinateur interne	Fiorenzo Vetrone INRS-EMT, Canada
Examinateur externe	Ségolène Callard Université de Lyon, France
Examinateur externe	Pablo Bianucci Concordia University, Canada
Directeur de recherche	Andreas Ruediger INRS-EMT, Canada
Codirecteur de recherche	Alexandre Merlen INRS-EMT, Canada Université de Toulon-MAPIEM, France

"*God made the bulk; surfaces were invented by the devil."*

Wolfgang Pauli

ACKNOWLEDGEMENTS

I would like to express my deepest gratitude to my esteemed supervisor, Prof. Andreas Ruediger. His exceptional guidance, profound expertise, and steadfast mentorship have been pivotal throughout my doctoral studies. His confidence in my abilities and his unwavering commitment to academic excellence have significantly shaped both my intellectual development and professional trajectory. I am sincerely grateful for the opportunity to work under his supervision and to benefit from his wisdom.

I also extend my heartfelt appreciation to my co-supervisor, Prof. Alexandre Merlen, for his valuable insights, constant encouragement, and dedicated support. His readiness to provide constructive feedback and his collaborative spirit have been instrumental in the successful completion of this thesis. I am especially thankful to my colleagues in the Nanophotonics group for their contributions to this project. I wish to acknowledge Dr. Andreas Doerfler, Dr. Azza Hadj Youssef, and Dr. Ifeanyichukwu Amaechi for their collegiality and technical assistance. I am also particularly grateful to Lilian Skokan, Daniel Gueckelhorn, and Katharina Kohlmann, whose dedication, support, and collaborative efforts played an important role in the advancement of this research. I wish to express my sincere gratitude to Dr. Reza Safaei for his guidance during the final year of my PhD, especially for his expertise in optics, and for enriching my understanding of high-power lasers and light–matter interactions. I also extend heartfelt thanks to Prof. François Légaré and the ALLS group for enabling me to deepen my knowledge in the field of high-power lasers and for helping me bridge my background in spectroscopy with the demanding field of intense laser systems

To my beloved wife, Sana, I owe a special debt of gratitude. Your unwavering support, enduring patience, and boundless encouragement have been a constant source of strength throughout this journey. You have always stood by me through the most challenging times, and your belief in me has never wavered. This work is ours together—I carried it with you at every turn.

To my parents, whose lifelong dedication and sacrifices laid the foundation for my academic pursuits, I offer my deepest thanks. Your unconditional support, encouragement, and values have guided me every step of the way. This accomplishment is a reflection of your love and investment in my future.

To each and every one of you, thank you for being an integral part of this journey.

Mohammad Bakhtbidar

ABSTRACT

Tip-enhanced Raman spectroscopy (TERS) has emerged as a powerful nano spectroscopic technique capable of simultaneously providing topographical and chemical information with sub-diffraction spatial resolution. This thesis leverages high-resolution TERS to investigate the surface vibrational properties, phase behavior, and chemisorption phenomena in two model perovskite oxides, polar barium titanate ($BaTiO_3$) and non-polar strontium titanate ($SrTiO_3$), with a particular focus on their surface. The thesis is structured around three peer-reviewed papers published during the course of this research.

In the first part, TERS is employed to probe the surface of $BaTiO_3$ nanoparticles, revealing both chemisorption and core-shell features. The highly localized electromagnetic (EM) field at the tip apex (~10^8 V/m) enables the detection of otherwise Raman-inactive (infrared-active) modes by modifying selection rules. Correlated TERS and topographic mapping reveal the presence of a carbonate monolayer on individual nanoparticles, undetectable by conventional characterization techniques, demonstrating the remarkable chemical sensitivity of TERS for surface studies.

The second part addresses the superparaelectric limit in individual $BaTiO_3$ nanoparticles with diameters approaching ~20 nm. Through combined analysis of TERS spectra and localized surface plasmon resonance (LSPR) mapping, a transition from the ferroelectric to the paraelectric phase is observed, evidenced by the attenuation of characteristic tetragonal Raman modes and a ~7 nm LSPR red-shift associated with a local refractive index change. Near-field imaging confirms a core–shell structure, with a ferroelectric core surrounded by a paraelectric shell, emphasizing size-dependent polarization loss at the nanoscale.

In the last part, the surface termination chemistry of $SrTiO_3$ (100) vicinal surfaces is explored using TERS and density functional theory (DFT). The study reveals selective chemisorption of ambient CO_2 on SrO-terminated terraces, leading to the formation of a surface carbonate layer, as identified by a distinct Raman peak at 1071 cm^{-1}. This monolayer modifies surface binding energies, initiating spontaneous delamination of SrO layers and resulting in the formation of $SrCO_3$ nanograins on the TiO_2-terminated surface, findings corroborated by spectral and topography evidence.

Overall, this work exploits plasmonic enhancement to significantly improve both the sensitivity and spatial resolution of Raman spectroscopy, enabling the investigation of material properties

that remain inaccessible with conventional techniques. These advances open new avenues for fundamental research in optics and materials science.

Keywords: Tip-Enhanced Raman Spectroscopy (TERS), Perovskite Oxides, Barium Titanate ($BaTiO_3$) Nanoparticles, Strontium Titanate ($SrTiO_3$) Surface Terminations, Surface Chemistry, Superparaelectric Limit, Localized Surface Plasmon Resonance (LSPR), High-Resolution Optical Mapping, Surface Characterization.

RÉSUMÉ

La spectroscopie Raman exaltée par pointe (TERS) s'est imposée comme une technique nanoscopique puissante, capable de fournir simultanément des informations topographiques et chimiques avec une résolution spatiale au-delà de la limite de diffraction. Cette thèse exploite la TERS à haute résolution pour étudier les propriétés vibrationnelles de surface, le comportement de phase et les phénomènes de chimisorption dans deux oxydes pérovskites modèles, le titanate de baryum polaire ($BaTiO_3$) et le titanate de strontium non polaire ($SrTiO_3$), avec un accent particulier sur leur surface. La thèse est structurée autour de trois articles évalués par les pairs, publiés au cours de cette recherche.

Dans la première partie, la TERS est employée pour sonder la surface de nanoparticules de $BaTiO_3$, révélant à la fois des caractéristiques de chimisorption et de structure cœur-coquille. Le champ électromagnétique (EM) fortement localisé à l'apex de la pointe (~10^8 V/m) permet la détection de modes autrement Raman-inactifs (actifs en infrarouge) en modifiant les règles de sélection. La cartographie corrélée TERS et topographique révèle la présence d'une monocouche de carbonate sur des nanoparticules individuelles, indétectable par les techniques de caractérisation conventionnelles, démontrant la sensibilité chimique remarquable de la TERS pour les études de surface.

La deuxième partie traite de la limite super-paraélectrique dans des nanoparticules individuelles de $BaTiO_3$ dont le diamètre approche ~20 nm. Grâce à une analyse combinée des spectres TERS et de la cartographie de la résonance plasmonique de surface localisée (LSPR), une transition de la phase ferroélectrique à la phase paraélectrique est observée, mise en évidence par l'atténuation des modes Raman caractéristiques de la phase tétragonale et par un décalage vers le rouge de ~7 nm de la LSPR associé à une variation locale de l'indice de réfraction. L'imagerie en champ proche confirme une structure cœur–coquille, avec un cœur ferroélectrique entouré d'une coquille paraélectrique, soulignant la perte de polarisation dépendante de la taille à l'échelle nanométrique.

Dans la dernière partie, la chimie de terminaison de surface des surfaces vicinales $SrTiO_3$ (100) est explorée en utilisant la TERS et la théorie de la fonctionnelle de la densité (DFT). L'étude révèle une chimisorption sélective du CO_2 ambiant sur les terrasses terminées par SrO, conduisant à la formation d'une couche de carbonate de surface, identifiée par un pic Raman distinct à 1071 cm^{-1}. Cette monocouche modifie les énergies de liaison de surface, initiant la

délamination spontanée des couches de SrO et entraînant la formation de nanograins de $SrCO_3$ sur la surface terminée par TiO_2, résultats corroborés par les preuves spectrales et topographiques.

Dans l'ensemble, ce travail exploite l'amplification plasmonique pour améliorer de manière significative à la fois la sensibilité et la résolution spatiale de la spectroscopie Raman, permettant l'investigation de propriétés matérielles inaccessibles avec les techniques conventionnelles. Ces avancées ouvrent de nouvelles perspectives pour la recherche fondamentale en optique et en science des matériaux.

Mots-clés : Spectroscopie Raman exaltée par effet de pointe (TERS), oxydes pérovskites, nanoparticules de titanate de baryum ($BaTiO_3$), terminaisons de surface du titanate de strontium ($SrTiO_3$), chimie de surface, limite superparaélectrique, résonance plasmonique de surface localisée (LSPR), cartographie optique à haute résolution, caractérisation de surface.

SOMMAIRE RÉCAPITULATIF

Cartographie Raman exaltée par effet de pointe de la transition superparaélectrique et de la chimisorption site-spécifique sur des nanostructures de pérovskite

Introduction

Les oxydes pérovskites (ABO_3) constituent une famille de matériaux polyvalents dont les propriétés structurales et électroniques donnent lieu à des phénomènes tels que la ferroélectricité, la piézoélectricité et l'activité catalytique [1,2]. Leur structure cristalline, identifiée pour la première fois dans le $CaTiO_3$, est à l'origine de fonctionnalités incluant des transitions métal–isolant, la conduction ionique et la supraconductivité [3]. Ces caractéristiques rendent les pérovskites particulièrement attractives pour des applications en électronique, conversion d'énergie et catalyse. Parmi elles, $SrTiO_3$ et $BaTiO_3$ se distinguent par leurs riches réponses diélectriques et ferroélectriques, tandis que leurs comportements de surface et d'interface à l'échelle nanométrique demeurent des sujets de recherche active [4].

Les surfaces de $SrTiO_3$ et de $BaTiO_3$ présentent des propriétés dépendantes de la terminaison (TiO_2 vs. SrO/BaO), avec des phénomènes d'adsorption jouant un rôle déterminant dans leur chimie de surface [5]. En particulier, l'adsorption du CO_2 modifie fortement l'activité catalytique, la structure électronique et la réactivité. Les nanoparticules de $BaTiO_3$ présentent également une suppression de la ferroélectricité en dessous d'un diamètre critique, définissant la limite superparaélectrique [6]. Bien que des modèles théoriques aient exploré ces effets, les études expérimentales au niveau de nanoparticules individuelles restent limitées, notamment concernant l'adsorption de CO_2 et la stabilité de phase à l'échelle nanométrique [7,8].

Le dépassement des limites des méthodes conventionnelles a conduit au développement de techniques de nano-imagerie de plus en plus avancées. Si la spectroscopie photoélectronique (XPS) et la diffraction des rayons X (XRD) ont révolutionné l'analyse chimique et structurale, leur résolution spatiale reste insuffisante pour la cartographie nanométrique. Les microscopies électroniques (TEM et SEM) offrent une résolution élevée mais nécessitent des conditions contraignantes et peuvent endommager les matériaux sensibles. Les approches par microscopie à sonde locale (STM, AFM) permettent une imagerie atomique mais avec une spécificité chimique limitée. Les spectroscopies vibrationnelles (IR et Raman) complètent ces méthodes par

l'identification de modes moléculaires, mais leur résolution latérale demeure contrainte par la limite de diffraction de la lumière.

La spectroscopie Raman en champ proche, ou TERS, combine la microscopie à force atomique locale et la spectroscopie Raman, et permet d'acquérir simultanément des informations topographiques et chimiques avec une résolution nanométrique. Basée sur le principe de la spectroscopie Raman exaltée de surface (SERS), la TERS repose sur la résonance plasmonique localisée au sommet métallique de la pointe, qui amplifie le signal Raman dans une région de champ proche confinée. Comme illustré à la Figure 1, la pointe plasmonique agit comme une nanoantenne optique qui, lorsqu'elle est éclairée par le laser d'excitation, concentre le champ électromagnétique à son apex et renforce le signal Raman rétrodiffusé provenant de la surface de l'échantillon. Cette configuration expérimentale permet de dépasser la limite de diffraction et d'atteindre une sensibilité chimique allant jusqu'à l'échelle de la molécule unique. Malgré les défis techniques liés à la reproductibilité des pointes et à leur alignement précis, la TERS offre un accès inédit aux structures et aux phénomènes chimiques à l'échelle nanométrique.

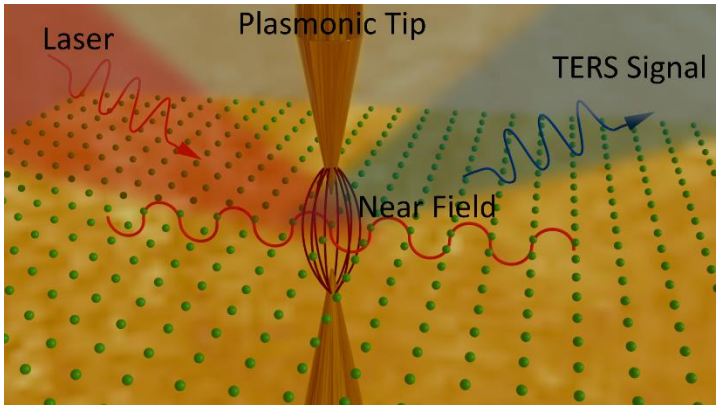

Figure 1 : Illustration d'une configuration expérimentale TERS. Les sphères vertes représentent la structure atomique de la surface du matériau, tandis que la forme conique correspond à l'image de charge de la pointe. Le champ électromagnétique localisé entre la pointe et la surface, lié à cet effet d'image, correspond au mode dit "*gap-TERS"*, qui sera détaillé à la Section 2.3.

Motivation et Objectifs

La miniaturisation des oxydes fonctionnels exige une compréhension approfondie de l'influence de l'adsorption de surface, des transitions de phase et des effets de taille finie sur les performances à l'échelle nanométrique. La TERS fournit une approche unique pour sonder ces phénomènes dans les nanoparticules de $BaTiO_3$ et de $SrTiO_3$. Cette thèse vise à :

- Caractériser les couches chimisorbées sur les surfaces de $BaTiO_3$.
- Localiser l'adsorption de CO_2 sur les terrasses (100) de $SrTiO_3$.

- Étudier les phénomènes de délamination à la surface de $SrTiO_3$.
- Explorer la limite superparaélectrique dans des nanoparticules individuelles de $BaTiO_3$.

À travers ces objectifs, ce travail contribue à l'élucidation des mécanismes nanométriques essentiels pour la catalyse, la nanoélectronique et le développement de dispositifs de prochaine génération.

THÉORIE ET FONDAMENTAUX

Microscopie à force atomique

L'invention du microscope à effet tunnel (STM) en 1981 par Binnig et Rohrer a permis l'imagerie à l'échelle atomique grâce aux courants de tunnel [9]. Toutefois, son application est restreinte aux échantillons conducteurs, ce qui limite sa portée. Pour surmonter cette contrainte, le microscope à force atomique (AFM) a été introduit en 1986, étendant l'imagerie nanométrique aux surfaces conductrices et isolantes par l'exploitation d'interactions atomiques à courte et longue portée [10].

Le principe fondamental de l'AFM repose sur l'interaction entre la pointe de la sonde et la surface de l'échantillon, généralement décrite par le potentiel de Lennard-Jones. Ce modèle combine l'attraction de van der Waals à longue portée et la répulsion de Pauli à courte portée [11]. À l'équilibre, ces contributions s'annulent, définissant la distance minimale d'interaction. La variation de l'énergie potentielle d'interaction en fonction de la distance pointe–échantillon est illustrée dans la Figure 2, où l'attraction domine au-delà d'environ 1 nm, tandis que la répulsion apparaît en dessous de 0,5 nm.

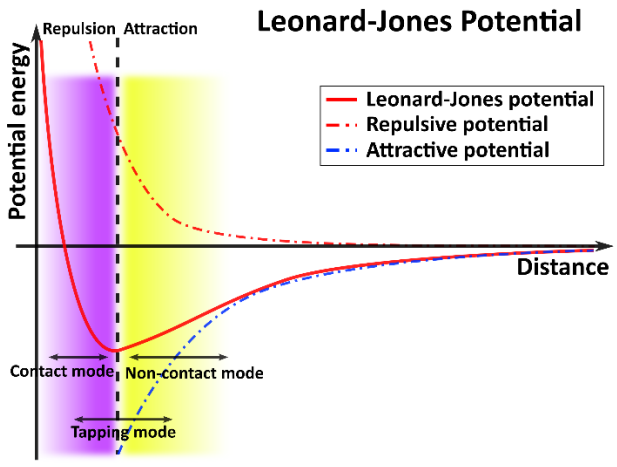

Figure 2: Variation de l'interaction entre la pointe et la surface en fonction de la distance.

Différents modes de fonctionnement adaptent l'AFM à diverses applications. En mode contact, la pointe reste en contact permanent avec la surface, offrant une haute résolution mais au prix d'une usure rapide et d'une possible déformation des matériaux mous. Le mode tapping (ou contact intermittent) consiste à faire osciller le cantilever près de sa fréquence de résonance, réduisant les forces latérales et prolongeant la durée de vie de la pointe. Enfin, le mode non-contact opère dans le régime attractif, la pointe restant à quelques nanomètres de la surface. La sensibilité repose alors sur la détection des décalages de fréquence de résonance, exprimés par:

$$f = f_0 \sqrt{1 - \frac{\partial F}{\partial d} \frac{1}{k_0}} \qquad 1$$

où f_0 est la fréquence de résonance naturelle, k_0 la raideur du cantilever, et $^{\partial F}/_{\partial d}$ le gradient de force, et d la distance pointe–échantillon.

Au-delà des systèmes à levier classique, les diapasons à quartz (QTF) se sont imposés comme de puissants capteurs de force en AFM [12]. Initialement développés pour la microscopie en champ proche, ils offrent des facteurs de qualité très élevés (~10^4 dans l'air, ~10^5 sous vide), permettant de détecter de très faibles décalages de fréquence liés aux interactions pointe–échantillon. Leur fréquence de résonance se situe généralement autour de 32,768 kHz, identique à celle des montres à quartz, ce qui les rend disponibles à faible coût. En fixant une pointe métallique affûtée sur une branche du diapason, les forces d'interaction modifient sa raideur et sa fréquence propre. Ces variations sont suivies électroniquement par un démodulateur à boucle à verrouillage de phase (PLL), supprimant ainsi le besoin de systèmes optiques de détection.

L'AFM basé sur diapason présente plusieurs avantages : il permet une imagerie stable à très faible amplitude d'oscillation, réduit l'usure de la pointe, simplifie l'instrumentation et se prête particulièrement bien aux expériences en conditions extrêmes (cryogéniques, ultravide ou sensibles à la lumière). Cette configuration en fait une technique robuste et polyvalente pour l'imagerie et la spectroscopie à haute résolution à l'échelle nanométrique.

Diffusion Raman et Fondamentaux Plasmoniques

La spectroscopie Raman et infrarouge sont deux techniques complémentaires qui sondent les modes vibrationnels des molécules excitées par un rayonnement électromagnétique (EM). Pour une molécule composée de N atomes, le nombre de modes normaux de vibration est 3N−6 pour les molécules non linéaires, ou 3N−5 pour les molécules linéaires. Ces vibrations se divisent en deux grandes catégories : les vibrations d'étirement et les vibrations de déformation. Dans le

premier cas, les atomes oscillent le long de l'axe de liaison, modifiant la longueur des liaisons, tandis que dans le second cas, les angles de liaison varient, entraînant des distorsions structurales [13].

Les fréquences vibrationnelles des molécules diatomiques peuvent être décrites en fonction des masses atomiques et de la constante de force de liaison. Dans une description quantique, les états vibrationnels sont souvent modélisés par le potentiel de Morse, qui rend compte à la fois de l'énergie de dissociation et de la présence de modes vibrationnels de second ordre et de bandes combinées [14]. Une vibration est active en IR lorsqu'elle induit une variation du moment dipolaire, tandis qu'elle est active en Raman si elle provoque une variation de la polarisabilité. Selon le principe d'exclusion mutuelle, dans les molécules centrosymétriques, les modes actifs en IR sont inactifs en Raman, et inversement.

Lorsqu'un rayonnement monochromatique interagit avec une molécule, le champ électrique oscillant du faisceau incident déforme le nuage électronique et induit un moment dipolaire. Dans l'approximation dipolaire — valable puisque la longueur d'onde incidente est beaucoup plus grande que les dimensions moléculaires — le moment dipolaire induit s'écrit :

$$p = \alpha E \qquad 1$$

où α est le tenseur de polarisabilité. Un mode vibrationnel est actif en Raman uniquement s'il module α. En développant le tenseur de polarisabilité en série de Taylor et en insérant les coordonnées normales de vibration, on obtient [15]:

$$\vec{p} = \bar{\bar{\alpha}}_0 \vec{E}_0 cos(\omega_0 t) + \frac{1}{2}\sum_k \vec{E}_0 \bar{\bar{\alpha}}'_k Q_{k_0}\{cos[(\omega_0 - \omega_k)t] + cos[(\omega_0 + \omega_k)t]\} \qquad 3$$

L'équation (3) met en évidence les trois composantes de la diffusion lumineuse : la diffusion Rayleigh élastique (sans échange d'énergie), et les diffusions inélastiques Stokes et anti-Stokes, correspondant respectivement à une perte ou un gain d'énergie par le photon. Malgré sa grande spécificité chimique, la spectroscopie Raman présente deux limites principales: (i) la très faible section efficace de diffusion, plusieurs ordres de grandeur en dessous de la fluorescence, et (ii) une résolution spatiale limitée par la diffraction de la lumière. L'intensité du signal Raman est proportionnelle à la section efficace de diffusion σ_k, qui croît comme la puissance quatrième de la fréquence d'excitation. L'utilisation de longueurs d'onde plus courtes augmente donc l'efficacité Raman, mais au prix d'une augmentation du bruit de fluorescence.

En microscopie optique en champ lointain, la plus petite distance latérale résoluble est fixée par le critère de Rayleigh, $d \approx 1.22\ {}^{\lambda}/_{NA}$. Ce volume limité par diffraction empêche d'accéder directement à des structures nanométriques. Pour dépasser cette barrière, les méthodes de champ proche, comme la spectroscopie Raman exaltée par pointe, exploitent les champs plasmoniques localisés afin d'atteindre une résolution nanométrique.

Principes plasmoniques

Les nanoparticules de métaux nobles présentent des propriétés optiques singulières par rapport aux métaux massifs. Leur interaction avec la lumière est dominée par des oscillations collectives des électrons de conduction — appelées plasmons. Ces phénomènes expliquent les couleurs des vitraux médiévaux et d'objets tels que la coupe de Lycurgue de l'époque romaine [16].

Les modes plasmoniques se distinguent par leur confinement spatial. Comme illustré à la Figure 3, trois catégories principales existent : les plasmons de volume, les polaritons de plasmon de surface (SPP) et les plasmons de surface localisés (LSP). Les plasmons de volume (Figure 3a) sont des oscillations du gaz électronique à l'intérieur du métal, généralement excitées par des faisceaux d'électrons. Les SPP (Figure 3b) sont des ondes de charge se propageant le long d'une interface métal–diélectrique, avec un champ électromagnétique décroissant exponentiellement perpendiculairement à la surface. Enfin, les LSP (Figure 3c) apparaissent lorsque la taille des nanoparticules métalliques est bien inférieure à la longueur d'onde incidente : les oscillations électroniques sont confinées, générant d'intenses champs locaux.

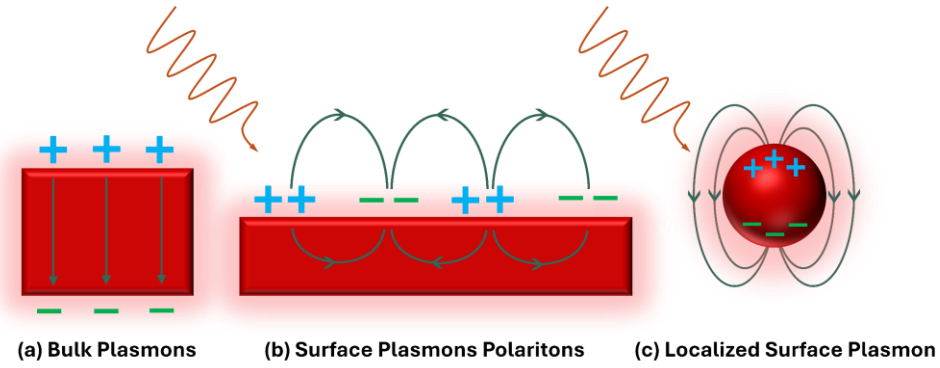

Figure 3: Illustration des modes plasmoniques. (a) Plasmons de volume : oscillations de charge dans un métal. (b) Polaritons de plasmon de surface : modes se propageant aux interfaces. (c) Plasmons de surface localisés : oscillations confinées dans les nanoparticules.

Parmi ces modes, la résonance plasmonique de surface localisée (LSPR) joue un rôle central dans l'amplification Raman. Dans une nanoparticule métallique, les électrons de conduction oscillent collectivement en résonance avec l'onde incidente, générant des champs

électromagnétiques fortement confinés [17]. Pour une nanoparticule sphérique, le dipôle induit est donné par $p = \alpha E$, avec une polarisabilité :

$$\alpha = 4\pi\varepsilon_0 R^3 \frac{\varepsilon_m - \varepsilon_d}{\varepsilon_m + 2\varepsilon_d} \qquad 4$$

où R est le rayon de la particule, ε_m la permittivité du métal et ε_d celle du milieu environnant. La résonance apparaît lorsque $\varepsilon_m(\omega) = -2\varepsilon_d$. La composante imaginaire de ε_m introduit un amortissement, limitant le gain mais permettant néanmoins un fort confinement lumineux à l'échelle nanométrique.

Influence de la composition du matériau

La réponse plasmonique dépend fortement de la permittivité optique du métal. Les spectres d'extinction expérimentaux et théoriques démontrent des comportements distincts pour Al, Cu, Ag et Au. Comme présenté à la Figure 4, les spectres expérimentaux (Figure 4a) révèlent le déplacement des longueurs d'onde et l'élargissement des pics selon le métal, tandis que les calculs théoriques (Figure 4b) reproduisent ces tendances. L'aluminium génère des résonances larges et décalées vers le bleu, l'argent offre des pics étroits en raison d'un faible amortissement, l'or équilibre stabilité chimique et résonances visibles–NIR, et le cuivre présente des résonances plus larges dues aux transitions interbandes [18].

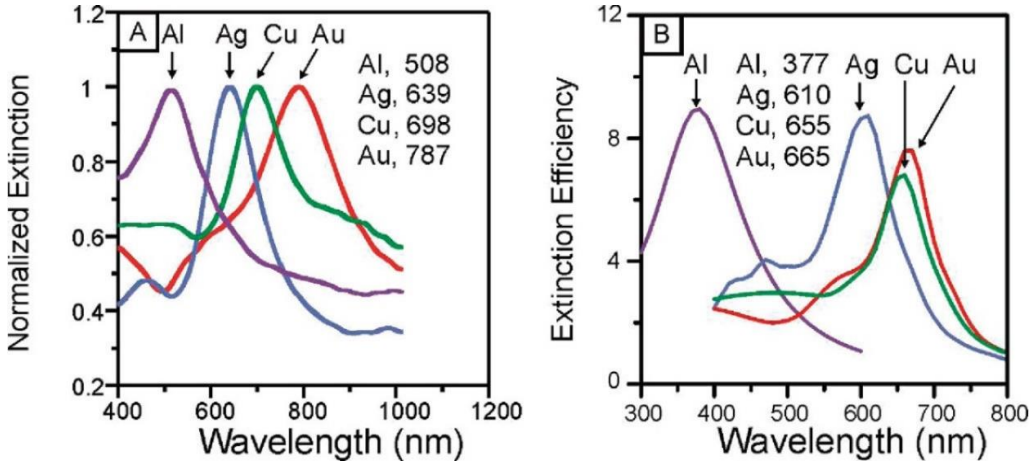

Figure 4: Spectres d'extinction expérimentaux (A) et théoriques (B) pour des réseaux de nanoparticules d'Al, Cu, Ag et Au. La figure illustre comment le choix du métal influence la longueur d'onde de résonance, la largeur spectrale et l'intensité [18].

Cette comparaison montre que les métaux nobles, en particulier l'or et l'argent, restent les plus efficaces pour l'exaltation Raman. L'aluminium et le cuivre trouvent des applications plus

spécifiques [19,20]. Enfin, les alliages (ex. Au–Ag) permettent d'ajuster la résonance en combinant la stabilité de l'or avec la netteté spectrale de l'argent.

Effets de l'environnement (version condensée)

Le milieu diélectrique entourant les nanoparticules influence également la LSPR [21]. Une augmentation de l'indice de réfraction entraîne un décalage vers le rouge du pic de résonance. Ce principe est fondamental pour les capteurs plasmoniques, où de faibles variations environnementales se traduisent par des signatures optiques mesurables.

Spectroscopie Raman amplifiée par pointe (TERS)

Le dépassement de la limite de diffraction de la lumière, définie par le critère d'Abbe, a conduit au développement de méthodes optiques en champ proche. Parmi elles, la spectroscopie Raman amplifiée par pointe, plus connue sous son acronyme TERS (issu de l'anglais Tip-Enhanced Raman Spectroscopy), s'est imposée comme l'une des techniques nanospectroscopiques les plus puissantes. Elle combine la spécificité moléculaire de la diffusion Raman avec la résolution spatiale nanométrique offerte par les microscopies à sonde locale.

En TERS, une pointe métallique — généralement en or (Au) ou en argent (Ag) — est placée à quelques nanomètres de la surface de l'échantillon. Lorsqu'elle est illuminée par un faisceau laser lointain (E_0), l'apex métallique soutient des résonances plasmoniques de surface localisées (LSPR), qui confinent et amplifient le champ électromagnétique (EM) pour générer un champ proche intense ($E_{loc} = gE_0$), où g est le facteur d'amplification. Plusieurs mécanismes contribuent à cette amplification:

- l'effet de pointe (*lightning rod effect*), qui concentre les charges à l'extrémité de la pointe[22].
- le gap-TERS, où la présence d'un substrat métallique crée une nanocavité entre la pointe et l'échantillon, renforçant le confinement [23].
- l'amplification chimique, liée aux transferts de charge entre les molécules adsorbées et la surface métallique [24–27].
- et l'amplification par LSPR, qui maximise la résonance entre le faisceau incident et les modes plasmoniques [28].

La synergie de ces effets permet d'obtenir des volumes sondés extrêmement réduits, allant jusqu'à la détection de molécules uniques, tout en acquérant simultanément des cartes

topographiques et chimiques. Dans ce contexte, le facteur global d'amplification est souvent résumé par la dépendance en E^4:

$$g_{TERS}(\omega_1) \approx \frac{|E_{loc}(\omega_{loc})|^4}{|E_0|^4} \quad 5$$

Cette relation souligne l'extrême sensibilité de la TERS, avec des amplifications théoriques pouvant atteindre 10^{12}, et des valeurs expérimentales plus courantes comprises entre 10^4 et 10^8 [29,30]. Le champ proche décroît très rapidement avec la distance selon une loi approchée $E \propto {}^{1}/_{(d+r)^{10}}$, où r est le rayon de courbure de la pointe et d la séparation pointe–échantillon, garantissant ainsi un confinement spatial exceptionnel [30,31]. Une estimation pratique de l'amplification, tenant compte des artefacts du champ lointain, a été proposée par Kumar et collaborateurs. Elle conduit à :

$$g = \left(\frac{I_{TERS} - I_{champ\ lointain}}{I_{champ\ lointain}}\right) \cdot \left(\frac{d}{\left(1.22\frac{\lambda}{NA}\right)}\right)^2 \quad 6$$

où I_{TERS} et $I_{champ\ lointain}$ sont les intensités Raman mesurées avec la pointe engagée ou rétractée, $I_{champ\ lointain}$ est le diamètre effectif de l'interaction en champ proche, λ la longueur d'onde d'excitation, et NA l'ouverture numérique de l'objectif. Le terme $1.22\frac{\lambda}{NA}$ correspond au diamètre de la tache de diffraction en champ lointain. Ainsi, grâce à la combinaison de l'effet de pointe, du confinement gap-mode, des interactions chimiques, et des résonances plasmoniques localisées, la TERS constitue un outil incontournable pour la spectroscopie vibrationnelle à l'échelle nanométrique, reliant imagerie de haute résolution et sensibilité moléculaire.

Les Pérovskites

Les oxydes pérovskites, de formule générale ABO_3, constituent une famille de matériaux à la fois structurellement polyvalents et fonctionnellement riches, qui occupent une place centrale dans la science des matériaux contemporaine [32–34]. Leurs propriétés physiques et chimiques particulières proviennent du réseau d'octaèdres BO_6 à coins partagés, lequel offre une flexibilité cristalline exceptionnelle capable d'accueillir une large variété de cations en sites A et B [35,36]. Cette adaptabilité structurelle permet une gamme étendue de distorsions, de transitions de phase et de réponses fonctionnelles, soutenant des applications allant de l'électronique et de l'optique à la catalyse et aux technologies énergétiques. Parmi ces matériaux, le titanate de strontium ($SrTiO_3$) et le titanate de baryum ($BaTiO_3$) représentent deux exemples prototypiques. Le $SrTiO_3$

est paraélectrique à température ambiante [37–39], ses propriétés étant fortement influencées par la terminaison de surface et les perturbations extérieures, tandis que le $BaTiO_3$ est un oxyde ferroélectrique classique présentant des transitions de phase bien définies en fonction de la température.

La chimie de surface des oxydes pérovskites revêt une importance cruciale, notamment dans la catalyse, la croissance de couches minces et les dispositifs de détection. Les surfaces du $SrTiO_3$ peuvent se terminer soit par des couches de SrO soit par des couches de TiO_2, chacune présentant une réactivité spécifique vis-à-vis d'espèces atmosphériques comme H_2O et CO_2 [40–42]. Des reconstructions de surface ainsi que la formation spontanée de couches carbonatées modifient de manière significative le paysage électronique et chimique de ces matériaux. De leur côté, les nanoparticules de $BaTiO_3$ subissent des transformations dépendantes de la phase et de la taille, qui influencent fortement leurs propriétés ferroélectriques et leur comportement vis-à-vis de l'adsorption [43,44]. Comprendre comment les terminaisons de surface et les mécanismes d'adsorption modifient les réponses fonctionnelles est essentiel pour faire progresser leurs applications technologiques.

Structure et polyvalence des pérovskites ABO_3

La structure archétypale pérovskite consiste en un réseau tridimensionnel d'octaèdres BO_6 à coins partagés, les grands cations A occupant des cavités cuboctaédriques à 12 coordinations. Dans la maille cubique idéale (groupe d'espace Pm3m), le cation A est localisé au centre, le cation B aux sommets du cube et les anions oxygène au centre des faces [45–47]. Cette organisation hautement symétrique permet une flexibilité compositionnelle remarquable, capable d'accueillir des cations de tailles et de charges variées tout en préservant l'intégrité structurelle [48]. La Figure 5 illustre la structure cubique idéale d'un oxyde pérovskite, en prenant l'exemple du $BaTiO_3$. Les grandes sphères vertes représentent les cations A (par ex. Ba^{2+}), les sphères bleues correspondent aux cations B (par ex. Ti^{4+}), et les sphères rouges indiquent les atomes d'oxygène placés aux sommets des octaèdres. La connectivité par coins partagés des octaèdres constitue la signature de la structure pérovskite et explique sa capacité à supporter une grande diversité de phénomènes physiques.

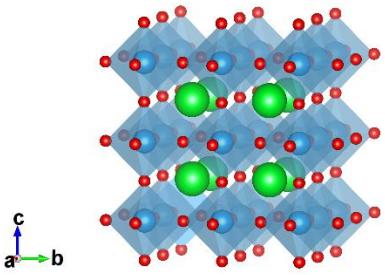

Figure 5: Structure cubique idéale d'une pérovskite ABO_3 (illustrée ici pour le $BaTiO_3$ en phase cubique). Les sphères bleues représentent les cations du site B (par ex. Ti^{4+}) situés au centre des octaèdres O_6 (rouges). Les grandes sphères vertes sont les cations du site A (par ex. Ba^{2+}) occupant des cavités cuboctaédriques à 12 coordinations.

Cette charpente structurale est intrinsèquement flexible. De légères distorsions de l'archétype cubique, vers des variantes tétragonales, orthorhombiques ou rhomboédriques, apparaissent fréquemment en raison de différences de taille ionique ou d'effets électroniques. Plus important encore, la substitution ou le dopage sur les sites A ou B permet un ajustement fin des propriétés ferroélectriques, piézoélectriques, électroniques et catalytiques. De ce fait, les pérovskites constituent une plateforme universelle pour les oxydes multifonctionnels, allant des ferroélectriques et diélectriques à haute permittivité aux supraconducteurs et catalyseurs.

Titanate de strontium ($SrTiO_3$)

Le $SrTiO_3$ cristallise dans la structure cubique pérovskite, avec un paramètre de maille d'environ 3,905 Å. À température ambiante, il est centro-symétrique et paraélectrique, sans polarisation spontanée [49]. À basse température, il approche d'une instabilité ferroélectrique, mais les fluctuations quantiques suppriment l'ordre polaire à longue portée, maintenant le matériau paraélectrique jusqu'aux températures cryogéniques. Le $SrTiO_3$ est un isolant électrique avec un gap électronique d'environ 3,3 eV, qui peut toutefois devenir conducteur par dopage ou introduction de lacunes d'oxygène [50]. Son indice de réfraction élevé et sa compatibilité avec l'épitaxie d'oxydes en font un substrat de référence pour la croissance de couches minces.

La surface (100) du $SrTiO_3$ peut être terminée soit par une couche de SrO, soit par une couche de TiO_2. Les deux terminaisons sont électriquement neutres mais chimiquement distinctes. La terminaison TiO_2 est souvent privilégiée pour le dépôt de couches minces, tandis que la terminaison SrO se montre beaucoup plus réactive vis-à-vis des gaz atmosphériques. Sous conditions ambiantes, les surfaces terminées par SrO adsorbent fortement le CO_2, formant des espèces carbonatées stables. Cette adsorption peut modifier la structure électronique, induire des reconstructions de surface et altérer l'énergie de surface. En revanche, les surfaces

terminées par TiO_2 interagissent beaucoup plus faiblement avec le CO_2, l'adsorption étant principalement limitée aux défauts comme les lacunes d'oxygène [51,52]. Cette chimie de surface dépendante de la terminaison joue un rôle déterminant en catalyse, dans les interfaces de dispositifs électroniques et dans la croissance de couches minces.

Titanate de baryum ($BaTiO_3$)

Le $BaTiO_3$ est la pérovskite ferroélectrique par excellence. À l'état massif, il présente une série de transitions structurales en fonction de la température : cubique paraélectrique → tétragonale ferroélectrique → orthorhombique ferroélectrique → rhomboédrique ferroélectrique. En phase tétragonale, à température ambiante, l'ion Ti^{4+} se déplace de sa position centrale au sein de l'octaèdre O_6, générant une polarisation spontanée. Cette distorsion structurelle engendre des modes phononiques Raman intenses et des propriétés piézoélectriques marquées.

À l'échelle nanométrique, le $BaTiO_3$ subit une suppression de la ferroélectricité, connue sous le nom de limite superparaélectrique. Les nanoparticules de moins de 20 nm perdent souvent leur ordre ferroélectrique, adoptant une structure cubique paraélectrique même à température ambiante [53,54]. Cette suppression résulte d'une combinaison d'effets : augmentation de l'énergie de surface, champs dépolarisants et volume insuffisant pour stabiliser des domaines ferroélectriques. Les études par spectroscopie Raman et diffraction des rayons X montrent un affaiblissement des modes phononiques ferroélectriques et la fusion des pics de diffraction tétragonaux avec la diminution de la taille des particules [55–57]. Ces observations illustrent le rôle critique de la taille, de l'énergie de surface et des distorsions locales dans la stabilisation de la ferroélectricité.

Les surfaces du $BaTiO_3$ présentent également une réactivité marquée. Les régions terminées par BaO adsorbent facilement le CO_2, formant des couches de $BaCO_3$. Ces couches agissent comme des barrières passivantes, modifiant les propriétés diélectriques et parfois inhibant la croissance des grains dans les céramiques. Pour les nanoparticules, l'effet est amplifié, des couches monomoléculaires de carbonates se formant spontanément à l'air ambiant [58]. Ce comportement influe directement sur l'interprétation des propriétés ferroélectriques à l'échelle nanométrique, car l'adsorption de surface peut neutraliser la polarisation ou modifier les paramètres de maille.

Exploration des pérovskites par TERS

Les propriétés structurelles et de surface uniques du $SrTiO_3$ et du $BaTiO_3$ en font des systèmes idéaux pour une exploration par TERS (Tip-Enhanced Raman Spectroscopy, spectroscopie Raman amplifiée par pointe). Cette technique combine l'imagerie topographique locale et la

spectroscopie vibrationnelle avec une résolution nanométrique, permettant de détecter des empreintes vibratoires issues de monocouches ou d'espèces adsorbées, invisibles pour les méthodes Raman conventionnelles.

Dans le cadre de cette thèse, les recherches menées par TERS sur les surfaces de $SrTiO_3$ et $BaTiO_3$ ont conduit à trois résultats majeurs, chacun ayant donné lieu à un article scientifique constituant respectivement les chapitres 4, 5 et 6 :

- Chapitre 4 : Analyse par TERS des nanoparticules de $BaTiO_3$, mettant en évidence la présence de monocouches carbonatées issues de l'adsorption du CO_2 atmosphérique et l'activation de modes infrarouges rendus visibles dans le spectre Raman, révélant des effets de rupture locale de symétrie.
- Chapitre 5 : Étude de la limite superparaélectrique dans le $BaTiO_3$, démontrant la suppression dépendante de la taille des modes Raman ferroélectriques et corrélant ces évolutions avec la perte de l'ordre polaire.
- Chapitre 6 : Investigation de l'adsorption carbonatée sur les surfaces (100) du $SrTiO_3$, permettant de distinguer la réactivité propre à chaque terminaison et d'identifier comment la formation de carbonates influence les reconstructions de surface, la délamination locale et les mécanismes de stabilisation électrostatique.

Ces trois études montrent comment le TERS apporte une vision unique des phénomènes chimiques et structuraux à l'échelle nanométrique, reliant directement les processus de surface aux propriétés fonctionnelles, avec des implications majeures pour l'électronique, la catalyse et les technologies énergétiques.

Système TERS

Les expériences de spectroscopie Raman exaltée par effet de pointe présentées dans ce travail ont été réalisées à l'aide d'un microscope à sonde locale SmartSPM (AIST-NT Inc.), un instrument commercial conçu pour les études optiques en champ proche. Ce système intègre à la fois un balayage mécanique de grande amplitude (5 mm × 5 mm × 18 mm) et un balayage piézoélectrique de haute résolution (100 µm × 100 µm × 15 µm), avec une boucle de rétroaction fermée permettant d'atteindre une précision verticale (axe z) de l'ordre de 0,1 nm, tandis que la résolution latérale (axes x–y) reste limitée par le rayon de la pointe, généralement de quelques nanomètres. Ce niveau de contrôle est essentiel pour maintenir une séparation pointe–échantillon à l'échelle nanométrique durant de longues acquisitions Raman.

La fonctionnalité TERS repose sur l'utilisation de pointes plasmoniques. Dans ce travail de thèse, des pointes en or ont été utilisées en raison de leurs propriétés plasmoniques favorables, de leur stabilité chimique et de leur reproductibilité. Toutes les pointes ont été fabriquées au laboratoire par une gravure électrochimique de fils d'or massif, suivie d'un rinçage et d'un séchage afin d'obtenir des géométries coniques lisses avec des rayons d'apex de l'ordre de 10–20 nm. Après fabrication, les pointes ont été fixées sur des diapasons de quartz (AB38T32.768 kHz, Abracon) à l'aide d'un adhésif polymérisable aux UV (NOA68, Norland Optical Adhesives). Les diapasons fonctionnaient en mode de force de cisaillement avec rétroaction en amplitude, atteignent généralement des facteurs de qualité supérieurs à 2000. La dérive en fréquence est reste inférieure à 0,02 Hz/min, ce qui correspond à une stabilité de la pointe d'environ 0,25 nm lors de balayages prolongés.

L'excitation optique a été assurée par un laser hélium–néon (He–Ne) linéairement polarisé à 632,8 nm (CVI Melles Griot 25-LHP-928-249), dont la longueur d'onde coïncide avec la résonance plasmonique de surface localisée des pointes en or. Le système employait une géométrie d'illumination latérale avec un objectif Mitutoyo Plan Apochromat (NA 0,70, distance de travail 6,0 mm) positionné à un angle de 65° par rapport à l'axe de la pointe. Le faisceau laser était conditionné par un filtre de densité neutre, un expanseur de faisceau et une lame demi-onde rotative, avant d'être réfléchi dans l'objectif via un miroir dichroïque. Le signal Raman rétrodiffusé était collecté par le même objectif, transmis dans un spectromètre Czerny–Turner (focale 520 mm, réseaux de 150, 600 et 1800 traits/mm), puis détecté par une caméra CCD refroidie thermoélectriquement (Andor iDus 420 BU, refroidie à –80 °C). Cette configuration offre une résolution spectrale d'environ 2 cm^{-1} par pixel à 632,8 nm, permettant d'effectuer des cartographies Raman de haute qualité en champ proche.

Fabrication et géométrie des pointes TERS

La reproductibilité de l'exaltation TERS dépend de manière critique de la géométrie de la pointe. Les pointes en or ont été fabriquées selon une méthode électrochimique en deux étapes : une étape DC pour un amincissement rapide du fil, suivie d'une étape pulsée pour affiner l'apex. Un circuit électronique de coupure automatique interrompt le processus de gravure au moment de la « chute » du fil, évitant le sur-attaque et garantissant la formation d'apex reproductibles.

Les pointes obtenues ont été caractérisées par microscopie électronique à balayage (MEB). Comme illustré dans la Figure 6, les sondes présentent des apex aigus avec des rayons d'environ 11 nm, des profils coniques lisses et des demi-angles compris entre ~20° et 30°. Ces caractéristiques géométriques sont particulièrement adaptées pour générer un confinement

électromagnétique intense à l'apex tout en assurant une robustesse mécanique lors des balayages.

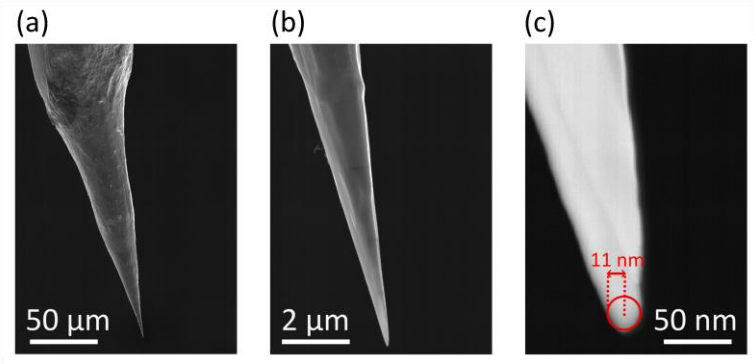

Figure 6: Images MEB représentatives d'une pointe en or obtenue par gravure électrochimique avec coupure électronique contrôlée. (a–c) montrent la géométrie globale, la texture de surface et l'apex affûté. Le rayon de l'apex est d'environ 11 nm, optimisé pour une exaltation plasmonique forte et une résolution spatiale élevée.

Étalonnage avec des nanotubes de carbone

Afin de valider les performances du système TERS avant l'étude de matériaux plus complexes tels que les oxydes pérovskites, des nanotubes de carbone monofeuillets (SWCNTs) ont été choisis comme échantillons de référence. Les CNTs constituent un système test idéal car leurs diamètres (~1–2 nm) sont beaucoup plus petits que le foyer limité par diffraction, ils présentent une forte réponse Raman résonante à 632,8 nm, et leurs modes vibrationnels sont stables et bien connus.

Les CNTs ont été déposés sur des lames de verre recouvertes d'une couche d'or. Une couche d'or de 50 nm a été déposée par pulvérisation cathodique, puis recuite à 550 °C, réduisant la rugosité de surface de ~0,66 nm à ~0,2 nm RMS. Cette surface recuite offrait de larges terrasses planes, favorables à l'exaltation en mode « gap ». Les CNTs ont ensuite été déposés par dépôt goutte à partir d'une solution bien dispersée, donnant une distribution clairsemée avec une densité d'environ 2 CNTs/µm^2.

La microscopie à force atomique a confirmé la présence de structures linéaires isolées correspondant à des CNTs individuels, avec des longueurs allant de 100 nm à plusieurs micromètres. Cette distribution clairsemée était idéale pour les mesures TERS, permettant de sonder sélectivement des nanotubes individuels sans interférence significative du fond. Les cartographies TERS ont été acquises sur des zones de 500×500 nm² avec des grilles de 64×64 pixels, correspondant à une résolution spatiale d'environ 8 nm. La Figure 7 présente une image

AFM topographique (panneau a) ainsi que les cartes TERS correspondantes pour l'intensité de la bande G (panneau b) et de la bande D (panneau c).

Les résultats démontrent clairement une forte corrélation entre la topographie du nanotube et le signal Raman localisé. La bande G, qui correspond aux vibrations d'élongation C–C, est confinée de manière très localisée au CNT, confirmant l'origine nanométrique de l'exaltation. La résolution spatiale obtenue (~8 nm) est près de deux ordres de grandeur inférieure à la limite de diffraction (~1100 nm), soulignant la capacité du TERS à franchir la barrière de diffraction.

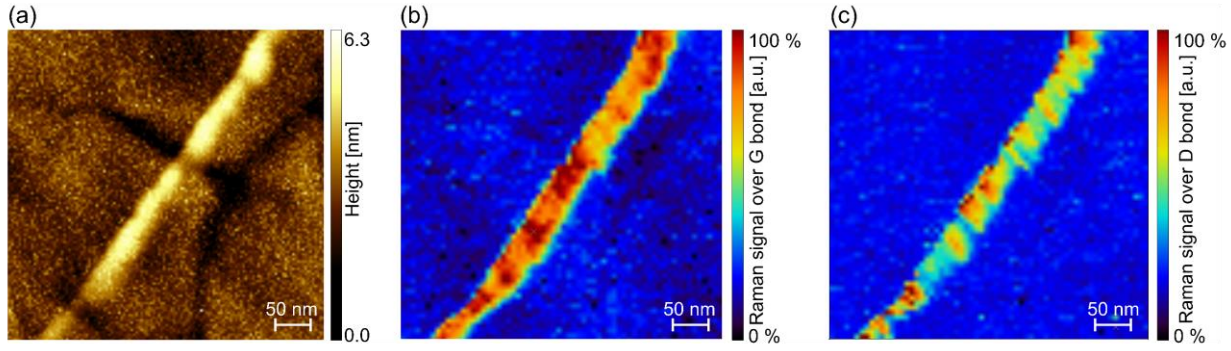

Figure 7: (a) Image AFM en hauteur d'un CNT unique déposé sur un substrat d'or recuit. (b) Carte TERS de l'intensité de la bande G (1550–1650 cm^{-1}). (c) Carte TERS de l'intensité de la bande D (1300–1400 cm^{-1}). Les cartes Raman en champ proche démontrent une localisation nanométrique des modes vibrationnels avec une résolution spatiale d'environ 8 nm.

Modes Raman des CNTs

Pour améliorer le rapport signal/bruit, les spectres Raman de cinq pixels adjacents le long du nanotube ont été moyennés. Le spectre résultant, présenté dans la Figure 3.14, met en évidence les principales signatures vibrationnelles des CNTs. La bande G se dédouble en composantes G^+ et G^-, correspondant respectivement aux modes phononiques optiques longitudinaux (LO) et transverses (TO), sensibles à la chiralité du tube. La bande D (~1325 cm^{-1}) révèle la présence de désordre structural localisé [59], tandis que la bande M (~1750 cm^{-1}) est associée aux singularités de van Hove et à la rupture de symétrie induite par la courbure [60].

De plus, le mode de respiration radiale (RBM) observé à 196 cm^{-1} permet d'estimer le diamètre à l'aide de la relation empirique [61]:

$$\upsilon_{RBM} = \frac{234}{d} - 10 \qquad 7$$

À partir de ce mode, le diamètre du CNT a été calculé à ~1,26 nm, en accord avec les spécifications du fournisseur.

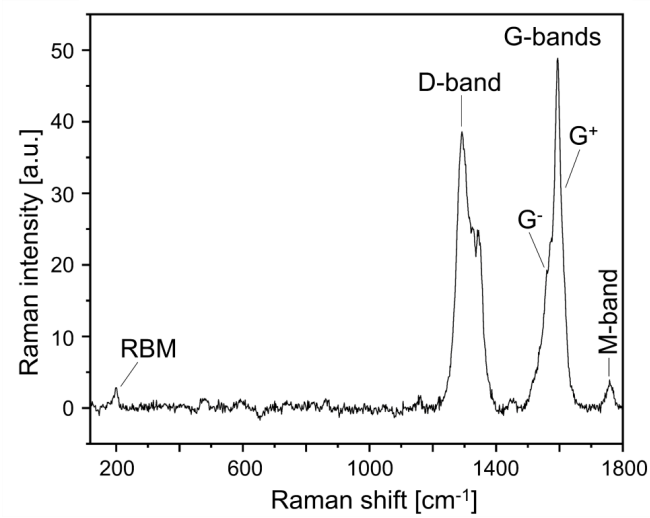

Figure 8: Spectre TERS obtenu par moyennage du signal Raman sur cinq pixels adjacents le long d'un CNT. On distingue clairement le dédoublement de la bande G, la bande D (~1325 cm^{-1}), la bande M (~1750 cm^{-1}) ainsi que le mode de respiration radiale (RBM) à 196 cm^{-1} correspondant à un diamètre de ~1,26 nm.

Afin de confirmer que l'exaltation Raman observée provient bien du champ proche à l'apex de la pointe, des mesures de type spec-stack ont été réalisées en rétractant progressivement la pointe du nanotube. Comme le montre la Figure 9 (a), le signal Raman décroît rapidement lorsque la distance pointe–échantillon augmente de 0 à 20 nm. Les spectres représentatifs de la Figure 9 (b) montrent l'intensité de la bande G à trois positions : directement sur le CNT (0 nm), légèrement déplacée (~2 nm), et éloignée de la surface (~100 nm). La chute d'intensité nette confirme que l'exaltation est bien confinée au nano-junction et régie par le confinement plasmonique.

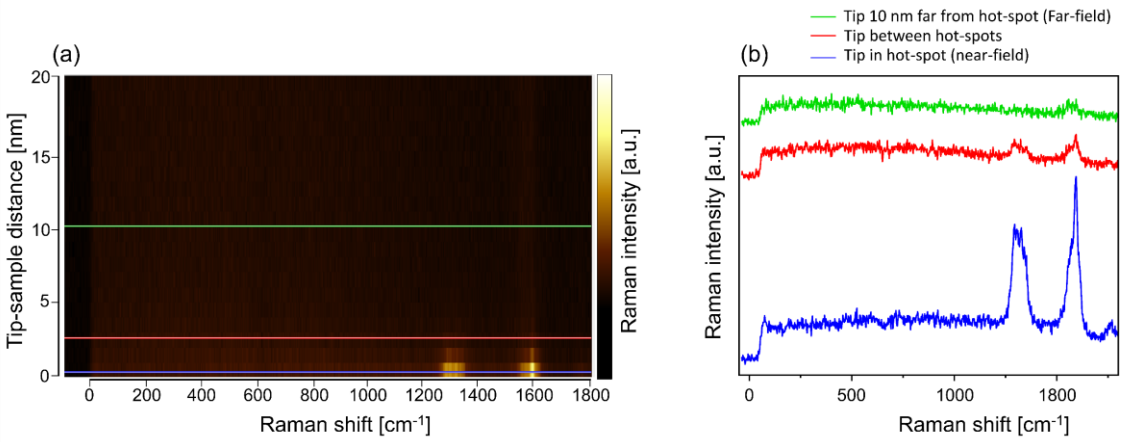

Figure 9: (a) Carte spec-stack montrant la décroissance du signal Raman lorsque la pointe TERS est rétractée de 0 à 20 nm au-dessus d'un CNT. (b) Spectres Raman acquis à trois positions de la pointe : directement sur le CNT (0 nm, bleu), légèrement déplacée (~2 nm, vert), et loin du CNT (~100 nm, rouge). Les résultats confirment l'origine en champ proche de l'exaltation.

Le facteur d'exaltation (EF) constitue une mesure quantitative de l'amplification du signal Raman en TERS. Pour la bande G des CNTs, le rapport champ proche/champ lointain était d'environ 7. En utilisant l'expression :

$$g = \left(\frac{I_{TERS} - I_{far\text{-}field}}{I_{far\text{-}field}}\right) \cdot \left(\frac{A_{far\text{-}field}}{A_{TERS}}\right) \quad 8$$

l'EF a été estimé à ~4,2 × 10^4. Cela correspond à un facteur d'amplification de champ électrique:

$$E_{enh} = g^{1/4} \approx 14{,}3 \quad 9$$

Ces valeurs sont cohérentes avec celles attendues pour des pointes plasmoniques en or de haute qualité en configuration gap-mode, confirmant que le système AIST-NT atteint une amplification suffisante pour sonder des modes vibrationnels faibles à l'échelle nanométrique.

Article de recherche I – Observation directe de la chimisorption de carbonate sur les surfaces de titanate de baryum par spectroscopie Raman améliorée par la pointe (TERS, Tip-Enhanced Raman Spectroscopy)

Le titanate de baryum ($BaTiO_3$) est un oxyde ferroélectrique de référence qui présente une permittivité diélectrique élevée, des propriétés piézoélectriques et pyroélectriques, ainsi qu'un effet photovoltaïque en volume lié à sa structure non centro-symétrique à température ambiante. Ces propriétés multifonctionnelles rendent le $BaTiO_3$ particulièrement pertinent pour des applications variées, notamment dans les condensateurs, dispositifs mémoire, capteurs et procédés photocatalytiques [62–66]. Toutefois, au-delà des propriétés de volume, la chimie de surface du $BaTiO_3$ joue un rôle déterminant dans ses performances fonctionnelles. En particulier, la chimisorption du dioxyde de carbone atmosphérique, conduisant à la formation de monocouches carbonatées sur les surfaces de $BaTiO_3$, peut modifier la réactivité, les voies catalytiques et la stabilité. Bien que la théorie ait depuis longtemps suggéré la prévalence d'une telle adsorption carbonatée, les preuves expérimentales directes à l'échelle nanométrique sont restées limitées en raison des contraintes de résolution des techniques classiques d'analyse de surface [67,68]. Dans ce travail, nous employons la spectroscopie Raman améliorée par la pointe avec des pointes plasmoniques en or afin de sonder directement la chimisorption du carbonate sur des nanoparticules de $BaTiO_3$, atteignant une sensibilité monomoléculaire et une résolution spatiale de l'ordre du nanomètre.

Résultats et discussion

Afin d'établir les bases structurales et morphologiques, la diffraction des rayons X (XRD) et la microscopie électronique en transmission (TEM) ont d'abord été utilisées. Le diagramme de diffraction confirme la phase tétragonale du $BaTiO_3$, avec des pics caractéristiques correspondant aux standards de référence, tandis que les images TEM révèlent des nanoparticules quasi sphériques de taille moyenne ~25 ± 5 nm. Ces dimensions sont cohérentes avec la phase tétragonale ferroélectrique et fournissent un système adapté à l'étude des modifications de surface. Il est important de noter que le spectre de diffraction montre également un faible pic associé au carbonate, en accord avec l'adsorption de CO_2 atmosphérique sur les facettes terminées par BaO [69]. Bien que ces résultats préliminaires suggèrent la présence d'une contamination carbonatée, ils manquent de la sensibilité chimique et spatiale nécessaire pour identifier des monocouches, ce qui souligne la pertinence de la TERS.

Les mesures TERS ont été effectuées sur des nanoparticules de $BaTiO_3$ déposées sur des substrats en verre recouverts d'une fine couche d'or. La Figure 10 (a) montre un balayage topographique sur une zone de 200 × 200 nm^2 obtenu en mode de force de cisaillement, révélant une nanoparticule d'environ 12 nm de hauteur. Le profil correspondant (Figure 10 (b)) confirme la taille et la morphologie, tandis que la Figure 10 (c) présente la cartographie TERS enregistrée simultanément sur la même région. La distribution d'intensité spectrale autour de 480–540 cm^{-1}, assignée au mode phononique TO_4 du $BaTiO_3$, se corrèle spatialement avec la localisation de la nanoparticule, démontrant ainsi la capacité de la TERS à identifier chimiquement des nanoparticules individuelles au-delà de la limite de diffraction confocale.

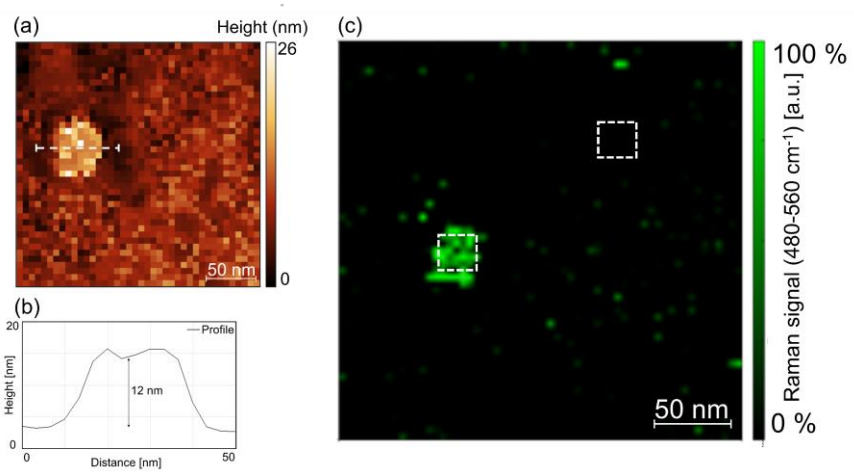

Figure 10: (a) Balayage topographique sur une région de 200 nm x 200 nm avec 60 x 60 pixels révélant une nanoparticule individuelle de titanate de baryum. (b) Profil indiquant la taille de la particule mesurée le long de la ligne blanche pointillée en (a). (c) Cartographie TERS acquise simultanément dans la même zone que (a) révélant un signal intense dans la gamme spectrale 480 - 540 cm^{-1} à la position de la nanoparticule avec un pas de 3,3 nm.

Pour évaluer quantitativement l'amplification, des spectres ont été moyennés sur la région de la nanoparticule et comparés à ceux provenant du substrat en or nu. Alors que le signal issu de la surface d'or reste au niveau du bruit, un spectre champ proche net et bien défini apparaît sur la nanoparticule, montrant clairement les modes vibrationnels du $BaTiO_3$. Le facteur d'amplification (EF) a été calculé selon la relation [70]:

$$EF = \frac{I_{NF} - I_{FF}}{I_{FF}} \times \frac{A_{FF}}{A_{NF}} \quad 10$$

où I_{NF} et I_{FF} représentent les intensités enregistrées en champ proche et en champ lointain, tandis que A_{NF} et A_{FF} correspondent aux aires effectives d'interaction. En considérant un diamètre de pointe d'environ 10 nm et une taille de tache confocale de ~1,1 µm, un EF de ~4,6 × 10^5 est obtenu, correspondant à un facteur d'amplification de champ local d'environ 26 selon l'approximation en E^4. Cette valeur dépasse largement celles rapportées dans la littérature (~10^2–10^3), soulignant le fort effet plasmonique atteint avec les pointes en or de notre système [71,72].

Pour valider les assignations spectrales, le spectre

de la nanoparticule a été comparé à des mesures Raman confocales sur le $BaTiO_3$ massif. Comme illustré dans la Figure 11, les deux spectres présentent les pics Raman caractéristiques du $BaTiO_3$ tétragonal dans la gamme 100–800 cm^{-1}, incluant les modes A1(TO) et E(TO). Fait essentiel, le spectre champ proche révèle également une intensification du pic carbonaté à ~1060 cm^{-1}, cohérente avec la chimisorption du CO_2 formant du $BaCO_3$ de surface. Cela démontre que la TERS permet non seulement de résoudre les modes vibrationnels intrinsèques du $BaTiO_3$ mais aussi de détecter avec une grande sensibilité les espèces carbonatées adsorbées en monocouche.

Au-delà de la détection du carbonate, des bandes vibrationnelles supplémentaires apparaissent dans les spectres champ proche à ~1260, 1449 et 1550 cm^{-1}. Absentes des mesures lointaines, elles correspondent à des modes actifs en infrarouge (IR) du $BaTiO_3$ et des espèces carbonatées. Leur activation en TERS est attribuée à l'effet Raman de champ de gradient (GFR, gradient field Raman), qui se manifeste lorsque de forts gradients de champ électrique local au sommet de la pointe modifient les règles de sélection Raman. Selon Ayars et Hallen, le moment dipolaire induit peut être exprimé par [73]:

$$\mu_a = \& \left\{ \underbrace{\left(\frac{d\mu_a^p}{dQ}\right)_0}_{IR\ absorption} + \underbrace{\left(\frac{d\alpha_{ab}}{dQ}\right)_0 E_b}_{Raman} + \underbrace{\alpha_{ab}\left(\frac{dE_b}{dQ}\right)_0}_{gradient\ field\ Raman\ (GFR)} + \underbrace{\frac{1}{3}\frac{\partial E_b}{\partial c}\left(\frac{dA_{abc}}{dQ}\right)_0}_{quadrupole\ Raman} \right\} Q \qquad 11$$

où α décrit le tenseur de polarisabilité, Q désigne la coordonnée vibrationnelle, (a, b, c) se réfèrent aux coordonnées spatiales (x, y, z), μ^p décrit le moment dipolaire permanent et A est un tenseur qui détermine le dipôle induit par un gradient de champ ainsi que le quadrupôle induit par un champ uniforme. Le troisième terme met en évidence la manière dont les gradients de champ local peuvent activer des modes infrarouges interdits en Raman, apportant des informations uniques sur les distorsions de symétrie et les reconstructions de surface à l'échelle nanométrique.

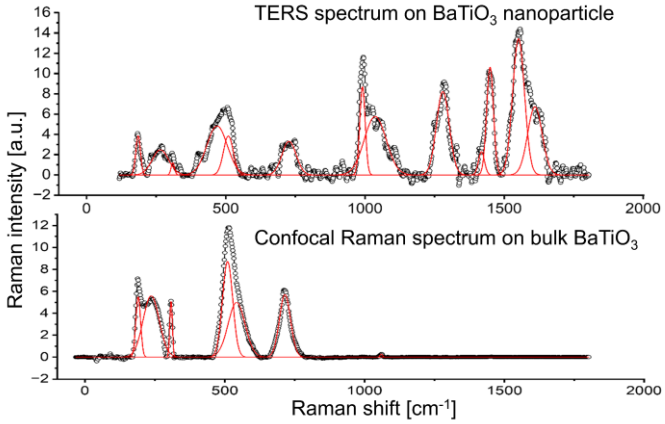

Figure 11: Comparaison du spectre champ proche d'une nanoparticule individuelle de $BaTiO_3$ et du spectre Raman confocal du $BaTiO_3$ massif.

Pour visualiser ces effets de manière spatiale, des cartographies TERS haute résolution ont été acquises sur différentes gammes vibrationnelles. La Figure 12 (a–d) montre les distributions d'intensité des modes carbonatés (~1060 cm^{-1}), 1260 cm^{-1}, 1449 cm^{-1} et 1550 cm^{-1} sur une zone de 200 × 200 nm^2. Ces cartes localisent clairement les signatures vibrationnelles sur les nanoparticules de $BaTiO_3$, excluant toute contribution du substrat en or environnant. Le spectre Raman cumulé de la même région est présenté en Figure 12 (e), confirmant la co-localisation des espèces carbonatées et des nouveaux modes activés.

L'apparition de bandes IR-actives dans les spectres TERS représente une expansion qualitative des capacités de la spectroscopie Raman. En particulier, la bande à 1260 cm^{-1} est attribuée à l'élongation C=O dans COO–Ba, tandis que les pics à 1449 cm^{-1} et 1550 cm^{-1} correspondent respectivement aux vibrations carbonatées asymétriques et à l'élongation du COO^-. Leur présence indique fortement une rupture de symétrie induite par la chimisorption de CO_2 sur les

surfaces de $BaTiO_3$. De plus, la capacité de la TERS à activer et détecter de tels modes démontre son utilité pour étudier les distorsions moléculaires, les reconstructions induites par adsorption et les défauts de surface inaccessibles aux méthodes de champ lointain.

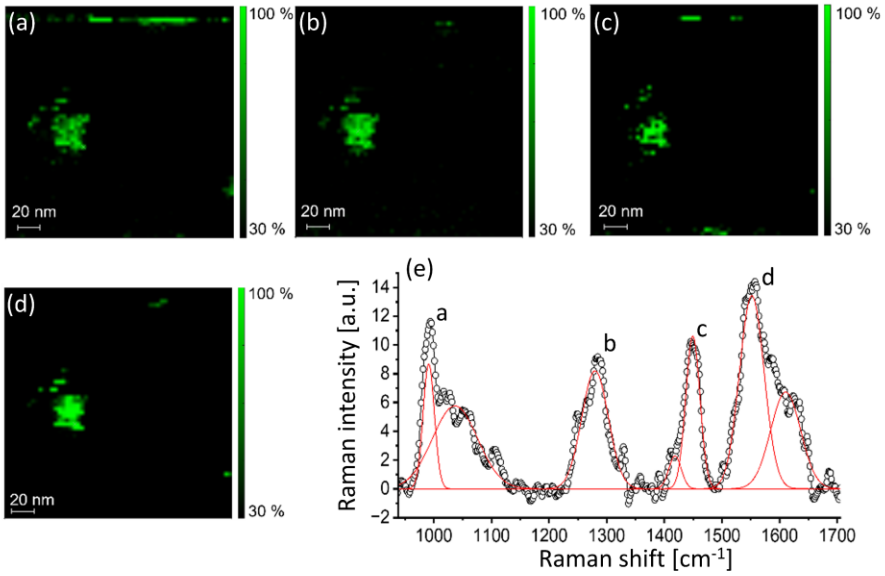

Figure 12: Cartographie TERS d'une nanoparticule de $BaTiO_3$ sur or dans une région de 200 nm x 200 nm, capturée par une matrice de 60 x 60 pixels. L'intensité du signal a été intégrée sur différentes gammes spectrales : (a) pic carbonaté, (b) 1260 cm^{-1}, (c) 1449 cm^{-1}, et (d) 1550 cm^{-1}. Les barres de couleur indiquent les niveaux d'intensité, bornés par les valeurs minimales et maximales avec 0 % représentant le bruit de fond du CCD. (e) Spectre Raman cumulé de la région 200 nm x 200 nm.

Dans l'ensemble, ces résultats démontrent l'extraordinaire sensibilité et la résolution de la TERS pour sonder la chimie de surface du $BaTiO_3$. La combinaison d'un fort effet plasmonique lié aux pointes en or, de l'effet "paratonnerre" et du confinement champ proche a permis l'observation directe de monocouches carbonatées et l'activation de modes infrarouges. Ce travail fournit non seulement une preuve à l'échelle nanométrique de la chimisorption du CO_2 sur le $BaTiO_3$, mais illustre également comment la TERS peut révéler des modes vibrationnels autrement cachés, liés à des ruptures de symétrie. De telles observations sont essentielles pour améliorer la compréhension de la réactivité de surface des pérovskites, avec des implications pour la catalyse, la stabilité environnementale et la fonctionnalisation à l'échelle nanométrique.

Article de recherche II – Transition Ferroélectrique–Paraélectrique Probed par Spectroscopie Raman Améliorée par Pointe (TERS)

L'étude des transitions de phase ferroélectrique–paraélectrique dans le $BaTiO_3$ à l'échelle nanométrique est essentielle pour comprendre comment les effets de taille finie influencent la stabilité de l'ordre ferroélectrique. Lorsque les dimensions se réduisent, les contributions

d'énergie de surface, les champs de dépolarisation et les contraintes mécaniques dominent sur les propriétés de volume, entraînant des modifications de la polarisation et, en fin de compte, la suppression de la ferroélectricité. Ce phénomène est souvent associé à la limite superparaelectrique, en dessous de laquelle la polarisation spontanée ne peut plus être maintenue. Identifier l'apparition de cette transition au niveau d'une particule unique reste un défi critique, car les techniques conventionnelles basées sur des ensembles tendent à moyenner le comportement de plusieurs particules et à masquer la véritable nature des transitions dépendantes de la taille. La spectroscopie Raman améliorée par pointe offre une voie pour ces investigations, car elle permet de sonder directement les modes vibrationnels tout en surveillant simultanément les propriétés diélectriques localisées via les décalages de la résonance plasmonique.

Résultats et discussion

Dans cette étude, la TERS a été utilisée pour sonder des nanoparticules de $BaTiO_3$ de deux tailles différentes, d'environ 44 nm et 18 nm de hauteur. Les mesures révèlent une corrélation directe entre la disparition des signatures Raman ferroélectriques, l'évolution de l'indice de réfraction et la transition structurale de la phase tétragonale ferroélectrique vers la phase cubique paraélectrique. Cette corrélation est établie en combinant l'analyse vibrationnelle Raman avec le suivi de la résonance plasmonique de surface localisée à l'apex d'une pointe plasmonique en or. Ensemble, ces observables offrent une image cohérente de la manière dont les effets de taille finie déstabilisent la ferroélectricité dans les nanocristaux de $BaTiO_3$.

Les spectres Raman des nanoparticules de $BaTiO_3$, présentés dans la Figure 13, mettent en évidence cette transition dépendante de la taille. Plusieurs modes phononiques sont visibles, notamment les vibrations A1(TO), A1(TO2), A1(TO3) et l'adsorption de carbonates à 185, 270, 520 et 1062 cm^{-1}. Parmi ceux-ci, les pics à 306 cm^{-1} et 721 cm^{-1} sont d'un intérêt particulier, car ils constituent des marqueurs spectroscopiques de la ferroélectricité tétragonale. Le mode à 306 cm^{-1} correspond à la vibration B1+E(TO3+LO2), reflétant les étirements et flexions des liaisons Ti–O associés aux distorsions tétragonales, tandis que le mode à 721 cm^{-1} correspond à la vibration A1(LO3+LO4), liée à l'étirement des liaisons Ti–O le long de l'axe polaire. Ces deux modes sont extrêmement sensibles aux distorsions structurelles sous-jacentes à l'ordre ferroélectrique. Une comparaison entre les deux nanoparticules révèle que la particule de 44 nm conserve une forte intensité dans ces deux pics, alors qu'ils sont nettement atténués dans la particule de 18 nm. Cet affaiblissement suggère la suppression des distorsions tétragonales et

l'émergence de la phase cubique, cohérente avec la transition ferroélectrique–paraélectrique induite par l'effet de taille.

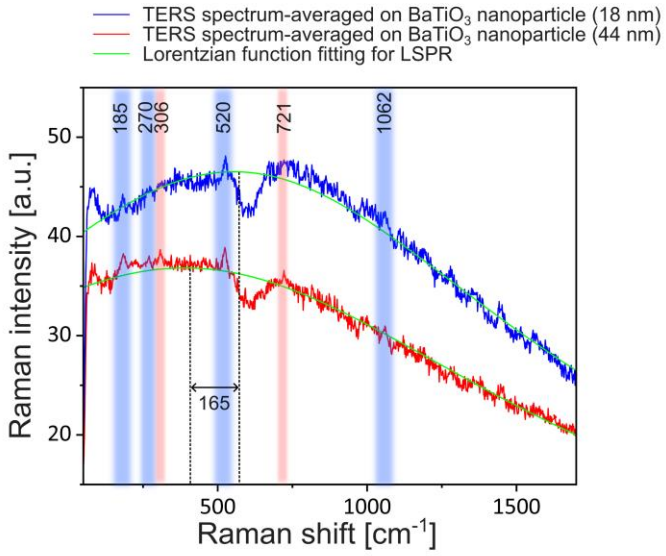

Figure 13: Spectres TERS moyennés sur les nanoparticules de $BaTiO_3$, où le spectre bleu correspond à la nanoparticule de 18 nm et le spectre rouge représente la nanoparticule de 44 nm. La courbe verte illustre l'ajustement de Lorentzienne de la LSPR pour les deux spectres. La ligne noire en pointillés marque le centre du décalage LSPR, indiquant un décalage de 165 cm^{-1} entre les deux nanoparticules.

En plus des modes vibrationnels, les spectres de champ proche ont montré un fond de luminescence plasmonique provenant de la pointe en or. Ce fond est très sensible aux variations diélectriques dans l'environnement immédiat de l'apex de la pointe. Lorsque la phase ferroélectrique se transforme en phase cubique paraélectrique, l'indice de réfraction du $BaTiO_3$ augmente d'environ 0,1 unité, ce qui modifie la constante diélectrique locale et produit un décalage mesurable vers le rouge du pic LSPR de la pointe en or [74]. Les données de la Figure 13 montrent que le pic de luminescence de l'or se décale d'environ 165 cm^{-1} (~7 nm) en comparant la nanoparticule ferroélectrique de 44 nm à la nanoparticule paraélectrique de 18 nm. Selon des simulations antérieures, ce décalage correspond à une augmentation d'environ 0,11 de l'indice de réfraction, en excellent accord avec les valeurs rapportées pour la transition ferroélectrique–paraélectrique en volume. Cet accord quantitatif confirme fortement que le décalage LSPR observé est une signature optique directe de la transition structurale du $BaTiO_3$ à l'échelle nanométrique.

La cartographie TERS révèle en outre l'inhomogénéité spatiale de cette transition. Les cartes d'intensité des modes Raman à 306 cm^{-1} et 720 cm^{-1}, présentées dans la Figure 14, démontrent clairement une suppression localisée des phonons ferroélectriques. Pour la nanoparticule de 18

nm, les deux modes sont fortement réduits sur toute la particule, confirmant sa transition vers la phase cubique. En revanche, la nanoparticule de 44 nm montre une forte intensité dans la plupart des régions mais une suppression marquée sur sa partie inférieure. Cela indique la coexistence de domaines ferroélectriques et paraélectriques au sein de la même particule, avec des frontières de grains ou des champs de contrainte locaux favorisant la déstabilisation de la ferroélectricité. Ces observations révèlent que les transitions de phase induites par la taille ne sont pas uniformes mais nucléent dans des régions particulières avant de se propager à l'ensemble de la particule.

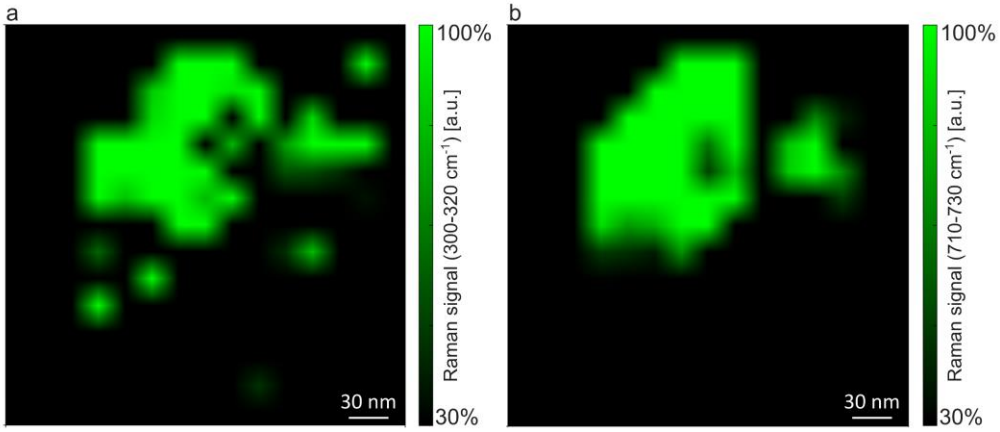

Figure 14: Cartes TERS d'une zone de 300 × 300 nm² de $BaTiO_3$. (a) Pic à 306 cm^{-1} (B1+E(TO3+LO2)), (b) pic à 720 cm^{-1} (A1(LO3+LO4)). Leur suppression révèle la transition tétragonale–cubique. Une baisse d'intensité sur la nanoparticule de 44 nm indique une frontière de grain et des inhomogénéités de phase.

La cartographie de la luminescence plasmonique fournit une confirmation supplémentaire de cette hétérogénéité. Comme illustré dans la Figure 15, un décalage vers le rouge d'environ 7 nm de la LSPR a été observé sur la nanoparticule de 18 nm et sur la partie inférieure de la particule de 44 nm, par rapport aux régions ferroélectriques. Ce décalage correspond à une augmentation d'indice de réfraction d'environ 0,11, renforçant son rôle comme indicateur diélectrique de la transition tétragonale–cubique. Fait intéressant, un léger décalage vers le bleu a été observé dans la région centrale de la particule de 18 nm, suggérant que son cœur conserve un ordre ferroélectrique tétragonal tandis que la coquille a évolué vers la phase cubique. Cette observation est cohérente avec les modèles théoriques prédisant une configuration cœur–coquille dans les nanoparticules ferroélectriques, où des gradients de polarisation stabilisent un cœur ferroélectrique entouré d'une coquille paraélectrique. De tels effets cœur–coquille offrent une explication naturelle à la coexistence de signatures ferroélectriques et paraélectriques dans les petites particules, ainsi qu'aux variations spatiales détectées dans les particules plus grandes.

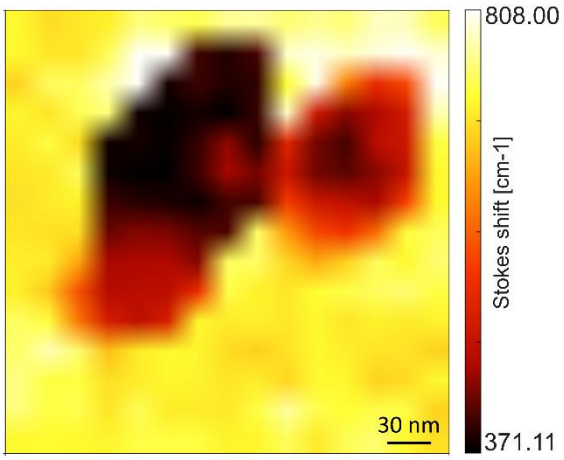

Figure 15: Carte haute résolution du décalage du LSPR sur une nanoparticule de $BaTiO_3$, montrant un décalage vers le rouge d'environ 7 nm ($\Delta n \approx 0{,}11$), associé à la transition tétragonale–cubique.

Les données Raman et LSPR établissent une relation claire entre transition de phase, indice de réfraction et signal TERS. La suppression des modes Raman ferroélectriques marque la perte d'ordre tétragonal, tandis que le décalage simultané vers le rouge du pic LSPR fournit une preuve indépendante du contraste diélectrique associé à la phase cubique. Dans le $BaTiO_3$ massif, l'indice de réfraction augmente d'environ 0,1 unité à travers la transition [75]; ici, les décalages LSPR mesurés correspondent à ~0,11 unité, démontrant que les sondes optiques de champ proche peuvent quantifier cette propriété à l'échelle d'une particule unique. De plus, la cartographie à l'échelle nanométrique révèle que ces transitions ne sont pas uniformes mais influencées par la microstructure locale, les frontières de grains et la stabilisation cœur–coquille, soulignant la complexité de l'instabilité ferroélectrique à dimensions réduites.

Dans l'ensemble, ces résultats montrent que la TERS permet de corréler directement les empreintes vibrationnelles et les propriétés diélectriques, permettant de résoudre les transitions ferroélectrique–paraélectrique à l'échelle nanométrique avec une grande précision spatiale. Pour les nanoparticules de $BaTiO_3$, cette approche révèle que les particules de 18 nm présentent une suppression quasi complète de l'ordre ferroélectrique et une augmentation correspondante de l'indice de réfraction, confirmant la stabilisation de la phase cubique paraélectrique. En revanche, les particules de 44 nm montrent un comportement mixte, avec coexistence de domaines ferroélectriques et paraélectriques. Ces résultats apportent de nouveaux éclairages sur la dynamique des transitions de phase induites par la taille et soulignent la puissance des techniques de champ proche pour démêler l'interaction complexe entre structure, fonction diélectrique et stabilité ferroélectrique dans les oxydes pérovskites à l'échelle nanométrique.

Article de recherche III : Autoréparation des surfaces vicinales (100) du titanate de strontium contaminées par les carbonates, imagées par spectroscopie Raman amplifiée par pointe (TERS)

Le titanate de strontium ($SrTiO_3$) est un oxyde pérovskite présentant des propriétés diélectriques, catalytiques et interfaciaux remarquables. L'un des principaux défis dans l'étude de sa surface réside dans sa forte interaction avec le dioxyde de carbone en conditions ambiantes, interaction susceptible de modifier de manière significative la stabilité des terminaisons de surface. Des investigations à haute résolution sont donc nécessaires pour comprendre comment l'adsorption du CO_2 reconfigure les surfaces de $SrTiO_3$, en particulier sur les orientations vicinales (100) où les terrasses et les marches conditionnent la réactivité chimique. Dans cette étude, nous combinons la spectroscopie Raman amplifiée par pointe avec la microscopie à force atomique pour sonder l'adsorption du CO_2, la reconstruction de surface et les transformations induites par les carbonates. La préparation des échantillons et les traitements complémentaires sont décrits, avec davantage de détails disponibles dans les informations complémentaires.

Préparation des échantillons et structure vicinale de surface

Les substrats de $SrTiO_3$ utilisés étaient des monocristaux commerciaux (CrysTec GmbH), orientés selon le plan (100) avec un angle de désorientation inférieur à 0,5°. Chaque substrat avait des dimensions de 10 × 10 × 0,5 mm et présentait des terrasses associées aux terminaisons alternées SrO et TiO_2. Dans la structure cubique idéale des pérovskites (a_0 = 0,3905 nm), l'empilement alterne entre couches de SrO et de TiO_2, séparées par la moitié du paramètre de maille (~0,20 nm). En pratique, lors des étapes de coupe et de polissage, de petits angles de désorientation produisent des surfaces vicinales avec marches périodiques, permettant la coexistence des deux terminaisons [76].

Afin d'obtenir des terminaisons bien définies, SrO et TiO_2, les échantillons ont subi un traitement hydrothermal dans de l'eau désionisée suivi d'un recuit thermique sous atmosphère d'oxygène. Ce protocole permet de créer des terrasses planes tout en préservant la périodicité en hauteur des marches.

Résultats et discussions

Adsorption des carbonates sur les terrasses de $SrTiO_3$

Les images AFM ont révélé deux types de terrasses caractérisées par des hauteurs de marche distinctes. En mode tapping, comme illustré sur la Figure 16 (a), la surface du $SrTiO_3$ présentait des terrasses uniformes sur une zone de 1 µm × 1 µm. L'analyse des profils de hauteur (Figure

16 (b)) a mis en évidence des distributions centrées autour de 0,1 nm et 0,3 nm, confirmées par un ajustement gaussien et indiquant deux niveaux distincts. L'imagerie de phase (Figure 16 (d)) a permis de distinguer davantage ces terminaisons, montrant qu'une des surfaces présentait une rugosité plus élevée. L'écart observé entre la hauteur attendue (0,2 nm) et les valeurs mesurées (0,1/0,3 nm) est attribué à l'adsorption moléculaire, en particulier aux molécules de CO_2 (~0,1 nm) se liant sélectivement à une terminaison.

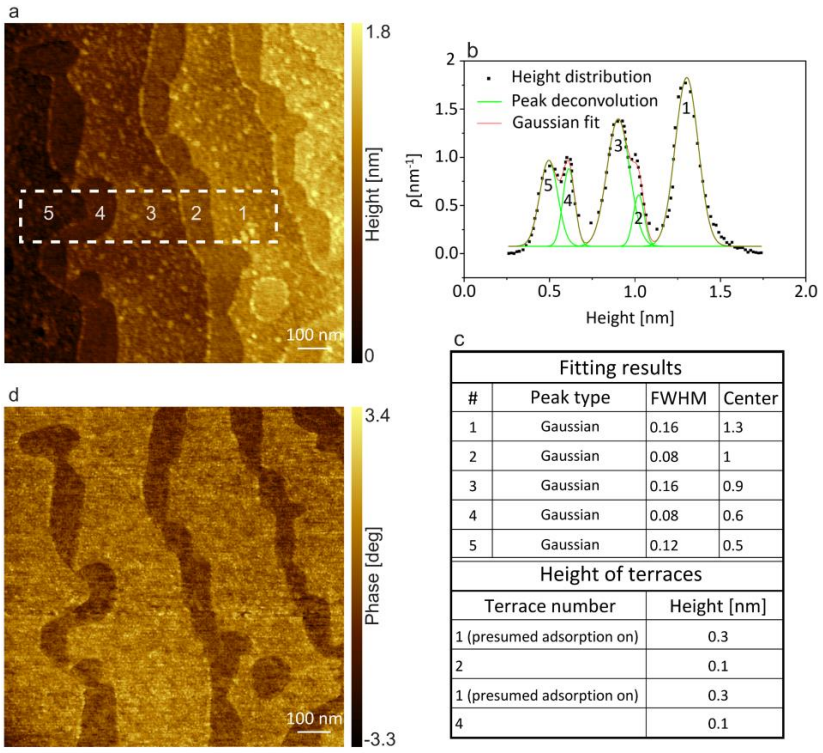

Fitting results			
#	Peak type	FWHM	Center
1	Gaussian	0.16	1.3
2	Gaussian	0.08	1
3	Gaussian	0.16	0.9
4	Gaussian	0.08	0.6
5	Gaussian	0.12	0.5

Height of terraces	
Terrace number	Height [nm]
1 (presumed adsorption on)	0.3
2	0.1
1 (presumed adsorption on)	0.3
4	0.1

Figure 16: Topographie AFM et analyse des terrasses montrant des marches de 0,1 et 0,3 nm, attribuées à l'adsorption du CO_2 sur une terminaison spécifique.

La spectroscopie TERS a ensuite été utilisée pour déterminer l'identité chimique des espèces adsorbées. Dans une zone de 200 × 200 nm^2, des cartographies topographiques et spectroscopiques simultanées ont été réalisées. La topographie (Figure 17 (a)) montre deux terrasses, l'une lisse et l'autre plus rugueuse, avec des structures granulaires localisées. La carte TERS correspondante (Figure 17 (b)), intégrant l'intensité Raman entre 1060 et 1080 cm^{-1}, a révélé des signaux forts uniquement sur la terminaison rugueuse, en particulier dans les régions granulaires. Cette gamme vibrationnelle correspond aux groupements carbonates, indiquant directement que l'adsorption du CO_2 se produit préférentiellement sur les terminaisons SrO.

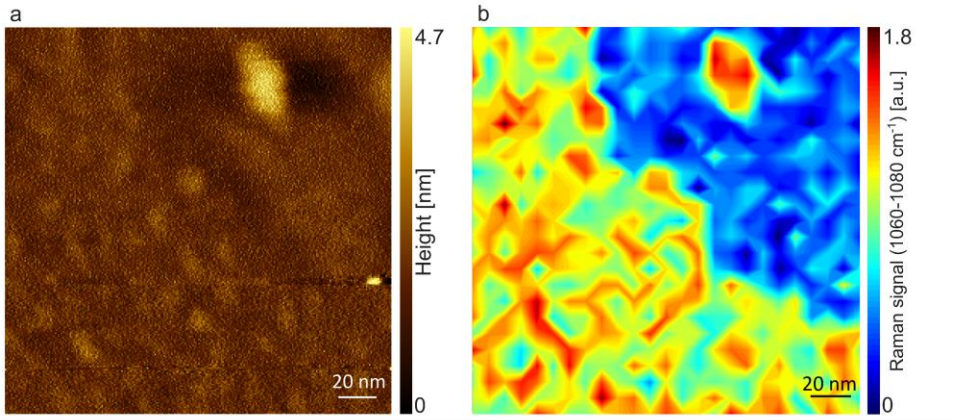

Figure 17: Topographie AFM des terrasses et carte TERS montrant le signal carbonate (1060–1080 cm^{-1}) localisé sur la terminaison SrO rugueuse.

En moyennant les spectres de plusieurs pixels, un pic Raman prononcé à 1071 cm^{-1} a été observé sur la terminaison rugueuse, correspondant à l'étirement symétrique des carbonates (v_1 du CO_3^{2-}) [77]. Aucun pic équivalent n'a été détecté sur les terminaisons TiO_2. Cette adsorption préférentielle s'explique par la réactivité accrue des ions Sr^{2+}, capables de former facilement du $SrCO_3$, tandis que les terminaisons TiO_2 demeurent plus inertes. L'adsorption de carbonates constitue ainsi un marqueur sensible permettant de distinguer les terminaisons de surface et de suivre la contamination en conditions ambiantes.

Délamination de surface et formation de nanograins

Des expériences de vieillissement prolongé ont révélé des changements morphologiques notables à la surface du $SrTiO_3$. Après 18 mois de stockage dans un dessiccateur, les images AFM ont montré l'apparition de nombreux nanograins recouvrant la surface. Comme le montre la Figure 18 (a), des structures granulaires abondantes se sont formées dans des zones de 1 × 1 μm^2. L'analyse de distribution de hauteur (Figure 18 (b)) a révélé des marches d'environ 0,4 nm, suggérant une transition de surfaces à terminaisons mixtes vers des surfaces majoritairement TiO_2. L'analyse volumique a confirmé une augmentation du volume lié aux carbonates et nanograins, passant de ~1,5 × 10^{-4} μm^3 à ~2,4 × 10^{-4} μm^3.

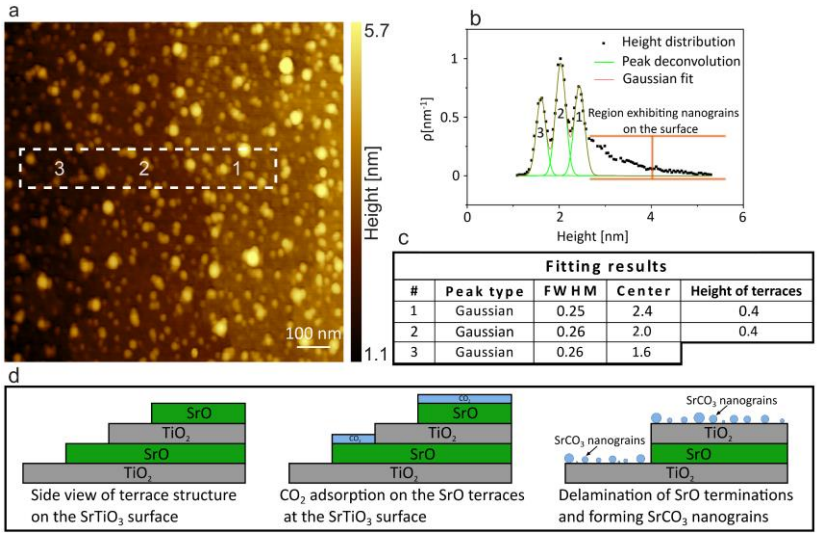

Figure 18: Image AFM d'une surface vieillie de $SrTiO_3$ montrant la formation de nanograins ; analyse en hauteur confirmant une délamination des couches SrO.

Ces résultats suggèrent que l'adsorption du CO_2 affaiblit l'énergie de liaison entre les couches SrO et TiO_2, entraînant finalement la délamination des terminaisons SrO. Le SrO détaché réagit avec le CO_2 pour former des nanograins de $SrCO_3$ qui persistent en surface. Ce processus explique la conversion progressive des surfaces initialement mixtes en surfaces majoritairement TiO_2 après vieillissement.

Détection TERS des carbonates et des phonons TiO_2

Afin d'analyser plus en détail les différences chimiques entre nanograins et terrasses, des spectres Raman de champ proche ont été moyennés sur différentes régions. Comme illustré dans la Figure 19, les nanograins présentent des signatures carbonatées nettes avec deux pics dominants : une vibration d'étirement symétrique à 1071 cm^{-1} et un mode de flexion basse fréquence vers 148 cm^{-1}. Ces signatures sont caractéristiques du $SrCO_3$, confirmant la nature carbonatée des nanograins.

En revanche, les spectres enregistrés sur les terrasses dépourvues de nanograins présentent des caractéristiques totalement différentes, avec de faibles pics à 683 cm^{-1}, 762 cm^{-1} et 866 cm^{-1}. Ces modes correspondent à l'étirement des liaisons Ti–O et aux vibrations rotationnelles des octaèdres TiO_6, invisibles dans le volume mais activés en surface par rupture de symétrie.

Cette observation démontre la coexistence de deux processus : la délamination des terminaisons SrO, donnant naissance aux nanograins de $SrCO_3$, et la stabilisation des terrasses restantes vers des terminaisons TiO_2. La TERS permet ainsi d'identifier à la fois la nature chimique des espèces présentes et la dynamique de transformation des terminaisons à l'échelle nanométrique.

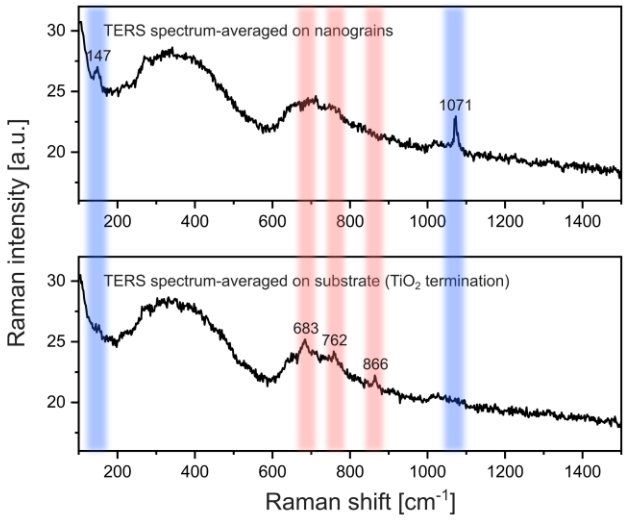

Figure 19: Spectres de champ proche comparatifs. Les nanograins présentent des pics carbonates (1071, 148 cm^{-1}), tandis que les terrasses montrent des phonons de surface liés à TiO_2 (683, 762, 866 cm^{-1}).

L'ensemble des résultats AFM et TERS met en évidence un mécanisme d'autoréparation dans lequel les surfaces de $SrTiO_3$ se stabilisent progressivement en présence de CO_2 ambiant. Initialement, les terminaisons SrO et TiO_2 coexistent, l'adsorption sélective des carbonates se produisant uniquement sur les terrasses SrO. Avec le temps, l'incorporation de CO_2 réduit l'énergie de liaison entre les couches SrO et TiO_2, provoquant la délamination des couches SrO. Le SrO détaché réagit avec le CO_2 pour former des nanograins de $SrCO_3$, tandis que la surface sous-jacente évolue vers une terminaison TiO_2.

Ce scénario explique pourquoi les surfaces (100) de $SrTiO_3$, dans leur état "tel que reçu", apparaissent souvent terminées par TiO_2 malgré l'alternance théorique des couches dans la structure idéale. De façon plus générale, ces résultats montrent comment le CO_2 environnemental entraîne une restructuration spontanée des oxydes, les nanograins de $SrCO_3$ apparaissant comme sous-produits de la stabilisation des terminaisons. Cette étude démontre également comment la TERS peut suivre de tels processus nanométriques en corrélant identité chimique et évolution morphologique en temps réel.

TABLE OF CONTENTS

LIST OF FIGURES

LIST OF TABLES

LIST OF CONTRIBUTIONS

Peer-reviewed Journal Articles

[A1] **Mohammad Bakhtbidar**, Ifeanyichukwu Amaechi, Andreas Dörfler, Alexandre Merlen, and Andreas Ruediger. "Direct Observation of Carbonate Chemisorption on Barium Titanate Surfaces by Tip-Enhanced Raman Spectroscopy." Advanced Materials Interfaces 11, no. 15 (2024): 2300993. doi:10.1002/admi.202300993.

[A2] **Mohammad Bakhtbidar**, Alexandre Merlen, and Andreas Ruediger. "Ferroelectric-to-paraelectric phase transition probing via high-resolution tip-enhanced Raman spectroscopy." Optics Communications (2025): 132058. doi: 10.1016/j.optcom.2025.132058.

[A3] **Mohammad Bakhtbidar**, Daniel Gueckelhorn, Marivi Fernández-Serra, Yon Leandro Leibas López, Alexandre Merlen, and Andreas Ruediger. "Self-Recovery of Carbonate-Contaminated Strontium Titanate (100) Vicinal Surfaces Imaged by Tip-Enhanced Raman Spectroscopy." Advanced Materials Interfaces (2025): 2401024. doi: 10.1002/admi.202401024.

[A4] Dong, Fang, Mingjie Wu, Zhangsen Chen, Ning Chen, **Mohammad Bakhtbidar**, Andreas Ruediger, Gaixia Zhang, and Shuhui Sun. "In situ reconstruction of bimetallic heterojunctions encapsulated in N/P co-doped carbon nanotubes for long-life rechargeable zinc-air batteries." Nano Energy 133 (2025): 110497. doi: 10.1016/j.nanoen.2024.110497.

[A5] Leibas, Y. L., **M. Bakhtbidar**, A. Kharade, S. Obernberger, A. Tejeda-Cruz, G. Santana, A. Hernandez-Garcia et al. "Selective deposition of Mo5O14/MoO3 composite onto MoO2 surfaces induced by MoO3/MoO2 interfacial reaction." Journal of Solid State Chemistry 343 (2025): 125166. doi: 10.1016/j.jssc.2024.125166.

[A6] Peláiz-Barranco, Aimé, Yon Leandro Leyvas-López, Alejandro Carlos Iglesias-Jaime, José de los Santos Guerra, **Mohammad Bakhtbidar**, Andreas Ruediger, and Tongqing Yang. "Abnormal dielectric behavior and domain reorientations in the (Bi0.5Na0.5)0.92Ba0.08TiO3 ceramic below the critical temperatures." Functional Materials Letters (2025): 2551039.

Conference Presentations

[B1] **M. Bakhtbidar**, I. Amaechi, D. Gueckelhorn, A. Merlen, A. Ruediger, “Unveiling surface properties of barium titanate through high-resolution tip-enhanced Raman spectroscopy “ in International Conference on Raman Spectroscopy (ICORS) 2024 .

[B2] **M. Bakhtbidar**, I. Amaechi, A. Doerfler, A. Merlen, A. Ruediger, “Nanoscale surface investigation using tip-enhanced Raman spectroscopy“, in Colloque Scientifique INRS EMT 2024.

[B3] **M. Bakhtbidar**, I. Amaechi, A. Merlen, A. Ruediger, “Optical Near Field Investigation on Polar Perovskite Nanostructures” in Photonics North 2023.

[B4] A. Ruediger, A. Youssef, **M. Bakhtbidar**, A. Merlen, “Detection of regions with reduced symmetry in crystal surfaces via tip-enhanced Raman spectroscopy” in Enhanced Spectroscopies and Nanoimaging 2022.

LIST OF ABBREVIATIONS

AFM	Atomic Force Microscopy (or Microscope)
AM	Amplitude Modulation
aSNOM	Apertureless Scanning Near-field Optical Microscopy
CNT	Carbon Nano Tube
c-SNOM	Collection Scanning Near-field Optical Microscopy
EM	Electromagnetic
FIB	Focused Ion Beam
FM	Frequency Modulation
FTIR	Fourier-transform infrared spectroscopy
FWHM	Full Width at Half Maximum
GFR	Gradient Field Raman
IR	Infrared
LO	Longitudinal Optical
NA	Numerical Aperture
PL	Photoluminescence
PFM	Piezoresponse Force Microscopy
QTF	Quartz Tuning Forks
RRS	Resonance Raman Scattering
RMS	Root Mean Square
SEM	Scanning Electron Microscopy (or Microscope)
SNOM	Scanning Near-field Optical Microscopy
SPM	Scanning Probe Microscopy (or Microscope)
STM	Scanning Tunneling Microscopy (or Microscope)
SNR	Signal-to-Noise Ratio
SP	Surface Plasmon
SPP	Surface Plasmon Polariton
SERS	Surface-Enhanced Raman Spectroscopy
TERS	Tip-Enhanced Raman Spectroscopy (or Microscope)
TEM	Transmission Electron Microscopy (or Microscope)
TO	Transversal Optical
UV	Ultraviolet

XPS	X-Ray Photoelectron Spectroscopy
XRD	X-Ray Diffraction

1 INTRODUCTION

1.1 Perovskite oxides

Perovskite oxides form a class of materials with the formula ABO_3, where A and B are cations of different sizes fulfilling the Goldschmidt rule [78]. These materials have attracted significant interest due to their diverse range of structural and electronic properties, including ferro-, pyro-, piezoelectricity, as well as catalytic activity. The name "perovskite" originates from the mineral $CaTiO_3$, which was discovered by the Russian mineralogist Lev Perovski in 1839 [79] and which is the most abundant crystal structure in the Earth's lower mantle [80]. Perovskite-structured oxides are known to exhibit a wide variety of interesting phenomena, such as metal-insulator transitions, ionic conduction, and even superconductivity [1], making them attractive for a broad range of applications in electronics [81], energy conversion [82,83], and catalysis [84] (Figure 1.1).

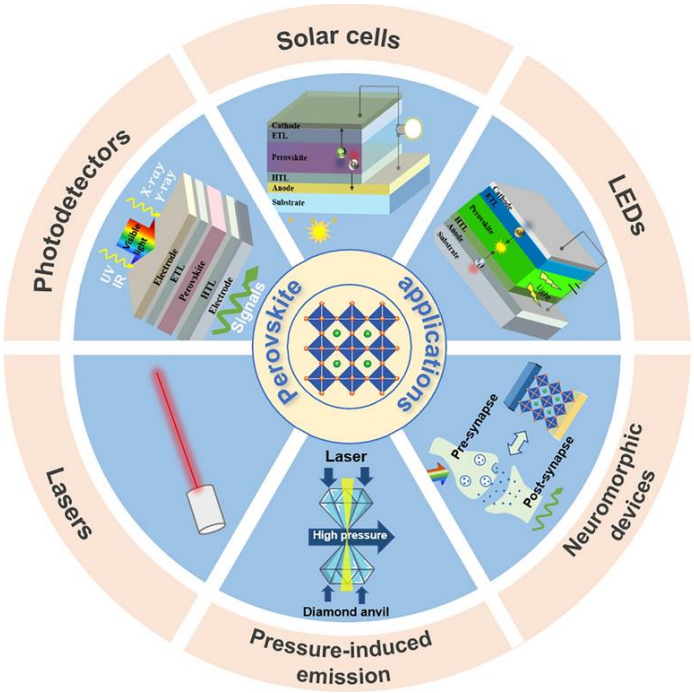

Figure 1.1: Applications of perovskites across various sectors. (Figure adapted from Ref. [85])

Among the perovskite oxides, strontium titanate ($SrTiO_3$) and barium titanate ($BaTiO_3$) are the most investigated materials already exhibiting rich dielectric, ferroelectric, and piezoelectric properties that arise from the interplay between their crystal structures and electronic configurations [86–88]. While barium titanate is a room temperature bulk ferroelectric, strontium

titanate is cubic (thus neither piezo,- pyro, nor ferroelectric) and close to a phase transition into phases that allow for spontaneous dipole formation. Strontium titanate and barium titanate have both been extensively studied in their bulk, ceramic, and thin-film forms, the behavior of these materials at the nanoscale, particularly the surface and interface properties, remains an area of active research.

1.2 Strontium titanate and barium titanate

The surfaces of $SrTiO_3$ and $BaTiO_3$ exhibit complex behavior influenced by crystallographic orientation, defect structure, and environmental adsorbates. This work primarily addresses the chemically most stable (100) surfaces, both under clean and chemisorbed conditions. On both materials, the (100) surface presents vicinal surfaces with TiO_2- or SrO/BaO terminations, depending on preparation conditions, see Figure 6.6. Since surface reconstruction only occurs under extreme conditions of oxygen partial pressure and temperature [89], it will not be given further consideration in this work.

Under ambient conditions, CO_2 adsorption occurs naturally from the 0.04% of CO2 in the atmosphere. Given that it is based on chemisorption, it has so far been considered irreversible, a conclusion that we shall revise later. Anyways, CO_2 adsorpion plays a crucial role in modifying surface properties, including catalytic activity, electronic structure, and binding energies [62]. Carbon dioxide adsorption on the surfaces of materials such as TiO_2, ZnO, and Al_2O_3 has been recognized and studied for decades [90,91]. These studies, conducted as early as the 1960s, have demonstrated that CO_2 adsorption significantly impacts surface properties, such as photocatalytic activity, wettability, and reactivity [92,93] i.e. those properties related to the outermost layer. In addition to surface chemistry, $BaTiO_3$ nanoparticles exhibit size-dependent ferroelectric behavior, where the transition to a paraelectric, non-polar phase occurs below a critical size - referred to as the superparaelectric limit. Understanding this limit is crucial for the integration of ferroelectric nanomaterials into nanoscale devices, where phase stability and polarization directly affect performance.

While several theoretical studies have explored these effects, there is a notable lack of direct experimental investigations at the level of individual nanoparticles. Specifically, the influence of CO_2 adsorption on both the surface chemistry and structure of $SrTiO_3$ and $BaTiO_3$ remains poorly understood. Furthermore, probing the superparaelectric limit in individual $BaTiO_3$ nanoparticles is essential for a comprehensive understanding of their functional behavior at the nanoscale. Previous studies were either conducted on ensembles of particles, where a size-dispersion and

possible electrostatic coupling between particles blurs the transition [94] or relied on negative findings on individual particles [7] , where the conclusion of a superparaelectric limit is easily challenged by experimental side-effects. Any deeper analysis of this topic calls for techniques that are both spatially resolved to the level of individual nanoparticles and quantitative, in order to make statements beyond the mere existence of polar order. To this extent, tip-enhanced Raman spectroscopy competes with transmission electron microscopy [95].

1.3 Material characterization techniques

Figure 1.2 presents the timeline of major nano-imaging advancements, reflecting the evolution of techniques designed to overcome the diffraction limit and enhance material characterization. While early optical microscopy, developed nearly 400 years ago, was limited to resolutions of several hundred nanometers, modern nano-imaging methods now provide complementary, high-resolution insights into material properties.

In parallel, techniques such as X-ray photoelectron spectroscopy (XPS) and x-ray diffraction (XRD) emerged in the mid-20th century [96], expanding the materials characterization toolkit. The discovery of x-rays by Wilhelm Röntgen in 1895, followed by the demonstration of the wave nature of x-rays by Laue, Friedrich, and Knipping in 1912, laid the foundation for XRD. The subsequent development of x-ray diffraction analysis by W.H. and W.L. Bragg, awarded the Nobel Prize in 1915, established XRD as a cornerstone for probing crystal structures [97].

In the 1960s, Kai Siegbahn developed XPS, enabling surface chemical analysis through photoelectron energy measurements—a contribution that earned him the 1981 Nobel Prize [98]. However, both XPS and XRD offer limited spatial resolution, providing averaged information over large surface areas and making them unsuitable for surface mapping with nanoscale lateral resolution.

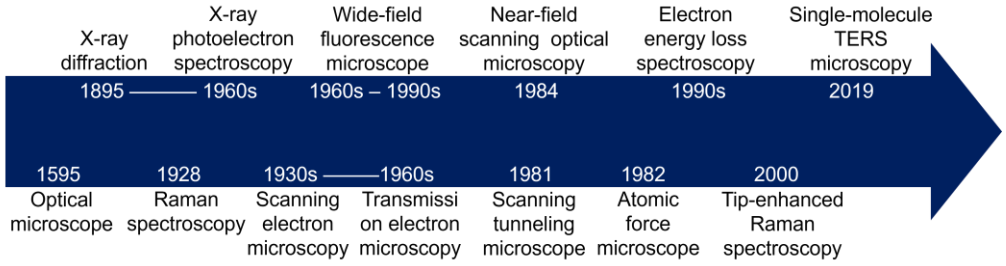

Figure 1.2: Timeline of major advancements in nano-imaging techniques, illustrating the evolution and diversification of methods developed to overcome optical limitations and enhance material characterization.

Efforts to surpass the optical diffraction limit accelerated in the 1930s with the advent of electron microscopy [99]. The transmission electron microscope (TEM), developed by Ernst Ruska and Max Knoll in 1931, utilized short-wavelength electron beams to achieve nanometer-scale resolution [100]. This was followed by the development of scanning electron microscopy (SEM), which provided high-resolution surface imaging via focused electron beam scanning [101]. While high-resolution TEM enables atomic-scale imaging, it requires extensive sample preparation and high vacuum conditions, may induce damage in sensitive materials—limitations that drive the need for alternative high-resolution, surface-sensitive techniques.

Scanning probe microscopy (SPM) marked a major advancement by enabling atomic-scale imaging without vacuum environments [102,103]. The invention of the scanning tunneling microscope (STM) by Binnig and Rohrer allowed atomic orbital visualization via tunneling current measurements [9], while the subsequent development of atomic force microscopy (AFM) extended imaging to non-conductive materials through mechanical tip-sample interactions. However, despite their high spatial resolution, STM and AFM provide limited chemical specificity compared to spectroscopic techniques.

Optical vibrational spectroscopy techniques, such as infrared (IR) and Raman spectroscopy, provide complementary molecular-level information based on characteristic vibrational modes. IR spectroscopy detects the absorption of IR radiation by molecular bonds, enabling the identification of functional groups through their vibrational fingerprints. The Raman effect, originally predicted by Smekal in 1923 [29] and confirmed by Landsberg, Mandelstam [104], and Raman and Krishnan [105–107], gained practical utility with the advent of lasers [108], which enabled strong, monochromatic excitation. Modern micro-Raman systems now allow high-resolution chemical mapping, though the lateral resolution remains limited to several hundred nanometers due to the diffraction limit of light.

1.4 Breaking the diffraction limit of light

Tip-enhanced Raman spectroscopy (TERS) has emerged as a powerful technique to overcome the spatial resolution limits of conventional Raman microscopy. By combining SPM with Raman spectroscopy, TERS enables simultaneous acquisition of topographical and chemical information with nanoscale resolution. The concept of overcoming the diffraction limit traces back to Edward Synge’s 1928 research of subwavelength apertures [109], later explored experimentally by Ash et al. [110] and refined in scanning near-field optical microscopy (SNOM) using tapered fiber tips [111]. However, SNOM's reliance on apertures led to significant signal loss, limiting its application

to weak Raman scattering. While SNOM initially only referred to aperture-based techniques, it soon became necessary to distinguish between aperture-based and aperture-free SNOM that became known as a-SNOM and s-SNOM respectively. S-SNOM refers to scattering-based near-field microscopy and tip-enhanced Raman spectroscopy was among the first successful demonstrations.

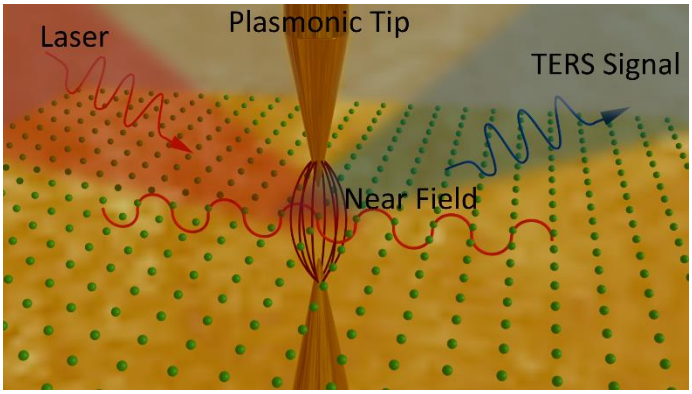

Figure 1.3: Illustration of a TERS experimental configuration. The green spheres represent the atomic structure at the surface of the material, while the conical shape at the bottom corresponds to the image charge of the tip. The localized electromagnetic field established between the tip and the surface arises from the image charge effect, a configuration commonly referred to as gap-TERS, which will be discussed in detail in Section 2.3.

Based on the principle of surface-enhanced Raman spectroscopy (SERS) , discovered by Martin Fleischmann in 1974 [112], TERS uses a noble metal-coated AFM or STM tip to locally amplify the electromagnetic field via surface plasmon resonance, (see Figure 1.3) . This enhancement, theorized by Wessel in 1985 [113] and demonstrated experimentally by Stöckle et al. in 2000 [114] and Hayazawa et al. [115], allows Raman signals to be detected from regions as small as a few nanometers. The Raman effect has a notoriously low scattering cross-section, so that an increase of the spatial resolution alone (i.e. a signal coming from a smaller sample volume) would result in such a weak signal, that the detection would be almost hopeless. However, since the high spatial resolution relies on a localized surface plasmon resonance (based on the same physics as SERS), it also comes with an amplification of the Raman signal. This effect often associated with the “g^4-term”, even though our group has brought corrections.

Under resonance conditions tuned by tip geometry, material, and excitation wavelength, TERS achieves single-molecule sensitivity and sub-molecular spatial resolution [116]. Despite technical challenges in tip reproducibility and alignment, TERS keeps evolving as a powerful tool for high-resolution chemical characterization at the nanoscale.

1.5 Motivation

The continued miniaturization of electronic and optoelectronic devices demands materials that retain functionality at the nanoscale. At these dimensions, phenomena such as surface adsorption, phase transitions, and finite-size effects critically influence performance, particularly in perovskite oxides like $BaTiO_3$ and $SrTiO_3$. As mentioned above, conventional characterization techniques often lack the combination of spatial resolution and chemical sensitivity required to probe these nanoscale effects.

TERS has emerged as a powerful tool for addressing this challenge, offering simultaneous chemical and structural insights with nanometer precision. Recent TERS studies have demonstrated the technique's utility in optical crystallography on the nanoscale by selectively probing different transverse optical phonon modes to identify intrinsic ferroelectric domains in $BaTiO_3$ nanocrystals [117]. In this work, we will extend the technique to the investigation structural inhomogeneities, phase transitions, and finite-size effects with nanoscale precision and chemical specificity. We will furthermore deploy TERS to the study of catalytic surfaces and a long-standing question about the single-termination nature of as-received (100) surfaces.

This thesis is thus motivated by the need to better understand surface chemisorption and finite-size effects in perovskite oxides at the nanoscale. Using TERS to study $BaTiO_3$ and $SrTiO_3$ nanoparticles, the work elucidates how local adsorption and structural transitions influence surface reactivity and polarization stability.

1.6 Objectives

- **Characterization of surface adsorption**

Utilize TERS to investigate the structural properties of chemisorbed layers on $BaTiO_3$ at the nanoscale. Through near-field vibrational mapping of individual nanoparticles under ambient conditions, this objective aims to reveal the nature, distribution, and organization of surface adsorbates. The main experimental challenge is that the technique requires single-layer sensitivity. While single-layer sensitivity had been demonstrated in so-called “gap-TERS” in the case of monolayers on gold substrates, the technique requires a much better amplification factor from the near-field antenna in “non gap-TERS” conditions that we encounter on the surface of the perovskite dielectrics.

- **Localization of CO_2 adsorption on $SrTiO_3$ (100) surfaces**

Utilize TERS to spatially resolve and map CO_2 adsorption on $SrTiO_3$ (100) terraces. This objective aims to localize carbonate species at the nanoscale and correlate their distribution with surface terminations, providing insights into adsorption behavior critical for optimizing surface functionality in catalytic and electronic applications.

- **Investigation of delamination effects**

Apply high-resolution TERS to investigate the formation, structure, and spatial distribution of nanograins on $SrTiO_3$ (100) surfaces. This objective seeks to identify the chemical stability of the chemisorbed CO_2 layer, to interpret agglomeration phenomena on the surface, and to develop approaches to stabilize the surface for improved catalytic and electronic properties. This investigation relies on samples aged under ambient conditions.

- **Study of the superparaelectric limit in individual $BaTiO_3$ nanoparticles**

Study the finite-size effects on the ferroelectric-to-paraelectric phase transition in $BaTiO_3$ nanoparticles using TERS. This objective focuses on how size reduction influences the tetragonal-to-cubic transition, offering nanoscale insights into the superparaelectric limit on an individual nanoparticle.

2 THEORY AND FUNDAMENTALS

2.1 Atomic force microscopy

The development of the scanning tunneling microscope by G. Binnig and H. Rohrer in 1981 [9] enabled atomic-scale surface imaging through tunneling currents between a conductive tip and sample, surpassing the diffraction limit of optical microscopy [118]. Its operating principle is based on a tunneling current, which arises when a voltage difference is applied between a conductive tip and the sample, allowing electrons to quantum-mechanically tunnel across the gap when the tip is positioned at angstrom-scale distances from the surface. Despite its atomic-scale resolution, the STM is limited to conductive samples, which significantly restricts its applications. To address this, the atomic force microscope was developed in 1986 [10], employing atomic force interactions rather than tunneling currents, thus allowing imaging of both conductive and insulating materials.

Given that both barium titanate and strontium titanate are wide bandgap semiconductors with negligible conductivity, our experimental conditions are based on atomic force microscopy. The core principle of AFM is based on the interaction between the probe tip and the sample surface, typically modeled by the Lennard-Jones potential (Figure 2.1). This potential combines a long-range van-der-Waals attraction (dominant >1 nm) and short-range Pauli repulsion (<0.5 nm) [11]. The interaction is expressed as:

$$V(z) = 4\varepsilon\left[\left(\frac{\sigma}{z}\right)^{12} - \left(\frac{\sigma}{z}\right)^{6}\right] \tag{2.1}$$

where ε and σ are model parameters, and z is the tip-sample distance. At the potential minimum z_{min} , the attractive and repulsive forces counterbalance each other, theoretically resulting in no net force acting on the probe. The force gradient, defined as:

$$k(z) = \frac{dF}{dz} = \frac{d^2V}{dz^2} \tag{2.2}$$

describes the variation of force with respect to the tip-sample distance. To convert the forces on the AFM tip (in the order of nanonewtons) into measurable signals, the probe is mounted at the end of a microscale cantilever. The cantilever serves as a transducer, bending upwards under attractive forces and downwards under repulsive forces. The resulting deflection is given by:

$$\Delta z = \frac{F}{K_0} \tag{2.3}$$

where K_0 denotes the cantilever stiffness constant, which in commercial AFM probes ranges from 0.01 N/m to 50 N/m, enabling adaptation to diverse force measurement applications.

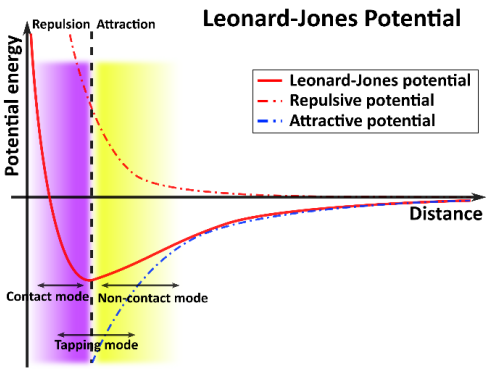

Figure 2.1: Variation of the interaction between the tip and the surface as a function of the distance

While in first order, the resolution of atomic force microscopy is given by the nature of interaction i.e. the range of the forces that are probed, for any given interaction, the AFM resolution is largely dictated by tip geometry. Lateral resolution depends on tip sharpness, while vertical resolution can reach sub-angstrom levels (~ 2 Å). Ideally, an AFM tip would have a single-atom apex, ensuring minimal convolution in imaging. However, in practical applications, commercial AFM tips exhibit apex curvatures typically in the range of 5–20 nm. This rationale applies primarily to topography information, we shall see that the optical near-field implies additional considerations.

2.1.1 Detection methods in AFM

With the above information, it is now possible to further categorize atomic force microscopy in two main sections: the nature of the interaction (non-contact, intermittent or tapping, and contact) on one side and the nature of the detection of this interaction.

In AFM, cantilever deflections must be converted into electrical signals to form interpretable surface scans. This is achieved using various detection methods, including optical, interferometric, piezoelectric, capacitive, and piezoresistive techniques. Among these, the optical lever method is the most widely employed. In the course of this thesis, the optical lever technique has been used to obtain high resolution topography maps while TERS has been conducted in a tuning-fork configuration that will be detailed further below.

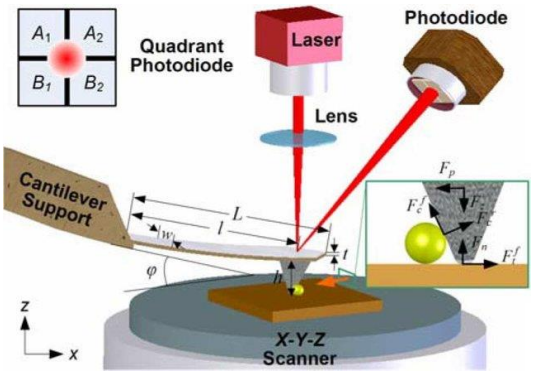

Figure 2.2: Schematic of a beam deflection detection system using the optical lever method : In an AFM, surface features cause the cantilever to bend by *t*, vertically shifting the laser spot on the four-quadrant photodiode. The controller adjusts the sample's vertical position in a feedback loop to maintain a constant interaction between tip and surface and thus follow the topography. (Figure adapted from reference [119])

In this approach, a laser beam is directed onto the back of a cantilever, and its reflection is monitored by a four-quadrant photodiode, which detects both vertical and lateral deflections, see Figure 2.2. Vertical signals [(A+B) − (C+D)] provide topographic information, while lateral signals [(A+C) − (B+D)] offer insight into friction and shear forces; in both cases, the signals are normalized by dividing by the total intensity to compensate for any fluctuations. The AFM system includes a high-precision piezoelectric scanner for controlled motion in the X, Y, and Z directions, enabling nanoscale mapping. To enhance positioning accuracy and minimize trajectory errors during scanning, position sensors are often integrated.

The feedback mode for the distance between the surface and the tip provides an error signal from the PID-controller. The error signal is the difference between the set point of the microscope (e.g. the chosen strength of the interaction) and the actual strength at the next measurement point.

Contact mode

In contact mode AFM, the tip remains in continuous contact with the sample surface, while scanning. Surface features induce cantilever deflection, which is monitored using an optical detection system. A feedback loop maintains constant interaction force by adjusting the tip's vertical position [10]. This mode offers the advantage of functionalized techniques through the physical contact with a possibly conducting tip and therefore is crucial for techniques like spreading-resistance AFM (also known as conductive AFM) and piezoresponse force microscopy [120]. However, lateral forces during scanning will soon deform whatever is softer between the tip and the surface [121] , and prolonged tip-sample contact inevitably causes tip contamination and wear, reducing resolution and requiring frequent tip replacement [122].

Intermittent contact mode (tapping mode)

To minimize tip wear and surface modifications, intermittent contact mode—also known as tapping mode—was introduced. In this mode, the cantilever oscillates near its resonance frequency (typically hundreds of kHz) with an amplitude typically between 5 and 20 nm. The tip periodically interacts with the sample, reducing lateral friction forces. Two primary modulation techniques exist, amplitude modulation (AM) and frequency modulation (FM).

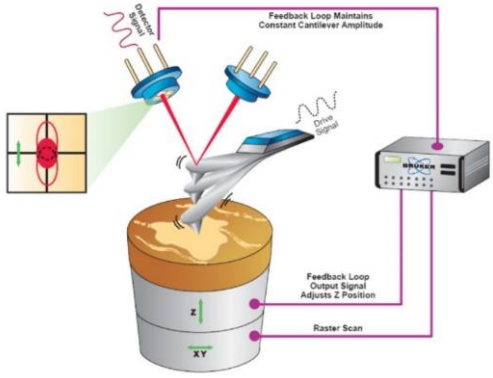

Figure 2.3: Representation of amplitude modulation intermittent contact mode

In AM mode [123], the piezoelectric actuator drives the cantilever with a fixed amplitude and frequency near its resonance. As the tip approaches the sample, interactions modify the oscillation amplitude and phase. The feedback system compensates for these variations by maintaining either amplitude or phase constant, ensuring consistent tip-sample interaction (Figure 2.3). However, AM mode exhibits a response delay due to the high-quality factor (Q) of the cantilever, which slows its ability to adapt to rapid changes in surface topography. The response time is given by:

$$\tau = \frac{2Q}{\omega_0} \qquad 2.4$$

For a typical tapping-mode AFM probe with $\omega_0 = 300\,KHz$ and $Q = 300$, the response time is approximately 2 ms. In vacuum conditions, where *Q* can reach 10,000, the response time increases to 67 ms. To overcome this delay, Albrecht, Grütter, Horne, and Rugar (1990) introduced FM mode, where the cantilever oscillates at its resonance frequency and responds to force gradient variations. This interaction causes frequency shifts that can be detected using a phase-locked loop (PLL) demodulator [124].

In addition to the aforementioned error signal, intermittent AFM provides a phase signal, where – except from an experimental offset – the phase designates the lag between the periodic excitation of the cantilever and the periodic oscillation of the laser on the 4-quadrant photo-diode. Depending on the "stickyness" of the surface that is expressed by the Hamaker constant of the van-der-Waals potential, this phase signal changes depending on the surface termination and is a very sensitive, even though only qualitative, handle on the termination of a surface.

Non-Contact Mode

Non-contact AFM, first introduced by Martin et al. [123], operates in the attractive force regime, with the tip remaining at tens of angstroms to nanometers above the sample surface (attraction region in Figure 2.1). Unlike contact and intermittent mode, where repulsive forces dominate, non-contact mode detects weaker van der Waals interactions. To achieve sufficient sensitivity, the cantilever is dynamically excited at its resonance frequency, with an oscillation amplitude in the nanometer range. The effective stiffness of the cantilever is influenced by the force gradient $\partial F/\partial d$, modifying its resonance frequency as:

$$f = f_0 \sqrt{1 - \frac{\partial F}{\partial d}\frac{1}{k_0}} \qquad 2.5$$

While non-contact mode overcomes the challenges of tip wear, it is prone to provide ambiguous topography information under ambient conditions as it will interact with the surface of physisorbed water.

2.1.2 Tuning fork atomic force microscopy

As we will see further below, the optical near-field that we use under the illumination of a 632.8 nm ruby laser relies on soft gold tips while the reach of the optical near-field is in the range of a few nanometers at most. So, the softness of gold tips voids both contact and intermittent mode, as both would immediately change the shape of the tip and thus the localized plasmon resonance. As for non-contact mode AFM that relies on a periodic modulation of the tip-sample distance, we would face a continuously modulated intensity of the optical near-field which causes an increase in the detection time. Scanning tunneling microscopy provides a very small and stable tip-sample distance and was indeed the first feedback configuration in early TERS experiments, but it relies on conducting surfaces. For these reasons, we opted for lateral tuning fork microscopy, which provides an almost constant tip-sample distance on any kind of surface.

Quartz tuning forks (QTFs) were introduced to near-field microscopy by Günther et al. [125] and later refined by Karrai and Grober [126], as well as Giessibl et al. [127] for atomic-resolution AFM. QTFs have since been employed in diverse environments, including cryogenic and high magnetic fields [12], with the first metrological AFM implementation developed at MIT in 2000 using an optical fiber tip mounted on one prong [128].

QTFs are characterized by high quality factors (~10^4 in air, ~10^5 in vacuum), enabling detection of minute frequency shifts due to tip-sample interactions. Their resonance frequencies range from 20 kHz to 100 kHz, with 32,768 kHz (2^{15} Hz) being the most common. Their widespread availability and low cost—originating from their use in quartz watches—make them an attractive alternative to conventional AFM cantilevers.

A key advantage of QTF-based AFM is the elimination of optical detection systems. As the QTF oscillates near the surface, interaction forces cause measurable frequency shifts. These shifts are tracked using a phase-locked loop (PLL), allowing precise regulation of tip-sample distance. This enables scanning at very low oscillation amplitudes, minimizing tip wear and sample damage. At this point, it should be noticed that the attachment of a tip to the free tuning fork will typically deteriorate the quality factor and while it brings it down to several thousand, this is still more than necessary to conduct the aforementioned experiments.

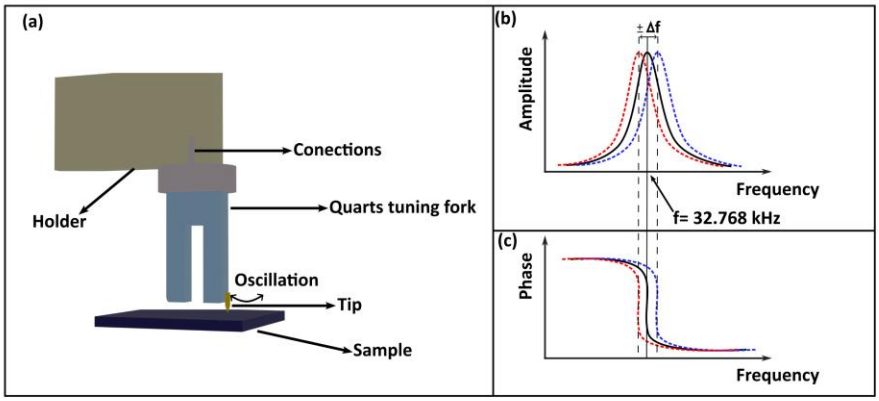

Figure 2.4: Illustration of tuning fork microscopy. (a) The tuning fork is equipped with a tip and excited near its resonance frequency. Tip-sample interactions cause a measurable shift in the resonance frequency. (b) amplitude and (c) phase of the free oscillation (black) as a function of the excitation frequency, illustrating the frequency shift (Δf) due to interaction forces (red: attractive, blue: repulsive).

Figure 2.4 illustrates the QTF operational principle, a sharp metallic tip is attached to one prong of a decapsulated tuning fork, which is excited either mechanically or electrically. Tip-sample interactions modify the effective stiffness of the fork, resulting in frequency and phase shifts.

These shifts are detected and processed by a phase-locked loop (PLL), which dynamically adjusts the tip's vertical position to maintain a constant interaction force.

Before initiating a scanning sequence, a reference resonance curve of the freely oscillating tuning fork is recorded, which serves as a baseline. The natural resonance frequency of the tuning fork is primarily determined by its momentum of inertia and spring constant. As the tip approaches the surface, the interaction force gradient alters the resonance frequency, inducing a measurable phase shift, as shown in Figure 2.4 (b, c). The high slope of the phase response near resonance allows for precise frequency shift detection, which is converted into a feedback signal for distance regulation. This laser-free, electrically detected method offers high-resolution topographic imaging while minimizing system complexity. Due to its compactness, high Q-factor, and suitability for light-sensitive materials, QTF-based non-contact AFM presents a robust alternative to conventional cantilever-based techniques.

2.2 Raman Scattering

Raman and infrared spectroscopy probe the vibrational dynamics of molecules excited by electromagnetic (EM) radiation. For a molecule with N atoms, the number of vibrational modes is 3N−6 (or 3N−5 for linear molecules). These vibrations are broadly categorized into valence (stretching) and deformation (bending) modes, illustrated for a triatomic molecule in Figure 2.5. In valence vibrations, atoms oscillate along the bond axis, altering bond lengths, while deformation vibrations cause variations in bond angles, leading to structural distortions [13].

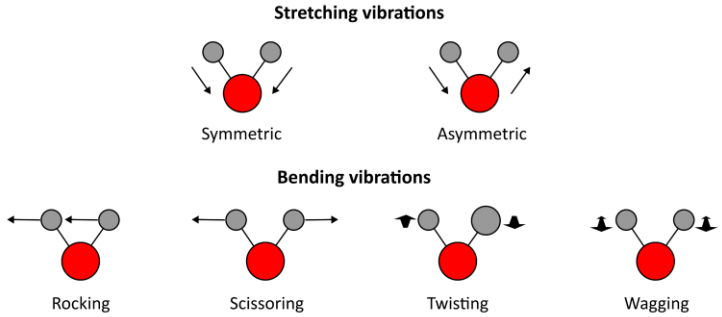

Figure 2.5: Stretching and bending vibrations of a triatomic molecule.

The vibrational frequencies of diatomic molecules can be derived from quantum mechanics by considering the atomic masses m_1 and m_2 and the bond force constant f. The vibrational frequency $\tilde{\nu}$ is expressed as:

$$\tilde{\nu} = \frac{1}{2\pi c}\sqrt{f\left(\frac{1}{m_1}+\frac{1}{m_2}\right)} \qquad 2.6$$

Vibrational energy levels are often modeled using the Morse potential, which accounts for dissociation energy, and the presence of overtones and combination bands [14]. When light interacts with molecules, it can be absorbed or scattered, leading to IR absorption (Figure 2.6 (a)) or Raman scattering (Figure 2.6 (b)), respectively. A vibration is IR-active if it involves a change in the dipole moment, while it is Raman-active if it involves a change in polarizability. In centrosymmetric molecules, the mutual exclusion principle states that vibrations active in IR are inactive in Raman and vice versa.

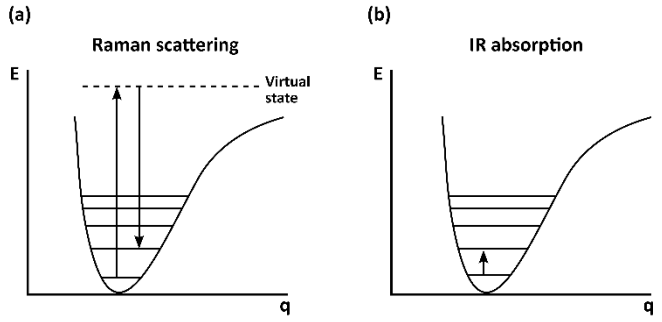

Figure 2.6: Interaction of light with a molecule : (a) Raman scattering, (b) IR absorption. *E* and *q* represent excitation energy and vibrational coordinates, respectively.

2.2.1 Electric dipole moment and polarizability tensor

When a monochromatic electromagnetic (EM) wave interacts with a neutral molecule, it induces oscillations in the electron cloud. To simplify the mathematical treatment, the dipole approximation is employed, valid under the condition that the wavelength of the incident light is significantly larger than the molecular dimensions. Thus, the electric field $\vec{E}$ of the EM wave can be assumed spatially uniform across the molecule and is described as:

$$\vec{E} = \vec{E}_0 cos(\omega_0 t) \qquad 2.7$$

The interaction of $\vec{E}$ with the molecule induces a dipole moment $\vec{p}$, expressed as a power series:

$$\vec{p} = \vec{p}^{(1)} + \vec{p}^{(2)} + \vec{p}^{(3)} + \ldots = \bar{\bar{\alpha}} \cdot \vec{E} + \frac{1}{2}\bar{\bar{\beta}} \cdot \vec{E} \cdot \vec{E} + \frac{1}{6}\bar{\bar{\gamma}} \cdot \vec{E} \cdot \vec{E} \cdot \vec{E} + \cdots \qquad 2.8$$

where $\bar{\bar{\alpha}}$ is the linear polarizability tensor, and $\bar{\bar{\beta}}$, $\bar{\bar{\gamma}}$ are the first and second hyperpolarizability tensors, respectively. In first-order Raman scattering, only the first term is relevant, yielding:

$$\vec{p} = \vec{p}^{(1)} = \bar{\bar{\alpha}}\vec{E} \tag{2.9}$$

The polarizability tensor $\bar{\bar{\alpha}}$, describing a reversible effect, is represented by a symmetric 3×3 matrix with components α_{ij}, whose components define how the electronic distribution deforms under $\vec{E}$. A spherical distribution corresponds to equal diagonal elements, while anisotropic distributions lead to ellipsoidal clouds (Figure 2.7). While it might be diagonalized in its own coordinate system, it will generally have non-diagonal elements in the coordinate system of the light polarisation. For the sake of simplicity, but without loss of generality, we will discuss a single tensor element representing a specific scattering geometry in the following sections.

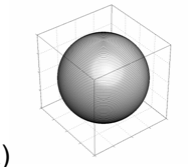

(a)

$$\bar{\bar{\alpha}} = \begin{pmatrix} \alpha & 0 & 0 \\ 0 & \alpha & 0 \\ 0 & 0 & \alpha \end{pmatrix}$$

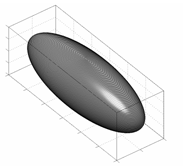

(b)

$$\bar{\bar{\alpha}} = \begin{pmatrix} \alpha_1 & 0 & 0 \\ 0 & \alpha_2 & 0 \\ 0 & 0 & \alpha_3 \end{pmatrix}$$

Figure 2.7: Representation of electron cloud shapes corresponding to different polarizability matrices. (a) Spherical electron distribution; (b) Ellipsoidal electron distribution.

2.2.2 Frequency dependence of Raman scattering

Raman activity arises only from vibrational modes that modulate $\bar{\bar{\alpha}}$. Under the harmonic approximation, the normal coordinate of the *k*-th vibrational mode is given by [15]:

$$Q_k = Q_{k0} cos(\omega_k t) \tag{2.10}$$

where Q_{k0} is the amplitude of the oscillation, and ω_k is its vibrational frequency. The polarizability tensor α_{ij} can be expanded in a Taylor series as:

$$\alpha_{ij} = (\alpha_{ij})_0 + \sum_k \left(\frac{\partial \alpha_{ij}}{\partial Q_k}\right)_0 Q_k + \frac{1}{2}\sum_{k,l} \left(\frac{\partial^2 \alpha_{ij}}{\partial Q_k \partial Q_l}\right)_0 Q_k Q_l + \cdots \tag{2.11}$$

Here, the subscript 0 denotes the equilibrium configuration of the system. Since higher-order terms are generally insignificant, the polarizability tensor simplifies to:

$$\bar{\bar{\alpha}} \approx \bar{\bar{\alpha}}_0 + \sum_k \bar{\bar{\alpha}}'_k Q_{k_0} where\ \bar{\bar{\alpha}}'_k = \left(\frac{\partial \bar{\bar{\alpha}}}{\partial Q_k}\right)_0 \quad 2.12$$

Inserting Equations (2.7) and (2.12) into (2.9) yields:

$$\vec{p} = \bar{\bar{\alpha}}_0 \vec{E}_0 cos(\omega_0 t) + \frac{1}{2}\sum_k \vec{E}_0 \bar{\bar{\alpha}}'_k Q_{k_0} \{cos[(\omega_0 - \omega_k)t] + cos[(\omega_0 + \omega_k)t]\} \quad 2.13$$

This equation is central to the classical[1] interpretation of Raman scattering, as it reveals the three frequency components of the scattered light. The term $cos(\omega_0 t)$ represents elastic Rayleigh scattering, where no energy is exchanged. The inelastic components, $cos[(\omega_0 - \omega_k)t]$ and $cos[(\omega_0 + \omega_k)t]$, correspond to Stokes and anti-Stokes Raman scattering, indicating energy loss and gain by the photon, respectively. These processes are schematically illustrated in Figure 2.8.

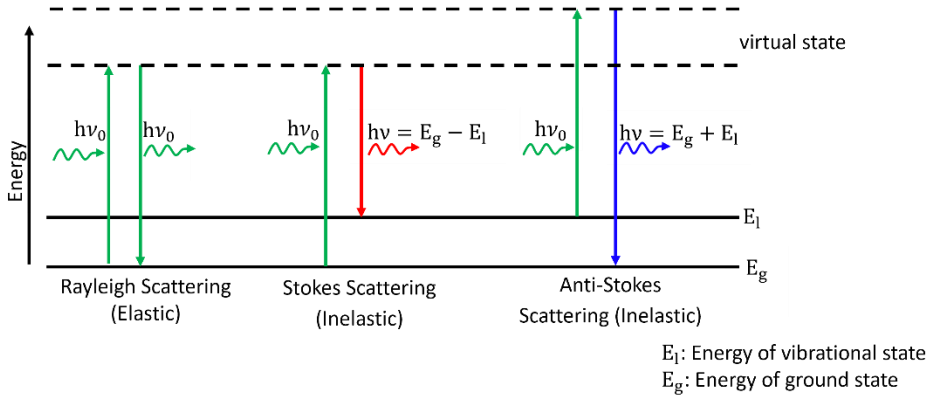

Figure 2.8: Energy-level Diagram Illustrating Rayleigh and Raman Scattering

2.2.3 Limitations of Raman spectroscopy

Despite its versatility and chemical specificity, Raman spectroscopy suffers from two primary limitations, low signal intensity and limited spatial resolution due to the diffraction limit of light. These constraints become particularly critical when studying nanoparticle or thin films.

[1] "Classic" refers to the treatment of the light-matter interaction. While a quantitative description of the Raman cross-sections requires a quantum-mechanical treatment of matter, the electromagnetic radiation is always treated in a classic way rather than a quantum-field-theory.

2.2.3.1 Raman cross section

A central parameter influencing signal strength is the Raman scattering cross section, σ_k, which defines the scattering efficiency for a given vibrational mode k. The intensity of the Raman signal is given by:

$$I_k \propto \sigma_k I_0 \tag{2.14}$$

where I_0 is the intensity of the incident light. Since Raman cross sections are typically several orders of magnitude lower than those of fluorescence or Rayleigh scattering, the signal is inherently weak. A more precise form accounts for the differential cross section over a solid angle $\delta\Omega$, determined by the numerical aperture (NA) of the optical system:

$$I_k \propto \frac{d\sigma_k}{d\Omega} I_0 \delta\Omega \tag{2.15}$$

For Stokes scattering, the differential cross section is expressed as [129]:

$$\left(\frac{d\sigma_k}{d\Omega}\right)_k^S \propto (\nu_0 - \nu_k)^4 \left(\frac{45\alpha_k'^2 + 7\gamma_k'^2}{45}\right)\left(1 - exp\left(\frac{-hc\nu_k}{k_B T}\right)\right)^{-1} \tag{2.16}$$

This equation shows that the Raman intensity depends on the excitation frequency (ν^4), vibrational mode symmetry (α_k' , γ_k'), and thermal population distribution (Boltzmann factor, is generally close to 1 for most Raman-active modes under ambient conditions. However, it plays a significant role in determining the relative intensities of Stokes and anti-Stokes Raman scattering). While shorter excitation wavelengths enhance signal intensity substantially, they are also prone to cause a fluorescence background, which can obscure Raman features.

Classical theories fail to fully describe Raman intensities, especially at the quantum level. Therefore, semi-classical or quantum mechanical models (e.g. density functional theory as in section 6.3.2) are necessary for accurate prediction. For instance, the ring-breathing mode of benzene at 992 cm^{-1} under 514.5 nm excitation has a Raman cross section of ~4.0×10^{-28} cm^2 [130], compared to fluorescence cross sections on the order of 10^{-17} cm^2 in the UV range [131]. To overcome these limitations, different approaches have been used, they include resonant Raman scattering, where the photon is absorbed, leading to a resonant coupling of the Raman effect to an electronic transition, which however amplifies vibrational signatures based on their symmetry. If absorption by the sample is not possible or undesirable, plasmonic-based methods are explored and will be discussed in the following sections.

2.2.3.2 Spatial resolution - diffraction limit of light

In far-field optical microscopy, spatial resolution is fundamentally limited by the diffraction of light. It is defined as the minimum lateral distance d between two points that can still be resolved, governed by the Rayleigh criterion (Figure 2.9). The resulting image of a point source forms an Airy disk, with resolution determined by:

$$d \approx 1.22 \frac{\lambda}{NA} \qquad 2.17$$

where λ is the excitation wavelength and $NA = n \cdot sin\alpha$, is the numerical aperture of the objective lens with *n* as the refractive index of the medium and α being the opening angle between the maximum beam diameter at the objective and the focal spot.

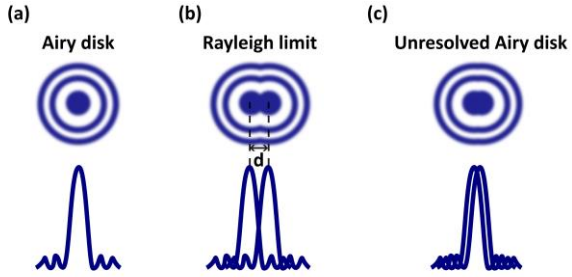

Figure 2.9: The Airy pattern observed in the image plane of the microscope (top row) and the corresponding intensity represented in two dimensions (bottom row). (a) Image of a point light sources. (b) and Images of two point light sources separated by a distance greater than the Rayleigh criterion limit "d," making them resolvable, and (c) by a smaller distance where they can no longer be separated.

This diffraction-limited volume defines the smallest volume from which Raman signals can be collected if focussed into a transparent medium. Due to the Gaussian profile of the focused laser beam, signal intensity peaks at the center and gradually decays outward. Thus, features smaller than half the excitation wavelength cannot be spatially resolved using conventional Raman microscopy. A similar argument hold true for the focal depth, which is of the same order as the beam waist. To overcome these limits, near-field techniques such as TERS have been developed for nanoscale characterization.

2.3 Near-field optical microscopy

The theoretical foundation of near-field optical microscopy (NSOM or SNOM) was established in 1928, demonstrating that optical imaging beyond the diffraction limit is possible by exploiting the extremely close proximity between a local probe and the sample under investigation [109]. At the

nanoscale, evanescent waves—decaying exponentially from the emitter—contain high spatial frequency components of the excitation field. Since these waves are confined to a limited spatial region, they enable the visualization of fine structural details at the nanometer scale. By positioning a subwavelength aperture or a diffracting object within a distance much smaller than the wavelength of light, evanescent waves at the interface can be directly converted into propagating waves, which can then be detected in the far-field. Two main approaches to SNOM have been developed based on this principle [132]:

- **Aperture-based SNOM**, where incident light passes through a nanometric opening in the probe tip before interacting with the sample (Figure 2.10 (a)). Apertures imply a trade-off between signal intensity that can be transmitted and spatial resolution and experimental configurations are generally limited to those where either the excitation or the emission to be detected are transmitted through the aperture, but not both.
- **Apertureless SNOM**, which employs scanning probe microscopy techniques (such as AFM or STM)) with external illumination. Light is diffracted by the probe, enhancing interactions at the sample surface. Among these, tip-enhanced near-field optical microscopy has gained significant prominence, particularly in its application to tip-enhanced Raman spectroscopy, which will be described in detail later (Figure 2.10 (b)).

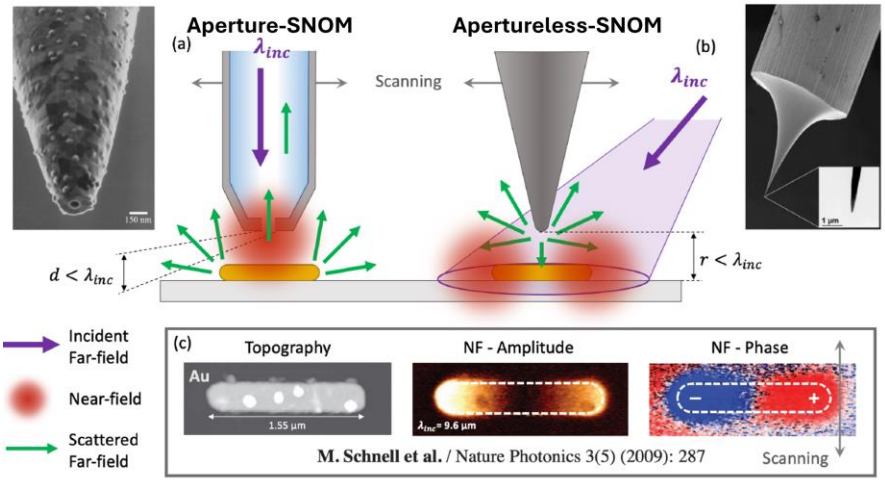

Figure 2.10: Two near-field microscopy techniques SNOM and TERS : (a) Aperture-based SNOM; (b) Tip-enhanced near-field optical microscopy.

The first experimental demonstration of "contact optical microscopy" was conducted by Fischer et al. in 1981 [133], achieving an optical image with a spatial resolution of 100 nm. In this approach, the resolving power was determined by the distance between the object and the probe, rather than by the wavelength of light. This work laid the foundation for near-field scanning optical

microscopy, which was introduced in 1984 by Pohl et al. [134]. The method was colloquially termed the "optical stethoscope" due to the analogy between near-field optical evanescent waves and acoustic waves in a traditional stethoscope. In both cases, the probe is significantly smaller than the wavelength and operates in extreme proximity to the source of the evanescent wave.

The earliest SNOM probes were developed by Betzig [135] and Lewis [136], achieving resolutions as fine as 12 nm (~λ/43). However, in practical applications, spatial resolutions are generally around 50 nm. One of the most widely used tip-enhanced near-field optical microscopy techniques integrates an SNOM setup with a shear-force scanning probe microscope coupled to an optical microscope [137]. In such configurations, optical fibers are utilized for tip illumination, exhibiting a lateral stiffness constant of approximately 0.1-300 N/m and a higher longitudinal stiffness, distinguishing them from conventional AFM probes [138]. Due to these mechanical properties, optical fiber probes are particularly sensitive to shear forces.

2.3.1 Plasmonic particle

One of the distinctive optical properties of noble metals is their high reflectivity, which gives them their characteristic luster. However, unlike their bulk counterparts, noble metal nanoparticles interact with visible light in a fundamentally different manner. The unique optical behavior of these nanoparticles has been known since antiquity and was utilized in the fabrication of stained glass. Historical artifacts, such as the Lycurgus Cup from the Roman period, now is in the British Museum, and the richly colored stained glass windows of Gothic cathedrals, owe their coloration to the presence of noble metal nanoparticles or metal salts embedded in the glass.

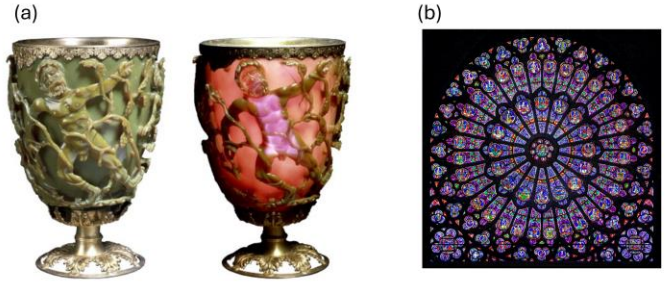

Figure 2.11: Showcasing the use of plasmonic nanoparticles. (a) the Roman-era Lycurgus Cup, (b) the North Rose window of Notre Dame de Paris [139,140].

This color variation arises because only specific wavelengths are scattered or transmitted, a phenomenon fundamentally governed by particle plasmons [16]. These plasmons correspond to the collective oscillations of conduction band electrons within noble metal nanoparticles, and their

resonance conditions depend on both the metal type and nanoparticle size. The early theoretical understanding of these effects was pioneered by Faraday [141] and later refined by Mie [142], laying the groundwork for modern research. Over the past decades, significant advancements have been made in the field, further elucidating the optical properties of metal nanoparticles.

2.3.2 Drude-Sommerfeld model

To further describe the plasmonic properties of nanoparticles quantitatively, the interaction between metals and EM waves can be modeled using the Drude-Sommerfeld theory [143]. Metals can be described as consisting of a periodic lattice of positively charged, heavy, and stationary ions, through which conduction electrons move freely. To explain the dynamics of this free-electron gas, Drude proposed a model in 1908, in which the motion of a conduction electron is governed by the following equation of motion:

$$m_e \frac{dv}{dt} + m_e \Gamma v = -eE \tag{2.18}$$

where m_e is the effective mass of the electron (accounting for the presence of surrounding positive charges), v represents the electron velocity, and e is the elementary charge. The term $m_e \Gamma v$ corresponds to a damping force, where Γ acts as a phenomenological damping constant. This term accounts for various inelastic interactions, including electron-electron scattering and electron-phonon coupling. The term $-eE$ represents the force exerted on the electron by an external electric field. Solving the motion equation yields an induced dipole moment per electron, $p = er_0$ where r_0 is the electron displacement from equilibrium. The macroscopic polarization is then $P = n_e p$, with n_e being the conduction electron density. Using the relation between polarization and polarizability α, it follows that $P = n_e \alpha p$. For metals in the optical regime, the dielectric function is described by the Drude model, where the electrical susceptibility χ_D relates to the free-electron response:

$$\varepsilon(\omega) = 1 + \chi_D = 1 - \frac{\omega_p^2}{\omega^2 + i\Gamma\omega} \tag{2.19}$$

Here, ω_p represents the Drude plasma frequency, defined as:

$$\omega_p = \sqrt{\frac{ne^2}{\varepsilon_0 m^*}} \tag{2.20}$$

where m^* is the effective electron mass, n is the conduction electron density, and ε_0 is the permittivity of free space. At optical frequencies, where $\omega \gg \Gamma$, the real and imaginary components of the dielectric function can be approximated as:

$$\varepsilon_1(\omega) \approx 1 - \frac{\omega_p^2}{\omega^2}$$
$$\varepsilon_2(\omega) \approx \frac{\Gamma \omega_p^2}{\omega^3} \qquad 2.21$$

These expressions highlight that, at frequencies below the plasma frequency, metals exhibit negative real permittivity, leading to strong reflection and metallic behavior. Conversely, at frequencies beyond ω_p, the material becomes transparent as the dielectric function approaches positive values. More rigorous descriptions require advanced quantum mechanical models. However, in practical applications, the dielectric function of metals is often obtained from experimental data, such as the widely used measurements by Johnson and Christy [144].

2.3.3 Bulk plasmons

The conduction electron density within a metal can oscillate in response to an external EM field. When the local electron density decreases, the positively charged ion lattice is no longer fully screened by the negative electron cloud. This imbalance generates an attractive force on neighboring electrons, leading to charge redistribution. The resulting Coulomb repulsion among electrons induces motion in the opposite direction, establishing a cyclic process that gives rise to transverse oscillations of the electron gas, commonly referred to as plasma oscillations. These collective excitations are associated with a quasiparticle known as a plasmon (Figure 2.12).

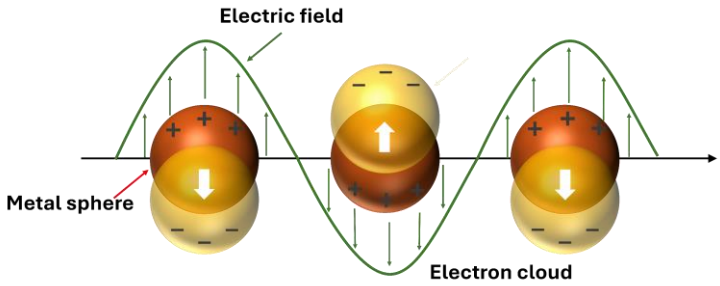

Figure 2.12: Schematic representation of plasma oscillations in a metallic nanoparticle , illustrating the displacement of the electron cloud (white arrows) relative to the nanoparticle's center under the influence of an external EM excitation field (green arrows).

Under specific conditions (described later), these oscillations can couple with external EM waves, giving rise to plasmon resonances. While the Drude model (Section 2.3.2) effectively describes

the behavior of free electrons, it does not fully capture the optical response of noble metals, where valence electrons contribute via interband transitions. These transitions limit plasmon excitations above ~2 eV for gold and ~4 eV for silver [145].

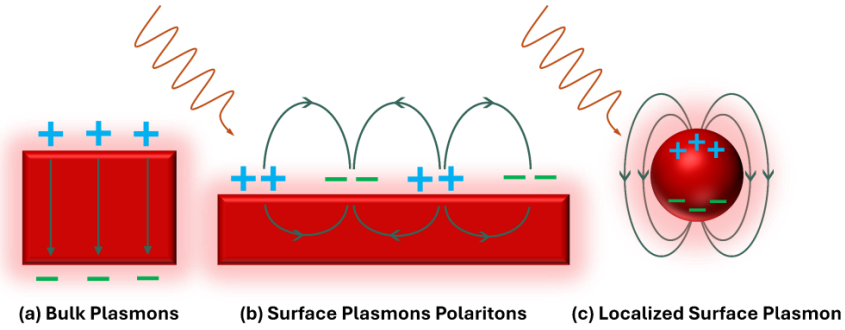

Figure 2.13: Illustration of plasmonic modes. (a) Bulk plasmons: volume charge oscillations within a metal. (b) Surface plasmon polariton: charge waves propagating along a metal-dielectric interface. (c) Localized surface plasmons: confined oscillations in a metallic nanoparticle.

Plasmonic phenomena are classified based on spatial confinement; bulk plasmons, surface plasmon polaritons (SPPs), and localized surface plasmons (LSPs), see Figure 2.13. Bulk plasmons, excited by electron beams but not by light due to momentum mismatch, are quantized volume oscillations with an energy $\hbar\omega_p = \hbar\sqrt{\frac{ne^2}{m_e\varepsilon_0}}$, where ω_p is the plasma frequency. SPPs are propagating charge density waves at metal-dielectric interfaces, while LSPs occur when metallic nanoparticles are smaller than the incident wavelength, leading to confined, non-propagating EM fields critical for applications like TERS and plasmonic sensing.

2.3.4 Surface plasmon

Surface plasmon polaritons were first described by Ritchie et al. [146] in 1957 as EM waves coupled to oscillations of conduction electrons at the interface between a metal and a dielectric medium. These surface waves propagate along the interface, with their field intensity decaying exponentially into both materials [147,148]. Unlike bulk plasmons, which are distributed within the volume of the metal, SPPs are confined to the interface and can be excited by light under specific conditions. However, due to momentum mismatch between free-space photons and SPP modes, direct optical excitation is not possible in conventional settings. Instead, phase-matching techniques such as prism coupling (Kretschmann or Otto configurations) or periodic grating structures are employed to facilitate their excitation [17]. The dispersion relation governing the propagation of surface plasmon polaritons at a metal-dielectric interface can be expressed as: [149]:

$$k_{SPP} = \frac{\omega}{c}\sqrt{\frac{\varepsilon_d \varepsilon_m(\omega)}{\varepsilon_d + \varepsilon_m(\omega)}} \qquad 2.22$$

where k_{SPP} is the complex wave vector of the SPP, ω the angular frequency, c the speed of light in vacuum, and ε_d and ε_m are the permittivity of the dielectric and metal, respectively. The real part of k_{SPP} defines the plasmon wavelength λ_{SPP}, while the imaginary component determines the propagation depth of the SPPs before attenuation due to dissipative losses. The penetration depth δ of the SPP field into both media is given by:

$$\delta_d = \frac{1}{k''_{z,d}}; \qquad \delta_m = \frac{1}{k''_{z,m}} \qquad 2.23$$

where $k''_{z,d}$ and $k''_{z,m}$ are the imaginary components of the wavevector in the dielectric and metal, respectively. The propagation length L_{spp}, representing the distance over which the intensity of the SPP decreases to $\frac{1}{e}$, is expressed as:

$$L_{spp} = \frac{1}{2k''_{spp}} \qquad 2.24$$

This relation highlights the evanescent nature of SPPs, where their intensity exponentially decays perpendicularly to the interface. As illustrated in Figure 1.6, the SPP dispersion curve asymptotically approaches the surface plasmon frequency ω_{sp}. , approximated by $\omega_{sp} = \omega_p\sqrt{\frac{1}{1+\varepsilon_d}}$, where ω_p is the bulk plasma frequency. This sets the upper limit for SPP excitation, ensuring that below ω_{sp}, SPPs remain confined to the metal-dielectric interface.

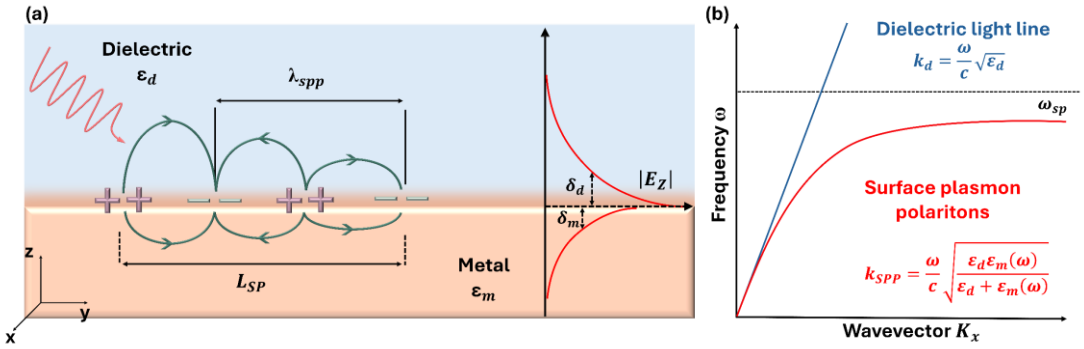

Figure 2.14: Schematic illustration of a surface plasmon polariton (SPP) showing its penetration depth into both the metal and dielectric medium. (b) Dispersion relation of light in a dielectric ($\varepsilon_d > n_{air}$, blue curve) and the dispersion relation of SPPs (red curve). The wavevector k_{SPP} asymptotically approaches a frequency proportional to the plasmon frequency ω_{sp}, which is determined using the Drude model.

2.3.5 Localized surface plasmon resonance (LSPR)

Localized surface plasmon resonance (LSPR) is a fundamental optical phenomenon that occurs in metallic nanoparticles when conduction electrons collectively oscillate in resonance with an incident EM wave. This effect is particularly significant in noble metals such as gold and silver, which possess free electron densities that allow for strong plasmonic interactions [148]. For small nanoparticles, typically those with diameters much smaller than the wavelength of the incident light, the electrostatic approximation can be applied. In this case, the EM field is assumed to be uniform across the nanoparticle, leading to a simple dipolar excitation. For a spherical metallic nanoparticle, the induced dipole moment p under an applied electric field E is given by $p=\alpha E$, where α denotes the sphere's polarizability and given by

$$\alpha = 4\pi\varepsilon_0 R^3 \frac{\varepsilon_m - \varepsilon_d}{\varepsilon_m + 2\varepsilon_d} \tag{2.25}$$

where R is the radius of the nanoparticle, ε_m is the permittivity of the metal, ε_d is the permittivity of the surrounding medium, and ε_0 is the permittivity of free space. This formulation is derived from the Clausius-Mossotti equation, which is commonly used to describe the polarizability of dielectric and metallic materials. The polarizability determines how much the nanoparticle can enhance and confine EM fields when excited at its LSPR frequency. A resonance condition is achieved when the denominator in this equation approaches zero, which occurs at:

$$\varepsilon_m(\omega) = -2\varepsilon_d \tag{2.26}$$

This condition determines the LSPR frequency ω_{LSPR} , meaning that the resonance is highly dependent on the dielectric properties of both the metal and the surrounding medium. From the equation 2.26, one might expect that when the denominator approaches zero, the polarizability could become infinite, leading to an unbounded enhancement of the local electric field. However, in reality, this does not happen due to losses inherent in the system. The imaginary part of the permittivity ε_m prevents the polarizability from diverging to infinity. The total dielectric function of a metal is typically expressed as:

$$\varepsilon_m = \varepsilon' + i\varepsilon'' \tag{2.27}$$

Where ε' determines the dispersion of light, and ε'' determines the energy losses due to absorption and electron damping. The presence of the imaginary component ε'' leads to damping of the electron oscillations, which in turn limits the field enhancement at resonance. In metals such as

gold and silver, the damping is relatively low, allowing strong plasmonic enhancement, but it is never eliminated. LSPR is significantly influenced by several key parameters, including the material composition of the nanoparticle, its size, shape, and the surrounding dielectric environment. Each of these factors plays a crucial role in determining the resonance frequency, the intensity of the local electric field, and the efficiency of light absorption and scattering.

2.3.5.1 Effect of material on plasmonic properties

The plasmonic behavior of nanoparticles is strongly influenced by their material composition, with variations in permittivity $\varepsilon_m(\omega)$ playing a crucial role. As described in Equation 2.25, the resonance condition for a nanoparticle within a dielectric medium is inherently dependent on the metal's permittivity, which directly affects its plasmonic response. Since different metals possess distinct optical and electronic characteristics, their LSPR behavior varies significantly, impacting parameters such as resonance wavelength, bandwidth, and field enhancement.

The scattering spectra of spheroidal nanoparticles, depicted in Figure 2.15, illustrate how material choice affects spectral shifts and resonance properties. Figure 2.15 (a) presents the experimental extinction spectra for nanoparticle arrays composed of these metals, all fabricated with similar size and geometry, while Figure 2.15 (b) provides theoretical extinction spectra for the same materials. The LSPR peaks are observed at 377 nm for aluminum (Al), 610 nm for silver (Ag), 655 nm for copper (Cu), and 665 nm for gold (Au).

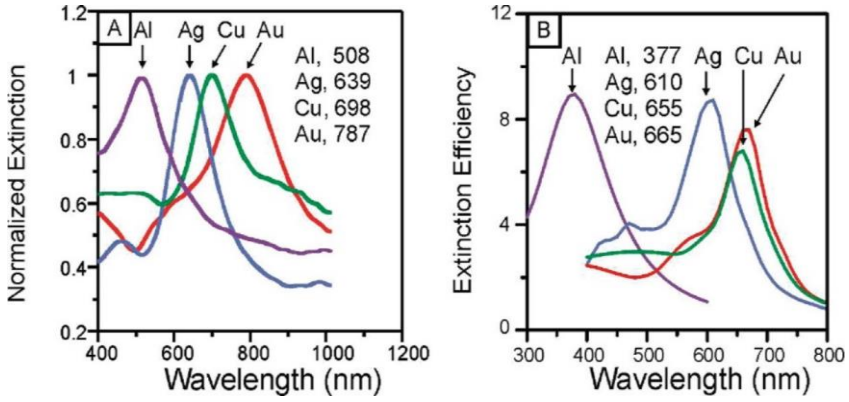

Figure 2.15: Normalized experimental (A) and theoretical (B) evaluation of the localized surface plasmon resonance properties of Al, Cu, Ag, and Au nanoparticles. This figure illustrates how material composition influences plasmonic behavior, showcasing differences in resonance wavelength, spectral broadening, and peak intensity among the metals (adapted from [18])

The plasmonic properties of these metals make them suitable for various technological applications, depending on their spectral response and stability. Aluminum demonstrates LSPR in the ultraviolet (UV) to visible spectrum, making it advantageous for deep-UV plasmonics and surface-enhanced fluorescence. However, its tendency to form an Al_2O_3 oxide layer upon air exposure leads to a redshift in the LSPR peak and a slight reduction in refractive index sensitivity [19,20]. Silver is widely regarded as having one of the sharpest plasmonic resonances, attributed to its low intrinsic damping, which makes it particularly effective for biosensing SERS and single-molecule detection However, its chemical stability is in the range of a few hours for the purpose of TERS tips, which imposes severe challenges for the preparation and alignment. Gold, on the other hand, supports LSPR in the visible to near-infrared (NIR) range and offers high chemical stability. While copper shares some plasmonic similarities with gold, its strong interband transitions introduce higher damping, resulting in broader resonance peaks and lower sensitivity. Its reaction with ambient oxygen causes the formation of strongly absorbing copper oxides, which suppress almost all LSPR. To further refine plasmonic performance, researchers have explored bimetallic nanostructures, such as Au-Ag and Cu-Ni alloys, which allow for tunable LSPR characteristics by modifying metal composition. These hybrid structures offer a balance between plasmonic efficiency and stability, making them promising candidates for nanoscale sensing and optoelectronic applications. In the context of this work, and for the sake of reproducibility of the tip production, we rely on gold tips.

2.3.5.2 Effect of surrounding environment on plasmonic properties

The dielectric properties of the surrounding medium significantly influence LSPR by altering the effective permittivity of the system, which in turn affects the resonance condition. As the refractive index of the surrounding medium increases, the resonance wavelength of LSPR undergoes a redshift. This shift occurs due to the modification of the local dielectric environment (see Equation 2.25), which changes the effective polarizability of the nanoparticle. The relationship between the LSPR peak shift $\Delta\lambda$ and the refractive index n follows an exponential dependence [21]:

$$\Delta\lambda = m\Delta n\left[1 - exp\left(-\frac{2d}{l_d}\right)\right] \qquad 2.28$$

where m represents the bulk refractive index response, d is the effective adsorbate thickness, and l_d is the characteristic EM decay length. Computational studies demonstrate a systematic redshift in LSPR when gold nanoparticles are coated with materials of increasing refractive index,

as shown in Figure 2.16, which presents extinction efficiency calculations for gold nanospheres under varying dielectric conditions.

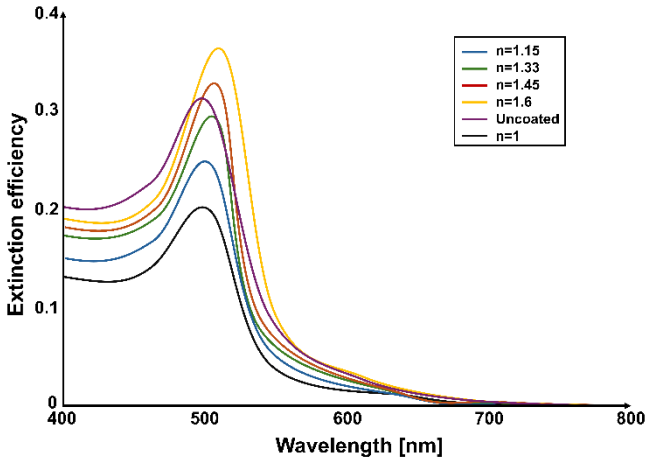

Figure 2.16: Extinction efficiency as a function of wavelength for a 7 nm gold nanosphere with a dielectric coating. The coating layer is 1.75 nm thick, and *n* denotes the refractive index of the surrounding material.

Experimental observations further support this trend [150,151], with studies showing that embedding gold or silver nanoparticles in different dielectric environments, such as air, water, or glass, consistently induces LSPR peak shifts. This phenomenon is well-described by the Maxwell-Garnett theory [152], which models the interaction between metal nanostructures and their surrounding dielectric medium. Furthermore, plasmon-enhanced photoluminescence (PL) exhibits a similar dependence on environmental permittivity, reinforcing the crucial role of surrounding dielectric properties in tuning plasmonic responses. These principles form the foundation for various applications, including LSPR-based refractive index sensors TERS-based chemical analysis, where subtle shifts in LSPR intensity and wavelength provide critical insights into molecular interactions. Our group has exploited this effect for the mapping of local refractive index changes with nanoscale resolution [153].

2.3.6 Surface-enhanced Raman spectroscopy

The discovery of surface-enhanced Raman scattering began with Fleischmann et al. [112] in 1974, who observed enhanced Raman signals of pyridine on a roughened silver electrode. Initially, the enhancement was attributed solely to increased surface area. However, later studies by Jeanmaire and Van Duyne [154], and Albrecht and Creighton [155] in 1977, demonstrated that the signal amplification—reaching five orders of magnitude—could not be explained by surface roughness alone. They identified the involvement of metallic substrates in amplifying Raman

scattering via electromagnetic and chemical mechanisms. Moskovits [156,157] later proposed that nanostructured features on the metal surface acted as sites for localized surface plasmon resonance, significantly enhancing the local EM field. By the 1990s, SERS had evolved into a powerful technique, enabling single-molecule detection, as shown by Kneipp [158] and Nie [159]. These studies revealed that not all metallic aggregates are SERS-active and that only specific regions—termed “hot spots”—produce dramatic enhancements, often exceeding 10^{14} times the conventional Raman signal. This led to the understanding that both the nanostructure and plasmonic properties of the substrate are crucial for SERS activity.

SERS is fundamentally based on the amplification of the incident electromagnetic field at or near the surface of a material. The resulting SERS spectrum reflects the interaction between incident photons and the vibrational energy levels of surface-bound molecules. The signal intensity is primarily influenced by three key parameters: the Raman cross-section of the adsorbed species, the number and quality of active sites (including their roughness, homogeneity, and composition), and the surface coverage of the analyte.

Since the discovery of the SERS phenomenon, researchers have tried to understand its underlying mechanisms. It is now widely accepted that the enhancement of the Raman signal arises from two main synergistic effects: the electromagnetic mechanism—already discussed in detail in the previous chapter—which originates from the interaction between the incident electromagnetic field and the localized surface plasmons of the metallic substrate; and the chemical mechanism, which is attributed to charge-transfer interactions between the adsorbed molecule and the metal surface. As for the electromagnetic field enhancement and confinement, it is particularly strong in the case of a dimer with distances of a few nanometers when the electric field points along the axis between the particles. This dimer configuration finds an analogy in gap-TERS, where the image charge of the tip below a metallic surface acts as the counterpart. Fundamentally, SERS builds upon the classical framework of Raman scattering, where the scattered intensity is governed by the induced dipole moment P. In the following section, both enhancement mechanisms will be discussed in detail.

2.3.6.1 Electromagnetic enhancement

The electromagnetic mechanism is fundamentally responsible for the observed enhancement, primarily through the perturbation of the local electric field vector $E_{\omega 0}$. This perturbation arises due to the excitation of surface SPR at the interface of the metallic substrate. Crucially, the interparticle spacing plays a significant role in modulating the amplitude of the Raman

enhancement. In closely coupled nanostructures—such as dimers or nanoparticles with sharp features—the enhancement factor can reach values up to 10^{11} [28]. This enhancement phenomenon was first attributed to surface plasmon excitation by B. Pettinger in 1980 [160] who demonstrated it using pyridine molecules adsorbed onto noble metal electrodes (gold, silver, and copper). These metallic nanostructures exhibit substantially higher polarizability and absorption cross-sections compared to isolated molecules, functioning effectively as nanoscale antennas for both receiving and re-radiating the Raman-scattered photons. The scattered light, re-emitted by the metal nanostructures, corresponds to the amplified Raman signal due to the decay of surface plasmon polaritons.

In the interstice between two metallic nanoparticles—commonly termed the “hotspot”—the Raman signal may be enhanced by 4 to 6 orders of magnitude relative to that of a single isolated nanoparticle, independent of its geometry (e.g., spherical or triangular). D.A. Weitz [161] proposed a relationship linking the electromagnetic enhancement factor in SERS to the plasmon absorption spectrum and the complex dielectric function $\varepsilon(\omega_0) = \varepsilon'(\omega) + i\varepsilon''(\omega)$ of the metal. The enhancement is given by:

$$g^{EM}(SERS) = \frac{|\varepsilon(\omega_0)|^2 |\varepsilon(\omega_{DR})|^2}{\varepsilon''(\omega_0)\varepsilon''(\omega_{DR})\omega_{DR}\omega_0} Abs(\omega_0) Abs(\omega_{DR}) \qquad 2.29$$

Here, Abs represents the experimentally measured absorbance at the laser excitation frequency ω_0, and $\omega_{DR} = \omega_0 - \omega_k$ is the Stokes-shifted Raman frequency, with ω_k corresponding to the molecular vibrational wavenumber. While this empirical formulation captures the spectral dependence of enhancement, it does not account for the contributions of non-radiative or dark plasmon modes, which are not observable via conventional UV-Vis absorption spectroscopy.

2.3.6.2 Chemical enhancement

Since the 1970s, the existence and the actual contribution of the so-called "chemical effect" in SERS have been the subject of ongoing debate within the scientific community. Despite numerous studies, this topic remains incompletely understood, partly due to the complex interplay between chemical and electromagnetic mechanisms that govern the overall enhancement process. Furthermore, there is no universally accepted definition of the chemical effect, and different interpretations persist among researchers. Nonetheless, a general consensus acknowledges that the chemical contribution arises from specific interactions between the adsorbed molecule and the metallic substrate. According to M. Moskovits [68], this effect is

characterized by a modification in the Raman polarizability tensor of the molecule, induced by the formation of a transient or permanent complex with the metal surface. This alteration can result in either an attenuation ("quenching") or an enhancement of the Raman signal, depending on the nature of the interaction.

Among the various mechanisms proposed to account for changes in polarizability, charge transfer between the metal and the adsorbate is the most frequently invoked. A significant body of literature discusses this topic in depth [24–27]. In a comprehensive review of relevant theoretical and experimental works [162–164], E.C. Le Ru and P.G. Etchegoin [165] identified three principal charge transfer pathways. In the simplest case, the presence of the metallic substrate perturbs the electronic structure of the adsorbed molecule without the formation of a covalent bond. This perturbation facilitates partial charge redistribution—either from the metal to the molecule or vice versa—leading to subtle modifications in the electronic density and the Raman polarizability tensor. As a consequence, certain vibrational modes exhibit an increased Raman activity. This scenario is illustrated in Figure 2.17, which shows the energy level alignment of a molecule-metal system across three stages: (a) before charge transfer, (b) during the charge transfer process, and (c) after the interaction, with energy levels shifted and the molecule in an electronically excited state. Such interactions can also occur indirectly, mediated by intercalated ions, leading to the creation of new localized electronic states within the molecular bandgap. These newly formed states may, under favorable conditions, position the system near resonant Raman scattering regimes.

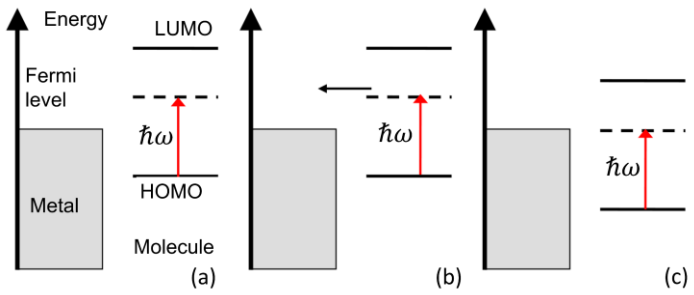

Figure 2.17: Energy level diagram of the molecule–metal system : (a) prior to charge transfer, (b) during the charge transfer process, and (c) following the transfer, showing energy level realignment and molecular excitation.

A more elaborate mechanism, depicted in Figure 2.18, involves resonant charge transfer through the metal's Fermi level. When the energy difference between the metal's Fermi level and either the highest occupied molecular orbital (HOMO) or the lowest unoccupied molecular orbital (LUMO) of the molecule matches the photon energy, a resonant transition can be established. In

this case, an electron could move from the HOMO to the Fermi level (or from an occupied metal state to the LUMO), enabling efficient coupling that significantly enhances the Raman scattering intensity.

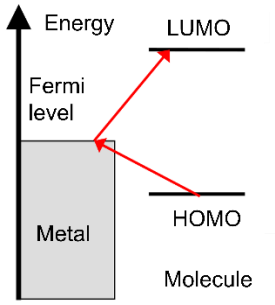

Figure 2.18: Energy diagram depicting the band structure of the metal nanostructure and the HOMO–LUMO gap of the adsorbed molecule.

The SERS effect, therefore, results from a synergistic combination of EM and chemical phenomena, which are often difficult to disentangle. Although extensive theoretical and experimental work has addressed each effect individually, integrative studies that explore their interdependence remain scarce. Notably, D.J. Masiello and G.C. Schatz [166,167] have developed a semi-classical theoretical framework that treats the molecule as a quantum system interacting with the classical surface plasmon field. Building on this concept, we will explore in the subsequent chapter a fully quantum-mechanical model describing the metal–molecule interaction, with the aim of bridging theory with experimental observations through various plausible interaction scenarios.

2.4 Tip-enhanced Raman spectroscopy

The pursuit of surpassing the diffraction limit of light—a fundamental barrier in conventional optical microscopy—has led to the development of several innovative techniques in near-field optics. This limit, defined by Abbe's criterion, states that two objects separated by less than half the excitation wavelength cannot be spatially resolved using standard far-field illumination. Over the past decades, advances in instrumentation and nonlinear optics, including the advent of confocal microscopy and spectroscopies like coherent anti-stokes Raman scattering (CARS), have pushed the boundaries of spatial resolution. However, it is the concept of scanning near-field optical microscopy (SNOM or NSOM) that has offered a radical departure from this limitation.

The idea of near-field microscopy was first articulated by E.H. Synge in 1928 [168], who envisioned using a sub-wavelength aperture probe to collect optical signals in the proximity of a

sample surface. Although unrealized at the time, his concept laid the groundwork for later experimental breakthroughs. In 1972, Ash and Nicholls [169] built a prototype capable of sub-diffraction resolution using microwave radiation. Building on the principles of scanning tunneling microscopy (STM), Pohl and collaborators achieved the first practical optical near-field system in 1984 [134]. This marked the emergence of a new class of local-probe-based optical microscopies. Soon after, Betzig formally introduced the acronyms NSOM (nearfield scanning optical microscopy) and SNOM (scanning nearfield optical microscopy) [170], and researchers such as Courjon, De Fornel, and Chaigneau contributed significantly to advancing both instrumentation and probe fabrication [171–173]. Among the techniques born from near-field optics, tip-enhanced Raman spectroscopy has emerged as a particularly powerful tool for nanoscale chemical imaging. TERS combines the chemical and structural specificity of Raman spectroscopy with the high spatial resolution of scanning probe methods such as atomic force microscopy or STM. In addition to this, it also promotes the sensitivity through an enhancement of the local electric field. In this approach, a metallic probe—often silver or gold-coated—is used to confine and locally enhance the EM field at its apex. The lateral spatial resolution is strongly affected by the curvature of the tip apex, its material properties, and the tip–sample separation distance and may be as low as a single chemical bond [174].

TERS operates on the principle that the incident far-field laser radiation (E_0) excites localized surface plasmons at the apex of the metallic tip. This excitation results in the generation of a highly confined and enhanced near-field ($E_{loc} = gE_0$), where g represents the local field enhancement factor. This factor is strongly dependent on the complex dielectric function of the surrounding environment and the metal composing the tip. The field enhancement is further intensified at the apex due to the synergistic effects of surface plasmon resonance and the "lightning rod" effect—a geometrical phenomenon that concentrates the field at sharply curved metallic structures [175]

As the tip scans across the sample surface, a Raman spectrum is recorded at each spatial coordinate, allowing for the simultaneous acquisition of topographic and chemical maps with nanometer-scale resolution. The dual benefit of intense field confinement and high spatial precision makes TERS uniquely suited for extremely small sample volumes, including the detection of individual molecules. Similar to conventional SERS, the observed enhancement in TERS arises from both EM and chemical mechanisms. The electromagnetic contribution is driven by plasmonic coupling and local field amplification, while the chemical component results from molecule–metal interactions that modify the Raman polarizability tensor. In the specific geometry

of TERS, an additional enhancement is attributed to the lightning rod effect, which is intrinsically linked to the sharpness and curvature of the tip apex.

Together, these mechanisms enable TERS to operate as a powerful nanospectroscopic technique that bridges the gap between topographical imaging and vibrational spectroscopy at the molecular scale. It has become an indispensable tool in nanoscience and materials characterization, especially in the study of surface chemistry, molecular orientation, and low-dimensional systems.

2.4.1 Lightning rod effect

The lightning rod effect—also referred to in electrostatics as the "tip effect"—originates from the work of Benjamin Franklin in 1752, who first conceptualized the use of sharp conductive elements for lightning protection [22]. Centuries later, this geometrical principle found significant relevance in nanophotonics, particularly in the context of field enhancement in TERS. The essence of the lightning rod effect lies in the accumulation of electric charges at the apex of a sharply pointed conductor. The smaller the radius of curvature at the tip apex, the stronger the localization and amplification of the electric field.

This phenomenon is purely geometrical in origin, although its efficiency is modulated by the alignment between the tip axis and the polarization of the incident EM field [176]. The most intuitive TERS configuration, either in transmission or backscattering geometry, is for a laser beam with incidence parallel to the tip axis. This configuration however does not provide an electric field component between tip and sample surface (*p*-polarisation) with the use of linearly polarized lasers. To provide an electric field component parallel to the *k*-vector and along the tip axis, either a radially polarized beam or a semi-blocked beam are required. Neither of these solutions is straight-forward to implement experimentally without jeopardizing e.g. the shape and size of the confocal volume. For this reason, most TERS setups operate with confocal side-illumination to ensure maximal excitation of LSPRs with a strongly enhanced electric field between tip and surface and optimal field confinement at the tip apex. The near-field tends to be strongly depolarized, rendering the scattering geometry, as e.g. defined by the Porto-notation, hard to assess. The material composition of the tip plays an equally crucial role in determining the effectiveness and stability of the enhancement. Various fabrication methods have been explored to produce sharp and optically responsive metallic tips. Among these, electrochemical etching in concentrated hydrochloric acid (HCl) and ethanol mixtures [177], as well as vacuum deposition techniques [178], have yielded reliable tip geometries suitable for TERS applications.

Gold tips are widely preferred due to their superior reproducibility and long-term stability. Gold exhibits a complex dielectric function characterized by a large negative real part and a relatively small imaginary component. This combination enables efficient confinement of the localized field and facilitates the enhancement of luminescence signals generated at the tip apex via localized plasmon excitation. Furthermore, the chemical inertness of gold ensures that the tip remains stable under ambient conditions over extended periods. However, the mechanical softness of gold imposes restrictions on the interaction mechanism between tip and sample, contact as any direct contact between the tip and the surface, intentional (for e.g. chemical enhancement) or unintentional (slow feedback loop), will not only change the shape of the tip but also its LSPR.

Silver tips, while offering even larger field enhancement due to their more favorable plasmonic response in the visible spectrum, suffer from chemical instability. In particular, silver is prone to oxidation and sulfidation when exposed to air, which significantly degrades its performance over time on the scale of a few hours. For this reason, silver tips are typically used immediately after fabrication and under controlled environmental conditions to slow down surface contamination and deterioration.

2.4.2 Electromagnetic field enhancement

As introduced earlier, the enhancement factor in Raman spectroscopy characterizes the order of magnitude by which the Raman signal is amplified in the presence of a metallic nanostructure as compared to the same experiment without metal nanostructure, sometimes referred to as “tip-in” versus “tip-out” experiments. In TERS, this enhancement becomes pronounced when the excitation wavelength resonates with the surface plasmon frequency of the metallic tip. Under these conditions, the induced local electric field E_{loc} may differ substantially from the incident field E_0 in both magnitude and orientation, giving rise to strong localized field intensities at the tip apex. In both TERS and SERS, the metal influences the field enhancement through three principal mechanisms:

2.4.3 Local field enhancement

Near a nanostructure, the incident electric field undergoes significant spatial confinement and amplitude modulation. When the excitation wavelength coincides with the plasmonic resonance of the metallic system, particularly at specific positions where particles are closely spaced or geometrically confined (commonly referred to as "hot spots"), a highly localized electric field is generated. This results from strong coupling between LSPs at the metallic surface, leading to a

substantial amplification of the dipolar excitation. The intensity-based local field enhancement factor can be expressed as [179]:

$$g_{loc}(\omega_l) = \frac{|E_{loc}(\omega_{loc})|^2}{|E_0|^2} \sim g^2 \quad 2.30$$

This parameter reflects the degree of electric field concentration near the tip but does not account for changes in field polarization.

2.4.4 Radiative enhancement (backscatter light enhancement)

In certain conditions—particularly in the near-field—a molecular dipole oscillating in proximity to a metallic nanostructure may experience radiative enhancement. This mechanism depends on the metal's dielectric function, its geometric characteristics, and the dipole's position and orientation relative to the tip. For metals supporting surface plasmons, especially those satisfying $Re\big(\varepsilon(\omega)\big) < 0$, the radiated field is enhanced via resonant coupling with the radiative component of localized plasmons. The corresponding radiative enhancement factor is [179]:

$$g_R(\omega_R) = \frac{|E_{loc}(\omega_R)|^2}{|E_0|^2} \sim g^2 \quad 2.31$$

where ω_R is the radiation frequency and represents the re-emission component of the Raman process.

2.4.5 Total field enhancement in TERS

When considering both excitation and re-emission contributions, the overall TERS enhancement factor can be approximated as the product of local and radiative field enhancements:

$$Enhancement \approx g_{loc}(\omega_1) g_R(\omega_R) = \frac{|E_{loc}(\omega_{loc})|^2}{|E_0|^2} \frac{|E_{loc}(\omega_R)|^2}{|E_0|^2} \quad 2.32$$

In most practical cases, since the Raman shift is relatively small, the approximation $\omega_R = \omega_l$ holds, leading to the well-known E^4 dependency:

$$Enhancement \approx \frac{|E_{loc}(\omega_{loc})|^4}{|E_0|^4} \approx g^4 \quad 2.33$$

This expression emphasizes the 4th power sensitivity of the Raman enhancement to local field strength. Previous research from our group [180] demonstrated that it is indeed an approximation

that holds true as long as the Stokes-shift is small compared to the width of the localized surface plasmon resonance. These resonances have a typical full width at half maximum (FWHM) around 50 nm. Within the visible spectrum, theoretical predictions suggest that the TERS enhancement (signal of TERS compared to confocal signal) may reach magnitudes up to 10^{12}, corresponding to a local field enhancement of 1000. Experimentally, signal enhancement values more commonly fall within the range of 10^4 to 10^8, as reported in several studies [29,30]. Such a significant enhancement, however, is still highly localized and occurs primarily at the apex of the scanning tip, where the intensity of the localized surface plasmon is maximal. The strength of the electric field decreases rapidly with increasing distance from the tip, following a phenomenological power-law dependence approximated by [30,31]:

$$E \propto \frac{1}{(d+r)^{10}} \tag{2.34}$$

Here, r denotes the radius of the tip apex and d represents the distance between the tip and the sample surface. This high field gradient explains the exceptional spatial confinement of the near-field region, which is responsible for the nanoscale resolution characteristic of TERS. As the plasmonic tip scans across the surface, it enables the highly localized detection of single-molecular signals, reaching spatial resolutions on the order of a few nanometers or even below.

2.4.6 Enhancement factor

Determining the enhancement factor g is essential for evaluating the performance of TERS tips. However, this parameter is often overestimated due to contributions from far-field artifacts. N. Kumar et al. [70] investigated this overestimation by comparing TERS signal intensities to background Raman signals collected in the far-field. To correct for these discrepancies, they introduced a normalization method accounting for the effective sampling volumes and intensities of the near-field (TERS) and far-field contributions:

$$g = \left(\frac{I_{TERS} - I_{far\text{-}field}}{I_{far\text{-}field}}\right) \cdot \left(\frac{V_{far\text{-}field}}{V_{TERS}}\right) \tag{2.35}$$

Where I_{TERS} denotes the Raman intensity acquired with the tip engaged (in contact with the sample), $I_{far\text{-}field}$ corresponds to the Raman intensity measured with the tip retracted (non-contact configuration). V_{TERS} and $V_{far\text{-}field}$ represent the effective interaction volumes contributing to the near-field and far-field signals, respectively. For ultrathin samples, where the vertical sampling depth is negligible, these volumes are often approximated by the corresponding surface areas

probed by the near-field and far-field components denoted A_{TERS} and $A_{far\text{-}field}$. Under this approximation, equation 2.35 can be rewritten as:

$$g = \left(\frac{I_{TERS} - I_{far\text{-}field}}{I_{far\text{-}field}}\right) \cdot \left(\frac{d}{\left(1.22\frac{\lambda}{NA}\right)}\right)^2 \qquad 2.36$$

Here, d denotes the effective diameter of the TERS interaction area, λ is the excitation wavelength, and NA is the numerical aperture of the objective lens. The denominator $\left(1.22\frac{\lambda}{NA}\right)$ represents the diffraction-limited spot size in the far-field, assuming an Airy disk profile. This equation provides a more practical and geometry-based estimation of the TERS enhancement factor, particularly suitable for thin films and nanoparticles. While the determination of the confocal volume or area is generally straight-forwarded, the determination of the volume or area that experiences noticeable near-field enhancement bears far more uncertainties and does not only vary from tip to tip but also across a single scan depending on topography and tip-wear. Our tips have provided estimated field-enhancement factors of up to 20 [181].

2.5 Perovskites

Perovskite oxides, with the general formula ABO_3, constitute a structurally versatile and functionally rich class of materials that underpin a wide range of applications in electronics, optics, catalysis, and energy technologies [32–34]. Their unique combination of chemical flexibility, lattice dynamics, and electronic properties arises from the corner-sharing network of BO_6 octahedra and the ability to host diverse A- and B-site cations, enabling tuning of structural distortions and functional responses [35,36]. Among these materials, strontium titanate ($SrTiO_3$) and barium titanate ($BaTiO_3$) serve as prototypical perovskites, each exemplifying key aspects of perovskite behavior. $SrTiO_3$ is a paraelectric at room temperature, but exhibits high sensitivity to surface structure, termination, and external perturbations [50,182–185]. In contrast, $BaTiO_3$ is a classical ferroelectric oxide with well-defined structural phase transitions as a function of temperature and size [37–39].

The surface chemistry of perovskite oxides is of critical importance in catalysis, thin-film growth, and sensor applications. $SrTiO_3$ (100) surfaces can terminate in either SrO or TiO_2 layers (vicincal surfaces), each exhibiting distinct reactivity, particularly toward atmospheric species such as H_2O and CO_2 [40–42]. Surface reconstructions, delamination phenomena, and the spontaneous formation of carbonate monolayers under ambient conditions significantly modify the electronic

and chemical landscape of these materials [63,186,187]. Likewise, $BaTiO_3$ nanoparticles are known to undergo phase-dependent and size-dependent transformations that influence their ferroelectric properties and surface adsorption behavior, particularly in relation to the stabilization or suppression of polarization at the nanoscale [43,44].

In this chapter, we present a detailed scientific overview of the crystallographic, surface, and chemical properties of $SrTiO_3$ and $BaTiO_3$, with a focus on how surface terminations, adsorption mechanisms, and phase transitions can be explored using TERS. This background lays the foundation for the experimental investigations that follow in subsequent chapters.

2.5.1 Structure and versatility of ABO_3 perovskites

Perovskite oxides (chemical formula ABO_3) are a broad class of materials named after the mineral perovskite ($CaTiO_3$). They adopt a characteristic crystal structure consisting of a network of corner-sharing BO_6 octahedra with larger A-site cations occupying 12-coordinate cavities formed in between (often described as cuboctahedral sites) [45–47]. In the ideal cubic perovskite unit cell (space group *Pm*3*m*), the A cation sits at the cell center (½, ½, ½ position), the B cation at the corner (0,0,0), and oxygen anions at face-centered positions (½, 0, 0) etc., such that each B cation is octahedrally coordinated by oxygens and each A cation is 12-fold coordinated by oxygens [48]. This highly symmetric structure can accommodate a remarkable variety of cation sizes and charges. Many compounds adopt the perovskite structure or slight distortions thereof, making ABO_3 a versatile structural template. The flexibility of the lattice allows substitution or doping on both A and B sites, enabling fine-tuning of properties and the incorporation of many elements into the structure [1,188,189]. Minor distortions from the cubic archetype often occur depending on ionic size or electronic factors, leading to lower-symmetry variants (tetragonal, orthorhombic, rhombohedral, etc.), but the essential connectivity of the octahedral framework remains. Figure 2.19 illustrates an ideal cubic ABO_3 lattice, showing the A-site cations (green) in a 12-fold coordinated cuboctahedra environment and B-site cations (blue) inside corner-sharing O_6 octahedra (oxygen anions in red).

Perovskite oxides are renowned for their multifunctional behavior, rooted in their structural flexibility and complex electronic configurations. Many ABO_3 oxides are ferroelectric, piezoelectric, or higher-κ dielectrics, making them crucial in electronic and electromechanical applications. For example, $BaTiO_3$ and $Pb(Zr,Ti)O_3$ (PZT) are classic ferroelectric perovskites used in capacitors, sensors, and actuators due to their high dielectric constants (often tens of thousands near the Curie temperature) and substantial piezoelectric coefficients [190,191].

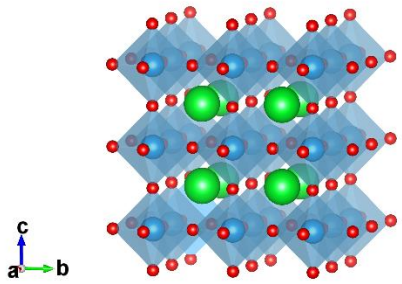

Figure 2.19: The ideal cubic perovskite structure of an ABO_3 oxide (illustrated here for $BaTiO_3$ in its cubic phase). Blue spheres represent B-site cations (e.g. Ti^{4+}), which reside in the centers of O_6 octahedra (red spheres at the octahedral corners). Large green spheres are A-site cations (e.g. Ba^{2+}) occupying the 12-coordinate cavities formed by neighboring octahedra. The corner-sharing network of octahedra is the hallmark of the perovskite structure.

The perovskite structure's tolerance to substitution allows tuning of ferroelectric Curie temperatures and piezoelectric response by chemical modification [191]. In ferroelectric perovskites, a structural distortion (typically a cation off-centering) below the Curie temperature produces a switchable spontaneous polarization. This polarization can couple to surface chemistry: the termination surfaces of a ferroelectric may carry bound charges forcing the structure to compensate through the adsorption of ionic species [192]. Even in non-ferroelectric perovskites, the concept of surface polarity is important. Depending on how the crystal is terminated, the alternating charged layers in an ionic ABO_3 lattice can create a polar surface (with a net surface dipole) unless reconstruction or compensation occurs. According to Tasker's rules for ionic crystals, perovskites with neutral layer stacking (e.g., $SrTiO_3$ with alternating charge-neutral SrO and TiO_2 layers along (100)) can maintain bulk terminations, whereas those with charged layers (e.g., $KTaO_3$ with $K^{+}O^{2-}$ and $Ta^{5+}O_2^{2-}$ layers along (100)) tend to undergo significant reconstruction to avoid a diverging surface electrostatic energy [193]. In general, non-polar terminations (charge-neutral AO or BO_2 layers) are stable and often reflect the bulk composition, while polar terminations drive compensating processes such as atomic rearrangement, adsorption of charged species, or faceting [193]. The ability of perovskite surfaces to stabilize or eliminate polar discontinuities is a key aspect of their surface chemistry and is closely tied to phenomena like surface reconstructions and adsorption.

Beyond electric polarization, ABO_3 oxides exhibit diverse electronic and chemical functionalities. Materials such as $SrTiO_3$ behave as wide-bandgap semiconductors and become more conductive via doping or oxygen vacancies [194], while rare-earth manganites exhibit rich magnetic behavior

[195], and doped systems like $BaPb_{1-x}Bi_xO_3$ can become superconducting with critical temperatures up to 13 K [196]. Their capacity for mixed ionic-electronic conduction makes them promising candidates for electrochemical devices. Catalytically active compositions, such as $La_{1-x}Sr_xCoO_3$, are effective in oxygen electrocatalysis [197], and compounds like $LaFeO_3$ and $BaTiO_3$ have demonstrated gas sensing capabilities through surface-induced conductivity modulation [198,199].

2.5.2 Strontium titanate ($SrTiO_3$)

2.5.2.1 Bulk crystal structure of $SrTiO_3$

Strontium titanate ($SrTiO_3$) is a prototypical perovskite oxide that crystallizes in the cubic perovskite structure (space group Pm3m) at ambient conditions. Its lattice parameter is approximately 3.905 Å, with Sr^{2+} occupying the A-site and Ti^{4+} the B-site in the ABO_3 lattice [49]. At room temperature, $SrTiO_3$ is centrosymmetric and paraelectric, meaning it does not exhibit spontaneous polarization. The perfect cubic structure of $SrTiO_3$ consists of rigid TiO_6 octahedra with Ti–O–Ti bonds at 180°. In the cubic phase, all optical phonon modes of the ideal crystal are Raman-silent; first-order Raman scattering is symmetry-forbidden by the center of inversion [200]. However, disorder or defects induce weak Raman features even in nominally cubic $SrTiO_3$, a point relevant for detecting incipient polar order [201]. In other words, first order Raman modes in $SrTiO_3$ are a highly sensitive, qualitative indicator of deviations from the perfect crystal structure.

In terms of its physical properties, $SrTiO_3$ is a wide bandgap semiconductor with a band gap of approximately 3.3 eV that can be rendered more conducting (n-type) through oxygen vacancies or doping with donor cations (e.g., Nb^{5+} substituting Ti^{4+}) [50]. It has a high refractive index (~2.4 in the visible and infrared spectrum) and is sometimes used in optics, such as in nonlinear optics [202]. In ceramic form, it finds use in varistors and as a substrate for growing other perovskite oxide thin films due to its lattice matching with many materials [203,204]. It also serves as a common substrate in epitaxy, further promoting the interest in its surface and interface properties.

2.5.2.2 (100) Surface structure: SrO vs. TiO_2 terminations

The most common facet of $SrTiO_3$ is the pseudo-cubic (100) surface (often referred to as (001) in crystallographic notation for perovskites, since all of the cubic axes are equivalent). Cleaving or terminating $SrTiO_3$ along the (100) direction exposes either a SrO layer or a TiO_2 layer also known as vicinal surfaces. These are the two possible terminations of the ABO_3 stacking sequence: one

where the surface layer is the alkaline earth oxide (SrO) and one where it is the transition metal oxide (TiO_2). Both SrO and TiO_2 layers in $SrTiO_3$ are electrically neutral so the ideal SrO-terminated or TiO_2-terminated (100) surfaces are non-polar. However, the two terminations have very different surface chemistry and can be selectively prepared by appropriate treatments.

Surface preparation and stability: Achieving a uniformly TiO_2 or SrO terminated surface often requires specific etching and annealing procedures. Historically, the method of choice to obtain a single-termination, atomically flat, TiO_2-terminated $SrTiO_3$ (100) surface was to chemically etch in a buffered HF solution (to preferentially leach SrO) followed by annealing in oxygen at high temperature. This leaves a predominatlyTiO_2-terminated surface albeit with a partial substitution of oxygen by fluorine. Our team has established a hydrothermal process based on pure water in a microwave oven to accomplish equal quality of surface termination without the integration of fluorine into the surface and without need for problematic chemicals [205].

Conversely, annealing in a Sr-rich or high oxygen partial pressure environment can produce a SrO-terminated surface by causing Sr to segregate to the surface [206]. In fact, studies have shown that under oxygen-rich conditions at elevated temperature, perovskite surfaces tend to become AO-terminated (A-site oxide at the surface), effectively burying the B-site cations one layer below the surface. $SrTiO_3$ conforms to this trend: after annealing in air or O_2, one often observes a Sr-enriched surface (SrO termination), whereas annealing in vacuum or reducing conditions tends to produce TiO_2-rich surfaces (Sr being somewhat volatile or sublimating as SrO).

Commercially available $SrTiO_3$ substrates often have a slight intentional or unintentional misorientation relative to the (100) plane. Upon cleaving or after thermal annealing, this miscut leads to the formation of step-terrace structures composed of alternating SrO and TiO_2 terminations. These mixed-terminated surfaces result in a sequence of single-atomic steps, where each terrace corresponds to a step height of approximately 0.2 nm, which is half the $SrTiO_3$ lattice parameter (~0.4 nm) [207]. A typical way to express this miscut is through the miscut angle that is defined as $\varphi = arctan(\frac{terrace\ height}{terrace\ width})$.

2.5.2.3 Carbonate adsorption

One of the most significant chemical processes on $SrTiO_3$ surfaces in ambient conditions is the adsorption of carbon dioxide (CO_2) from the atmosphere, often leading to the formation of surface carbonate species [51,52]. Experiments and computations consistently show that CO_2

preferentially chemisorbs on SrO-terminated $SrTiO_3$(100), forming stable carbonate (CO_3^{2-}) species bonded to the surface, whereas a TiO_2-terminated surface has a much lower affinity for CO_2 [208].

When CO_2 interacts with a SrO-termination, it forms surface-bound carbonate species with different bonding geometries. In one configuration, the CO_2 molecule bends and attaches to the surface via a single oxygen atom bonding directly to a surface Sr^{2+} ion, while the other oxygen atoms remain loosely associated, either interacting electrostatically with neighboring Sr atoms or with surface oxygen atoms, Figure 2.20 (a). In another, more stable configuration, two oxygen atoms of the carbonate group anchor to two separate Sr^{2+} ions on the surface, creating a bridge-like structure Figure 2.20 (b) [209]. These configurations can be distinguished experimentally by their vibrational fingerprints in infrared or Raman spectra. For instance, a surface carbonate species with a single strong bond to Sr typically shows a symmetric stretching vibration around 1060–1100 cm^{-1} and an asymmetric stretch near 1400 cm^{-1}, similar to what is observed in bulk $SrCO_3$. Bridging carbonate species, or partially protonated forms like bicarbonate (HCO_3^-), exhibit their own unique vibrational modes.

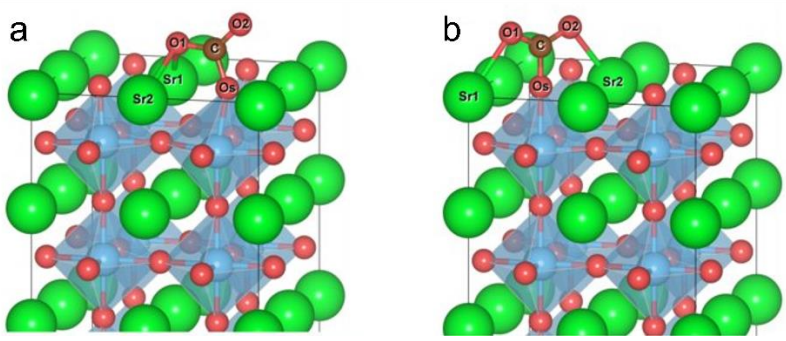

Figure 2.20: Illustration of CO_2 adsorption configurations on the SrO-terminated $SrTiO_3$ surface.

On a fully SrO-terminated $SrTiO_3$ surface, the calculated adsorption energy is about –2 eV per molecule [210]. This strong interaction typically results in the formation of a dense layer of carbonate species that effectively transforms the topmost SrO layer into a thin $SrCO_3$-like surface. Once this layer is complete, it passivates the surface by blocking further CO_2 adsorption. In contrast, on TiO_2-terminated $SrTiO_3$ surfaces, CO_2 adsorption energy is appreciably weaker (e.g., around –1.2 eV in one study) although still chemisorptive rather than mere physisorption [211]. In this case, CO_2 molecules only bind at specific surface defects, such as oxygen vacancies, or remain weakly physisorbed without significant chemical interaction. As a result, TiO_2-terminated surfaces are far less reactive toward CO_2 under ambient conditions compared to their SrO-

terminated counterparts [212]. Since this surface adsorption process can significantly alter the chemical and electronic properties of $SrTiO_3$, it becomes essential to employ surface-sensitive techniques capable of probing these changes with high spatial and chemical resolution.

2.5.3 Barium titanate ($BaTiO_3$)

2.5.3.1 Crystallographic phases of $BaTiO_3$ and ferroelectric properties

Barium titanate ($BaTiO_3$) is another important perovskite oxide, renowned as the first-discovered ferroelectric oxide with a perovskite structure. $BaTiO_3$ shares the same ABO_3 framework as $SrTiO_3$, but Ba^{2+} (A-site) is larger than Sr^{2+}, and this difference leads to strikingly different behavior. Bulk $BaTiO_3$ is a ferroelectric material at room temperature. It undergoes a series of temperature-driven phase transitions (see Figure 2.21), each marked by changes in symmetry and the emergence or disappearance of a spontaneous polarization:

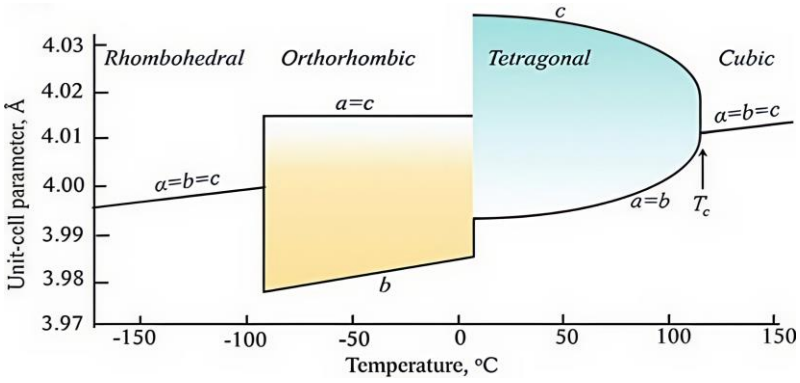

Figure 2.21: Illustration of the temperature-induced phase transitions in $BaTiO_3$. As the temperature decreases, $BaTiO_3$ transforms from a high-symmetry cubic phase into tetragonal, orthorhombic, and rhombohedral ferroelectric phases.

- At high temperatures (T > ~130 °C), $BaTiO_3$ is in a cubic phase (space group *Pm*3*m*) with the ideal perovskite structure. This phase is paraelectric (non-polar); Ba^{2+} sits at the center of its cube, Ti^{4+} at the center of an O_6 octahedron, and O^{2-} at the face centers, with perfect cubic symmetry [213], an exact analogy to the room temperature phase of $SrTiO_3$.
- At the Curie temperature $T_C \approx 120–130$ °C, bulk $BaTiO_3$ undergoes a phase transition from cubic to tetragonal (space group *P4mm*). This is the classic ferroelectric transition: in the tetragonal phase, the Ti^{4+} ion shifts off-center within the TiO_6 octahedron (and the 4 equatorial O^{2-} ions shift slightly opposite), resulting in a dipole moment along one of the cubic axes (conventionally the *c*-axis). While the titanium offset causes a long-range electrostatic interaction, it is the oxygen sublattice that stabilizes the polar order through nearest-neighbor

coupling between adjacent unit cells. The lattice elongates slightly in that direction (c/a > 1). Its crystal class (4mm) lacks inversion symmetry, so it exhibits pyro-, piezoelectricity, and strong first-order Raman-active modes corresponding to the polar optic phonons (which are silent in the cubic phase).

The Raman spectrum of tetragonal $BaTiO_3$ at room temperature is illustrated in Figure 2.22. As shown, several distinct phonon modes characteristic of the tetragonal phase are observed. These include peaks near 185 cm^{-1}, 270 cm^{-1}, 306 cm^{-1}, 519 cm^{-1}, and 716 cm^{-1}, which correspond to the A_1(TO), A_1(TO2), B_1+E (TO3+LO2), A_1(TO3), and A_1+E(LO3+LO4) modes, respectively—most of which originate from first-order Raman scattering processes [214–216]. The A_1 modes primarily involve bending vibrations of the O–Ti–O bonds within the TiO_6 octahedra, while the B_1+E mode is attributed to torsional vibrations involving Ti–O_3 units.

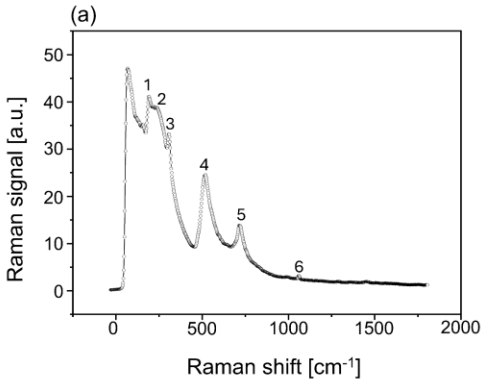

(b)

Raman modes of $BaTiO_3$		
#	Wavenumber in cm^{-1}	Mode character
1	185	A_1(TO)
2	270	$A_1(TO_2)$
3	306	B_1+E(TO_3+LO_2)
4	520	$A_1(TO_3)$
5	720	$A_1(LO_3+LO_4)$
6	1060	CO_3^{2-}

Figure 2.22: Raman characterization of tetragonal $BaTiO_3$ at room temperature. (a) Raman spectrum of $BaTiO_3$ showing distinct phonon modes characteristic of the tetragonal phase. (b) Summary of peak positions (in cm^{-1}) and corresponding vibrational mode assignments.

- At T ≈ 5 °C, $BaTiO_3$ undergoes a second phase transition from tetragonal to orthorhombic (space group *Amm2*), where polarization rotates from the c-axis toward the pseudocubic [110] direction, maintaining ferroelectricity but with altered direction and magnitude.
- At T ≈ –90 °C, a third phase transition occurs from orthorhombic to rhombohedral (space group R3m), with polarization along the [111] direction. The unit cell becomes slightly skewed but remains ferroelectric.

2.5.3.2 Superparaelectric limit in $BaTiO_3$

The behavior described above for $BaTiO_3$ assumes bulk crystals or large grains. When $BaTiO_3$ is prepared as nanoparticles or thin films, the phase transition characteristics are markedly altered

due to finite size effects, surface tension, and strain. As the crystal dimensions decrease, particularly into the nanometric regime, ferroelectric order is destabilized. This phenomenon, commonly termed the superparaelectric limit, denotes a critical size below which long-range dipolar ordering can no longer be sustained, and the material becomes paraelectric—even at temperatures where the bulk counterpart would be ferroelectric.

Experimental studies indicate that $BaTiO_3$ particles larger than ~0.2–0.3 μm (200–300 nm) exhibit bulk-like tetragonal behavior at room temperature. As the particle size decreases below ~100 nm, the tetragonal distortion progressively weakens. Powders around 50 nm may still retain ferroelectricity, but at ~20 nm or smaller, $BaTiO_3$ typically becomes cubic at room temperature [53,54]. The suppression of ferroelectricity in nanoscale $BaTiO_3$ is primarily due to three interrelated factors: surface energy and depolarizing fields, finite size effects, and strain-induced lattice distortions [94,217–219]. As particle dimensions shrink, the surface-to-volume ratio increases, when particle sizes approach the correlation length of polarization, the material lacks sufficient volume to support domain walls, resulting in a homogeneous paraelectric state. Additionally, surface tension and associated lattice strains can modify local structural parameters, such as the c/a ratio in tetragonal $BaTiO_3$, promoting a transition toward a cubic lattice configuration and further suppressing ferroelectricity [220,221].

Raman spectroscopy reveals that as $BaTiO_3$ particle sizes decrease below approximately 20 nm, characteristic ferroelectric Raman modes weaken, indicating a transition to the paraelectric phase [55–57]. It is important to note that these measurements are conducted on ensembles of nanoparticles rather than individual particles due to resolution limits and isolation challenges. The observed size-dependent ferroelectric behavior therefore represents the collective response of many particles, influenced by size distribution, interparticle coupling, and agglomeration. This complexity makes it difficult to pinpoint the true critical size for ferroelectricity in $BaTiO_3$ and highlights the need for single-particle characterization techniques.

A quantitative approach to monitor the phase transition of barium titanate as a function of temperature or size is through the softening of a specific phonon branch at low wavenumbers following the Lyddane-Sachs-Teller relation. The Raman spectrometer used in the present studies was however not equipped to access Raman modes at the relevant low wavenumbers.

2.5.3.3 Surface adsorption on $BaTiO_3$

Very similar to the case of strontium titanate, the (100) surface of barium titanate exhibits terminations with either barium oxide (BaO) or titanium dioxide (TiO_2) layers. As discussed in sections 2.5.2.2 and 2.5.2.3, the AO-terminated surfaces (here BaO) are far more reactive toward atmospheric gases. The adsorption mechanism closely follows that described for $SrTiO_3$: CO_2 chemisorbs on BaO-terminated regions to form carbonate complexes bridging Ba^{2+} and O^{2-} sites. Experimental observations confirm that $BaTiO_3$ powders and ceramics stored in ambient air often have a thin layer of $BaCO_3$ on the surface [63].

This surface carbonate layer effectively forms a core–shell structure, in which the $BaTiO_3$ core is coated by a thin $BaCO_3$-like shell with significant implications for its electrical and microstructural properties. While theoretical studies and indirect experimental evidence e.g. on nanopowders suggest the formation of surface carbonates on $BaTiO_3$ nanoparticles, direct experimental observations are limited by the sensitivity and resolution of conventional surface analysis techniques.

2.6 Conclusion

Tip-Enhanced Raman Spectroscopy has emerged as a uniquely powerful tool for investigating complex surface phenomena at the nanoscale. By coupling the molecular vibrational sensitivity of Raman spectroscopy with the sub-diffraction-limit spatial resolution of scanning probe microscopy, TERS enables site-specific analysis of surface structure, chemical bonding, and local symmetry. This capability is especially critical for perovskite oxides such as $SrTiO_3$ and $BaTiO_3$, where subtle variations in surface termination, adsorbate distribution, and domain configuration can have profound implications for ferroelectric, electronic, and catalytic behavior.

For $SrTiO_3$, TERS provides a route to directly examine the (100) surface terminations—either SrO or TiO_2—and their interaction with atmospheric species such as CO_2. These interactions often lead to carbonate adsorption, which can significantly alter the surface energy, induce reconstructions, and even promote local delamination. Through TERS, we are able to spatially resolve such adsorbates and detect vibrational fingerprints even from monolayer species, which would be invisible in conventional Raman techniques due to weak cross-sections or selection rule limitations.

In the case of $BaTiO_3$ nanoparticles, TERS has proven essential in probing the surface activation of infrared (IR)-only modes that become Raman-active due to local symmetry breaking or strong

tip-enhancement effects. This includes carbonate species adsorbed from atmospheric CO_2 and surface-related phonon modes that reflect deviations from bulk symmetry. Furthermore, TERS offers a nanoscale window into the evolution of ferroelectricity as particle size decreases, providing direct evidence of the superparaelectric transition and correlating the disappearance of specific Raman-active modes with phase instability. The forthcoming part of the thesis presents experimental results obtained via TERS, structured into three key chapters:

1. TERS analysis of $BaTiO_3$ nanoparticles

This chapter explores the presence of carbonate monolayers resulting from atmospheric CO_2 adsorption. By activating and detecting IR modes within the Raman spectrum, TERS reveals unique insights into the local vibrational environment and symmetry-breaking effects at the nanoparticle surface. The results were published in: Advanced Materials Interfaces 11.15 (2024): 2300993. doi: 10.1002/admi.202300993

2. Probing the superparaelectric limit of $BaTiO_3$

Here, we investigate the ferroelectric-to-paraelectric crossover at the nanoscale by tracking changes in the Raman-active modes as a function of nanoparticle size. The disappearance of specific modes serves as a spectral signature of the superparaelectric transition. The results were published in: Optics Communications, 132058, (2025): doi: 10.1016/j.optcom.2025.132058

3. Carbonate adsorption on $SrTiO_3$ (100) and self-cleaning effect

In this section, TERS is used to resolve the chemical identity and distribution of surface-bound species on differently terminated $SrTiO_3$ (100) surfaces. We also investigate how carbonate adsorption correlates with local delamination, surface reconstruction, and electrostatic stabilization mechanisms. The results were published in: Advanced Materials Interfaces (2025): 2401024. Doi : 10.1002/admi.202401024.

All experimental and analytical procedures—TERS measurements, tip fabrication, sample preparation, data analysis, and interpretation—were conducted by the first author, Mohammad Bakhtbidar. Computational support and theoretical analysis in the third paper, particularly Density Functional Theory (DFT) simulations, were provided by Daniel Gueckelhorn, a fellow PhD student in our group.

3 EXPERIMENTAL METHODS

3.1 Introduction

Having established the theoretical foundations and enhancement mechanisms of tip-enhanced Raman spectroscopy, this chapter shifts focus to the practical implementation of the technique. The performance and reliability of TERS measurements are critically dependent on the precision and integration of its experimental components. In particular, three essential subsystems must operate in harmony: the optical excitation and collection pathway, the atomic force microscopy unit responsible for topographic imaging and tip positioning, and the plasmonic tip itself, which acts as the core of near-field enhancement.

This chapter begins by detailing the optical setup used in the TERS system, including the laser source, focusing optics, and detection components. Following this, the integration of atomic force microscopy with the optical system is described, outlining the scanning mode employed and the feedback mechanisms used to maintain precise tip–sample interaction.

Finally, the chapter provides a thorough description of the fabrication procedures used to produce gold tips suitable for TERS applications. Methods such as electrochemical etching and thermal coating are discussed, along with post-fabrication characterization techniques. Emphasis is placed on achieving reproducible tip shapes and plasmonic activity to ensure consistent enhancement performance across experiments.

3.2 TERS setup

To address the analytical demands of non-transparent and non-conductive samples common in the field of nanoelectronics, a custom-configured TERS system was developed. The system is built around a SmartSPM scanning probe microscope (AIST-NT Inc.) which incorporates a sample scanner with a mechanical travel range of 5 mm × 5 mm × 18 mm, and a high-precision piezoelectric scanning range of 100 μm × 100 μm × 15 μm. The closed-loop feedback system provides a spatial accuracy of 0.1 nm, essential for maintaining nanometric control during measurements.

In order to ensure consistency and quality of the TERS probes, all metallic tips are fabricated within the laboratory through electrochemical etching of bulk gold wires. These etched tips are subsequently affixed to quartz tuning forks (AB38T 32.768kHz, Abracon Corporation) using a UV-curable adhesive (NOA68, Norland Optical Adhesives). The tuning forks operate in shear-force

mode, stabilized via amplitude feedback, with typical quality factors exceeding 2000. The high stability of the resonance frequency (~0.02 Hz/min) ensures that tip-sample distance drift remains below 0.25 nm during prolonged scanning sessions, supporting stable and repeatable TERS measurements [222].

The optical layout of the TERS system employs a side-illumination geometry. A Mitutoyo plan apochromat objective with a numerical aperture (NA) of 0.7 and a working distance of 6.0 mm is positioned at an angle of 65° relative to the tip axis. This geometry is chosen to optimize laser coupling at the tip-sample junction, particularly for opaque and non-conductive samples. The objective is mounted on a piezoelectric scanning stage capable of precise movements in all three spatial directions (30 µm × 30 µm × 12 µm), enabling nanometer-level control over the alignment of the laser focal spot with the tip apex. This alignment is without feedback stabilization and relies on a small mechanical loop to minimize drift during scans. Typically, the tip remains within the confocal area for at least one hour.

Excitation is achieved using a linearly polarized helium-neon laser (25-LHP-928-249, CVI Melles Griot) operating at 632.8 nm, which aligns with the localized surface plasmon resonance of gold tips. The beam is processed through an optical conditioning module (Nanofinder 30, Tokyo Instruments Inc.) comprising a neutral density filter (power tunability from 10 mW to 10 µW), a beam expander to match the beam diameter to the entrance pupil of the objective, and a rotatable half-wave plate to control the polarization. A dichroic mirror positioned in the beam path reflects the excitation light into the objective while allowing for efficient collection of the backscattered signal.

Backscattered light from the sample is directed through the detection path where it is spectrally separated by the same dichroic mirror. Rayleigh-scattered light is deflected towards a photomultiplier tube (PMT), whereas the red-shifted Raman and fluorescence components are transmitted through an additional dichroic mirror to further suppress residual Rayleigh light. These signals are then focused onto the entrance slit of a Czerny-Turner type spectrometer with a focal length of 520 mm. The spectrometer features a motorized turret with diffraction gratings of 150, 600, and 1800 lines/mm, allowing for flexible spectral resolution. Signal detection is performed using an iDus 420 BU CCD camera (Andor Technology), thermoelectrically cooled to –80 °C to minimize thermal noise. The CCD array consists of 255 × 1024 pixels, yielding a spectral resolution of approximately 2 cm^{-1} per pixel when using the 600 lines/mm grating at 632.8 nm excitation wavelength. The system is operated with vertical binning to enhance the signal to noise-ratio for each of the 1024 pixel rows.

Precise spatial overlap between the laser focus and the TERS probe is essential for maximizing signal enhancement. This is achieved through the piezoelectric scanner integrated with the objective lens, which enables fine alignment adjustments. In addition, the microscope body itself is equipped with an independent three-axis translation system, allowing for micrometer-level positioning flexibility. Altogether, the system offers nine degrees of freedom, ensuring high-precision alignment between the tip, sample, and optical axis. The detailed alignment procedure is presented in the later sections of this thesis.

3.2.1 Scanning probe operation modes in TERS

As discussed in Chapter 2, scanning probe microscopy enables nanoscale surface mapping and serves as the foundation for TERS. The choice of scanning mode is critical for optimizing spatial resolution, near-field enhancement, and mechanical stability. Depending on the sample's conductivity, TERS can operate in either STM or AFM configurations (Figure 3.1). STM-based TERS (Figure 3.1 (a)) is ideal for conductive samples, using a metallic tip in constant-current mode to maintain sub-nanometer tip–sample spacing through tunneling feedback. This configuration achieves extremely high and stable enhancement as well as spatial resolution but is limited to conductive substrates and is sensitive to electronic noise.

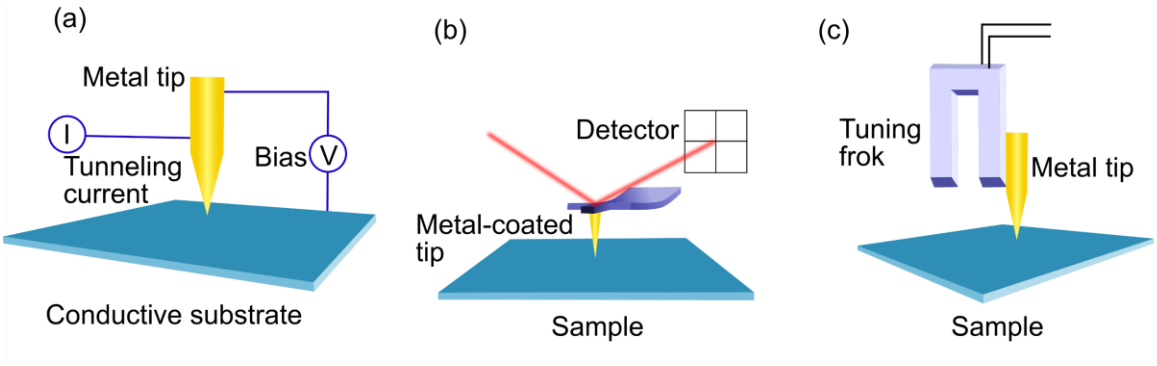

Figure 3.1: Schematically illustrates the SPM feedback mechanisms employed in TERS systems : (a) STM-based control (a) AFM-based control, and (c) lateral shear-force tuning fork configuration.

AFM-based TERS (Figure 3.1 (b)) extends the applicability to insulating materials such as oxides, polymers, and biomolecules. Among AFM modes, contact mode provides maximum enhancement but suffers from tip wear; non-contact mode preserves tip sharpness but requires sensitive control and commonly implies oscillation amplitudes that exceed the range of the optical near-field so that the configuration only yields tip-enhancement during a small portion of the oscillation. In conventional AFM-TERS, metallic coatings on cantilevers also yield limited reproducibility. To overcome this, tuning fork-based AFM (Figure 3.1 (c)) employs an

electrochemically etched metal tip attached to a quartz tuning fork operating in lateral shear-force mode. This setup eliminates optical feedback interference, improves stability, and allows tip reuse, offering a robust, cost-effective platform for TERS on non-conductive surfaces.

3.3 TERS probes

In TERS, the tip geometry and surface characteristics are crucial in determining the extent of local electromagnetic enhancement and spatial resolution. For our shear-force TERS system based on quartz tuning forks, we adopted a reproducible and accessible method to fabricate all-metallic gold tips via electrochemical etching. This approach is favored over more complex techniques such as focused ion beam (FIB) milling due to its simplicity, low cost, and ability to yield tips with sharp apexes and desirable plasmonic properties.

3.3.1 Material

As discussed in Section 2.3.5.1, a critical aspect in achieving efficient and reproducible TERS measurements lies in the careful selection of tip material and its precise fabrication. A suitable TERS tip material must exhibit a surface plasmon resonance within the operational spectral window of Raman spectroscopy, typically spanning the ultraviolet, visible, or near-infrared regions. This requirement is expressed through the resonance condition $\varepsilon_{tip} = -2\varepsilon_{env}$ where ε_{tip} is the permittivity of the tip material and ε_{env} is the permittivity of the surrounding medium, as shown Equation 2.26. This condition implies that the tip material should possess a negative real part of the permittivity Re[ε], facilitating SPR in a medium of positive permittivity, while maintaining a minimal imaginary component Im[ε] to reduce optical losses due to absorption [223]. Moreover, the material should possess high polarizability for strong field confinement and be chemically inert to maintain amplification stability over time.

The most widely employed materials are gold, silver, and increasingly, aluminum. Gold supports SPR in the red to near-infrared spectral region, silver across the visible range, and aluminum in the ultraviolet [224–226]. Figure 3.2 illustrates the real and imaginary parts of the permittivity of these metals as a function of wavelength. As shown, silver exhibits the lowest Im[ε] in the visible region, which accounts for its superior field enhancement. However, its surface readily oxidizes, leading to a rapid decline in enhancement performance within hours under ambient conditions [227,228]. Gold, while having slightly higher Im[ε], offers substantial chemical stability, maintaining its enhancement for weeks or even months without requiring special handling [229]. Aluminum, like silver, oxidizes in air, however with an optically transparent oxide layer that shifts the plasmon

resonance without suppressing it. They key challenge for the use of aluminium tip is the closely related to its appeal: operation in the UV domain would provide opportunities for resonant TERS (the Raman effect coupled to an electronic transition) but the already demanding alignment would have to be conducted with an invisible laser beam [230]. Alternative materials such as titanium nitride (TiN) have been proposed due to their plasmonic tunability and robustness, but current enhancement factors remain lower than those for noble metals [231–233].

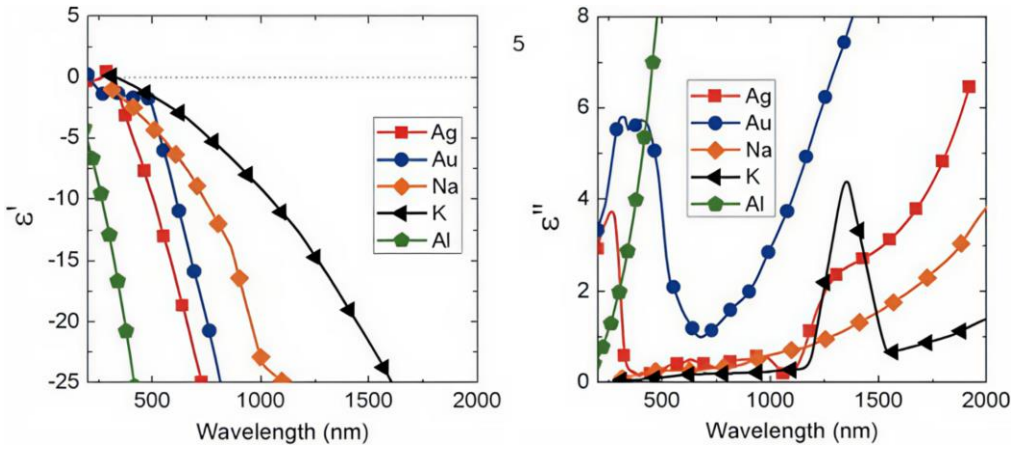

Figure 3.2: Spectral dependence of the complex permittivity for selected metals—silver (Ag), gold (Au), sodium (Na), potassium (K), and aluminum (Al). (a) illustrates the real part of the permittivity (Re[ε]), highlighting the spectral regions where Re[ε] is negative, a prerequisite for supporting surface plasmon resonances (SPR). (b) presents the imaginary part of the permittivity (Im[ε]), where lower values correspond to reduced optical losses and enhanced field enhancement.

In this thesis, gold has been selected for the fabrication of TERS tips due to its combination of optical performance, chemical stability, and compatibility with fabrication processes. Its relatively low imaginary permittivity (Im[ε]) in the red-visible range enables efficient electric field enhancement under ~600 nm excitation [223,234]. Gold tips have demonstrated stable operation for over 60 hours in tuning fork shear-force mode [229], confirming their suitability for long-duration measurements. Combined with the relative simplicity and consistency of electrochemical etching, these properties make gold an optimal choice for reliable, high-resolution TERS performance in the visible to near-infrared region.

3.3.2 Fabrication process of tips

High-performance TERS requires metallic tips with smooth apices and a tip radius below 20 nm to ensure strong localized field enhancement and nanometer-scale spatial resolution. Gold tips with an LSPR in the red spectral range are compatible with the main emission line of a HeNe-laser at 632.8 nm and considering their good stability, they are our preferred choice. Unlike silver-

based tips, which readily oxidize or react with contamination of the surface of the perovskites, bulk gold tips maintain structural and optical integrity, enabling reproducible measurements. In this work, we use electrochemical etching process—combining direct-current and pulsed-voltage modes—to fabricate Au tips with typically 15 nm apex radius. We determine the tip-radius through scans across carbon nanotubes [235].This approach yields probes optimized for both optical enhancement and stable operation in a tuning fork–based shear-force AFM-TERS configuration.

The electrochemical etching of gold tips is driven by redox reactions at the electrode–electrolyte interfaces. Applying a potential between the gold anode and the counter-electrode cathode initiates gold oxidation, forming soluble gold chloride complexes. The main reactions are [236]:

- Anodic oxidation of gold:

$$Au + (n+1)HCl \rightarrow HAuCl_{n+1} + nH^+ + ne^- \quad 3.1$$

- Electrolysis of water at the anode:

$$2H_2O \rightarrow O_2 + 4H^+ + 4e^- \quad 3.2$$

- Reduction of gold chloride at the cathode:

$$HAuCl_{n+1} + nH^+ + ne^- \rightarrow Au + (n+1)HCl \quad 3.3$$

- Cathodic hydrogen evolution:

$$2H_2O + 2e^- \rightarrow H_2 + 2OH^- \quad 3.4$$

Here, $n = \{1,3\}$ corresponds to the possible oxidation states of gold. These processes dissolve gold at the anode and generate O_2 and H_2, critically influencing tip geometry.

3.3.3 Etching process

The fabrication of gold tips is performed using a vertical electrochemical etching setup consisting of a gold wire (anode) and a platinum ring (cathode) immersed in a freshly prepared 1:1 (v/v) mixture of concentrated hydrochloric acid (37%, Sigma Aldrich) and ethanol, as illustrated in Figure 3.3. This electrolyte provides chloride ions for gold dissolution while the ethanol component reduces surface tension, stabilizing the meniscus at the air–liquid interface.

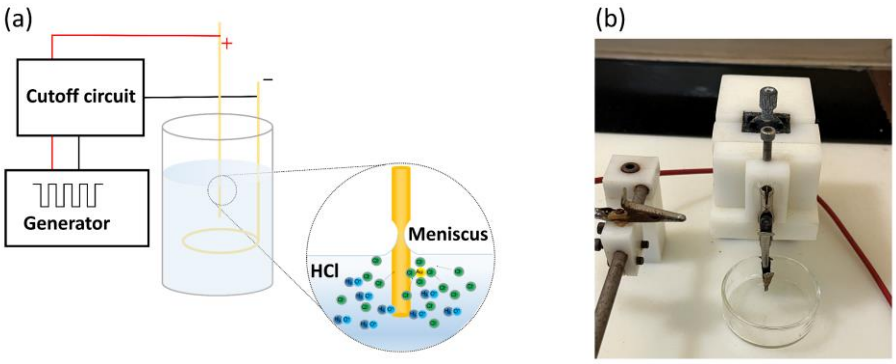

Figure 3.3: (a) Schematic representation of the electrochemical etching setup , where the gold wire is submerged approximately 1 mm into the electrolyte. The arbitrary waveform generator is linked to a circuit breaker that powers the etching cell (anode and cathode) and halts the process once the cell voltage drops to the cutoff threshold. (b) Photograph of the assembled etching setup, showing the crocodile clip securing the gold wire in place.

The setup is powered using a DC supply and a function generator (Agilent 33210A) to provide both constant and pulsed bias voltages. A custom-built cutoff circuit is integrated into the setup to automatically stop the etch once tip formation is complete. The fabrication process proceeds in the following stages:

Immersion of electrodes: Gold wires (GoodFellow, 99.999% purity, 125 µm diameter, pre-annealed) are cut to 7 mm, cleaned, and mounted vertically at the center of a Pt ring electrode. Both are immersed in the HCl–ethanol electrolyte, with the Pt ring submerged a few millimeters and the Au wire ~1 mm. Capillary action formed a stable meniscus defining the etching zone, while a fixed 5–10 mm electrode gap ensured a uniform electric field and reproducible etching conditions.

Application of DC etching bias: A DC bias (5–10 V) is applied between the Au anode and Pt cathode to initiate anodic dissolution, predominantly at the meniscus, tapering the wire diameter. Gold atoms oxidized and dissolved into the acidic chloride solution, while the current remains steady during bulk etching and dropped as the wire thins, indicating progression toward tip formation.

Transition to pulsed etching: After sufficient narrowing, etching is switched to a pulsed regime for finer tip shaping. A 3 kHz rectangular-pulse with controlled duty cycle alternates anodic etching on/off, smoothing the tip, facilitating bubble delamination, and promoting electrolyte replenishment at the meniscus. During “on” pulses, Au dissolves actively; during “off” intervals, diffusion restores electrolyte composition. This intermittent etching improved curvature uniformity

[175,237]. Huh et al. [238] reported that optimized pulse-width modulation yields ~20 nm apex radii with clean surfaces. In our process, a brief 10–30 s pulsed stage after DC etching enhances tip smoothness and reproducibility.

End-point detection (cut-off): Tip formation is identified by a sudden anodic current drop as the lower gold wire detaches (“drop-off”). A custom cutoff circuit terminates power within milliseconds once the current falls below a set threshold or a sharp inflection is detected, preventing over-etching and preserving tip integrity. Automatic cut-off is essential for reproducibility; without it, residual etching blunts or distorts tips. Billot et al. [239] demonstrated that current-threshold termination consistently yields sharp radii. In our setup, this method is based on an Arduino-circuit and produces well-defined apex geometries. Considering the yield strength of gold of typically a few hundred MPa (depending on crystallinity, grain size etc.), we take note that the predominant mechanism for the very final stage of the tip production may not be the electrochemical etching but mechanical rupture due to the weight of the submerged part of the gold wire that strains the ever-decreasing neck. An approximation considering the uncertainties of the yield strength of our gold wire as well as the actual dimension of the remaining gold wire in solution (which is also subject to progressive albeit slower etching than at the meniscus) indicates that mechanical rupture will compete with etching for radii of less than 20 nm. In other words, our technique allows for a precise control down to approximately 20 nm, while the exact shape of the tip is beyond our immediate control.

Tip rinsing and mounting: After the etching process is terminated, the Au tip is immediately removed and rinsed sequentially with deionized water, HCl (to remove residual $AuCl_x$), and absolute ethanol, producing a clean surface. Once dried, it is cut to 200-300 micron length and mounted onto one prong of a quartz tuning fork using the smallest possible amount of low-viscosity UV-curing adhesive, see Figure 3.4 (a-c). Precise alignment ensures optimal mechanical coupling for shear-force AFM operation in TERS. Finished probes are stored in clean, dry containers to preserve tip integrity. Cutting is required to minimize the additional weight on the prong of the tuning fork that adversely affects the quality factor.

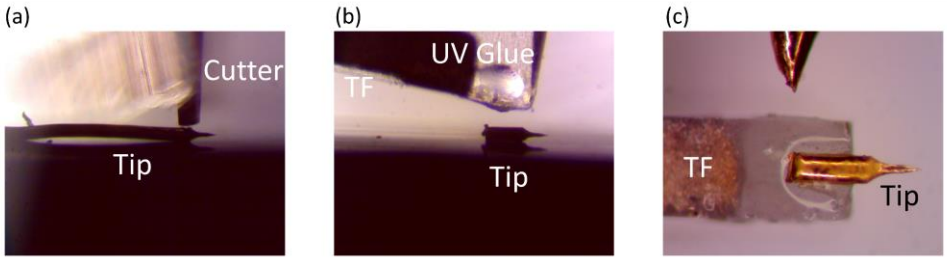

Figure 3.4: process of mounting the etched gold tip onto a quartz tuning fork : (a) The etched tip is cut from the upper segment of the gold wire. (b) A small amount of adhesive is applied to fix the tip onto one prong of the tuning fork. (c) Final alignment of the tip on the prong ensures precise positioning for optimal performance in AFM applications.

3.3.4 Optimization of etching process

Achieving a sharp apex with a smooth surface requires precise control of electrochemical etching parameters. In this work, a two-step voltage profile was employed, consisting of a high-voltage DC etch followed by a low-voltage pulsed etch to balance rapid material removal with fine apex shaping. The initial DC stage (~5–6 V) rapidly tapered the wire, while the subsequent pulsed stage (~2 V average) refined the apex and smoothed the surface. This approach builds upon methods reported by Lopes et al. [240], who achieved sub-50 nm radii using sequential fast and slow DC etching, and Foti et al. [241], who produced ~12 nm apices with a 5 V then 2 V sequence. In our method, the pulsed second step mimics a low DC bias on average while allowing brief bursts of higher etch rates during pulses. By adjusting the duty cycle, the etch rate can be tuned: shorter duty cycles reduce bubble formation and improve uniformity.

During optimization, the immersion depth of the Au wire is precisely measured and adjusted using a micrometer. A depth of ~5 mm is found to produce reproducible meniscus geometry, consistent initial currents, and stable cone angles. Shallower immersions yield shorter tapers, whereas greater depths often produce multiple menisci or irregular breakage. Voltage and current monitoring confirm that higher bias widens the cone angle, while a series resistor effectively suppresses current spikes during pulsing, reducing pitting and improving reproducibility. Post-etch rinsing in fresh HCl removes residual $AuCl_x$ species, and ethanol eliminates organic films, yielding consistently clean plasmonic surfaces with enhanced TERS optical performance.

Using these optimized conditions, the fabricated tips consistently show apex radii in the 10–20 nm range and a smooth conical profile. SEM images of the routinely fabricated tips (Figure 3.5) show that the lower shank (hundreds of microns long) sometimes retains gentle waviness from the initial etch, which straightens toward the apex due to the controlled final stage. The resulting tips, with cone half-angles of ~20–30°, are sharp, clean, and free of significant protrusions or grain

asperities—geometry well suited for maximizing TERS field enhancement while ensuring mechanical robustness.

3.4 Tip-objective optical alignment

Accurate focusing of the excitation laser at the TERS tip apex is essential for inducing localized surface plasmon resonance and maximizing near-field enhancement. To achieve optimal overlap between the laser spot and the apex, a systematic alignment protocol follows four stages: pre-alignment, coarse positioning, fine alignment, and signal optimization. Initial coarse alignment uses mechanical adjustment of the SPM head to position the tip within the objective's field of view, often assisted by observing the tip's shadow or projection. A side-view camera then centers the apex within the laser spot to within the diffraction-limited range.

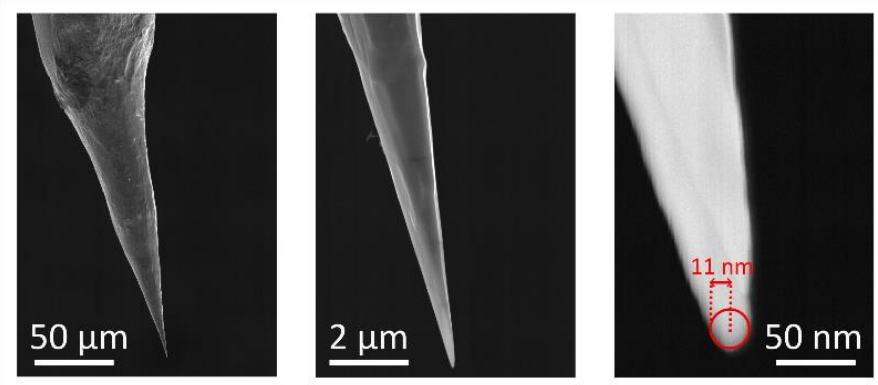

Figure 3.5: Representative images of a gold tip produced via pulsed electrochemical etching with circuit-controlled cutoff. (a–c) display the overall geometry of the tip, while (b) highlights details of the surface texture and smoothness. (c) shows the apex radius measured at approximately 11 nm, which is suitable for achieving high spatial resolution and generating strong electric field gradients at the tip apex—key factors for enhanced performance in near-field applications.

After the pre-alignment, refined positioning occurs by scanning the laser focal spot relative to the tip using a piezo-controlled objective scanner. Optical images of the tip form by raster-scanning the focal plane in both lateral (xy) and axial (xz) directions while monitoring the backscattered light, commonly with a photomultiplier tube (PMT), as illustrated in Figure 3.6. These scans reveal characteristic interference patterns, often shaped like a double-lobed or hourglass point spread function (PSF), which allow pinpointing the tip apex with sub-micrometer accuracy. The lateral PSF image localizes the apex within the transverse plane, while the axial scan ensures that the laser focuses along the tilted axis of the tip, which typically has an inclination angle of ~30°.

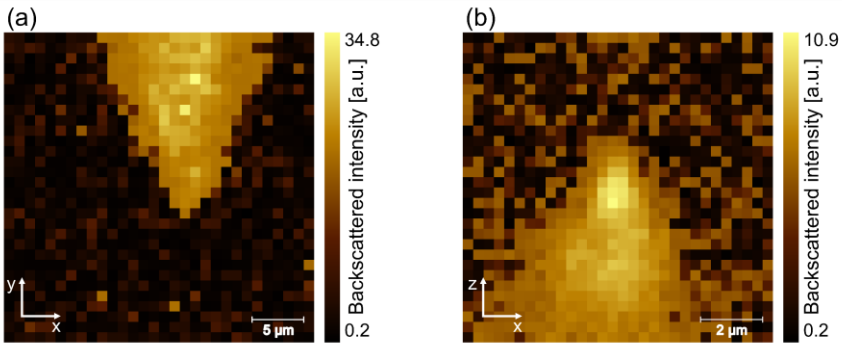

Figure 3.6: PMT-acquired luminescence intensity maps in the (a) xy and (b) xz planes. These spatial projections provide a coarse localization of the tip apex, based on the distribution of emitted signal intensity.

To verify that the tip is indeed at the LSPR-enhanced focus (the optical paths for the PMT and the Raman spectrometer may be slightly off-axis), spectral maps of the (xy) and (planes (xy, xz, yz) are acquired using the CCD detector to capture the luminescence or Raman signal. When the excitation frequency is resonant with the LSPR mode of the gold-coated tip, a confined and intense emission localized at the apex is expected. These emission maps can then be compared with simulated PSFs to assess the spatial confinement and resonance conditions. A broader or tilted emission pattern can indicate either optical aberrations from system components or misalignment due to the tip's angular orientation in the objective's frame.

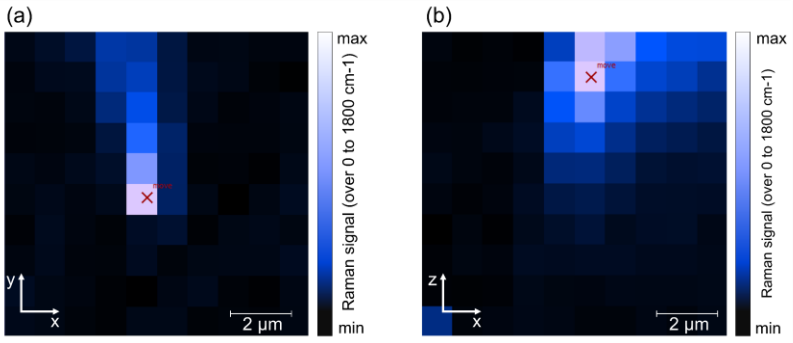

Figure 3.7: Raman intensity map integrated in the spectral range of 0 –1800 cm^{-1} , depicting the (a) xy and (b) xz planes. These spatial mappings facilitate the approximate localization of the tip apex by analyzing the emission intensity profiles.

The final alignment step takes place with the tip positioned a few nanometers above the sample surface. After selecting a target region—such as an isolated nanostructure or a carbon nanotube—the enhancement is evaluated by recording spectra in contact and non-contact modes. If no signal enhancement appears, a final spectral scan verifies the overlap between the focal spot and the sample-contact region. Misalignment or insufficient enhancement signals the need for repositioning or possibly replacing the tip.

3.5 Tip-sample distance

Controlling the tip–sample distance is achieved through a dual-parameter calibration using a gold tip positioned above a platinum substrate. The procedure begins with acquisition of a landing curve, in which the vertical displacement of the tip is monitored simultaneously with the tuning fork oscillation amplitude. As illustrated in Figure 3.8 (a), the point at which the amplitude approaches zero is interpreted as the moment of mechanical contact. This assumption is a standard method employed in vertical and lateral non-contact AFM for defining zero-distance calibration.

In a complementary measurement, the resonance frequency of the tuning fork is recorded during tip approach, as illustrated in Figure 3.8 (b). By correlating the frequency shift data with the amplitude-based contact point, absolute tip–sample separations are determined. A frequency shift of 5 Hz corresponds to a distance of approximately 2 nm.

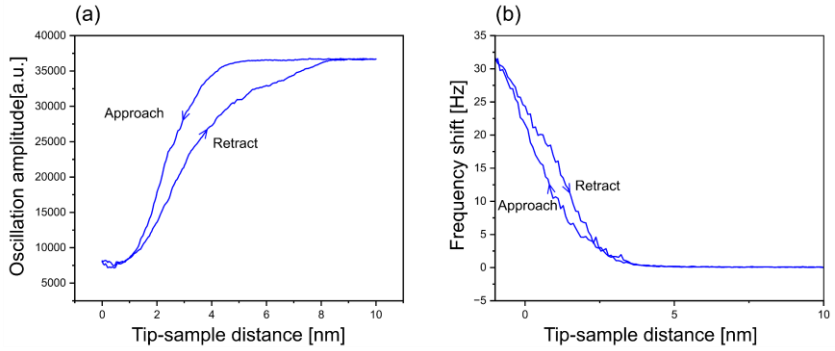

Figure 3.8: Tuning fork approach and retraction curves in AFM shear-force mode using a gold tip over a gold surface. (a) Oscillation amplitude as a function of tip-sample distance: during approach and retraction, the oscillation amplitude decreases with decreasing separation, reaching the detection limit upon mechanical contact. (b) Resonance frequency shift versus tip-sample distance: monitoring the resonance frequency shift provides insight into the tip-sample separation under measurement conditions. The tip-sample distance was calibrated using the oscillation amplitude curve shown in (a).

This combined amplitude and frequency-based calibration guarantees that all TERS measurements are conducted within a tightly confined nanometer-scale window—typically between 1 and 2 nm—where plasmonic field enhancement is strongest and most consistent. Within this regime, the lateral oscillation amplitude remains low, typically around 0.15 nm, ensuring high spatial stability and reproducibility during spectroscopic acquisition. Lower distances are in principle possible but change the coupling regime between tip and surface from capacitive to conductive; in other words, electrons start tunneling and reduce the electric field.

3.6 Mechanical quality factor of the quartz tuning fork

The mechanical quality factor (Q-factor) of a quartz tuning fork is a dimensionless parameter that characterizes the damping of its oscillations. It is defined as the ratio of the resonant frequency (f_0) to the full width at half maximum (Δf) of the resonance curve:

$$Q = \frac{f_0}{\Delta f} \tag{3.5}$$

A higher *Q*-factor indicates lower energy dissipation, resulting in a sharper resonance peak and enhanced frequency stability—attributes crucial for applications requiring precise measurements. Attaching additional mass, such as a tip and glue, to one prong of the tuning fork degrades the *Q*-factor. This degradation occurs because the added mass alters the fork's inertia and damping characteristics, leading to increased energy dissipation. To mitigate this effect, it is essential to minimize both the mass of the attached tip, and the amount of adhesive used during attachment. Studies have shown that attaching a counter mass to the opposite prong can rebalance the system and improve the *Q*-factor [242], however the procedure complicates the preparation.

Figure 1.18 displays the spectral power density of the tuning fork, which is fitted using a Lorentzian function to determine both the resonance frequency (f_0) and the full width at half maximum (Δf). In this case, the resonance peak is centered at $f_0 = 32.18\ kHz$, with a linewidth of $\Delta f = 2.6\ kHz$, resulting in a calculated *Q*-factor of 12.4×10^3. This analytical approach enables precise evaluation of the tuning fork's quality factor and serves as a reference point for calibrating the tip–sample separation in shear-force feedback systems.

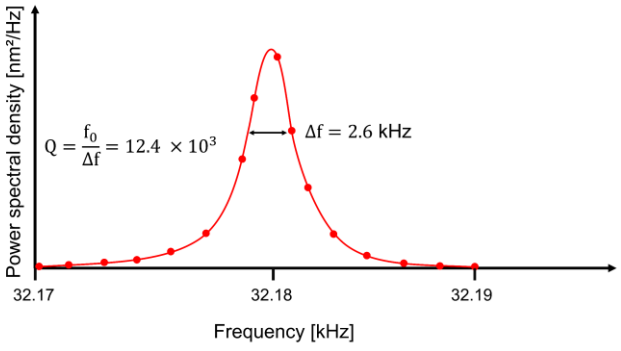

Figure 3.9: The mechanical quality factor (*Q*) is calculated by analyzing the power spectral density. The fundamental resonance frequency (f_0) and the full width at half maximum (FWHM, Δf) are extracted through nonlinear fitting employing a Lorentzian distribution.

3.7 TERS on Carbon nanotubes

In this work, single-walled carbon nanotubes (SWCNTs) are used as a benchmark reference sample to validate and optimize the performance of the TERS system prior to probing more complex perovskite materials. Carbon nanotubes (CNTs) provide a well-understood, quasi-one-dimensional test system that allows for the quantitative evaluation of the TERS optical enhancement, alignment precision, and lateral resolution. By first performing TERS experiments on CNTs, we can ensure that key parameters (e.g. enhancement factor, spatial resolution) are achieved and the system is properly calibrated, thereby building confidence for subsequent nanoscale investigations of perovskite samples. In particular, the establishment of the specific lateral resolution of a tip allows us to choose the best pixel size for the TERS experiment following the Nyquist-Shannon sampling theorem. The following sections detail the rationale for using CNTs as a reference, the sample preparation and characterization procedures, and mapping methods employed, interpretation of characteristic Raman features (radial breathing mode, G-band, D-band), and the key performance metrics obtained.

3.7.1 Rationale for using CNTs as a TERS benchmark

CNTs are an ideal reference sample for TERS for several important reasons. First, CNTs (particularly metallic single-walled nanotubes of ~1–2 nm diameter) can be strong resonant Raman scatterers under visible or red excitation, yielding intense characteristic Raman bands (such as the G-band) when illuminated at appropriate wavelengths. For example, our TERS excitation laser has a photon energy of ~1.96 eV (632.8 nm), which lies in resonance with the electronic transition of ~1.3 nm diameter metallic SWCNTs. This resonance condition greatly enhances the intrinsic Raman scattering from the CNT, providing a robust signal to test the tip enhancement.

Second, a single CNT presents an extremely small and localized target—its cross-section occupies only a tiny fraction of the diffraction-limited laser focus. This means that in a conventional far-field Raman measurement, an isolated CNT contributes little to the total signal (most of the laser spot hits the bare substrate), whereas in TERS the nanotube directly beneath the tip is selectively enhanced. As a result, the ratio between the near-field (tip-engaged) signal and the far-field background can be very large, facilitating a clear determination of the optical enhancement factor of the TERS tip.

Third, the one-dimensional geometry and nanometer-scale diameter of CNTs allow us to probe the spatial confinement of the TERS interaction. By scanning the tip across a nanotube, one

effectively measures how the Raman intensity drops off laterally, thereby gauging the size of the near-field optical hotspot and the lateral resolution of the system. In other words, the CNT's ~1–2 nm diameter is often smaller than the TERS spot, so it acts almost like a line probe of the tip's point spread function.

Finally, CNTs are chemically and thermally stable and can be prepared on substrates in a controlled way. Their well-defined and well-studied Raman features make interpretation straightforward, and their small size ensures minimal perturbation of the tip (reducing risk of sample or tip damage during scanning). These advantages have made CNTs a popular choice for TERS system validation in literature – from early near-field Raman studies achieving ~25 nm resolution on single nanotubes [243] to recent reports using SWCNTs to quantify TERS spatial resolution and enhancement reproducibly.

3.7.2 Sample preparation: substrate selection and CNT deposition

For CNT TERS measurements, a flat gold film on an inert support was used as the deposition substrate. This substrate enables gap-mode TERS, where the optical field is strongly amplified between the gold tip and gold surface [23]. The conductive substrate enhances the local field via image charge effects, yielding large Raman signals compared to non-metallic surfaces [244]. Standard microscope cover slips were chosen as substrates due to their flatness and negligible Raman background. As shown in Figure 3.10, the topography of a typical cover slip exhibits sufficiently low roughness to enable high-resolution TERS scanning.

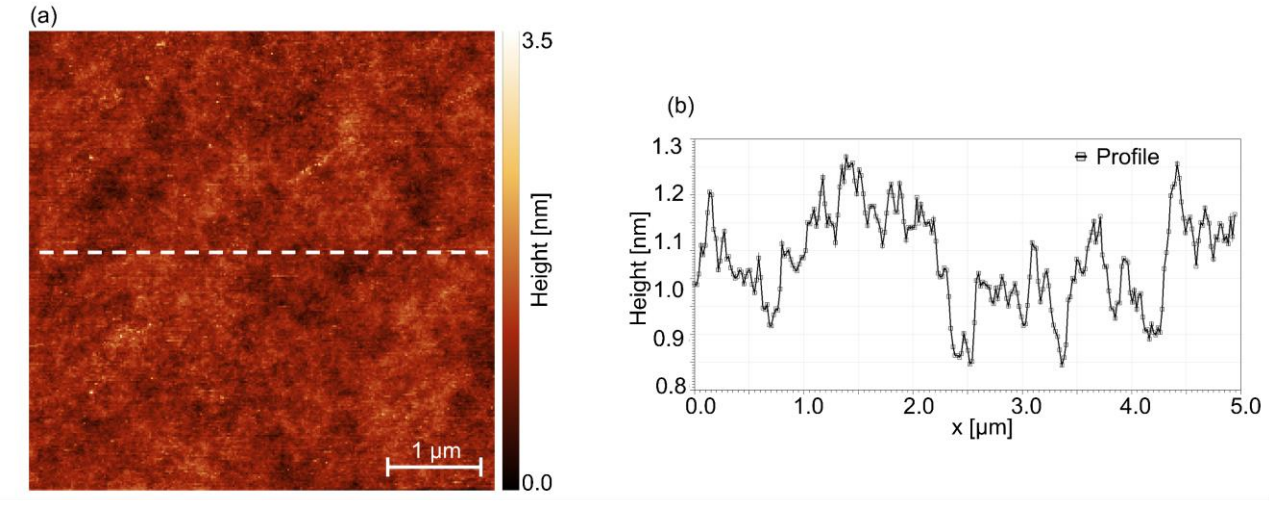

Figure 3.10: AFM image showing the topography of a glass cover slip surface (a). The white dashed line marks the path for the cross-sectional profile. (b) Profile corresponding to a roughness of 0.3 nm RMS.

A 50 nm gold film was deposited onto the glass cover slips using plasma sputtering, resulting in a continuous and conductive surface suitable for gap-mode TERS enhancement. As deposited, the film exhibited an RMS roughness of ~0.6 nm (Figure 3.11 (a)). Surface smoothing was achieved via thermal annealing: substrates were placed at the center of a tube furnace, heated to 550 °C for 1 minute, then cooled under nitrogen for 3 minutes. The recrystallized film (Figure 3.11 (b)) displayed extended flat islands and an RMS roughness of ~0.2 nm. To avoid contamination, especially from sulfur adsorption, all handling was performed with clean tools, and substrates were stored in a desiccator.

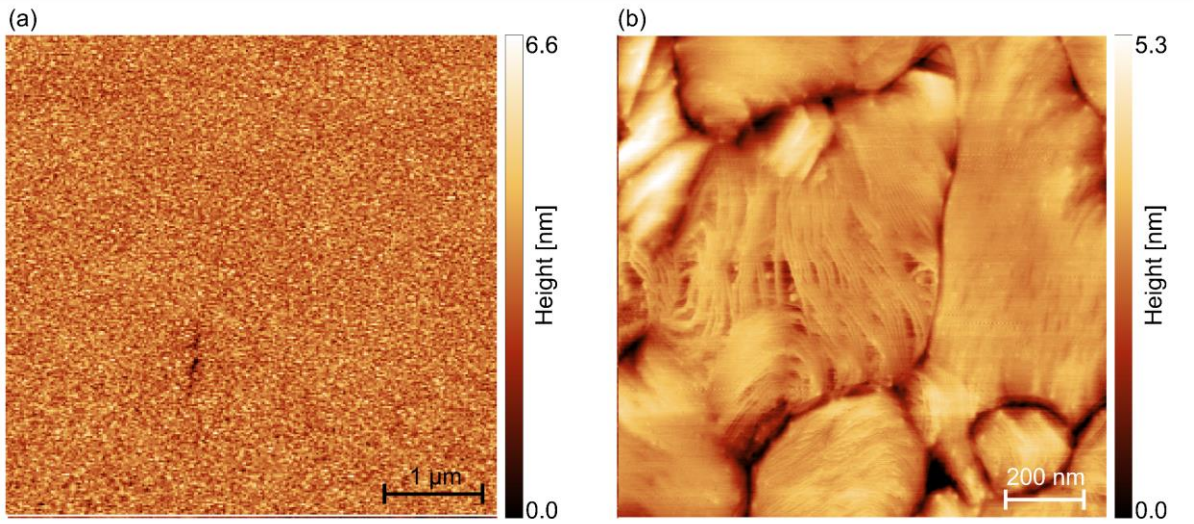

Figure 3.11: AFM scan of the gold film sputtered onto a glass cover slip (a), showing a relatively rough surface prior to annealing. (b) AFM scan of the same substrate after thermal annealing at 550 °C, revealing the formation of flat gold islands with reduced surface roughness (~0.2 nm RMS).

3.7.3 CNT solution and deposition

The carbon nanotubes used in this study were high-purity single-walled CNTs with a narrow diameter distribution centered around ~1.3 nm. We specifically employed a commercially enriched metallic SWCNT sample (90% metallic content, from NanoIntegris Inc.), to ensure a strong resonant Raman response at our excitation wavelength. The CNTs were supplied in an aqueous suspension, and we further processed this solution to achieve an appropriate dispersion for deposition. To break up any bundles and individualized the tubes, the stock solution was diluted (to ~10 µg CNT per mL) and ultrasonicated (~5 minutes). A small aliquot (typically 20–30 µL) of this diluted, well-dispersed CNT suspension was drop-cast onto multiple locations of the prepared 1.2 × 1.2 cm Au-coated slide. Droplets remained undisturbed in air for ~30 minutes, allowing CNTs to adsorb onto the gold surface via hydrophobic and van der Waals interactions

without additional functionalization. Excess liquid containing surfactants and non-adhered CNTs was removed by gently rinsing with ultrapure water and dried under a nitrogen flow.

The topography of the surface was measured by AFM in tapping mode to assess the distribution and density of nanotubes. The AFM topography images (Figure 3.12) showed individual linear features attributed to CNTs, with lengths ranging roughly from 100 nm up to 1–2 μm, consistent with the supplier's specifications. These tubes were relatively isolated from each other, with an estimated surface density of about 2 CNT per μm^2. Such a density is ideal for our TERS experiments: it is low enough that within any given ~1 μm^2 laser focus area, there is a high chance of finding only a single CNT (which simplifies spectral interpretation and ensures the near-field signal comes from one nanotube at a time), yet high enough that locating a CNT under the microscope is not too time-consuming. In practice, we found multiple suitable nanotubes in each scan region, allowing us to choose an optimal one (for example, an isolated, straight segment well separated from any clusters) as the target for TERS mapping.

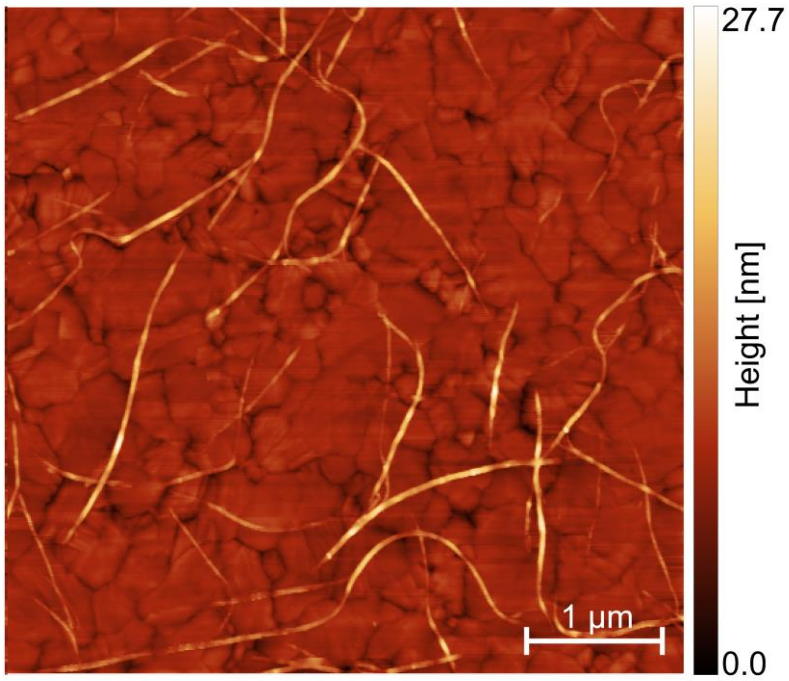

Figure 3.12: AFM topography image of carbon nanotubes (CNTs) deposited on a gold-coated substrate. The observed linear features correspond to individual single-walled CNTs, with lengths ranging from ~100 nm to 2 μm. The nanotubes appear well-dispersed and sparsely distributed (~2 CNT/μm²), providing an optimal surface density (lower Raman cross section) for TERS measurements.

3.7.4 TERS on CNTs: Raman features and enhancement factor

Once the tip and laser were aligned on a chosen CNT, TERS spectral maps were acquired to evaluate the near-field enhancement and its spatial resolution. A typical TERS map consisted of raster-scanning either the sample or tip in a two-dimensional grid (while keeping the focus fixed) and collecting a Raman spectrum at each pixel. For the CNT, a convenient strategy was to scan a line or small area that crosses the nanotube. Scan sizes of 100–500 nm were used, covering the CNT and part of the surrounding substrate, with fine step sizes (on the order of 8–10 nm or even 1 nm in some high-resolution scans). Due to the strong resonant Raman cross-section of the CNT, integration times as short as 0.1–0.5 s were sufficient to detect the G-band when the tip was positioned on the CNT.

To map the spatial distribution of Raman signals along individual carbon nanotubes, TERS measurements were carried out over a 500 nm × 500 nm area using a 64 × 64 pixel area, yielding an effective spatial resolution of approximately 8 nm. A 0.7 NA objective focused 300 µW of 632.8 nm p-polarized laser light onto the tip apex, and Raman spectra were acquired with 1-second integration per pixel. The resulting TERS maps were generated by integrating the intensity of the G-band (1550–1650 cm^{-1}) and D-band (1300–1400 cm^{-1}) at each pixel. TERS scans and AFM scans of the same region were recorded simultaneously to enable correlation of surface topography with Raman vibration modes (see Figure 3.13).

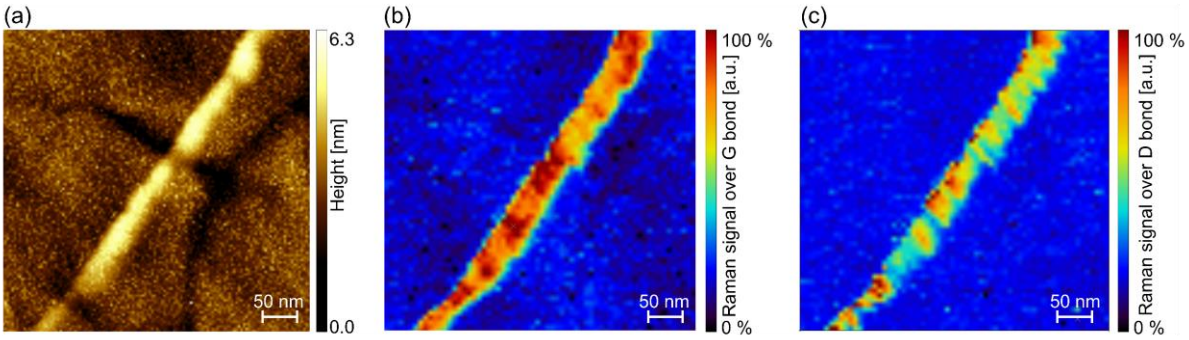

Figure 3.13: TERS measurement of CNTs on gold layer. (a)AFM height scan showing a single CNT on an annealed gold substrate, recorded simultaneously with TERS mapping. (b) and (c) Corresponding TERS maps over a 500 nm × 500 nm region with 8 nm spatial resolution, depicting Raman signal intensities integrated over the G-band (1550–1650 cm^{-1}) and D-band (1300–1400 cm^{-1}) regions, respectively, with 1-second integration time per pixel.

As shown in the TERS maps, there is a strong correlation between the topographic scan and the near-field Raman map, which confirms that the Raman signal enhancement is highly localized to the vicinity of the nanotube. In particular, the G-band TERS map, corresponding to the C–C bond stretching vibrations, reveals the spatial distribution of graphitic structure along the CNT with

~8 nm resolution. This far surpasses the diffraction-limited resolution of conventional Raman microscopy, which, based on the Airy disk diameter, is approximately 1100 nm for our setup. Thus, the TERS resolution represents an improvement by nearly a factor of 140, enabling chemical imaging well below the diffraction limit of light.

Moreover, the D-band TERS map allows identification of localized structural defects along the CNT with nanometer precision. These results demonstrate the capability of TERS not only to chemically identify materials at the nanoscale, but also to resolve spatially confined features such as defect sites that are otherwise inaccessible using conventional Raman spectroscopy.

To enhance the signal-to-noise ratio in our TERS measurements, we averaged the Raman spectra over five adjacent pixels along the carbon nanotube (CNT). As depicted in Figure 3.14, the resulting spectrum provides detailed insights into the CNT's structure. Notably, the G-band, associated with C–C bond vibrations, exhibits a characteristic splitting into G^+ and G^- peaks. These peaks correspond to the longitudinal optical (LO) and transverse optical (TO) phonon modes, respectively, with their energies influenced by the CNT's chirality and the vibration direction relative to the nanotube axis [245]. The G-band profile reveals the CNT's electronic nature; here, the pronounced and asymmetric G^- peak confirms its metallic behavior due to strong electron–phonon interaction.

The D-band, appearing around 1300 cm^{-1}, is indicative of structural defects or disorder within the CNT lattice, such as vacancies or amorphous carbon [59]. Additionally, the M-band near 1750 cm^{-1} comprises two components: M^-, which exhibits dispersive behavior (its frequency shifts with varying excitation energies), and M^+, which remains relatively constant. These modes are further enhanced by van Hove singularities—sharp peaks in the electronic density of states characteristic of one-dimensional systems like CNTs—and by symmetry-breaking effects associated with the nanotube's curvature [60]. Analysis of the M-band offers insights into the electronic transitions and curvature-induced symmetry alterations in CNTs.

Furthermore, the peak at 196 cm^{-1} corresponds to radial breathing modes which is radial oscillations perpendicular to the CNT axis and is inversely related to the CNT's diameter (d) by the relation [61]:

$$v_{RBM} = \frac{234\ nm}{d} - 10 \qquad 3.6$$

For the RBM detected at 196 cm^{-1}, substitution into Equation 3.6 yields a CNT diameter of approximately 1.26 nm. Modes in the ~180–200 cm^{-1} range were significantly enhanced in the

TERS spectra, allowing reliable diameter estimation despite the presence of low-frequency background arising from residual Rayleigh scattering and tip-related photoluminescence. In our measurements, the ~196 cm^{-1} RBM was distinctly resolved under 632.8 nm excitation, indicating a favorable resonance condition for this vibrational mode.

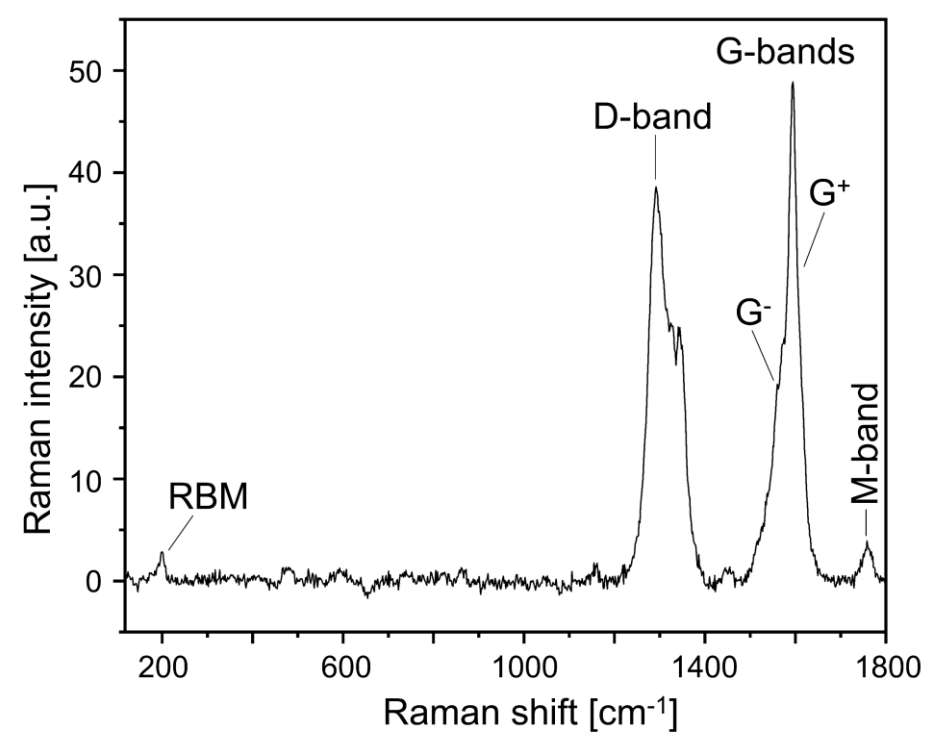

Figure 3.14: Near-field Raman spectrum obtained by averaging measurements over five adjacent pixels along CNT. The spectrum prominently displays the characteristic features of the CNT.

To confirm that the observed Raman signal enhancement originates from near-field effects, we conducted spectral-stack measurements. In these experiments, the TERS tip was retracted from the sample surface in ranging from 0 nm up to 20 nm, while simultaneously recording the Raman intensity (see Figure 3.15 (a)). This approach, known as a “spec-stack”, involves collecting a series of Raman spectra at varying tip-sample distances, effectively stacking the spectra to analyze changes correlated with tip position.

Raman spectra acquired at the hotspot, near the hotspot, and far from the hotspot are shown in Figure 3.15 (b). When the tip is positioned directly on the CNT at the hotspot (0 nm, blue line), the G-band at ~1580 cm^{-1} is clearly distinguishable. A slight lateral displacement of the tip (~2 nm) leads to a noticeable decrease in G-band intensity, while retracting the tip to ~10 nm above the CNT, the Raman signal diminishes further, approaching the far-field background level characteristic of the underlying sample. This spatial decay confirms that the enhanced Raman

response arises primarily from the nanotube directly beneath the TERS tip, demonstrating the high spatial confinement of the near-field enhancement.

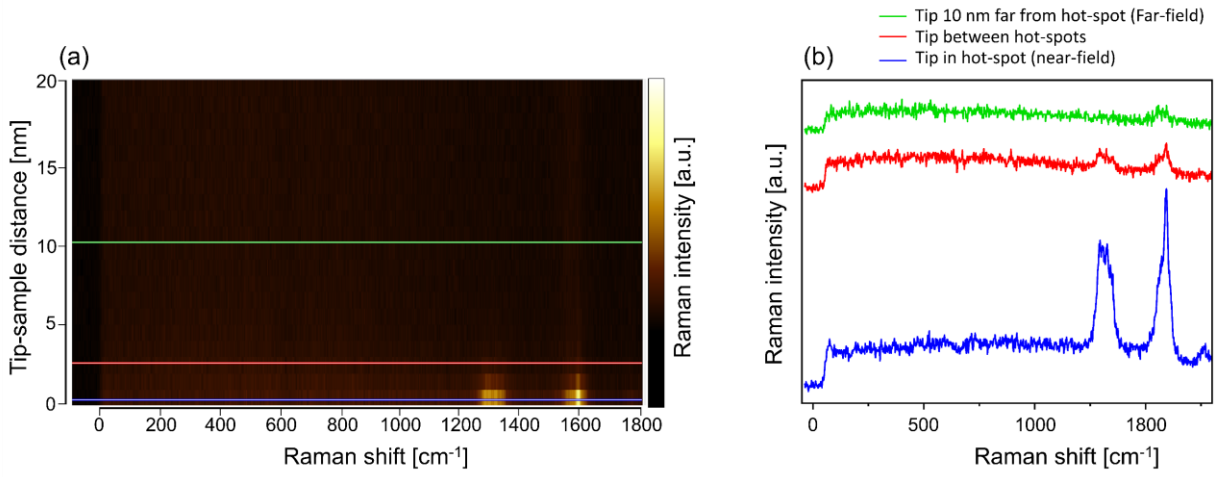

Figure 3.15: Spec-stack illustrating the variation in Raman signal intensity as the TERS tip is incrementally retracted from 0 nm to 20 nm above the carbon nanotube (CNT) surface (a). Each spectrum corresponds to a specific tip-sample distance, demonstrating the decay of the Raman signal with increasing separation. (b) Representative Raman spectra extracted from the spec-stack map at three distinct tip positions: (1) directly on the CNT at a "hotspot" (blue line), where the G-band at ~1580 cm^{-1} is highly prominent; (2) on the CNT but slightly away from the hotspot (~2 nm), showing a reduced G-band intensity; and (3) ~100 nm above the CNT, where the G-band is nearly absent. These spectra confirm the near-field nature of the TERS enhancement, with signal intensity diminishing rapidly as the tip is retracted from the CNT surface.

Notably, the D-band at ~1325 cm^{-1}, which is barely observable in far-field spectra, becomes pronounced in near-field measurements. Comparing the D/G intensity ratio between near-field and far-field spectra indicates that the near-field not only amplifies defect-related scattering but may also introduce slight structural distortions or charge transfer in the CNT, activating D-band scattering even in tubes with initially low defect density. Overall, these findings underscore the capability of TERS to provide highly localized chemical information, surpassing the diffraction limit and enabling detailed analysis of nanoscale materials.

3.7.5 Enhancement factor

In TERS, the enhancement factor (EF) quantifies the amplification of Raman signals due to the near-field effect at the tip apex. As discussed earlier, the enhancement factor for a 2D material is given by:

$$g = \left(\frac{I_{TERS} - I_{far\text{-}field}}{I_{far\text{-}field}}\right) \cdot \left(\frac{A_{far\text{-}field}}{A_{TERS}}\right) \qquad 3.7$$

Where I_{TERS} is the Raman intensity acquired with the tip engaged in contact mode, $I_{far\text{-}field}$ denotes the Raman intensity measured with the tip retracted, and $A_{far\text{-}field}$ and A_{TERS} represent the effective sampling areas in near-field and far-field conditions, respectively.

As illustrated in Figure 3.16, the experimental ratio of for the G-band is approximately 7. Substituting these values into Equation 2.35 yields an estimated enhancement factor of approximately 42,000 for our TERS setup. This calculation assumes a near-field radius of ~10 nm and a tip–sample gap of ~1 nm, with an excitation wavelength of 632.8 nm focused through an objective with a numerical aperture (NA) of 0.7. These parameters are crucial in defining the field confinement area and thus directly impact the observed signal enhancement.

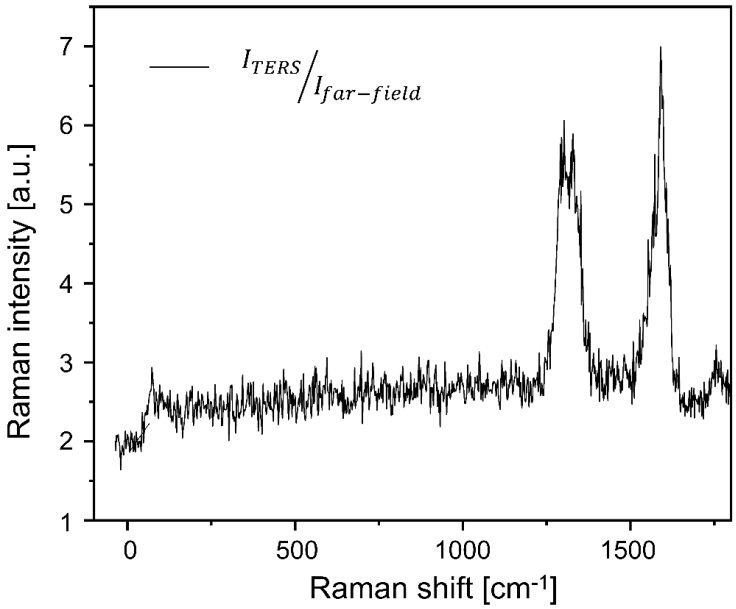

Figure 3.16: Comparison of Raman intensities acquired in TERS (tip engaged) and far-field (tip retracted) configurations for the carbon nanotube.

An enhancement factor of this magnitude implies a Raman signal amplification exceeding four orders of magnitude, attributable to the near-field effect at the tip apex. Given that the Raman scattering intensity scales with the fourth power of the local electric field enhancement, the corresponding electric field enhancement is:

$$E_{enh} = g^{1/4} \approx 14.3 \tag{3.8}$$

This level of field enhancement is consistent with expectations for high-quality gold tips operating in gap-mode configurations, where plasmonic coupling between the tip and the substrate is

optimized. The calculated EF demonstrates that the fabricated tip and optical setup are capable of delivering substantial Raman signal enhancement, sufficient for the detection of intrinsically weak signals such as those from individual CNTs. This EF estimate is conservative; in many cases, the far-field signal approached the noise threshold, implying that the actual enhancement may be significantly higher. Furthermore, localized variations in EF are possible due to grain boundaries or surface roughness on the tip, which can generate hotspots with even higher enhancement. These hotspots were identified experimentally as isolated regions of intense Raman signal, demonstrating dominant plasmonic activity at specific tip sites.

3.8 Summary

This chapter has detailed the design, alignment, and fabrication procedures used to develop a robust TERS system for high-resolution characterization of non-transparent and non-conductive materials. The setup integrates a SmartSPM operating in shear-force mode with a quartz tuning fork feedback system, providing sub-nanometer control of the tip–sample distance and minimizing mechanical drift during extended acquisitions. Optical excitation and collection were implemented in side-illumination geometry using a Mitutoyo Plan Apochromat 100× objective (NA = 0.7, WD = 6.0 mm), chosen to balance spatial resolution and working distance for the tuning fork assembly. Alignment of the laser to the tip apex followed a structured protocol: coarse mechanical positioning, fine raster scanning with photomultiplier feedback, and point spread function analysis in both xy and xz planes, refined via real-time Raman monitoring.

Gold TERS tips were produced using electrochemical etching process in a 1:1 HCl–ethanol electrolyte, using a vertical gold wire and a platinum ring counter-electrode. A two-step approach—high-voltage DC etching for rapid tapering followed by low-voltage pulsed etching—produced tips with 10–20 nm apex radii and smooth conical profiles. To evaluate both enhancement and spatial resolution, carbon nanotubes (CNTs) deposited on gold-coated glass cover slip were used as reference samples. TERS measurements showed pronounced enhancement of the G and D bands relative to far-field spectra, while lateral mapping confirmed sub-10 nm spatial resolution.

In summary, Chapter 3 presents a rigorous methodology for constructing and operating a high-resolution TERS platform. Advances in tip fabrication, optical alignment, and mechanical stability collectively enable reproducible nanoscale Raman measurements, establishing the system’s capability for probing the structural and chemical properties of complex materials such as perovskites.

4 RESEARCH ARTICLE I – INVESTIGATION OF CARBONATE MONOLAYER ADSORPTION ON BARIUM TITANATE

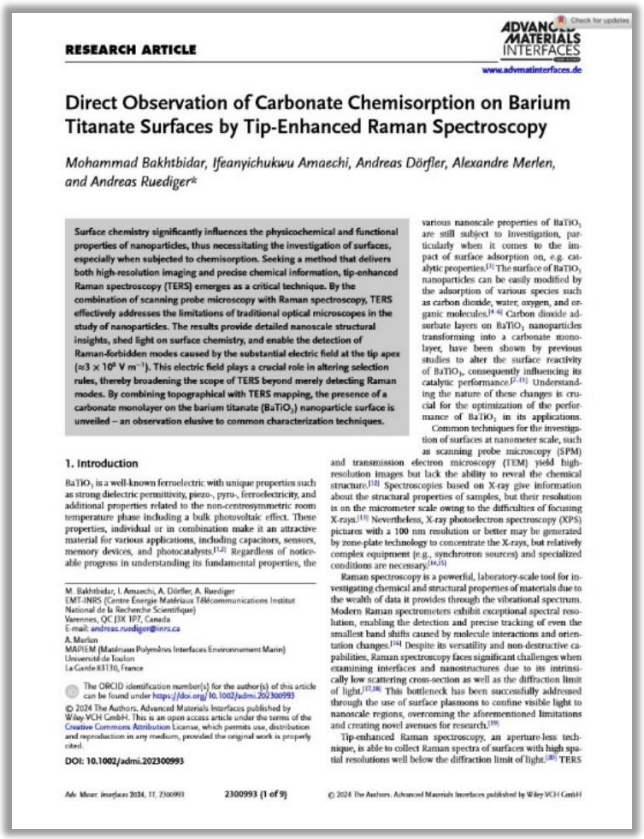

RESEARCH ARTICLE

ADVANCED MATERIALS INTERFACES

www.advmatinterfaces.de

Direct Observation of Carbonate Chemisorption on Barium Titanate Surfaces by Tip-Enhanced Raman Spectroscopy

Mohammad Bakhtbidar, Ifeanyichukwu Amaechi, Andreas Dörfler, Alexandre Merlen, and Andreas Ruediger*

Surface chemistry significantly influences the physicochemical and functional properties of nanoparticles, thus necessitating the investigation of surfaces, especially when subjected to chemisorption. Seeking a method that delivers both high-resolution imaging and precise chemical information, tip-enhanced Raman spectroscopy (TERS) emerges as a critical technique. By the combination of scanning probe microscopy with Raman spectroscopy, TERS effectively addresses the limitations of traditional optical microscopes in the study of nanoparticles. The results provide detailed nanoscale structural insights, shed light on surface chemistry, and enable the detection of Raman-forbidden modes caused by the substantial electric field at the tip apex ($\approx 3 \times 10^8$ V m^{-1}). This electric field plays a crucial role in altering selection rules, thereby broadening the scope of TERS beyond merely detecting Raman modes. By combining topographical with TERS mapping, the presence of a carbonate monolayer on the barium titanate ($BaTiO_3$) nanoparticle surface is unveiled – an observation elusive to common characterization techniques.

1. Introduction

$BaTiO_3$ is a well-known ferroelectric with unique properties such as strong dielectric permittivity, piezo-, pyro-, ferroelectricity, and additional properties related to the non-centrosymmetric room temperature phase including a bulk photovoltaic effect. These properties, individual or in combination make it an attractive material for various applications, including capacitors, sensors, memory devices, and photocatalysts.[1,2] Regardless of noticeable progress in understanding its fundamental properties, the various nanoscale properties of $BaTiO_3$ are still subject to investigation, particularly when it comes to the impact of surface adsorption on, e.g. catalytic properties.[3] The surface of $BaTiO_3$ nanoparticles can be easily modified by the adsorption of various species such as carbon dioxide, water, oxygen, and organic molecules.[4–6] Carbon dioxide adsorbate layers on $BaTiO_3$ nanoparticles transforming into a carbonate monolayer, have been shown by previous studies to alter the surface reactivity of $BaTiO_3$, consequently influencing its catalytic performance.[7–11] Understanding the nature of these changes is crucial for the optimization of the performance of $BaTiO_3$ in its applications.

Common techniques for the investigation of surfaces at nanometer scale, such as scanning probe microscopy (SPM) and transmission electron microscopy (TEM) yield high-resolution images but lack the ability to reveal the chemical structure.[12] Spectroscopies based on X-ray give information about the structural properties of samples, but their resolution is on the micrometer scale owing to the difficulties of focusing X-rays.[13] Nevertheless, X-ray photoelectron spectroscopy (XPS) pictures with a 100 nm resolution or better may be generated by zone-plate technology to concentrate the X-rays, but relatively complex equipment (e.g., synchrotron sources) and specialized conditions are necessary.[14,15]

Raman spectroscopy is a powerful, laboratory-scale tool for investigating chemical and structural properties of materials due to the wealth of data it provides through the vibrational spectrum. Modern Raman spectrometers exhibit exceptional spectral resolution, enabling the detection and precise tracking of even the smallest band shifts caused by molecule interactions and orientation changes.[16] Despite its versatility and non-destructive capabilities, Raman spectroscopy faces significant challenges when examining interfaces and nanostructures due to its intrinsically low scattering cross-section as well as the diffraction limit of light.[17,18] This bottleneck has been successfully addressed through the use of surface plasmons to confine visible light to nanoscale regions, overcoming the aforementioned limitations and creating novel avenues for research.[19]

Tip-enhanced Raman spectroscopy, an aperture-less technique, is able to collect Raman spectra of surfaces with high spatial resolutions well below the diffraction limit of light.[20] TERS

M. Bakhtbidar, I. Amaechi, A. Dörfler, A. Ruediger
EMT-INRS (Centre Energie Matériaux Télécommunications Institut National de la Recherche Scientifique)
Varennes, QC J3X 1P7, Canada
E-mail: andreas.ruediger@inrs.ca
A. Merlen
MAPIEM (Matériaux Polymères Interfaces Environnement Marin)
Université de Toulon
La Garde 83130, France

The ORCID identification number(s) for the author(s) of this article can be found under https://doi.org/10.1002/admi.202300993

DOI: 10.1002/admi.202300993

Direct observation of carbonate chemisorption on barium titanate surfaces by tip-enhanced Raman spectroscopy

Observation directe de la chimisorption de carbonate sur les surfaces de titanate de baryum par spectroscopie Raman exaltée par pointe

Mohammad Bakhtbidar,[1] Ifeanyichukwu Amaechi,[1] Andreas Dörfler,[1] Alexandre Merlen,[2] and Andreas Ruediger [1,*]

[1]EMT-INRS (Centre Énergie Matériaux Télécommunications, Institut National de la Recherche Scientifique), Varennes, QC H2X 1E3, Canada

[2]MAPIEM (Matériaux Polymères Interfaces Environnement Marin), Université de Toulon, 83130 La Garde, France

*andreas.ruediger@inrs.ca

Publication: Advanced Materials Interfaces 11.15 (2024): 2300993. doi: 10.1002/admi.202300993

Published: 17 April 2024

Author Contributions: The initial concept for investigating carbonate monolayers on barium titanate ($BaTiO_3$) surfaces using tip-enhanced Raman spectroscopy (TERS) was proposed by AR. MB developed the experimental methodology, including sample preparation and TERS tip fabrication, and conducted the measurements. IA performed the x-ray diffraction and transmission electron microscopy analyses on the $BaTiO_3$ nanoparticles. Data analysis and interpretation were carried out by MB and AD, with theoretical insights into the activation of infrared modes within the Raman spectrum due to nanoscale symmetry breaking provided by AR and AM. MB drafted the manuscript, and all authors contributed to its revision and approved the final version.

Abstract: Surface chemistry significantly influences the physicochemical and functional properties of nanoparticles, thus necessitating the investigation of surfaces, especially when subjected to chemisorption. Seeking a method that delivers both high-resolution imaging and precise chemical information, tip-enhanced Raman spectroscopy (TERS) emerges as a critical technique. By the combination of scanning probe microscopy with Raman spectroscopy, TERS effectively addresses the limitations of traditional optical microscopes in the study of nanoparticles. Our results provide detailed nanoscale structural insights, shed light on surface chemistry, and enable the detection of Raman-forbidden modes caused by the substantial electric field at the tip apex ($\sim 3\times10^{8}$ V/m). This electric field plays a crucial role in altering selection rules, thereby broadening the scope of TERS beyond merely detecting Raman modes. By combining topographical with TERS mapping, we unveil the presence of a carbonate monolayer on the $BaTiO_3$ nanoparticle surface – an observation elusive to common characterization techniques.

Keywords: plasmonic enhancement, tip-enhanced Raman spectroscopy, barium titanate, high-resolution surface imaging, Raman-forbidden modes

4.1 Introduction

$BaTiO_3$ is a well-known ferroelectric with unique properties such as strong dielectric permittivity, piezo-, pyro-, ferroelectricity and additional properties related to the non-centrosymmetric room temperature phase including a bulk photovoltaic effect. These properties, individual or in combination make it an attractive material for various applications, including capacitors, sensors, memory devices, and photocatalysts [246,247]. Regardless of noticeable progress in understanding its fundamental properties, the various nanoscale properties of $BaTiO_3$ are still subject to investigation, particularly when it comes to the impact of surface adsorption on, e.g. catalytic properties [248]. The surface of $BaTiO_3$ nanoparticles can be easily modified by the adsorption of various species such as carbon dioxide, water, oxygen, and organic molecules [249–251]. Carbon dioxide adsorbate layers on $BaTiO_3$ nanoparticles transforming into a carbonate monolayer, have been shown by previous studies to alter the surface reactivity of $BaTiO_3$, consequently influencing its catalytic performance [62–66]. Understanding the nature of these changes is crucial for the optimization of the performance of $BaTiO_3$ in its applications.

Common techniques for the investigation of surfaces at nanometer scale, such as scanning probe microscopy (SPM), transmission electron microscopy (TEM) yield high-resolution images but lack the ability to reveal the chemical structure [252]. Spectroscopies based on x-ray give information about structural properties of samples, but their resolution is on the micrometer scale owing to the difficulties of focusing x-rays [253]. Nevertheless, x-ray photoelectron spectroscopy (XPS) pictures with a 100 nm resolution or better may be generated by zone-plate technology to concentrate the x-rays, but relatively complex equipment (e.g. synchrotron sources) and specialized conditions are necessary [254,255].

Raman spectroscopy is a powerful, laboratory-scale tool for investigating chemical and structural properties of materials due to the wealth of data it provides through the vibrational spectrum. Modern Raman spectrometers exhibit exceptional spectral resolution, enabling the detection and precise tracking of even the smallest band shifts caused by molecule interactions and orientation changes [256]. Despite its versatility and non-destructive capabilities, Raman spectroscopy faces significant challenges when examining interfaces and nanostructures due to its intrinsically low scattering cross-section as well as the diffraction limit of light [67,68]. This bottleneck has been successfully addressed through the use of surface plasmons to confine visible light to nanoscale regions, overcoming the aforementioned limitations and creating novel avenues for research [257].

Tip-enhanced Raman spectroscopy, an apertureless technique, is able to collect Raman spectra of surfaces with high spatial resolutions well below the diffraction limit of light [258]. TERS combines scanning probe microscopy and Raman spectroscopy to concentrate visible photons into nanometer-scale regions, inducing an electromagnetic near-field intensity and yielding a substantially larger scattering cross-section [259]. The plasmonic enhancement mechanisms in TERS includes a localized surface plasmon resonance (LSPR), gap enhancement, and chemical enhancement [260].

LSPR enhancement occurs when the surface electrons of a metal nanoparticle, such as the gold tips used in our study, are resonantly excited by incident light of a specific wavelength. This interaction leads to a collective oscillation of the conduction electrons in the plasmonic tip, generating a confined electromagnetic field known as a plasmon resonance. Consequently, this amplifies both the incident laser as well as the Raman scattered signal emitted by the sample positioned nearby, effectively enhancing the intensity of Raman signal at the nanoscale. Given the large spectral width of the plasmon resonance phenomenon in comparison to the Stokes-shift of the Raman effect, it is often appropriate to consider the same amplification factor for the incident and backscatter light.

Gap enhancement occurs when the metal tip is within proximity (typically <5 nm) to a metal substrate. This proximity generates a stronger local electric field at the tip apex via a virtual image charge in the metal substrate, thus amplifying the Raman scattering signal from the sample through a virtual plasmonic dimer. LSPR generally prevails over gap enhancement in TERS [261], but gap TERS has so far been considered a crucial contribution to push TERS to the best possible enhancement.

Chemical enhancement is another mechanism to enhance the Raman scattering signal in TERS and surface-enhanced Raman spectroscopy (SERS). It relies on a direct contact between the tip and the sample through e.g. contact mode feedback of the scanning probe microscope [262]. The plasmon resonance of metal nanoparticles depends on their size, shape, and composition. Gold and silver are commonly used in TERS probes due to their strong plasmon resonances in the visible and near-infrared (IR) regions of the electromagnetic spectrum, where gold in comparison to silver provides lower amplification but easier handling due to the better chemical stability under ambient conditions [263–265].

The near-field effect in TERS, confined to a few nanometers near the plasmonic tip by the electromagnetic field's limited range, makes TERS exceptionally sensitive to surface phenomena [266]. Consequently, TERS is becoming a versatile tool for the analysis of surface processes

across multiple disciplines, including materials science, catalysis, and biotechnology. TERS has also been reported to possibly reduce the symmetry in samples, leading to a change of Raman selection rules through intense electric field and their gradients. Activation of additional modes for Raman scattering offers qualitative information on nanoscale surface features by capturing otherwise Raman-inactive modes [267]. Recent research revealed that in addition to the quantitative improvement of resolution and sensitivity, tip-enhanced Raman spectroscopy thus has the potential to qualitatively widen the scope of investigation through the activation of conventionally Raman-forbidden modes and surface modes. These modes provide additional and possibly crucial insights into material structural distortions, symmetry breaking and reconstruction. TERS therefore continues its contributions to the advancement of surface science [268,269].

Barium titanate at room temperature has a tetragonal perovskite structure with an *a* lattice parameter of 0.3994 nm and a *c/a* ratio close to 1.01 in a group P4mm where the {100} surfaces may be terminated with TiO_2 and BaO terminations, see Figure 4.1 (a) [270]. At approximately 130 °C, it undergoes a phase transition into a cubic, centrosymmetric phase, which is Raman-silent.

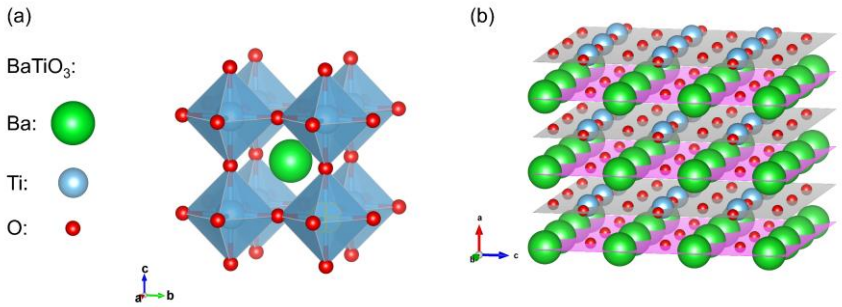

Figure 4.1: Crystal structure of $BaTiO_3$ highlighting the oxygen octahedra (a), (b) layered structure of $BaTiO_3$ (100) planes with BaO and TiO_2 vicinal surfaces. The visualization of the crystal structures in (a) and (b) was conducted using VESTA 3 [271].

Cleaving a $BaTiO_3$ crystal along a certain direction exposes surface atoms with unsaturated bonds, leading to possible surface reconstruction, chemi-, and physisorption. Under ambient conditions, the chemisorption of CO_2 onto BaO-terminated terraces frequently occurs to minimize surface energy. Despite numerous theoretical studies [272,273] that corroborated this effect, direct experimental evidence detailing the formation and structure of the carbonate monolayer on the surface of $BaTiO_3$ is still in its infancy. The shortage of experimental findings, especially on individual particles and surfaces is mainly due to the limited sensitivity and resolution of conventional surface probing techniques.

In this work, we identify a carbonate monolayer on the surface of an individual barium titanate nanoparticle using high-resolution TERS at a noticeable distance from the gold substrate, suggesting a small, possibly negligible contribution of the image charge. This study gives insight into the strength and nature of the chemical bond between the CO_2 molecule and the $BaTiO_3$ surface, paving the way to further investigate changes in the electronic structure and chemical reactivity of the $BaTiO_3$ surface due to the adsorption of CO_2 molecules. Furthermore, we report on the detection of previously non-reported Raman modes that we associate with the activation of infrared modes. Our calculations demonstrate that the electric field at the apex of the tip is indeed sufficiently strong to cause bond distortion and consequently, change the symmetry elements of the sample under investigation. This electric field therefore stimulates the appearance of novel modes in the Raman spectra, which exhibit a clear correlation in terms of both Stokes shift and intensity with the infrared modes.

4.2 Results and discussion

4.2.1 Microstructural analysis

Figure 4.2 (a) illustrates a typical XRD pattern of the $BaTiO_3$ nanoparticles. The pattern matches the reference (JCPDS card #: 01-089-1428), which has a characteristic intense peak at 2θ = 31.65° corresponding to the (101) diffraction plane, indicating a high crystallinity of the tetragonal phase [274]. However, a detectable peak associated to carbonate contamination is also observed at 2θ = 24.1°. The emergence of this thermodynamically stable barium carbonate product arises from the remarkable surface reactivity of barium titanate nanoparticles with atmospheric CO_2 on BaO-terminated surfaces [69]. Barium titanate nanoparticles in the tetragonal phase are distinguished from the cubic counterpart following the splitting of peak around 2θ = 45° into (002) and (200) diffraction planes, wherein the crystal distortion leads to a larger *c*-axis in comparison to the *a*-axis [275]. In nanosized tetragonal particles however, such peak splitting is usually obscured due to the Debye-Scherrer-induced peak broadening.

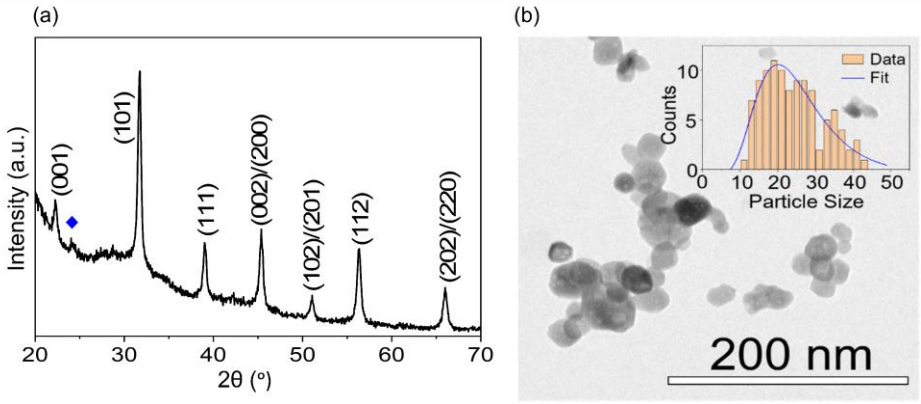

Figure 4.2: The XRD pattern (a), and TEM image (b) of the as-synthesized $BaTiO_3$ nanoparticles . "♦" denotes peak due to carbonate impurity. Inset of (b) is the histogram showing the particle size distribution.

A representative TEM image of the powder is shown in Figure 4.2 (b). The nanoparticles are slightly agglomerated and composed of grains with low shape anisotropy. The average particle size is estimated from a TEM image of approximately ~100 particles shown as a histogram in the inset of Figure 4.2 (b), where the average particle size is 25 ± 5 nm.

4.2.1 TERS measurement

The sample configuration is schematically illustrated in Figure 4.3 (a), showing $BaTiO_3$ nanoparticles spin-coated on Au/glass substrates. The thickness of the gold layer is approximately 50 nm, strongly attenuating any far-field Raman signature of the substrate, which becomes negligible with the use of glass. Figure 4.3 (b) displays the topography of the sample measured via tapping mode atomic force microscopy (AFM). The AFM topography image shows a relatively homogeneous distribution of the nanoparticles on the surface, with heights ranging from 10 to 50 nm, consistent with the size distribution extracted from TEM analysis. Due to the low Raman scattering cross-section and the small sample volume compared to the confocal volume, confocal Raman spectroscopy alone, i.e., spectral acquisition integrated over a diffraction-limited spot size of approximately 1 μm^2 for 1s exposure time, does not provide a detectable Raman signature of either $BaTiO_3$ nor the carbonate contamination.

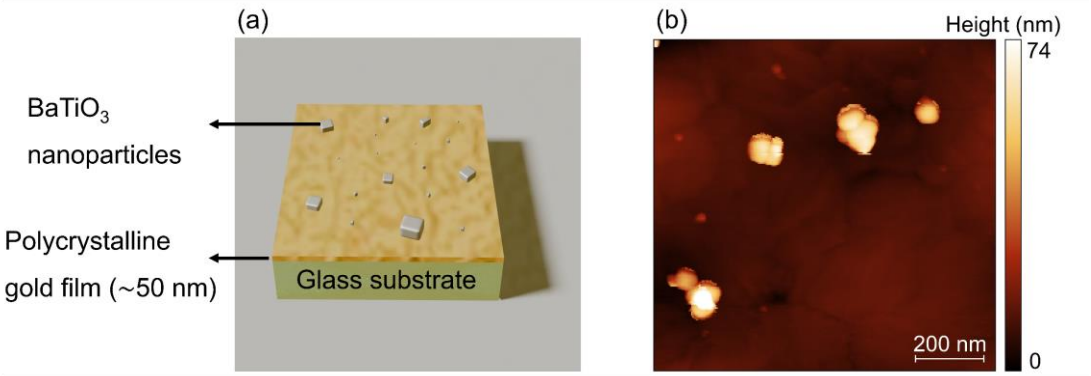

Figure 4.3: Schematic illustration of the sample configuration, depicting the distribution of $BaTiO_3$ nanoparticles onto Au-coated glass substrate (a). (b) 1µm × 1µm tapping-mode AFM topography image showing the $BaTiO_3$ nanoparticles on the polycrystalline gold surface.

Figure 4.4 shows the topography scan and TERS map obtained in shear force mode utilizing Au tips. The topography scan (Figure 4.4 (a)) unveils a nanoparticle of approximately 12 nm height, with its profile depicted as a line scan in Figure 4.4 (b). It is noteworthy that the presence of a barium titanate nanoparticle, combined with a distance exceeding 10 nm from the gold surface, substantially reduces the efficiency of gap-mode TERS, i.e., the enhancement of the near-field Raman signal through a virtual image charge in the gold surface. Figure 4.4 (c) displays a high-resolution

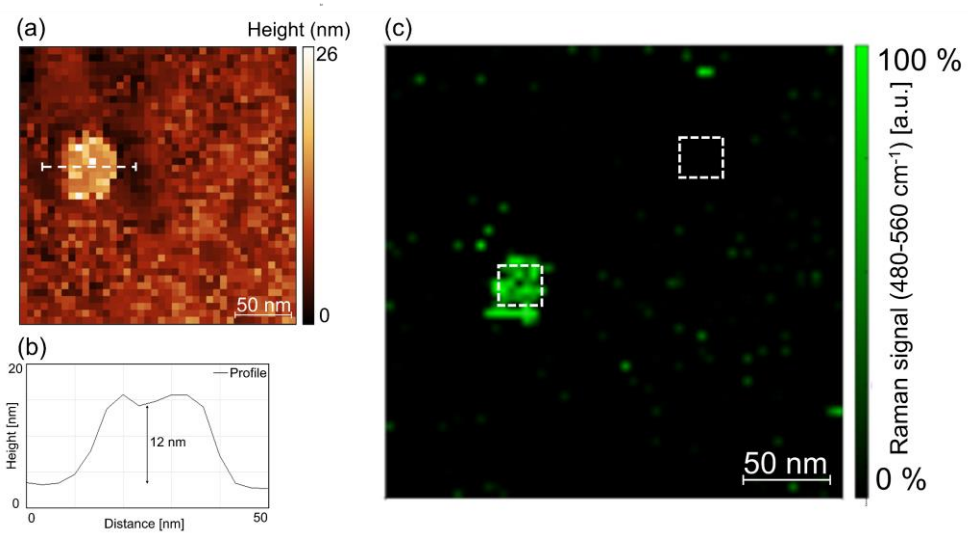

Figure 4.4: TERS measurement on the $BaTiO_3$ nanoparticle. (a) Topography scan over a 200 nm x 200 nm region with 60 x 60 pixels revealing an individual barium titanate particle. (b) Profile indicates the size of the particle as measured along the dotted white line in (a). (c) TERS map simultaneously acquired in the same area as in (a) revealing a strong signal in the 480 - 540 cm^{-1} spectral range at the location of the nanoparticle with a 3.3 nm step-size. The white dotted squares serve for a spatial integration of the Raman spectrum as displayed in Figure 4.5.

TERS map in a false-color image, where the spectral emissions around 540 cm^{-1} (corresponding to the $BaTiO_3$ TO_4 peak) are plotted as a function of position. This map clearly identifies the location of the barium titanate nanoparticle, exhibiting a pronounced correlation with the topography scan. In order to compare TERS spectra between the substrate and nanoparticle, spectral averaging was performed on both regions to enhance the signal-to-noise ratio, within the specific regions marked by white broken lines in Figure 4.4 (c). Individual spectra are provided as supplementary information (Figure 4.8).

The averaged results are presented in Figure 4.5, where the signal observed on the bare gold surface remains at the noise level, whereas a pronounced and well-distinguished spectrum emerges for the nanoparticle. By evaluating nanoparticle dimensions and comparing the near-field signals on both the nanoparticle and substrate, our findings indicate a substantial plasmonic enhancement at the apex of the Au tips. This enhancement results in a highly sensitive TERS signal, as previously discussed.

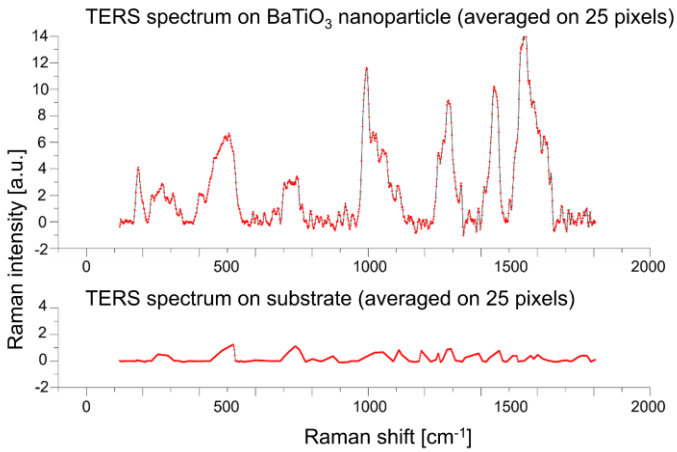

Figure 4.5: Comparison of near-field spectra on the nanoparticle and gold surface. The top spectrum corresponds to near-field spectrum on Ba**Ti**$\mathbf{O_3}$ nanograins, while the bottom shows the near-field spectrum on the gold surface ~50 nm away from a Ba**Ti**$\mathbf{O_3}$ grain. The near-field signature on the $BaTiO_3$ grains is roughly one order of magnitude above the noise floor; red dots are data points, and the black line guides the eye.

The amplification of the near-field spectrum can be quantified by calculating the enhancement factor (EF) [29]. For TERS measurement on a sufficient thin sample, EF is defined as follows [70]

$$EF = \frac{I_{NF} - I_{FF}}{I_{FF}} \times \frac{A_{FF}}{A_{NF}} \qquad 4.1$$

where I_{NF} corresponds to the intensity of the Raman signal captured within the near-field region, I_{FF} represents the intensity of the Raman signal obtained under far-field conditions, A_{NF} and A_{FF} denote the areas associated with the near-field and far-field measurements, respectively.

Comparison of areas instead of volumes takes into account that the relatively small thickness of the barium titanate nanograin is the limiting factor for both the far- and the near-field. The ratio between the near-field signal and the far-field with a value of 0.34 counts RMS yields an I_{NF}/I_{FF} ratio of 56. Considering the approximate diameter of the tip (~10 nm) and the laser spot size (~1.1 µm), the resultant enhancement factor amounts to 4.6×10^5. This corresponds to a local field enhancement at the apex of the tip of approximately 26 under the assumption of the g^4 dependence, where g denotes the enhancement factor of the optical near-field/far-field. It is noteworthy to emphasize that the observed enhancement stems solely from LSPR and does not incorporate chemical enhancement as the experiments were conducted in shear-force mode at a distance of approximately 1 nm.

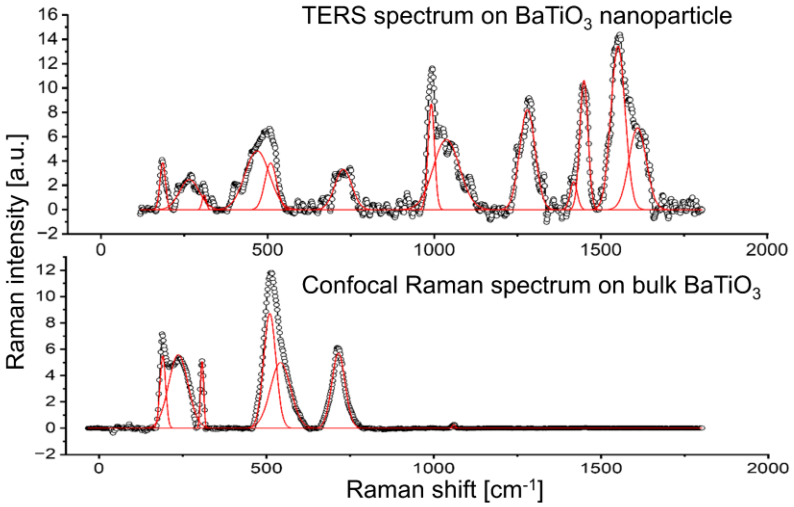

Figure 4.6: Comparison of the near-field spectrum from an individual $BaTiO_3$ nanoparticle and the confocal Raman spectrum of bulk $BaTiO_3$.

In comparison with existing literature, where enhancement factors typically range from 10^2 to 10^3 in similar experimental setups [71,72,243,276,277], the enhancement factor we report appears remarkable and is almost certainly due to an exceptionally strong plasmonic amplification among a series of various gold tips tested. This emphasizes the impact of our approach, which now suggests the opportunity for a chemical and structural analysis with monolayer sensitivity and a high spatial resolution without requiring a specific substrate.

A comparative analysis of the acquired TERS spectra was performed in pursuit of a more comprehensive understanding. In this regard, the TERS spectra from a single nanoparticle were compared against confocal Raman spectra from nanopowder. As depicted in Figure 4.6, a noticeable spectral resemblance between the confocal Raman and the near-field spectrum within

the range of 100 cm^{-1} – 800 cm^{-1} was observed. This region reflects characteristic Raman features of tetragonal $BaTiO_3$. The distinctive Raman peaks of $BaTiO_3$ are comprehensively presented in Table 4-1.

Table 4-1: Raman modes of $BaTiO_3$

#	Peak position (TERS)(cm^{-1})	Peak position (far-field) (cm^{-1})	Reported values (cm^{-1})	Possible modes assignment	Mode character	Ref.
1	183	180	180	A_1(TO)	Ba-TiO_3 vibration	[278]
2	270	270	280	E(TO_2)/E(LO)	(Ti-O) vibration	[279]
3	310	310	310	B_1 and E(TO_3)	(Ti-O_6) vibration	[279]
4	460	460	470	E(TO_4)/A(TO_3)	(Ti-O_6) vibration	[279]
5	510	510	520	E(TO_4)/A(TO_3)	(Ti-O_6) vibration	[280]
6	720	720	720	E(LO_4)/A(LO_3)	BO_6 stretching	[279]

Furthermore, comparing the carbonate peak located at ~1060 cm^{-1} in both spectra reveals a notable enhancement of the carbonate monolayer surface. Additional peaks emerge in the TERS spectrum, located at 1260 cm^{-1}, 1449 cm^{-1}, and 1550 cm^{-1}. From classical theory, the interaction of an electric field with molecular bonds triggers the generation of a Raman signal, with its strength being directly related to the electric field and gradient of polarizability. Interestingly, there is a way of generating an additional Raman signal, termed the gradient field Raman (GFR) signal. With a substantial gradient in the electric field, it becomes possible to alter the selection rules. Consequently, this may lead to the activation of previously Raman-silent modes, e.g., IR-active modes.

Ayars and Hallen pioneered the investigation into electric field gradients in the early 2000s [73]. The near-field gradient effect in TERS has garnered significant attention within the physics community. This interest is primarily attributed to the technique's capability to simultaneously uncover molecular infrared active modes, high-order Raman modes (including overtones), and combination modes [281–284]. For the dipole moment, we have [73]

$$\mu_a = \left\{ \underbrace{\left(\frac{d\mu_a^p}{dQ}\right)_0}_{IR\ absorption} + \underbrace{\left(\frac{d\alpha_{ab}}{dQ}\right)_0 E_b}_{Raman} + \underbrace{\alpha_{ab}\left(\frac{dE_b}{dQ}\right)_0}_{gradient\ field\ Raman\ (GFR)} + \underbrace{\frac{1}{3}\frac{\partial E_b}{\partial c}\left(\frac{dA_{abc}}{dQ}\right)_0}_{quadrupole\ Raman} \right\} Q \quad 4.2$$

where α describes the polarizability tensor, *Q* denotes the vibration coordinate, (*a*, *b*, *c*) refer to the spatial coordinates (*x*, *y*, *z*), μ^p describes the permanent dipole moment and *A* is a tensor that determines the dipole induced by a field gradient and the quadrupole induced by a uniform field [285,286]. In proximity to a metallic surface, the jellium model proposed by Feibelman [287] suggests that the electric field experiences almost its entire amplitude change within a mere 0.2 nm distance. Consequently, a significant electric field may induce the GFR term, leading to the emergence of new vibrational modes in the Raman spectrum. To gain a deeper understanding of this phenomenon, we quantify the strength of the electric field. According to theory, the intensity of the electric field is given by [288]

$$E = \left(\frac{2P}{Ac\epsilon_0}\right)^{\frac{1}{2}} \quad 4.3$$

where *P* stands for the laser power, *A* corresponds to the near-field area, *c* and ϵ_0 represent the speed of light and dielectric permittivity in vacuum, respectively. With a laser power of around 1.5 mW and considering near-field dimensions, the resulting electric field reaches about 3×10^8 V/m. This substantial strength potentially induces distortions in atomic vibrations and impact molecular polarizability. However, the high electric field is primarily localized at the surface of the nanoparticle, and its intensity diminishes rapidly with distance according to

$$E \propto (r+d)^{-10} \quad 4.4$$

where *r* represents the tip radius and *d* signifies the distance from the sample [30,289]. This rapid attenuation results in a pronounced electric field gradient at the tip apex. Our calculation provides strong evidence that the pronounced electric field gradient possesses the capacity to activate new modes from the gradient field Raman (GFR) term as defined in Equation 4.2. Consequently, when conventional IR-active modes are affected by changes in polarizability due to the GFR effect, they become more likely to manifest as Raman-active peaks. The preference for IR modes arises from the interplay between electric field gradients, molecular dipole moments, and polarizability, which collectively enhance the probability of observing IR-active vibrations as Raman peaks in TERS spectra. The IR modes of $BaTiO_3$ nanoparticles from different references are detailed in Table 4-2, and are consistent with our experimental results in the near-field spectrum. For instance, the

peak at 1263 cm^{-1} corresponds to the bending vibration of oxygen atoms in the $BaTiO_3$ lattice, belonging to the A_1 mode symmetry group that traditionally renders the lattice 'Raman inactive' [290]. The 1449 cm^{-1} and 1550 cm^{-1} peaks belong to the E symmetry group and culminate from the vibrations involving in- and out-of-phase stretching of oxygen atoms, respectively [291].

Table 4-2: Infrared modes observed on $BaTiO_3$ nanoparticles with carbonate surface contamination

Wavenumber (cm^{-1})		Vibrational Modes	Ref.
553		Ti-O	[292]
694	Very weak	(CO_3^{2-})	[291]
858			
1059			
1445			
1639			
1260		C=O stretching in COO-Ba	[290]
1449		$BaCO_3$	[291]
1563		$\nu(COO^-)$	[291]

The interaction between the intense electric field gradients and the crystal lattice vibrations disrupts the symmetry constraints that once rendered these modes Raman inactive. This augmented interaction effectively bridges the gap between traditionally inactive IR modes and their visibility through the Raman scattering process, leading to the emergence of well-defined peaks within the TERS spectrum. The experimental achievements emphasize the extraordinary sensitivity of TERS to localized electric field gradient. Such notable advancement not only enhances our comprehension of material vibrational dynamics but also amplifies TERS' analytical capabilities, which in turn opens avenues for additional chemical and structural information from the sample, as in the case of the activation of infrared modes in near-field Raman spectroscopy. At this point, we would like to mention the possibility that these modes are a consequence of an organic contamination that gets amplified by the TERS setup. Such contaminations have commonly been reported on gold surfaces, however, in our case, we do not see these modes on the bare gold surface and it would require a high binding selectivity to a relatively passive barium titanate surface to explain the results presented in Figure 4.7.

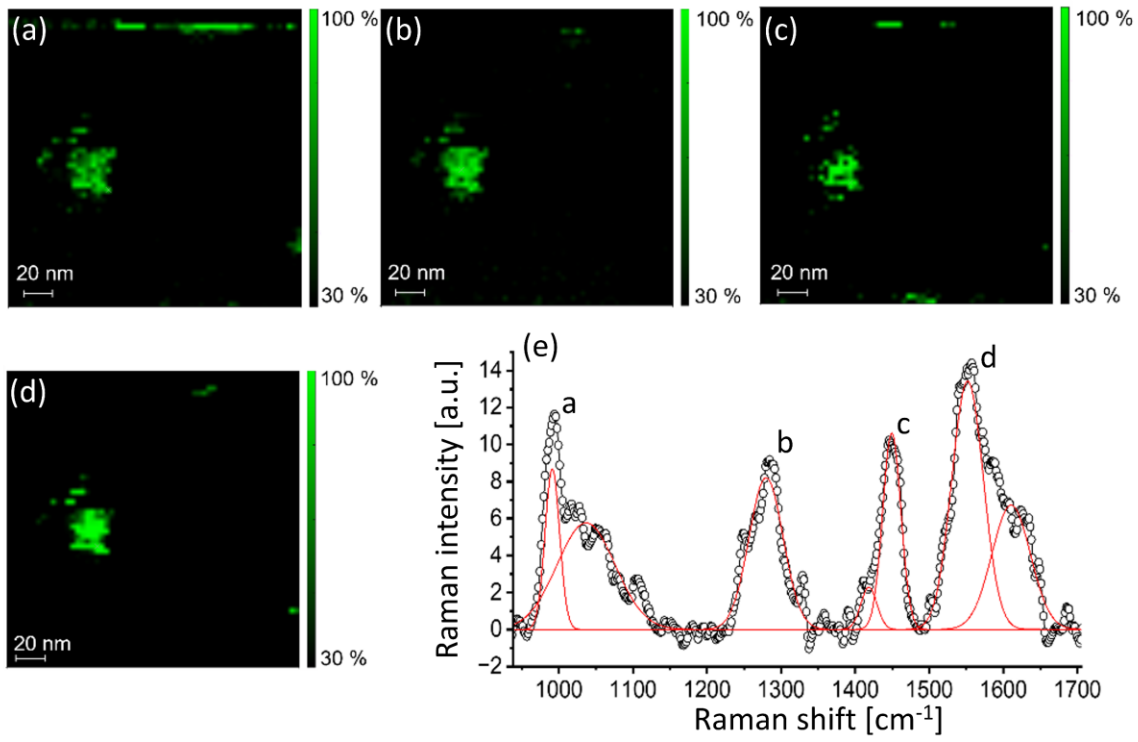

Figure 4.7: TERS map of a $BaTiO_3$ nanoparticle on gold in a 200 nm x 200 nm region, captured by a 60 x 60 pixels array . The signal intensity was integrated across distinct spectral ranges: (a) carbonate peak, (b) 1260 cm^{-1}, (c) 1449 cm^{-1}, and (d) 1550 cm^{-1}. The color bars indicate intensity levels, bounded by the minimum and maximum values with 0% representing the dark-count of the CCD. (e) Cumulative Raman spectrum of the 200 nm x 200 nm region.

4.2.1.1 High spatial resolution TERS maps of carbonate and infrared modes

Figure 4.7 displays the TERS maps over the Raman mode at 1060 cm^{-1} as well as new modes emerging from GFR effects on $BaTiO_3$ nanoparticles. The maps reveal the presence of carbonate at the location of the $BaTiO_3$ nanoparticle, which indicates chemisorption through a surface reaction with atmospheric CO_2. While theory predicts predominant binding of CO_2 to the BaO-terminated surface, the interaction between the Ti^{3+} ions, oxygen vacancies, and CO_3^{2-} ions has also been suggested to facilitate the segregation of $BaCO_3$ as these defects can potentially act as nucleation sites [293]. The carbonate ion, CO_3^{2-} bonded to Ba^{2+} has the D3h symmetry [294] with four (4) main asymmetric peaks between 900 and 1700 cm^{-1} (see Figure 4.7 (e)). Although, the characteristic Raman peak of CO_3^{2-} corresponding to the symmetric stretching vibrations reported here is located at ~1060 cm^{-1}, this band position differs across literature [291,295,296]. While the variation is typically ±6 cm^{-1}, such a difference in Raman shift is presumed to be caused by the interaction of moisture, i.e., H_2O with $BaTiO_3$ surface prior to the formation of the carbonate. The bending in- and out-of-plane vibrations in CO_3^{2-} are mostly IR active and appear at Raman

frequencies lower than 1000 cm^{-1} [294,296]. The peaks labelled *b, c* and *d* in Figure 4.7 (e) are both IR and Raman active and denote the asymmetric stretching vibrations of the carbonate. The carbonyl group designated by a carbon-oxygen double bond, C═O has stretching modes in the carboxylate salt, COO-Ba at 1263 cm^{-1} [290]. Generally, the carboxylate group is often negatively charged due to the donation of an electron pair from the oxygen to the carbon atom, which results in a resonance structure that stabilizes the charge distribution. Another characteristic Raman band of $BaCO_3$ structure is reflected by the asymmetric peak at 1449 cm^{-1}, which is deconvoluted into two peaks namely 1415±9 cm^{-1} and 1449±3 cm^{-1}. Although both are related to asymmetric vibrations of C═O, the former occurs in the bulk $BaCO_3$, whereas the latter occurs on the surface of the carbonate ion [68]. Their intensities are typically weak and depend on temperature [290]. The spectrum shows another prominent band at 1560±1 cm^{-1} with a shoulder at the higher frequency side (~1610±2 cm^{-1}), both of which are characteristics of asymmetric stretching vibrations of CO_3^{2-}. The presence of these IR-active modes is an indication that the CO_3^{2-} ion is antisymmetric. The undistorted carbonate ion is Raman active and has a fundamental signature at 1060±5 cm^{-1} due to the symmetrical trigonal planar structure of the three oxygen atoms with carbon atom. When distorted (i.e. either by charge distribution, defects etc.) they become less symmetric and this triggers the infrared activity [295]. The maps not only reveal the active Raman peaks but also extend to active infrared peaks — a new dimension of analysis enabling the detection of molecular species that elude the traditional Raman spectroscopy techniques.

4.3 Conclusions

Tip-enhanced Raman spectroscopy images of $BaTiO_3$ nanograins on a polycrystalline gold surface were obtained with a very pronounced enhancement of the tip, as we estimate contributions from gap-TERS to be relatively weak and as we may entirely rule out chemical enhancement. A few-tens-of-atoms-thick $BaTiO_3$ nanoparticles were synthesized by a microwave-assisted hydrothermal technique and crystalized in the tetragonal phase with a size distribution with sizes in the range of 10-50 nm as confirmed by TEM. TERS provides monolayer sensitivity and a spatial resolution of approximately 6.6 nm based on the Nyquist theorem. Its ability to detect Raman-forbidden and infrared (IR)-active modes made it possible to estimate a chemisorbed layer of $BaCO_3$, a common impurity originating from chemisorbed atmospheric CO_2. Our results demonstrate that TERS may activate non-active IR modes in the Raman response, thereby aiding the investigation of chemisorbed species on nanoscale surfaces and indicating distortions of chemisorbed molecules. The synergy between plasmonic enhancement and localized electric fields at the tip's apex resulted in a nanoscale spatial resolution with an electric

field enhancement factor at the apex of the tip close to 26. This implies that chemical modifications at the surface can be probed, thus opening avenues for applications in molecular surface chemistry in heterogeneous catalysis, semiconductor-based technology, and corrosion.

4.4 Experimental

4.4.1 Sample preparation

A 50 nm-thin sputtered gold film on a glass cover slip is utilized as the substrate. In order to reduce the surface roughness, the Au films were annealed at 500 °C for 1 minute under ambient atmosphere. The $BaTiO_3$ nanoparticles were hydrothermally synthesized from a homogeneous mixture of $Ti(OBu)_4$ and $Ba(OH)_2 \cdot 8H_2O$ solutions. Briefly, a 50 mM of $Ti(OBu)_4$ was dropped and stirred in 5 mL of ethanol. Thereafter, 75 mM of the barium salt was dissolved in preheated distilled water (>90 °C) and then gently added to the initial solution in the presence of H_2O_2 (2mL, 32% by volume) under constant stirring. H_2O_2 serves as a scavenger for residual hydroxyl groups that may deteriorate the electronic properties of barium titanate. A predetermined quantity of polyethylene glycol, PEG-8000 as surfactant was further added to the homogenously stirred solution before transferring to a 23 mL Teflon container. This Teflon container is then inserted into a polymer autoclave from Parr Instrument and then placed in a Panasonic Inverter microwave oven (2.45 GHz).

After microwave exposure (conditions: 360 W, 4 min), the reactor was allowed to cool down to room temperature and the resultant product was thoroughly washed in preheated distilled water and ethanol before drying under ambient atmosphere in an oven at 80 °C for 15 h. Subsequently, the dried $BaTiO_3$ nanoparticles were ultrasonically dispersed in ethanol (0.5 g/L) for 2 h prior to deposition onto the Au/glass substrates by spin-coating at 3000 rpm for 3 min. We would like to emphasize that both polyethylene glycol as well as PEG have a Raman signature that could possibly interfere with the optical near-field experiments. Therefore, after the rinsing in preheated distilled water and sonification in ethanol, we conducted far-field experiments on these nanopowders that are reported in Figure 3 (a) of reference [297] in which we did not find any evidence of residual contaminations, while the experiments were sufficiently sensitive to detect the presence of carbonate groups due to the large surface-to-volume ratio of the nanopowders.

4.4.2 Plasmonic tip fabrication

The plasmonic tips are produced by electrochemical etching of thermally pre-treated Au wires (Goodfellow, >99.99% purity) with a diameter of 100 µm. The Au wire, acting as the anode, is submerged ~1 mm into a 37% HCl solution (Sigma-Aldrich) and is connected to a waveform generator to apply a pulse sequence. In parallel, a gold ring with a diameter of around 20 mm is also immersed into the solution as the cathode. Voltage pulses of +4.5 V, 30 µs with a +0.5 V offset bias are applied to the tip with a frequency of 3 kHz, resulting in a duty cycle of 10% resulting in a smooth surface with typical tip radii ~10 nm, as depicted in scanning electron microscopy (SEM) images in Figure 3 of reference [298]. The comprehensive procedure is reported elsewhere [153].

4.4.3 Tip-enhanced Raman spectroscopy setup

We conduct TERS measurements under ambient conditions using an AIST-NT Omega Scope 1000 scanning probe, a NanoFinder 30 Raman spectrometer, and a thermoelectrically cooled Andor charge coupled device (CCD) detector. The Raman spectrometer is confocally combined with the atomic force microscope (SmartSPM, AIST-NT), laser excitation is achieved by a linearly polarized helium-neon laser (632.8 nm, TEM00). An optical neutral density filter of ND 0.5 results in an effective power of 1.5 mW on the sample. A Mitutoyo MPlan Apo 100× objective with a numerical aperture of 0.7 (0.7 NA) was implemented to focus on the tip via side access with an incident angle of 65°. The acquisition time of the spectral map is 1 second per pixel.

4.4.4 Characterization

The crystallographic structure of the powder is confirmed via x-ray diffraction (XRD). The XRD measurements were performed using a Bruker D8 Advance diffractometer equipped with a Cu K^{α} source (λ = 1.5406 Å) between $20° \leq 2\theta \leq 70°$. Complimentary bright field TEM images of the powder were acquired using a JEOL JEM-2100F transmission electron microscope. For this purpose, 2 mg of the powder was ultrasonically dispersed in ethanol prior to dip-coating unto Lacey carbon-coated Cu grids (LC400-Cu).

4.5 Acknowledgments

A.R. acknowledges funding from a CFI infrastructure grant, an NSERC Discovery Grant (No. RGPIN-2014-05024), and two NSERC strategic partnership grants (Nos. 506289-2017 and 506953-17).

4.6 Conflict of Interest

The authors declare no conflict of interest.

4.7 Supplementary information

ADVANCED MATERIALS INTERFACES
Open Access

Supporting Information

for *Adv. Mater. Interfaces*, DOI 10.1002/admi.202300993

Direct Observation of Carbonate Chemisorption on Barium Titanate Surfaces by Tip-Enhanced Raman Spectroscopy

*Mohammad Bakhtbidar, Ifeanyichukwu Amaechi, Andreas Dörfler, Alexandre Merlen and Andreas Ruediger**

Direct observation of carbonate chemisorption on barium titanate surfaces by tip-enhanced Raman spectroscopy

Observation directe de la chimisorption de carbonate sur les surfaces de titanate de baryum par spectroscopie Raman exaltée par pointe

Mohammad Bakhtbidar,[1] Ifeanyichukwu Amaechi,[1] Andreas Dörfler,[1] Alexandre Merlen,[2] and Andreas Ruediger [1,*]

[1]EMT-INRS (Centre Énergie Matériaux Télécommunications, Institut National de la Recherche Scientifique), Varennes, QC H2X 1E3, Canada

[2]MAPIEM (Matériaux Polymères Interfaces Environnement Marin), Université de Toulon, 83130 La Garde, France

*andreas.ruediger@inrs.ca

To establish that the peaks observed in the 1000 - 1700 cm^{-1} range are attributable to the activation of IR-modes rather than an organic contamination, Figure 4.8 displays the TERS spectra collected from five distinct points on a BaTiO3 nanoparticle. The consistency in peak intensity and location across these points favours the interpretation of a signature related to BaTiO3 and the carbonate monolayer rather than an organic contamination for which fluctuations of the intensity ratios would be expected.

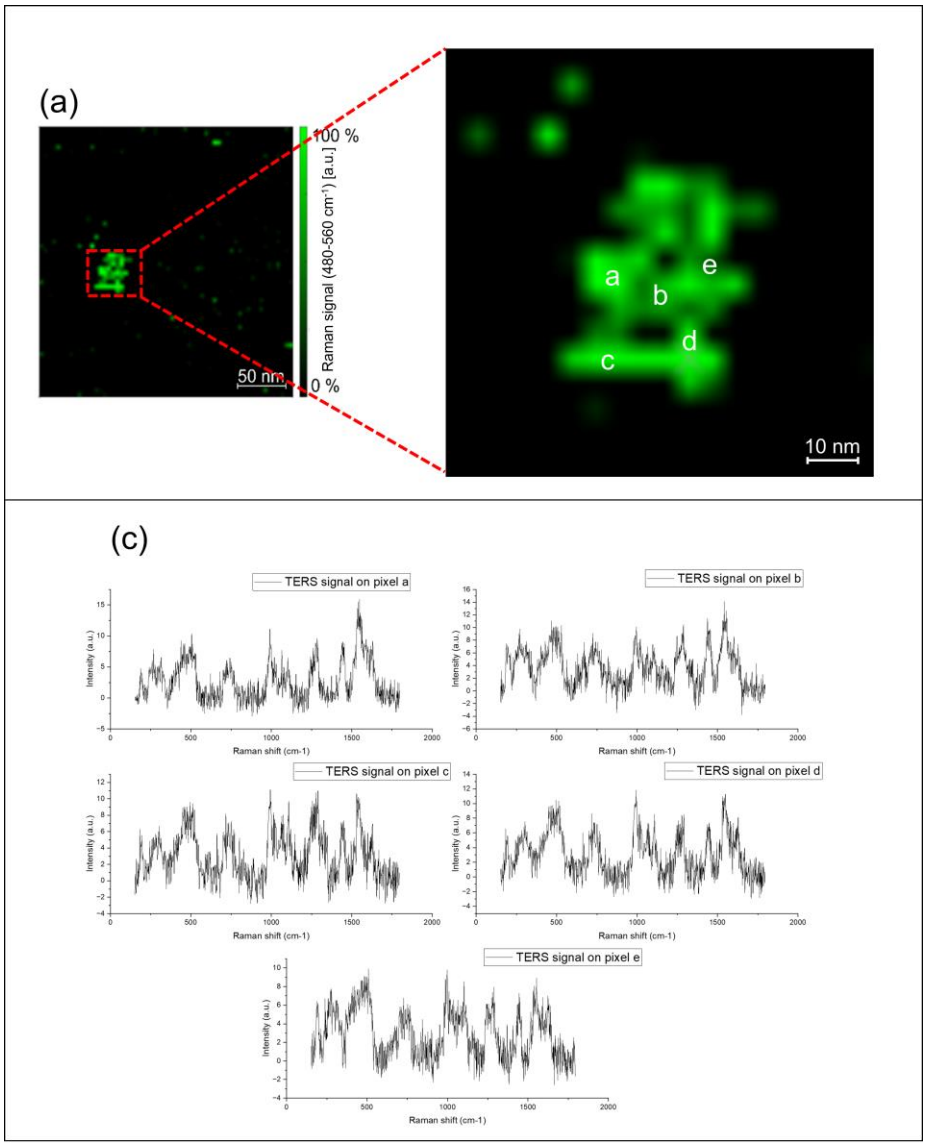

Figure 4.8: Controlling TERS spectrum collected from five distinct points on a BaTiO3 nanoparticle . (a) TERS map over a 200 nm x 200 nm region with 60 x 60 pixels on an individual barium titanate particle acquired over the 480 - 540 cm^{-1} spectral range. (b) Magnified visualization of the nanoparticle to accurately identify the selected pixels for spectrum analysis at those locations. (c) TERS spectrum across selected pixels to identify signals originating from carbonate adsorption on the $BaTiO_3$ nanoparticle.

5 ARTICLE II - SUPERPARAELECTRIC LIMIT IN INDIVIDUAL BARIUM TITANATE NANOPARTICLES

Optics Communications 591 (2025) 132058

Contents lists available at ScienceDirect

Optics Communications

journal homepage: www.elsevier.com/locate/optcom

Ferroelectric-to-paraelectric phase transition probing via high-resolution tip-enhanced Raman spectroscopy

Mohammad Bakhtbidar [a], Alexandre Merlen [a,b], Andreas Ruediger [a,*]

[a] EMT-INRS (Institut National de la Recherche Scientifique, Centre Énergie Matériaux Télécommunications), Varennes, QC, J3X 1P7, Canada
[b] MAPIEM (Matériaux Polymères Interfaces Environnement Marin), Université de Toulon, 83130, La Garde, France

ARTICLE INFO

Keywords:
Barium titanate
Localized surface plasmon resonance
Refractive index
Phase transition
Superparaelectric limit
Core-shell effect

ABSTRACT

Understanding the size-dependent phase transition in ferroelectric materials is essential for their integration into nanoscale electronic and energy-storage or -conversion applications. In this study, we utilize high-resolution tip-enhanced Raman spectroscopy (TERS) to investigate phase transitions in individual barium titanate ($BaTiO_3$) nanoparticles with diameters of approximately 20 nm and 40 nm close to the superparaelectric limit. Mapping localized surface plasmon resonance (LSPR) shifts and Raman vibrational modes, we identify a transition from ferroelectric to paraelectric phase in individual nanoparticles. The Raman peaks at 306 cm^{-1} and 720 cm^{-1}, characteristic of tetragonality in $BaTiO_3$, show significant intensity reduction in an 18 nm nanoparticle, indicating a suppression of ferroelectricity due to finite-size effects. LSPR mapping reveals a red-shift of approximately 7 nm, corresponding to a refractive index change of ~0.11, consistent with the bulk ferroelectric-to-paraelectric transition. Near-field imaging further confirms a core–shell structure, where the core retains ferroelectricity while the shell transitions to the paraelectric phase. These insights provide a deeper understanding of size-dependent ferroelectricity and offer a promising approach for advancing ferroelectric nanodevices.

1. Introduction

Tailoring the size of ferroelectrics is an essential approach for the development of advanced materials based on polar ordering in applications such as non-volatile memories, pyroelectric sensors, and piezoelectric devices [1–3]. At reduced dimensions, deviations from bulk behavior are expected as surface effects dominate over bulk effects, leading to changes in material properties and potential crystallographic transitions. This does not only lead to changes (decreases) in phase transition temperatures as a function of size and as a result to largely modified properties, even the nature of phase transitions has been reported to shift from 1st to 2nd order as the size shrinks [4].

Ferroelectricity is a fundamental property of certain materials characterized by the presence of spontaneous electric polarization, which can be reversed by an external electric field. This effect occurs due to the relative displacement of positively and negatively charged sublattices in an ionic crystal, such as barium titanate ($BaTiO_3$), which leads to spontaneous electric polarization. However, at the nanoscale, the stability of ferroelectric domains is significantly altered due to enhanced surface effects and electrostatic interactions.

Following Kittel's law, for a decreasing dimension along the polar axis, ever narrower domains occur in order to minimalize the electric field energy due to the spontaneous polarization. Single-domain structures in nanoparticles are therefore rather unstable unless the lateral dimension is substantially smaller than the expected domain width. For very small nanoparticles, typically in the range of a few tens of nanometers, the spontaneous polarization is no longer sustained, it irrevocably ceases below a critical size referred to as the superparaelectric limit [5]. Theoretical models [6–8] and experimental studies [9] have investigated this size-dependent phase transitions, but most experimental approaches so far fall into one of the following two categories: One common approach is the investigation on an ensemble of nanoparticles in e.g. powders or ceramics. Under these conditions, two challenges occur. For one, the dependence of the phase transition on the particle size is highly non-linear and even narrow particle size distributions tend to blur the nature of the underlying physics. For the other, as long as the nanoparticles are close together, they are electrostatically and possibly even mechanically coupled as e.g. observed through the

This article is part of a special issue entitled: Advances in Chemical Imaging published in Optics Communications.
* Corresponding author.
E-mail address: andreas.ruediger@inrs.ca (A. Ruediger).

https://doi.org/10.1016/j.optcom.2025.132058
Received 18 February 2025; Received in revised form 30 May 2025; Accepted 2 June 2025
Available online 2 June 2025
0030-4018/© 2025 Published by Elsevier B.V.

Ferroelectric-to-Paraelectric Phase Transition Probing via High-Resolution Tip-Enhanced Raman Spectroscopy

Exploration de la transition de phase ferroélectrique–paraelectrique par spectroscopie Raman exaltée par pointe à haute résolution

Mohammad Bakhtbidar,[1] Alexandre Merlen,[2] and Andreas Ruediger [1,*]

[1]EMT-INRS (Centre Énergie Matériaux Télécommunications, Institut National de la Recherche Scientifique), Varennes, QC H2X 1E3, Canada

[2]MAPIEM (Matériaux Polymères Interfaces Environnement Marin), Université de Toulon, 83130 La Garde, France

*andreas.ruediger@inrs.ca

Publication: Optics Communications, 132058, (2025): doi: 10.1016/j.optcom.2025.132058

Published: 02 June 2025

Author Contributions: The initial concept of investigating the superparaelectric limit in ferroelectric materials using tip-enhanced Raman spectroscopy (TERS) was proposed by AR. MB developed the experimental methodology, including sample preparation, TERS tip fabrication, and performed all measurements. M.B. also conducted the data analysis and interpretation. AM and AR supervised the project and provided scientific guidance throughout its development. AM contributed specifically to the consultation on Raman spectroscopy and the interpretation of vibrational modes. The first draft of the manuscript was prepared by MB, and all authors participated in revising the text and approved the final version. Financial support for the project was provided by AR.

Abstract: Understanding the size-dependent phase transition in ferroelectric materials is essential for their integration into nanoscale electronic and energy-storage or -conversion applications. In this study, we utilize high-resolution tip-enhanced Raman spectroscopy (TERS) to investigate phase transitions in individual barium titanate ($BaTiO_3$) nanoparticles with diameters of approximately 20 nm and 40 nm close to the superparaelectric limit. Mapping localized surface plasmon resonance (LSPR) shifts and Raman vibrational modes, we identify a transition from ferroelectric to paraelectric phase in individual nanoparticles. The Raman peaks at 306 cm^{-1} and 720 cm^{-1}, characteristic of tetragonality in $BaTiO_3$, show significant intensity reduction in an 18 nm nanoparticle, indicating a suppression of ferroelectricity due to finite-size effects. LSPR mapping reveals a red-shift of approximately 7 nm, corresponding to a refractive index change of ~0.11, consistent with the bulk ferroelectric-to-paraelectric transition. Near-field imaging further confirms a core–shell structure, where the core retains ferroelectricity while the shell transitions to the paraelectric phase. These insights provide a deeper understanding of size-dependent ferroelectricity and offer a promising approach for advancing ferroelectric nanodevices.

Keywords: barium titanate, localized surface plasmon resonance, refractive index, phase transition, superparaelectric limit, core-shell effect.

5.1 Introduction

Tailoring the size of ferroelectrics is an essential approach for the development of advanced materials based on polar ordering in applications such as non-volatile memories, pyroelectric sensors, and piezoelectric devices [190,299,300]. At reduced dimensions, deviations from bulk behavior are expected as surface effects dominate over bulk effects, leading to changes in material properties and potential crystallographic transitions. This does not only lead to changes (decreases) in phase transition temperatures as a function of size and as a result to largely modified properties, even the nature of phase transitions has been reported to shift from 1st to 2nd order as the size shrinks [301].

Ferroelectricity is a fundamental property of certain materials characterized by the presence of spontaneous electric polarization, which can be reversed by an external electric field. This effect occurs due to the relative displacement of positively and negatively charged sublattices in an ionic crystal, such as barium titanate ($BaTiO_3$), which leads to spontaneous electric polarization. However, at the nanoscale, the stability of ferroelectric domains is significantly altered due to enhanced surface effects and electrostatic interactions.

Following Kittel's law, for a decreasing dimension along the polar axis, ever narrower domains occur in order to minimalize the electric field energy due to the spontaneous polarization. Single-domain structures in nanoparticles are therefore rather unstable unless the lateral dimension is substantially smaller than the expected domain width. For very small nanoparticles, typically in the range of a few tens of nanometers, the spontaneous polarisation is no longer sustained, it irrevocably ceases below a critical size referred to as the superparaelectric limit [94]. Theoretical models [302–304] and experimental studies [6] have investigated this size-dependent phase transitions, but most experimental approaches so far fall into one of the following two categories: One common approach is the investigation on an ensemble of nanoparticles in e.g. powders or ceramics. Under these conditions, two challenges occur. For one, the dependence of the phase transition on the particle size is highly non-linear and even narrow particle size distributions tend to blur the nature of the underlying physics. For the other, as long as the nanoparticles are close together, they are electrostatically and possibly even mechanically coupled as e.g. observed through the continuity of domain walls across grain boundaries. Ensemble-based investigations have therefore been replaced by attempts to investigate individual grains. First experiments in this regard were conducted by Roelofs et al. [7] based on piezoresponse force microscopy. In

their study, the absence of a detectable piezoresponse in very small grains was interpreted as a signature of the superparaelectric phase. Apart from the fact that it is problematic anyways to interpret negative findings, future investigations highlighted the importance of the point contact between sample and atomic force microscopy probe and the difficulty to control it. The experience from these techniques calls for experiments that do not rely on a physical contact with the sample under investigation.

More recently, transmission electron microscopy has provided additional insight into the polar ordering near the size-induced phase transition [305]. While the atomic resolution of these images is unrivalled, the sample is exposed to ultrahigh vacuum conditions and a dense flow of electrons with partially inelastic interactions. Although any investigation at the nanoscale tends to be partially invasive, the approach of an optical near-field as suggested in this study offers the opportunity to balance between the signal-to-noise ratio and undesired effects through e.g. laser-induced heating. The latter has been demonstrated to be in the range of a few Kelvin for non-resonant Raman conditions, i.e. those without absorption through the sample and in the presence of surface water as it is the case here [306].

Research into ferroelectric thin films has garnered significant attention due to their relevance in integrated electronics, when e.g. Fong et al. demonstrating that lead titanate films maintain ferroelectric polarization even at thicknesses as small as 1.2 nm, corresponding to just three unit cells [8]. However, the ferroelectric behavior of individual nanocrystals at the nanoscale remains an open question [307–310]. In particular, it remains unclear at which size the superparaelectric limit occurs and how it depends on different environmental factors [311–315]. Investigations of isolated ferroelectric nanoparticles within the 10–100 nm range are relatively limited, as their ferroelectric properties are highly sensitive to factors such as composition, structural defects, and strain [316–318]. The purpose of this manuscript is not to provide a comprehensive answer to these questions but to rather indicate that optical near-field investigation is an appropriate tool for this endeavor.

In $BaTiO_3$, a well-known perovskite, ferroelectricity stems from the displacement of Ti atoms from their symmetric equilibrium positions within the unit cell structure counterbalanced by a smaller opposite displacement of the “equatorial” oxygen ions of the octahedral configuration. The main polarization originated from the displacement of the titanium ions that provide long-range electrostatic coupling, while the smaller offset of the oxygen ions provides a short-range

mechanical coupling between adjacent unit cells perpendicular to the polar axis. As the dimensions of $BaTiO_3$ crystals decrease, their ferroelectricity and crystallographic transitions have been extensively studied [319–321], though results often vary due to dependencies on synthesis methods and experimental conditions. Investigations of $BaTiO_3$ single crystals confined to dimensions below 70 nm have revealed both bulk-like behavior and unique domain structures [322,323]. It has also been observed that effects once attributed to size-dependent phenomena were previously thought to be often externally influenced, arising from factors such as oxygen vacancy distributions, grain boundaries , lattice strain, and surface modifications [324].

Previous research has primarily examined structural and electronic characteristics of $BaTiO_3$ through various methods, including Raman spectroscopy [316] and X-ray diffraction [221,321]. More advanced approaches, including electron holography [321] , have been employed; however, direct investigations of individual $BaTiO_3$ nanoparticles smaller than 50 nm remain unexplored. Early XRD studies of $BaTiO_3$ nanocrystals by Tanaka and subsequent work by Hoshina et al. [221] indicated that the outer regions tend to relax into a paraelectric, cubic phase, while the inner core retains its ferroelectric, tetragonal phase. As the nanocrystal size decreases, surface effects dominate, eventually suppressing ferroelectricity. Raman spectroscopy has been extensively applied to analyze structural phase transformations in bulk materials, nanostructures, and ultrathin layers, often focusing on the transition temperature (T_c) [325]. However, traditional techniques like XRD and Raman scattering average over the surface and interior of nanocrystals, making them insensitive to surface-specific effects additionally the sensitivity and resolution of these techniques is not sufficient to probe individual nanoparticles [326–328].

Scanning probe microscopy provides critical insights into the properties of ferroelectric surfaces, offering high spatial resolution for analyzing surface potential and electromechanical properties [329–332]. However, this method does not directly provide detailed chemical and structural information about the material. To address questions about nanoscale ferroelectricity and phase transitions, it is essential to employ methods capable of simultaneously probing surface polarization and phase-sensitive vibrational modes at high spatial resolution. The present study utilizes tip-enhanced Raman spectroscopy (TERS) to investigate vibrational modes and change of the refractive index associated with the size-driven phase transition, relying on gold tips as plasmonic probes on the $BaTiO_3$ nanoparticles.

Recent advances in TERS have considerably expanded its applicability to nanoscale investigations of both molecular and crystals structures. Kang et al. [333] demonstrated single-molecule hyperspectral TERS imaging at room temperature through molecular immobilization, enabling detection of conformational heterogeneity. Berweger et al. [117] utilized phonon-mode TERS to map local structural variations in $BaTiO_3$ nanocrystals, establishing optical nanocrystallography with sub-20 nm resolution. Building on these developments, we previously employed TERS to detect carbonate chemisorption on $BaTiO_3$ surfaces, revealing vibrational signatures inaccessible to conventional Raman spectroscopy [181]. Our lab-fabricated tips also enabled the observation of Raman-inactive modes via strong near-field enhancement. More recently, we used non-gap TERS to investigate self-delamination over the SrO-terminations of $SrTiO_3$ (100) surface, attributed to changes in surface binding energy caused by carbonate adsorption [181]. In the present work, we extend the application of TERS to probe size-dependent phase transitions in $BaTiO_3$ nanoparticles, combining high-resolution vibrational mapping with localized plasmon resonance tracking to explore symmetry breaking and dielectric contrast at the single-particle level.

TERS integrates Raman spectroscopy with scanning probe microscopy, where a laser is focused onto a plasmonic tip, generating localized surface plasmon resonance (LSPR). The TERS signal consists of far-field signal from sample and substrate, superimposed to a the near-field Raman signal from sample. In addition to this, for our case, we also observe a faint luminescence from the plasmonic tip that is amplified by a contribution of the localized surface plasmon resonance [180,334]. Among these, the near-field Raman signal and LSPR are critical for nanoscale resolution and sensitivity to probe the properties of materials. The near-field signal is enhanced by the highly localized electric field at the tip apex, interacting with the sample surface and enabling the detection of Raman vibrational modes as well as infrared modes in some cases, due to the strong electric field gradient at the tip apex [181,335]. The LSPR signal is influenced by the refractive index surrounding the TERS tip, which is mainly air and whatever material is within the optical nearfield. Within the 480–800 nm spectral range, the permittivity of gold (ε_r) can be described as a linear function of wavelength (λ) using the equation [336–338]:

$$\varepsilon_r = -0.07\lambda + 32$$

where ε_r represents the real component of the permittivity, and λ denotes the wavelength in nanometers. Under resonant conditions, this permittivity is directly linked to the effective refractive

index (n) of the medium in proximity to the tip apex, as described by the following equation, neglecting losses [339]:

$$\varepsilon_r = -2n^2$$

From these equations, it follows that during a TERS experiment, the position of the LSPR depends on the effective refractive index of the surrounding environment. With a relatively small birefringence at room temperature, there is a tangible difference between the ordinary and extraordinary refractive index of the tetragonal 4mm structure and the cubic phase [340,341]. In bulk $BaTiO_3$, this results in an approximate increase of 0.1 units in refractive index for the cubic phase, causing a significant red-shift in the plasmon absorption peak of gold tip above the $BaTiO_3$ nanoparticle [74,75].

We now demonstrate how precise this optical near-field approach is investigate size effects of $BaTiO_3$ nanoparticles based on the localized surface plasmon resonance (LSPR) and near-field Raman spectroscopy. TERS measurements reveal distinct phase-dependent behaviors for two individual nanoparticles, the 44 nm $BaTiO_3$ nanoparticles exhibit characteristics of the ferroelectric phase, whereas the 18 nm particles display paraelectric properties. By mapping the LSPR shift of gold tip across $BaTiO_3$ surfaces, we identify strong correlations between changes in permittivity due to phase transitions and variations in LSPR intensity. Furthermore, the Raman peaks at 306 cm^{-1} and 720 cm^{-1}, intrinsically linked to the tetragonality of $BaTiO_3$, demonstrate a significant intensity decrease due to the size effect. High-resolution near-field imaging further provides critical insights into this size effect, unveiling a phase transition within the 18 nm $BaTiO_3$ and the existence of two different grains within the nanoparticle with an apparent height of 44 nm. These findings highlight the excellent spatial resolution of TERS (albeit not as high as for transmission electron microscopy) in resolving nanoscale phase transitions and underscore its value for in-depth structural and refractive index analysis in nanoscale ferroelectrics.

5.2 Experimental

5.2.1 Sample preparation

A 50 nm gold film was deposited onto a glass cover slip via radiofrequency sputtering. To obtain a crystalline and smooth surface, the film was annealed at 500°C for 1 minute under ambient conditions. $BaTiO_3$ nanoparticles were synthesized using a hydrothermal method from a

homogeneous mixture of titanium butoxide ($Ti(OBu)_4$) and barium hydroxide octahydrate ($Ba(OH)_2 \cdot 8H_2O$). Specifically, 50 mM of $Ti(OBu)_4$ was dissolved in 5 mL of ethanol under continuous stirring. Separately, 75 mM of $Ba(OH)_2 \cdot 8H_2O$ was dissolved in preheated distilled water (>90°C) and subsequently introduced into the titanium solution along with 2 mL of 32% H_2O_2 under steady stirring. H_2O_2 functioned as a scavenger for residual hydroxyl groups, thereby preserving the insulating properties of $BaTiO_3$.

A surfactant, polyethylene glycol (PEG-8000), was incorporated into the mixture before it was transferred to a 23 mL Teflon container inside a polymer autoclave. The container was then subjected to microwave heating at 360 W for 4 minutes in a 2.45 GHz Panasonic Inverter microwave oven. Following the microwave treatment, the mixture was allowed to cool to room temperature, after which the synthesized $BaTiO_3$ nanoparticles were thoroughly rinsed with preheated distilled water and ethanol. The washed nanoparticles were subsequently dried at 80°C for 15 hours in an oven to remove any remaining solvents. The dried $BaTiO_3$ nanoparticles were ultrasonically dispersed in ethanol (0.5 g/L) for 2 hours and spin-coated onto Au/glass substrates at 3000 rpm for 3 minutes. To ensure no residual contaminants, particularly PEG, interfered with optical near-field experiments, far-field Raman experiments were performed on the nano powders to confirm the absence of residuals, as reported in Figure 3 (a) of reference [297]. These measurements demonstrated that the samples were free from residues of the synthesis, allowing accurate detection of surface groups such as carbonates, which are highly sensitive due to the large surface-to-volume ratio of the nanopowders.

5.2.2 Plasmonic tip fabrication

Plasmonic tips were fabricated through an electrochemical etching process using gold wires of high purity (>99.99%, Goodfellow) with a diameter of 100 µm. The gold wire, acting as the anode, was immersed approximately 1 mm into a 37% hydrochloric acid solution (Sigma–Aldrich) and connected to a waveform generator programmed with a predefined pulsing sequence [298]. A gold ring, approximately 20 mm in diameter, served as the cathode and was fully submerged in the solution. The etching process involved voltage pulses of +4.5 V with a duration of 30 µs and a +0.5 V offset bias at a frequency of 3 kHz, maintaining a 10% duty cycle. This method produced tips with smooth surfaces and apex radii of around 10 nm, as verified by scanning electron microscopy (SEM) in Figure 5.1. Previous studies [43] have demonstrated that the electric field at the apex of these tips can reach approximately 3×10^8 V/m, leading to a significant enhancement

of the local field on the material surface. This confined field, localized at the nanoscale near the tip apex, ensures exceptionally high spatial resolution for near-field optical measurements.

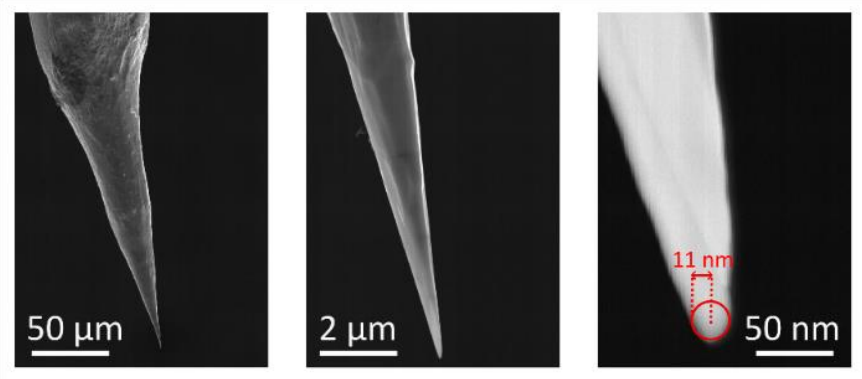

Figure 5.1: SEM images of a tip fabricated via pulsed electrochemical etching.

5.2.3 Tips-enhanced Raman spectroscopy setup

Near-field measurements were conducted under ambient conditions using an AIST-NT OmegaScope 1000 system coupled with a NanoFinder 30 Raman spectrometer and a thermoelectrically cooled Andor iDUS CCD detector. The excitation source was a linearly polarized helium-neon laser (632.8 nm, TEM00) with the polarization pointing between the tip and the surface. The laser beam, with an intensity of approximately 10 mW, was focused onto a gold tip affixed to a tuning fork operating in shear-force feedback mode. A Mitutoyo MPlan Apo 100× objective (NA 0.7), tilted at 65°, was employed for focusing. The tip-sample distance was maintained at approximately 1 nm to ensure effective near-field enhancement. Spectral mapping was performed with an exposure time of 1 second per pixel, allowing for high-resolution spatial and spectral imaging.

5.3 Results and discussion

The structural properties of the $BaTiO_3$ powder were analyzed through X-ray diffraction (XRD) using a Bruker D8 Advance diffractometer with Cu Kα radiation (λ = 1.5406 Å) over a 2θ range of 20° to 70°. Figure 5.2 presents the XRD pattern typical of $BaTiO_3$ nanoparticles, which aligns well with the reference data (JCPDS card #: 01-089-1428). A prominent peak observed at 2θ = 31.65° corresponds to the (101) diffraction plane, confirming the high crystallinity and tetragonal structure of the material [273]. However, an additional peak at 2θ = 24.1° indicates the presence of carbonate contamination, which likely results from the strong surface reactivity of $BaTiO_3$

nanoparticles with atmospheric CO_2 on BaO-terminated facets [69]. The tetragonal phase of $BaTiO_3$ can be distinguished from the cubic phase by the characteristic splitting of the peak near $2\theta \approx 45°$ into the (002) and (200) planes. This splitting refle cts the anisotropic lattice distortion, with the c-axis being longer than the a-axis [275]. For nanoscale tetragonal particles, however, this splitting is often masked by peak broadening due to the Debye–Scherrer effect, making it less discernible.

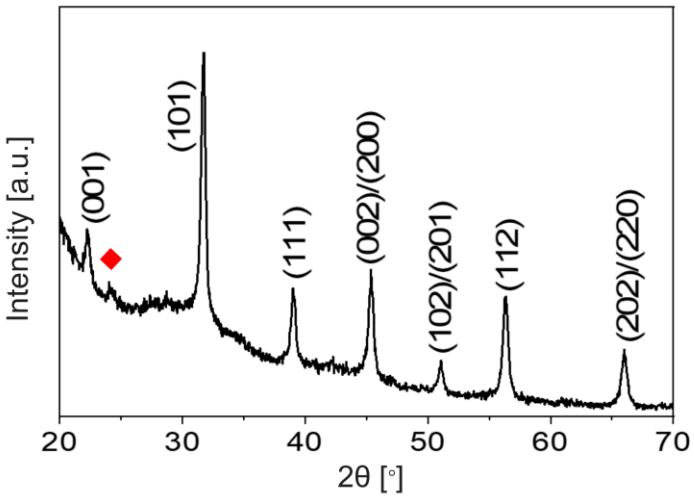

Figure 5.2: XRD pattern of the synthesized $BaTiO_3$ nanoparticles, the symbol "♦" marking the peak associated with carbonate adsorption.

The topography of the $BaTiO_3$/Au/Si sample shows what initially appears to be two nanoparticles with approximate heights of 44 nm and 18 nm deposited on the gold substrate, as demonstrated in Figure 5.3. Confocal Raman measurements, performed over the confocal, diffraction-limited area of approximately 1 μm^2, does not yield a detectable Raman signal even for integration times of 60 s (refer to the Figure 5.8 in supporting information). This absence is attributed to the inherently weak non-resonant Raman scattering cross-section combined with the limited sample volume.

A simultaneously scanned near-field intensity map over the 520 cm^{-1} peak, corresponding to the $BaTiO_3$ A1(TO3) mode, is presented in Figure 5.4. These measurements were performed using a gold tip, maintaining a precisely controlled distance over both the substrate and the $BaTiO_3$ nanoparticles. The intensity map over the A1(TO3) mode, precisely defines the spatial position of the barium titanate nanoparticles and exhibits a strong correlation with the topographic scan.

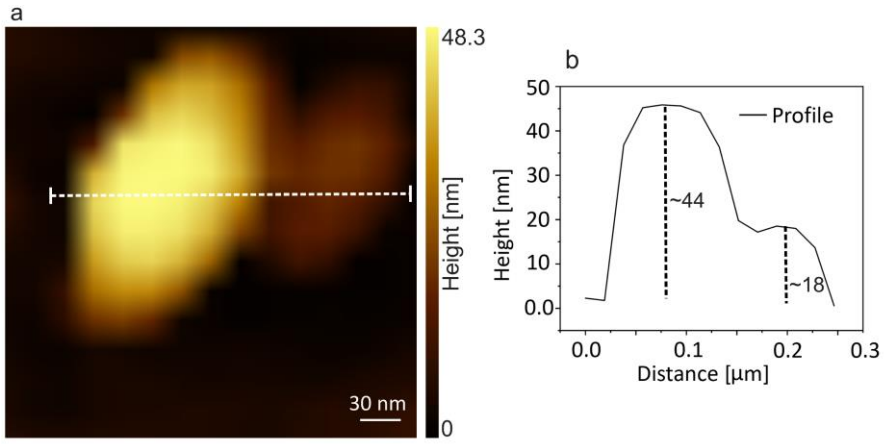

Figure 5.3: a) Shear-force mode scanning probe microscopy (SPM) image of a 300 nm × 300 nm area, 15 × 15 pixels, illustrating the presence of $BaTiO_3$ nanoparticles. b) The corresponding height profile extracted along the white dashed line in (a) shows the height of nanoparticles are approximately 44 nm and 18 nm. We rely on the height more than on the lateral dimension as the latter is convoluted with the tip-shape.

To generate the TERS maps in Figure 5.4 and Figure 5.5, spectral data at each pixel were preprocessed by applying a Savitzky–Golay filter for noise reduction, followed by baseline subtraction. The signal was then integrated over a narrow 20 cm^{-1} window centered on each target vibrational mode to enhance contrast. This approach isolates vibrational contributions from background fluctuations and allows for high-resolution spatial mapping, even when individual spectra display moderate signal-to-noise ratios.

To increase the signal-to-noise ratio (SNR), the near-field spectrum averaged across 3x3 pixels over each nanoparticles, is shown in Figure 5.5. The acquired spectrum comprises a combination of gold-enhanced luminescence and the near-field Raman signal originating from the $BaTiO_3$ nanoparticles. A small kink observed at 560 cm^{-1} arises from optical components within the system and does not correspond to any intrinsic vibrational modes of the sample. The distinct Raman peaks on both nanoparticles appear at 185, 270, 520 and 1062 cm^{-1}, corresponding to the A1(TO), A1(TO2), A1(TO3) and carbonate adsorption vibrational modes of $BaTiO_3$, respectively. To confirm that these Raman signature originate from the nanoparticles themselves and not from the substrate, we averaged TERS spectra over areas of the gold surface without any $BaTiO_3$ nanoparticles. The averaged spectrum from those pixels showed no identifiable $BaTiO_3$ vibrational signatures. These control data are provided in Figure 5.8 in the supporting information.

A comparative analysis between the spectra from both nanoparticles reveals a notable decrease in the intensity of the peaks at 306 cm^{-1} and 721 cm^{-1} in the smaller 18 nm nanoparticle. The 306 cm^{-1} peak is attributed to the B1+E(TO3+LO2) mode, which originates from the Ti-O bond stretching and bending vibrations in the tetragonal phase and is highly sensitive to structural distortions associated with ferroelectricity.

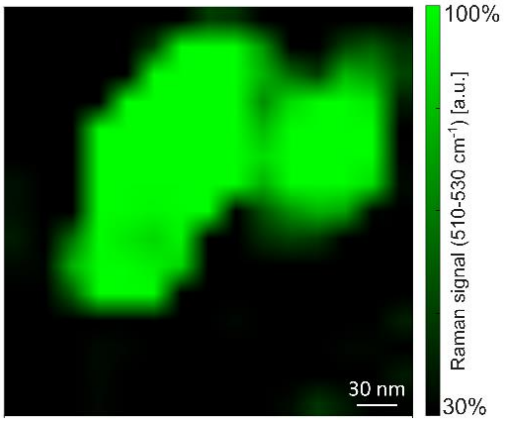

Figure 5.4: TERS intensity map obtained in the same region as Figure 5.3(a), showing a pronounced signal in the 510–530 cm^{-1} spectral range, corresponding to the A1(TO3) vibrational mode of $BaTiO_3$, specifically at the nanoparticle sites.

The 721 cm^{-1} peak corresponds to the A1(LO3+LO4) mode, primarily linked to Ti-O bond stretching along the c-axis of the tetragonal phase, making it another critical indicator of tetragonality in $BaTiO_3$. The stability of the ferroelectric phase in $BaTiO_3$ nanoparticles is significantly impacted by their size, as surface energy and depolarization fields contribute to destabilizing the tetragonal structure. The observed reduction in intensity of the 306 and 721 cm^{-1} Raman peaks suggests a diminishing tetragonality in the smaller nanoparticle, providing strong evidence for a size-dependent phase transition from the ferroelectric tetragonal phase to the paraelectric cubic phase.

The green line represents the fitted LSPR response over the nanoparticle. A comparison between the LSPR of the gold tip over the 18 nm and 44 nm nanoparticles reveals a distinct red-shift of approximately 165 cm^{-1} (~7 nm) as the particle size decreases. This observed shift toward longer wavelengths is a direct indication of a change in the refractive index. Considering the measured ~7 nm shift in LSPR and referencing prior simulations conducted by our group [343], which modeled LSPR shifts due to refractive index variations, we estimate that this shift corresponds to an approximate change of 0.11 in the refractive index. For the given height of the nanoparticles,

which substantially exceeds the depth of the optical near-field, this shift of the plasmon resonance may not be accounted for by the coupling of the gold tip to the gold surface.

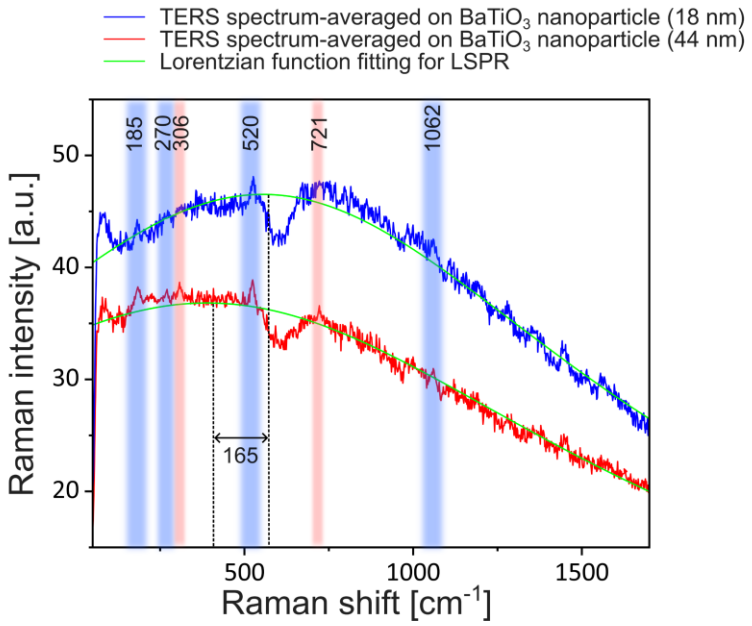

Figure 5.5: TERS spectra averaged over the $BaTiO_3$ nanoparticles, where the blue spectrum corresponds to the 18 nm nanoparticle and the red spectrum represents the 44 nm nanoparticle. The green curve illustrates the Lorentzian function fitting of the LSPR for both spectra. The black dashed line marks the center of the LSPR shift, indicating a LSPR shift of 165 cm^{-1} between two nanoparticle.

In bulk $BaTiO_3$, it is well-established that a refractive index increase of approximately 0.1 units occurs across the ferroelectric-to-paraelectric phase transition [74,75]. This change in high-frequency permittivity leads to a measurable red-shift in the localized surface plasmon resonance (LSPR) absorption peak of gold tip in the TERS measurement. Previous studies have estimated that the LSPR peak position of gold plasmonic nanoparticles, typically in the 500–700 nm wavelength range, exhibits a sensitivity of approximately 40–200 nm per unit change in the refractive index [344,345]. Considering the previous results and the LSPR shift over the nanoparticle we can conclude this shift is due to the phase transition from tetragonal to cubic phase arising from size effect.

To obtain deeper insights into the phase of the nanoparticles, near-field images taken over the Raman peaks at 306 cm^{-1} (B1+E(TO3+LO2)) and 720 cm^{-1} (A1(LO3+LO4)) are illustrated in Figure 5.6. The intensity of 306 and 720 cm^{-1} peaks shows a significant decrease for the smaller 18 nm nanoparticle and at the lower side of the 44 nm nanoparticle. The suppression of the 306

cm^{-1} and 721 cm^{-1} peaks in the Raman spectrum of the 18 nm nanoparticle indicates a transition to the paraelectric cubic phase, a phenomenon driven by finite-size effects that disrupt long-range dipole ordering. A similar behaviour is observed in the lower part of the 44 nm nanoparticle, where intensity variations point to the coexistence of two grains with distinct structural properties, and the lower side is near to the phase transition to the cubic phase. This may not be attributed to different domain orientations as the corresponding birefringence is insufficient to account for the observed LSPR shift.

Furthermore, a distinct increase in the intensity of 306 cm^{-1} and 721 cm^{-1} peaks at the central region of the smaller nanoparticle observed. Several theoretical models based on mean-field approximations suggest that ferroelectric nanoparticles exhibit a core–shell structure, where polarization gradients result in a ferroelectric core surrounded by a paraelectric shell [346–348]. Consequently, these increases in the intensity, which are characteristic of the tetragonal ferroelectric phase, suggests that the core retains its tetragonal ferroelectric character, while the outer shell undergoes a phase transition to the paraelectric state. This core–shell effect arises due to size-dependent constraints, which collectively influence the stability of the ferroelectric phase at reduced dimensions.

This observation is consistent with prior studies on lead titanate nano islands, conducted in our group, which demonstrate phase separation at grain boundaries, leading to the formation of a paraelectric shell surrounding a ferroelectric core [349]. Previous studies demonstrated that the peak position of the near-field enhanced gold emission at the tip apex provides a reliable measure of permittivity variations in the sample [334,337], as these changes directly influence the LSPR frequency [67,339]. Consequently, the observed shift in the gold luminescence peak is a direct indicator of localized refractive index modifications. This effect is mapped in detail, as shown in Figure 5.7, confirming the critical role of dielectric variations in nanoscale phase transitions.

As illustrated in Figure 5.7, the LSPR shift was mapped over the smaller nanoparticle and the lower grain region of the 44 nm nanoparticle. A distinct blueshift in the gold luminescence peak is observed when the tip transitions from the substrate to the nanoparticles, attributed to variations in permittivity distribution near the tip apex. These changes are influenced by topography and tip-substrate distance, where the effective refractive index sensed by the tip is primarily determined by the local dielectric environment rather than the full surrounding volume.

In both the 18 nm nanoparticle and the lower grain of the 44 nm nanoparticle, we consistently observe a red-shift of approximately 7 nm, from ≈649 nm to ≈656 nm, when moving from the larger nanoparticle to the smaller one. This shift is primarily attributed to a local change in refractive index associated with the ferroelectric-to-paraelectric phase transition where the cubic phase has a higher refractive index than either the ordinary or extraordinary index of the tetragonal phase. Tip-distance related effects due to an ever-so-small remainder of coupling between gold tip and gold surface, following the idea of gap-TERS even at these distances, should cause a blue shift of the LSPR in contrast to the observed red shift.

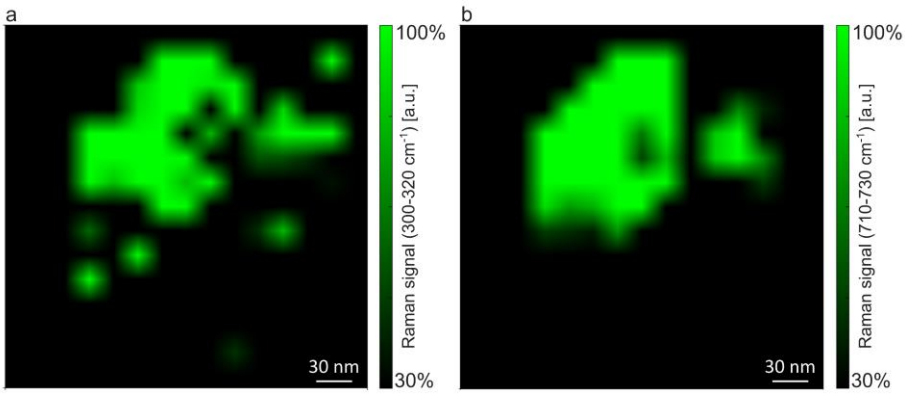

Figure 5.6: TERS maps of a 300 nm × 300 nm region containing $BaTiO_3$ nanoparticles , corresponding to the same area shown in Figure 5.3 (a). (a) Integration over the 306 cm^{-1} peak, associated with the (B1+E(TO3+LO2)) vibrational mode, and (b) integration over the 720 cm^{-1} peak, corresponding to the (A1(LO3+LO4)) mode. These vibrational modes are directly linked to the tetragonal phase of $BaTiO_3$, and their suppression indicates a phase transition from the tetragonal to the cubic phase. A noticeable decrease in intensity is observed over the lower side of the 44 nm nanoparticle (on the left), which suggests the presence of a grain boundary and potential phase inhomogeneities. The color bars represent intensity variations, normalized between the minimum and maximum detected values, with 0% corresponding to the CCD dark count.

Based on previous simulations performed in our group, which modeled LSPR shifts as a function of refractive index [343], we estimate that this red-shift corresponds to a refractive index change of approximately 0.11. Given that the reported refractive index variation across the ferroelectric-to-paraelectric phase transition in $BaTiO_3$ is approximately 0.1 [316], we conclude that this observed LSPR shift is directly associated with the phase transition from the tetragonal to the cubic phase, driven by the size-dependent stabilization of the paraelectric state. The observed 0.01 discrepancy in the refractive index derived from the LSPR shift compared to the reported value can be attributed to fitting uncertainties, as well as the impact of topographical variations and tip-sample distance fluctuations on the LSPR response. Additionally, the LSPR mapping exhibits a pronounced blueshift at the core of the 18 nm nanoparticle, as highlighted in Figure 5.6,

further supporting the presence of a core-shell structure. This finding suggests that while the nanoparticle's outer shell transitions into the paraelectric phase, the core remains in the ferroelectric state, reinforcing the size-dependent stabilization of distinct phase domains.

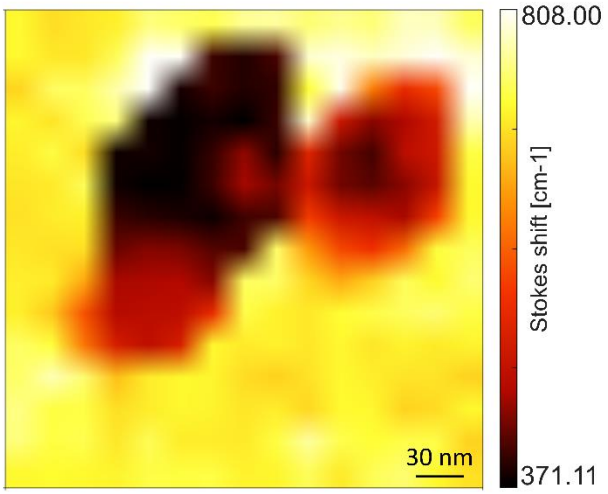

Figure 5.7: High-resolution map illustrating the LSPR shift on a $BaTiO_3$ nanoparticle, showing an approximate 7 nm red-shift over the 18 nm nanoparticle and the lower region of the 44 nm nanoparticle . This shift is attributed to a refractive index change of approximately 0.11, which correlates with the phase transition from the tetragonal to the cubic structure.

Our findings highlight the dynamics of the size-driven phase transition that nucleates on the surface, demonstrating the effectiveness of TERS in resolving nanoscale phase transitions with sufficient spatial resolution to discriminate the shell against the core.

5.4 Conclusion

In this study, we employed high-resolution tip-enhanced Raman spectroscopy to investigate the size-dependent phase transition in $BaTiO_3$ nanoparticles, focusing on the localized surface plasmon resonance (LSPR) shift and vibrational mode variations. By analyzing nanoparticles of 18 nm and 44 nm in diameter, we demonstrated a distinct correlation between nanoparticle size and ferroelectric-to-paraelectric phase transition, highlighting the role of finite-size effects on ferroelectric stability.

The Raman peaks at 306 cm^{-1} and 720 cm^{-1}, which are strongly associated with the tetragonal phase of $BaTiO_3$, exhibited a significant decrease in intensity for the 18 nm nanoparticle and in certain regions of the 44 nm nanoparticle. These findings are a direct observation for each individual nanoparticle and suggest that as the particle size decreases, depolarization fields and

surface energy effects promote indeed a structural transformation from the tetragonal ferroelectric phase to the cubic paraelectric phase. The presence of a core–shell structure, with a ferroelectric core surrounded by a paraelectric shell, was observed through near-field mapping, reinforcing theoretical predictions about polarization gradient stabilization at the nanoscale.

Additionally, LSPR mapping over the nanoparticle surface provided critical insights into the dielectric changes caused by the phase transition. A red-shift of approximately 7 nm in the gold luminescence peak, corresponding to a refractive index variation of 0.11, was observed for the smaller nanoparticle. This shift is in close agreement with the known refractive index change (~0.1) across the bulk $BaTiO_3$ phase transition, confirming the nanoscale stabilization of the paraelectric phase due to size effects. These results underscore the effectiveness of TERS as a powerful technique for characterizing phase transitions in nanostructured ferroelectrics with high spatial resolution. The ability to directly resolve LSPR shifts and vibrational mode variations at the nanoscale provides valuable insights into the interplay between crystallographic structure, dielectric properties, and local polarization effects. Our findings pave the way for further exploration of nanoscale ferroelectricity in functional materials and highlight the potential of TERS in advancing the design of next-generation electronic, sensing, and energy-storage devices.

5.5 Acknowledgments

A.R. acknowledges funding from a CFI infrastructure grant, an NSERC Discovery Grant (No. RGPIN-2014-05024), and two NSERC strategic partnership grants (Nos. 506289-2017 and 506953-17). The authors also express their gratitude to Ifeanyichukwu Amaechi and Julien Plathier for their valuable contributions in providing supplementary data.

5.6 Conflict of Interest

The authors declare no conflict of interest.

5.7 Supporting Information

Ferroelectric-to-Paraelectric Phase Transition Probing via High-Resolution Tip-Enhanced Raman Spectroscopy

Exploration de la transition de phase ferroélectrique–paraelectrique par spectroscopie Raman exaltée par pointe à haute résolution

Mohammad Bakhtbidar,[1] Alexandre Merlen,[2] and Andreas Ruediger [1,*]

[1]EMT-INRS (Centre Énergie Matériaux Télécommunications, Institut National de la Recherche Scientifique), Varennes, QC H2X 1E3, Canada

[2]MAPIEM (Matériaux Polymères Interfaces Environnement Marin), Université de Toulon, 83130 La Garde, France

*andreas.ruediger@inrs.ca

5.7.1 Control spectra for the validation of the TERS signal

Figure 5.8 presents control spectra that support the interpretation of the TERS results discussed in the main manuscript. Figure 5.8 (a) shows a TERS signal obtained by averaging over 9 pixels in the near-field map (refer to Figure 5.4 in the main manuscript), acquired directly on the gold substrate in a region free of $BaTiO_3$ nanoparticles. As evident from the spectrum, no vibrational features associated with $BaTiO_3$ are observed, confirming that the averaged TERS spectrum presented in Figure 5.5 of the main manuscript originates exclusively from the $BaTiO_3$ nanoparticles. The small feature near 560 cm^{-1} (kink) is an artifact arising from the optical setup and does not correspond to any material-specific vibrational mode.

Figure 5.8 (b) displays a confocal (far-field) Raman measurement collected from the $BaTiO_3$/Au/Si region using a diffraction-limited spot at 10 mW laser power with 20 s integration time. The measurement was performed in a standard backscattering geometry normal to the sample surface. Under these conditions, no Raman peaks attributable to $BaTiO_3$ are detectable. The only prominent feature is the ~520 cm^{-1} peak from the underlying Si substrate. This peak is not observed in the TERS spectra due to (i) the oblique collection angle (~65°) used in TERS, and (ii) the significantly lower laser power and shorter integration time used during near-field acquisition.

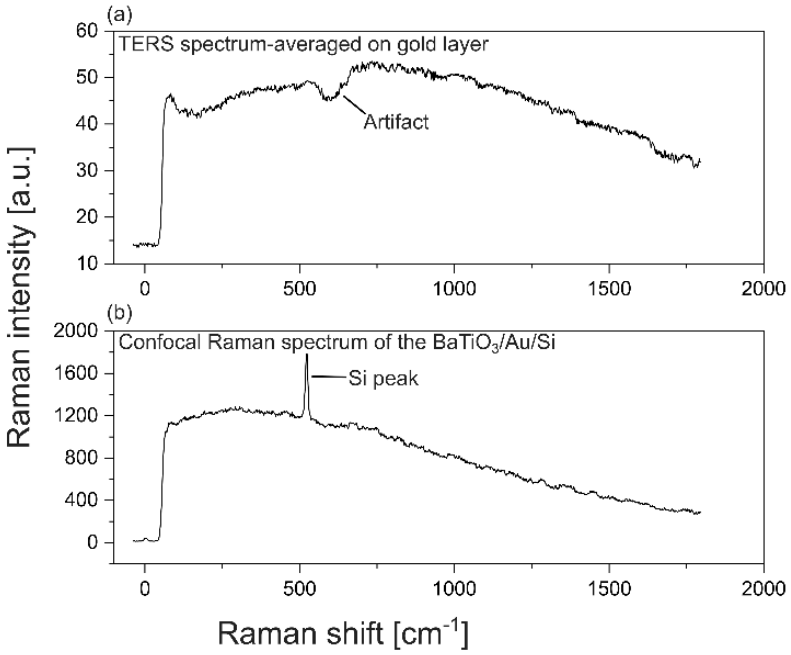

Figure 5.8: Control spectra supporting the TERS analysis . (a) Averaged TERS spectrum acquired on the gold substrate, showing no $BaTiO_3$-related signals. The negative peak near 560 cm^{-1} is an artifact from the optical setup. (b) Confocal Raman spectrum of the $BaTiO_3$/Au/Si sample, showing only the Si substrate peak at ~520 cm^{-1}. No $BaTiO_3$ modes are detected under far-field conditions.

6 RESEARCH ARTICLE III - CARBONATE ADSORPTION AND SURFACE SELF-CLEANING ON STRONTIUM TITANATE

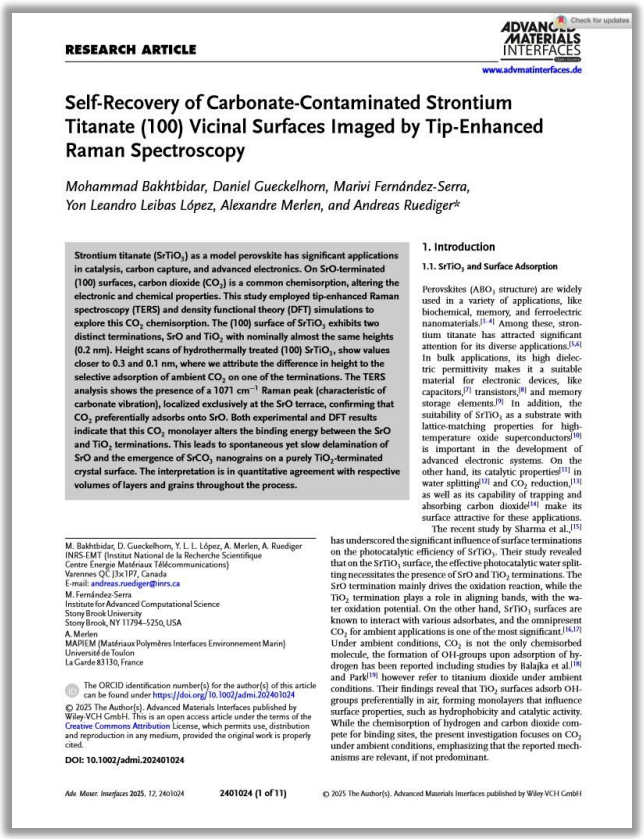

RESEARCH ARTICLE

ADVANCED MATERIALS INTERFACES

www.advmatinterfaces.de

Self-Recovery of Carbonate-Contaminated Strontium Titanate (100) Vicinal Surfaces Imaged by Tip-Enhanced Raman Spectroscopy

*Mohammad Bakhtbidar, Daniel Gueckelhorn, Marivi Fernández-Serra, Yon Leandro Leibas López, Alexandre Merlen, and Andreas Ruediger**

Strontium titanate ($SrTiO_3$) as a model perovskite has significant applications in catalysis, carbon capture, and advanced electronics. On SrO-terminated (100) surfaces, carbon dioxide (CO_2) is a common chemisorption, altering the electronic and chemical properties. This study employed tip-enhanced Raman spectroscopy (TERS) and density functional theory (DFT) simulations to explore this CO_2 chemisorption. The (100) surface of $SrTiO_3$ exhibits two distinct terminations, SrO and TiO_2 with nominally almost the same heights (0.2 nm). Height scans of hydrothermally treated (100) $SrTiO_3$, show values closer to 0.3 and 0.1 nm, where we attribute the difference in height to the selective adsorption of ambient CO_2 on one of the terminations. The TERS analysis shows the presence of a 1071 cm^{-1} Raman peak (characteristic of carbonate vibration), localized exclusively at the SrO terrace, confirming that CO_2 preferentially adsorbs onto SrO. Both experimental and DFT results indicate that this CO_2 monolayer alters the binding energy between the SrO and TiO_2 terminations. This leads to spontaneous yet slow delamination of SrO and the emergence of $SrCO_3$ nanograins on a purely TiO_2-terminated crystal surface. The interpretation is in quantitative agreement with respective volumes of layers and grains throughout the process.

1. Introduction

1.1. $SrTiO_3$ and Surface Adsorption

Perovskites (ABO_3 structure) are widely used in a variety of applications, like biochemical, memory, and ferroelectric nanomaterials.[1–4] Among these, strontium titanate has attracted significant attention for its diverse applications.[5,6] In bulk applications, its high dielectric permittivity makes it a suitable material for electronic devices, like capacitors,[7] transistors,[8] and memory storage elements.[9] In addition, the suitability of $SrTiO_3$ as a substrate with lattice-matching properties for high-temperature oxide superconductors[10] is important in the development of advanced electronic systems. On the other hand, its catalytic properties[11] in water splitting[12] and CO_2 reduction,[13] as well as its capability of trapping and absorbing carbon dioxide[14] make its surface attractive for these applications.

The recent study by Sharma et al.,[15] has underscored the significant influence of surface terminations on the photocatalytic efficiency of $SrTiO_3$. Their study revealed that on the $SrTiO_3$ surface, the effective photocatalytic water splitting necessitates the presence of SrO and TiO_2 terminations. The SrO termination mainly drives the oxidation reaction, while the TiO_2 termination plays a role in aligning bands, with the water oxidation potential. On the other hand, $SrTiO_3$ surfaces are known to interact with various adsorbates, and the omnipresent CO_2 for ambient applications is one of the most significant.[16,17] Under ambient conditions, CO_2 is not the only chemisorbed molecule, the formation of OH-groups upon adsorption of hydrogen has been reported including studies by Balajka et al.[18] and Park[19] however refer to titanium dioxide under ambient conditions. Their findings reveal that TiO_2 surfaces adsorb OH-groups preferentially in air, forming monolayers that influence surface properties, such as hydrophobicity and catalytic activity. While the chemisorption of hydrogen and carbon dioxide compete for binding sites, the present investigation focuses on CO_2 under ambient conditions, emphasizing that the reported mechanisms are relevant, if not predominant.

M. Bakhtbidar, D. Gueckelhorn, Y. L. L. López, A. Merlen, A. Ruediger
INRS-EMT (Institut National de la Recherche Scientifique
Centre Énergie Matériaux Télécommunications)
Varennes QC J3x1P7, Canada
E-mail: andreas.ruediger@inrs.ca
M. Fernández-Serra
Institute for Advanced Computational Science
Stony Brook University
Stony Brook, NY 11794–5250, USA
A. Merlen
MAPIEM (Matériaux Polymères Interfaces Environnement Marin)
Université de Toulon
La Garde 83130, France

The ORCID identification number(s) for the author(s) of this article can be found under https://doi.org/10.1002/admi.202401024

DOI: 10.1002/admi.202401024

Self-recovery of carbonate-contaminated strontium titanate (100) vicinal surfaces imaged by tip-enhanced Raman spectroscopy

Auto-régénération des surfaces vicinales (100) du titanate de strontium contaminées par des carbonates, révélée par spectroscopie Raman exaltée par effet de pointe

Mohammad Bakhtbidar,[1] Daniel Gueckelhorn,[1] Marivi Fernández-Serra,[2] Yon Leandro Leibas López,[1] Alexandre Merlen,[1,3] and Andreas Ruediger [1,*]

[1]EMT-INRS (Centre Énergie Matériaux Télécommunications, Institut National de la Recherche Scientifique), Varennes, QC H2X 1E3, Canada

[2]Institute for Advanced Computational Science, Stony Brook University, Stony Brook, NY 11794-5250, USA

[2]MAPIEM (Matériaux Polymères Interfaces Environnement Marin), Université de Toulon, 83130 La Garde, France
*andreas.ruediger@inrs.ca

Publication: Advanced Materials Interfaces (2025): 2401024. Doi : 10.1002/admi.202401024.

Published: 16 May 2025

Author Contributions: The initial concept of using TERS to study selective carbonate adsorption on the (100) surface of $SrTiO_3$ was proposed by MB. MB developed the experimental methodology, performed the measurements, analyzed the data, and investigated SrO layer delamination. DG and MF conducted the DFT simulations and contributed to their interpretation. AR and AM supervised the project, with AM providing guidance on Raman analysis. MB drafted the manuscript with contributions from DG on the simulation section. All authors revised and approved the final version. The project was financially supported by AR.

Abstract: Strontium titanate ($SrTiO_3$) as a model perovskite has significant applications in catalysis, carbon capture, and advanced electronics. On SrO-terminated (100) surfaces, carbon dioxide (CO_2) is a common chemisorption, altering the electronic and chemical properties. This study employed tip-enhanced Raman spectroscopy (TERS) and density functional theory (DFT) simulations to explore this CO_2 chemisorption. The (100) surface of $SrTiO_3$ exhibits two distinct terminations, SrO and TiO_2 with nominally almost the same heights (0.2 nm). Height scans of hydrothermally treated (100) $SrTiO_3$, show values closer to 0.3 nm and 0.1 nm, where we attribute the difference in height to the selective adsorption of ambient CO_2 on one of the terminations. Our TERS analysis shows the presence of a 1071 cm^{-1} Raman peak (characteristic of carbonate vibration), localized exclusively at the SrO terrace, confirming that CO_2 preferentially adsorbs onto SrO. Both experimental and DFT results indicate that this CO_2 monolayer alters the binding energy between the SrO and TiO_2 terminations. This leads to a spontaneous yet slow delamination of SrO and the emergence of $SrCO_3$ nanograins on a purely TiO_2 terminated crystal surface. Our interpretation is in quantitative agreement with respective volumes of layers and grains throughout the process.

Keywords: strontium titanate, surface delamination, carbon dioxide adsorption, nanoscale exploration of carbonate monolayer, tip-enhanced Raman spectroscopy.

6.1 Introduction

6.1.1 $SrTiO_3$ and surface adsorption

Perovskites (ABO_3 structure) are widely used in a variety of applications, like biochemical, memory, and ferroelectric nanomaterials [1,2,350,351]. Among these, strontium titanate has attracted significant attention for its diverse applications [3,4]. In bulk applications, its high dielectric permittivity makes it a suitable material for electronic devices, like capacitors [352], transistors [353], and memory storage elements [354]. In addition, the suitability of $SrTiO_3$ as a substrate with lattice matching properties for high-temperature oxide superconductors [355] is important in the development of advanced electronic systems. On the other hand, its catalytic properties [356] in water splitting [357] and CO_2 reduction [358], as well as its capability of trapping and absorbing carbon dioxide [359] make its surface attractive for these applications.

The recent study by Sharma et al. [360], has underscored the significant influence of surface terminations in the photocatalytic efficiency of $SrTiO_3$. Their study revealed that on the $SrTiO_3$ surface, the effective photocatalytic water splitting necessitates the presence of SrO and TiO_2 terminations. The SrO termination mainly drives the oxidation reaction, while the TiO_2 termination plays a role in aligning bands, with the water oxidation potential. On the other hand, $SrTiO_3$ surfaces are known to interact with various adsorbates, and the omnipresent CO_2 for ambient applications is one of the most significant [361,362]. Under ambient conditions, CO_2 is not the only chemisorbed molecule, the formation of OH-groups upon adsorption of hydrogen has been reported including studies by Balajka et al. [363] and Park [364] that however refer to titanium dioxide under ambient conditions. Their findings reveal that TiO_2 surfaces adsorb OH-groups preferentially in air, forming monolayers that influence surface properties, such as hydrophobicity and catalytic activity. While the chemisorption of hydrogen and carbon dioxide compete for binding sites, the present investigation focusses on CO_2 under ambient conditions, emphasizing that the reported mechanisms are relevant, if not predominant.

The study by Sopiha et al. [208] highlights that CO_2 adsorption on $SrTiO_3$ (100) surfaces induces notable changes in its electronic properties, depending on the specific surface termination involved. On the SrO-terminated surface, CO_2 adsorption increases the band gap from 1.55 eV to 1.82 eV, reducing surface conductivity while stabilizing the surface and impact its ability to

catalyze reactions. On the TiO_2-terminated surface, CO_2 adsorption leads to a more substantial band gap increase from 0.99 eV to 1.50 eV by passivating dangling bonds and eliminating surface states at the valence band maximum. This passivation significantly modifies the electronic structure, potentially hindering the surface's ability to engage in catalytic reactions.

Considering these impacts, it becomes essential to employ high-resolution and sensitive characterization technique, alongside theoretical research, to investigate the CO_2 adsorption on the (100) $SrTiO_3$ surface. These findings may pave the way for approaches to tailor the surface in order to boost $SrTiO_3$ resistance against degradation and improve its performance in applications such as carbon capture, storage, and catalysis [365]. Numerous theoretical studies have delved into understanding the (100) surface of $SrTiO_3$ crystals, like ab initio [366–369] and shell model studies [370]. The exploration of $SrTiO_3$ (100) has mostly focused on aspects such as the terraces of the surface [371–374], its local physical properties [374], morphology [375,376], and the emergence of non-stoichiometric phases [375]. Despite the extensive research efforts directed towards the surface of $SrTiO_3$ crystals, there remains a gap in the direct investigation of phenomena such as adsorption and formation of agglomeration on the $SrTiO_3$ (100) terraces [209,377,378].

6.1.2 Nanoscale characterizations

To investigate nanoscale phenomena, common techniques like transmission electron microscopy (TEM) and scanning probe microscopy (SPM), do not adequately reveal the chemical insights of the surface [252]. Conversely, x-ray photoelectron spectroscopy (XPS) and optical spectroscopy offer valuable chemical information but lack the spatial resolution required for a thorough analysis at the nanometer scale [253,256]. Over the past two decades, tip-enhanced Raman spectroscopy has evolved into a distinguished characterization technique for chemical and structural imaging at the nanoscale [67,259,379]. By integrating Raman spectroscopy with SPM, TERS emerges as a technique for detailed surface analysis even capable of detecting single molecules and self-assembled monolayers [68,380], even enabling the detection of vibrational modes that are not accessible with traditional Raman technique [225,381–383].

In the present study, we explore the surface characteristics of $SrTiO_3$ single crystals by combining TERS investigations with density functional theory (DFT) simulations. Thanks to a strong plasmonic near-field enhancement, we discover a carbonate monolayer localized on the SrO

terminations. We demonstrate that CO_2 adsorption on the SrO termination reduces the binding energy between SrO and TiO_2 terminations, triggering the spontaneous delamination of the SrO layers, leading to the formation of $SrCO_3$ nanograins on the TiO_2 terminations. Supported by DFT simulations, our study offers new insights into how carbon dioxide adsorption alters the surface properties of $SrTiO_3$ and why "as-received" (100) surfaces of this material exhibit a predominance of TiO_2 terminations. These findings are crucial for optimizing $SrTiO_3$-based applications in photocatalysis, where surface interactions with CO_2 can influence catalytic efficiency, and in nanoelectronics, where controlled surface terminations are essential for tailoring electronic properties and device performance.

6.2 Material and methods

6.2.1 Sample preparation

$SrTiO_3$ exhibits a perovskite cubic structure with a lattice parameter of a_0 = 0.3905 nm [49], as depicted in Figure 6.1 (a). In the absence of miscut angles, which represent the deviation of the surface orientation from the specified crystal plane, the cleaved surface of the crystal exhibits a single termination. This specific termination would promote a uniform chemical surface, enabling the creation of a coherent epitaxial interface. Nonetheless, during the preparation of a single crystal with a specific orientation through cutting and polishing, encountering substrate miscut angle is inevitable [76]. Such an angle leads to the macroscopic surface being misaligned both in-plane and out-of-plane relative to the nearest low index (hkl) plane, introducing terrace features on the real-world single crystal substrate surfaces [384]. Figure 6.1 (b) illustrates the (100) crystallographic orientation of $SrTiO_3$, where SrO and TiO_2 layers are systematically organized with a separation of $d_{100}/2$ ($a_0/2 \approx 0.2$ nm) along the <100> direction.

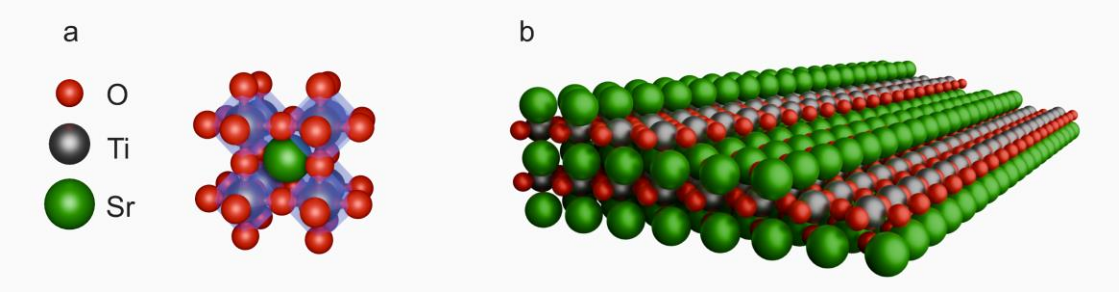

Figure 6.1: Crystal structure of $SrTiO_3$ (a) highlighting the oxygen octahedra (b) layered structure of $SrTiO_3$ (100) planes with SrO and TiO_2 vicinal surfaces. The visualization of the crystal structures in (a) and (b) was conducted using Blender and VESTA 3 [271,385].

For the present study, we utilized commercially available (100) oriented $SrTiO_3$, pure single crystal substrates of 10 x 10 x 0.5 mm, (CrysTec GmbH, miscut angle < 0.5°). The surface of the sample as received is terminated by terraces with the height of 0.39 nm which indicates a single terrace of either SrO or TiO_2, as illustrated in Figure 6.10 (supplementary information). To achieve a surface with both SrO and TiO_2 terminations, the substrate underwent a treatment process, fully detailed in the supporting information.

6.2.2 TERS tip fabrication

The plasmonic tips were fabricated by electrochemical etching of thermally pre-treated gold wires (Goodfellow, >99.99 % purity) with a diameter of 100 µm. The gold wire was immersed approximately 1 mm into a 37 % hydrochloric acid solution (Sigma–Aldrich) and connected to a waveform generator that applied a specific pulse sequence [298]. Concurrently, a gold ring with a diameter of 20 mm was submerged in the solution. Voltage pulses of +4.5 V with a duration of 30 µs and a +0.5 V offset bias were applied to the tip at a frequency of 3 kHz, resulting in a duty cycle of 10 %. This process produced a smooth surface with tip radii of approximately 10 nm, as illustrated in the scanning electron microscopy images provided in Figure 3 of reference [298]. As discussed in our earlier publication [181], the electric field at the tip apex could reach approximately 3×10^8 V/m, providing a significant field enhancement on the surface of the samples.

6.2.3 TERS set-up and measurements

TERS measurements are performed under ambient conditions utilizing a scanning probe (AIST-NT Omega Scope 1000), coupled with a Raman spectrometer (NanoFinder 30), in a confocal setup, along with a thermoelectrically cooled Andor CCD detector. Excitation was achieved using a linearly polarized helium-neon laser (632.8 nm, TEM00), with an optical neutral density filter (ND 0.5) reducing the laser power to an effective 1.5 mW on the sample. A Mitutoyo MPlan Apo 100x objective with a numerical aperture of 0.7 (NA 0.7) was employed to focus the laser on the tip at an incident angle of 65°. The spectral map was recorded with an exposure time of 1 second per pixel.

6.3 Results and discussions

6.3.1 CO_2 adsorption on SrO termination

Following the optimization of the hydrothermal etching procedure to achieve an $SrTiO_3$ surface with both TiO_2 and SrO terminations, as detailed in the supporting information, atomic force microscopy (AFM) measurements were conducted to characterize the surface topography. Figure 6.2 (a) presents the topography of the $SrTiO_3$ surface as measured via tapping mode in AFM (Smart SPM1000-AIST-NT Inc.). The sample was treated by hydrothermal etching in deionized (DI) water with a resistivity greater than 10 MΩ·cm, followed by a thermal treatment under an oxygen flow of 100 sccm. The heating cycle involved a controlled temperature increase at a rate of 25 °C per minute from room temperature to 1000 °C [205]. The substrate was maintained at 1000 °C for 30 minutes and subsequently cooled to room temperature over approximately 90 minutes under ambient conditions.

As shown in Figure 6.2 (a), the surface-treated $SrTiO_3$ crystal exhibits two distinct terminations. While the lattice spacing suggests step heights of approximately 0.2 nm, the AFM measured height distribution over the specified area (dashed line in Figure 6.2 (a)) deviates from this prediction. As depicted in Figure 6.2 (b), the height distribution indicates the presence of two distinct terrace types: steps with a height of 0.3 nm (with an RMS roughness of approximately 110 pm), and steps with a height of 0.1 nm (with an RMS roughness of around 50 pm). Notably, the RMS roughness of 50 pm is only 2.5 times greater than the theoretical thermal noise limit for the cantilever used in these measurements.

The deviation between the predicted and measured values is attributed to the selective adsorption of CO_2 molecules approximately 0.1 nm in size. As shown in the phase map (Figure 6.2 (d)), two distinct steps are present on the sample surface. Considering both the phase map and height scans, we conclude that selective adsorption occurs on one of these terminations, either SrO or TiO_2. This conclusion is further supported by the increased surface roughness observed on terraces where molecular adsorption is presumed to take place.

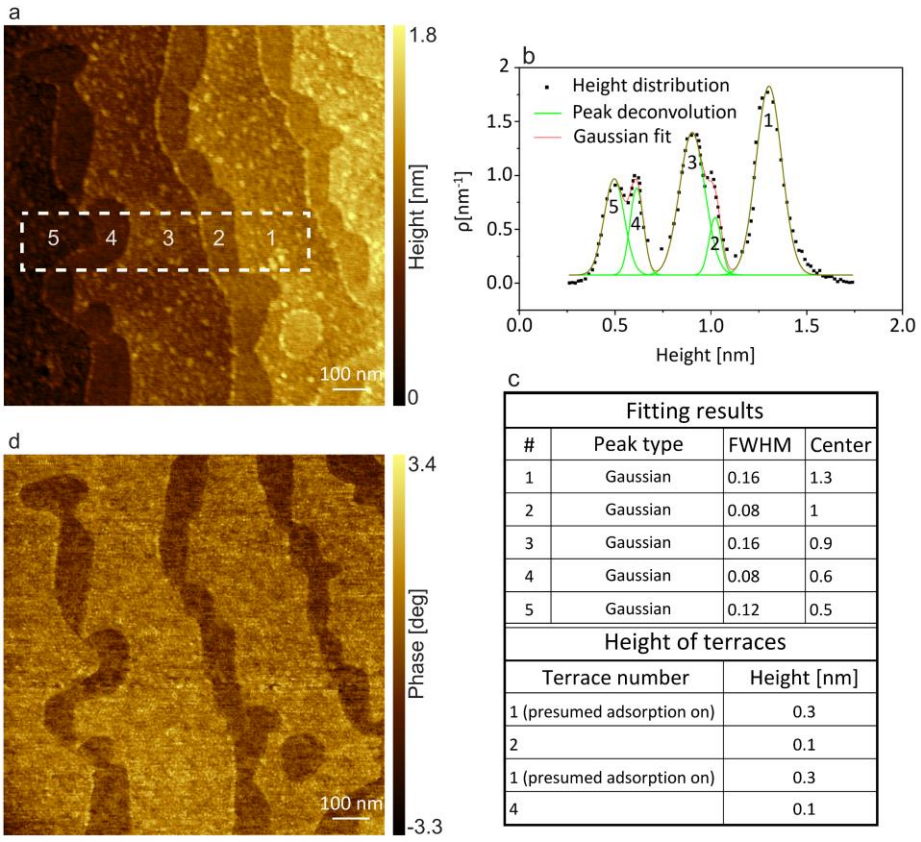

Fitting results			
#	Peak type	FWHM	Center
1	Gaussian	0.16	1.3
2	Gaussian	0.08	1
3	Gaussian	0.16	0.9
4	Gaussian	0.08	0.6
5	Gaussian	0.12	0.5

Height of terraces	
Terrace number	Height [nm]
1 (presumed adsorption on)	0.3
2	0.1
1 (presumed adsorption on)	0.3
4	0.1

Figure 6.2: AFM measurement on hydrothermally treated $SrTiO_3$ (100) crystal**.** (a) Tapping-mode AFM topography image of the $SrTiO_3$ surface, over a 1 µm × 1 µm area. The white dotted rectangle indicates the region used for height distribution analysis. (b) Height distribution over the surface steps, fitted with a Gaussian function. (c) Table summarizing the fitting results, including the FWHM and center of the peaks, indicating two distinct steps on the surface with heights of 0.1 nm and 0.3 nm. (d) Tapping-mode phase image illustrating two types of terminations.

To determine which termination (SrO or TiO_2) hosts adsorption and to characterize the structure of the adsorption layer, a detailed analysis was conducted using tip-enhanced Raman spectroscopy. The sample was scanned using a 200 nm × 200 nm topography scan, along with a simultaneously acquired TERS map obtained in shear force mode with gold tips, as illustrated in Figure 6.3**.** The topography scan (Figure 6.3 (a)) reveals two distinct steps on the surface, with the step in the upper right corner exhibiting lower surface roughness compared to the step in the lower left part, and a granular structure is observed in the upper central region.

In the corresponding high-resolution TERS map, a false-color image was created (Figure 6.3 (b)), where the spectral emission between 1060 and 1080 cm^{-1} including the carbonate signature is plotted as a function of position. The map reveals a marked increase in the Raman signal within this spectral range on the rougher termination, with the granular region in the upper center

displaying an even more pronounced intensity. This region of the spectrum (1060 and 1080 cm^{-1}) is associated with CO_2 adsorption on the $SrTiO_3$ surface. As a result, the observed adsorption on the surface is attributed to CO_2, which, as indicated in the previous section, selectively occurs on one termination.

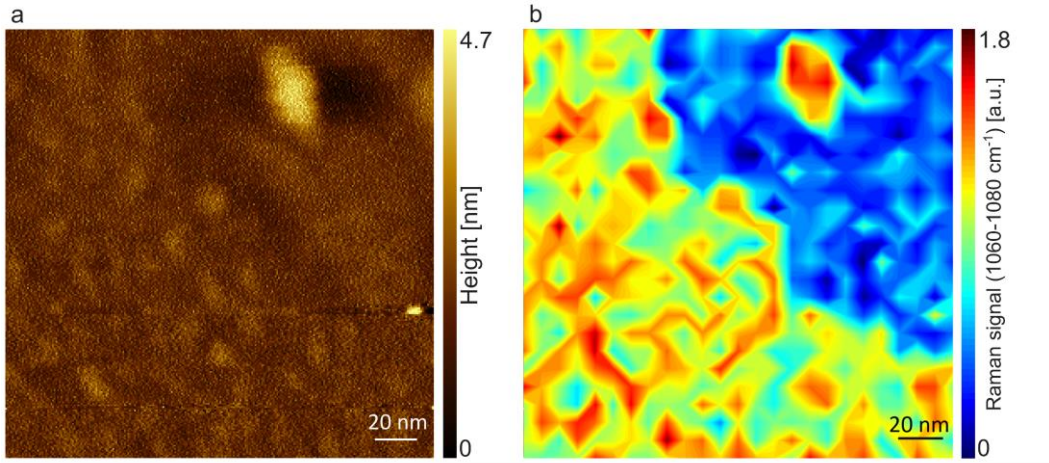

Figure 6.3: TERS measurement on SrO and TiO_2 terminations . (a) Topography scan of a 200 nm × 200 nm region of $SrTiO_3$ steps, showing two distinct steps and individual islands on one of the steps. (b) TERS map acquired in the same area as (a), with a resolution of 8 nm per pixel (25 × 25 pixels), displaying a strong signal in the 1060–1080 cm^{-1} spectral range localized only to the step with larger roughness.

To confirm that the observed peak is not due to noise and to facilitate a comparison of the TERS spectra between the two terminations, in Figure 6.4 spectral averaging was conducted over 30 pixels (on TERS map Figure 6.3) for each termination to increase the signal-to-noise ratio. As seen in Figure 6.4, there is a clear Raman signature at approximately 1071 cm^{-1} on the termination with higher surface roughness. This peak has previously been reported to be associated with carbon dioxide adsorption on the surface [77,386]. Sr^{2+} ions in the SrO terminated surface have a strong affinity to carbonate ions (CO_3^{2-}) due to their ability to form strontium carbonate ($SrCO_3$). In contrast, the TiO_2 surface generally has a lower surface energy compared to SrO, making it less reactive [387]. Therefore, CO_2 adsorption predominantly occurs over the SrO terraces, explaining the increased Raman intensity at 1071 cm^{-1} on the SrO terrace, as seen in Figure 6.3 (b), and the increased surface roughness, as shown in Figure 6.3 (b). Furthermore, as mentioned in the previous section, AFM scans reveals the adsorption of molecules with a height of approximately 0.1 nm on one of the steps. By considering the TERS measurement results and the size of the carbonate adsorption, which is roughly 0.1 nm [210], we can conclude

that the findings from both techniques, AFM and TERS, are consistent and support the preferential adsorption of CO_2 on the SrO termination.

According to the details provided by the substrate supplier (CrysTec), contamination levels are below the 0.01% total. This suggests that CO_2 layer on the surface occurs primarily due to the interaction between SrO terminations and CO_2 gas in the environment, rather than being affected by pre-existing contaminants. The XPS analysis of the same surface is presented in our recent publication [388]. Furthermore, as reported in [363,364], water adsorption on the surface is also possible. The Raman peaks of OH groups appear in the spectral range near 3600 cm^{-1} [389], corresponds to an emission wavelength of approximately 820 nm at an excitation wavelength of 632.8 nm. Given the FWHM of the localized surface plasmon resonance is ~50nm, it is not possible to simultaneously detect CO_2 and water adsorption under the same plasmonic enhancement conditions. As a result, the observed CO_2 adsorption competes with the presence of OH groups, potentially affecting surface interactions and adsorption dynamics.

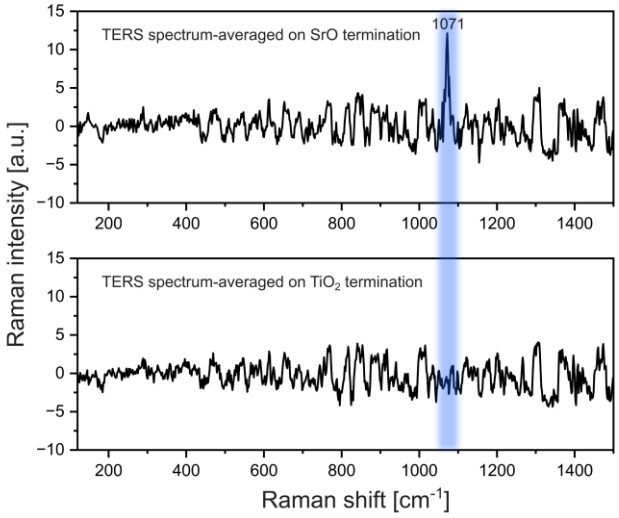

Figure 6.4: Comparison of the averaged near-field spectrum on the SrO termination and the TiO_2 termination . The peak at 1071 cm^{-1} (highlighted in blue) is characteristic signatures of $SrCO_3$. The near-field signature of $SrCO_3$ on the SrO termination indicates carbonate adsorption, which is approximately one order of magnitude above the noise level. The unphysical negative intensity values are the result of a baseline correction to remove an intrinsic luminescence signature of our gold tips.

6.3.2 DFT calculation of the vibrational modes of CO_2 adsorption on SrO-terminated $SrTiO_3$

We calculated the vibrational modes of CO_2 adsorbed on a SrO-terminated $SrTiO_3$ surface via density functional theory (DFT). We used the DFT code CRYSTAL23 in combination with the Perdew-Burke-Ernzerhof functional revised for solids (PBEsol) and POB-TZVP-REV2 basis sets [390–392]. Hereby, all species except strontium use all-electron basis sets. Strontium uses an effective core potential. As a reference, we use the Raman spectrum of $SrCO_3$ bulk (Pnma, 62), consisting of 20 atoms. We applied a 4x4x4 k-grid and periodic boundary conditions with resulting lattice constants of a = 0.5916 nm, b = 0.5096 nm, and c = 0.8413 nm, with excellent agreement with experimental values of a = 0.6020 nm, b = 0.5093 nm, and c = 0.8376 nm [393].

The surface geometry consists of a 2x2x3 $SrTiO_3$ supercell with an adsorbed CO_2 molecule, with 63 atoms in total. Here, we applied periodic boundary conditions parallel to the surface and a non-periodic boundary condition perpendicular to the surface. To simulate the underlying bulk, the two bottom atomic layers were constraint. The primitive cell of $SrTiO_3$ was sampled with a 6x6x6 k-grid and periodic boundary conditions resulting in a lattice constant of a_0 = 0.3890 nm, which is also in excellent agreement with the experimental value of a_0 = 0.3905 nm [394]. Therefore, a 3x3x1 k-grid was used for the surface geometry. The optimized structure is in very good agreement with previously reported results, as summarized in Table 6-1. Here, the bond length between the carbon and the oxygen of the adsorbed CO_2 molecule is 0.127 nm with a resulting bond angle of 122.1 °. The bond length of the carbon atom with the closest oxygen surface atom O_S is 0.133 nm.

Table 6-1: Comparison of geometrical parameters of the optimized $SrTiO_3$ surface geometry with an adsorbed CO_2 molecule.

Parameter	This work	U. Terranova et al. [210]	K. V. Sopiha et al. [208]
C-O_1 [nm]	0.127	0.127	0.129
C-O_2 [nm]	0.127	0.127	0.129
C-O_S [nm]	0.133	0.136	0.133
O_1-C-O_2 [°]	122.1	122.4	122

The calculated peak positions of $SrCO_3$ bulk are, besides a small systematic shift, in very good agreement with experimental values, as shown in Table 6-2. For the peaks of the adsorbed CO_2 molecule, we only focus on the range between 1000 cm^{-1} and 1600 cm^{-1}, because for lower wavenumbers DFT also obtains various surface states, which are more challenging to be experimentally observed.

Table 6-2: Comparison of simulated and experimental Raman peak positions of bulk $SrCO_3$.

Raman peak position of bulk $SrCO_3$ (Pnma, 63) [cm^{-1}]	
Simulation	Experiment
162	149 [77]
195	182 [77]
257	244 [77]
670	701 [77]
1053	1071 (this work)
1455	1463 [395]
1553	1548 [395]

We find peaks at 1039 cm^{-1}, 1368 cm^{-1}, and 1558 cm^{-1} for the adsorbed CO_2 molecule. The peaks result from a symmetrical stretching of the oxygen atoms around the carbon atom, as well as vertical and horizontal oscillation of the carbon atom, respectively, as visualized in Figure 6.5.

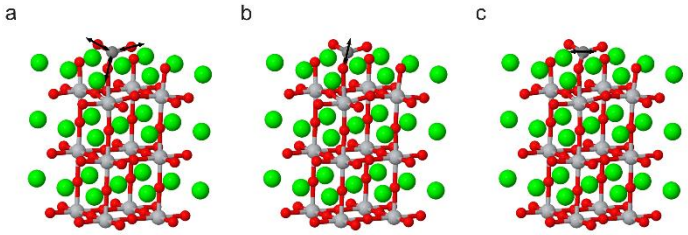

Figure 6.5: Vibrational modes for an adsorbed CO_2 molecule on a SrO-terminated $SrTiO_3$ surface . (a) 1039 cm^{-1} corresponds to a symmetrical stretching of the oxygen atoms around the carbon atom. (b) 1368 cm^{-1} is caused by the vertical oscillation of the carbon atom. (c) 1558 cm^{-1} is the result of a horizontal oscillation of the carbon atom. Figures were created with CRYSPLOT [396].

These peaks show a very similar peak position and the same vibrational modes as those found for bulk $SrCO_3$. The small deviation occurs because of the different geometry of a 20-atom $SrCO_3$ bulk cell and a single CO_2 forming a $SrCO_3$ molecule on a surface. While theory predicts three distinct peaks, only the lowest energy mode is usually experimentally observable in e.g. nanopowders of $SrTiO_3$ as an omnipresent surface contamination. The other two peaks have however been observed in the high-pressure phase of $SrCO_3$ [395]. Thus it is safe to say that the experimental peak arises from CO_2 forming $SrCO_3$ on a SrO-terminated $SrTiO_3$ surface.

6.3.3 Binding energy variation and delamination of SrO layer

During this study, it was observed that the surface of the $SrTiO_3$ substrate underwent changes over time. As shown in Figure 6.6 (a), the topography of the sample surface after 18 months, showing a noticeable increase in step height to 0.4 nm, along with the formation of nanograins.

Figure 6.6 (b) illustrates the height distribution along the dashed line in the height scan, which has been fitted using a Gaussian function. The corresponding results, presented in Figure 6.6 (c), reveal the presence of terminations with a height of 0.4 nm.

Considering the lattice constant of $SrTiO_3$, it is concluded that the surface of the hydrothermally etched $SrTiO_3$ substrate transitioned from two types of terminations (as shown in Figure 6.2) to a single type of termination with a height of 0.4 nm, accompanied by the formation of nanograins on the surface. To minimize the likelihood of contamination, the sample was stored in a desiccator, making it highly unlikely that the nanograins are a result of environmental contamination.

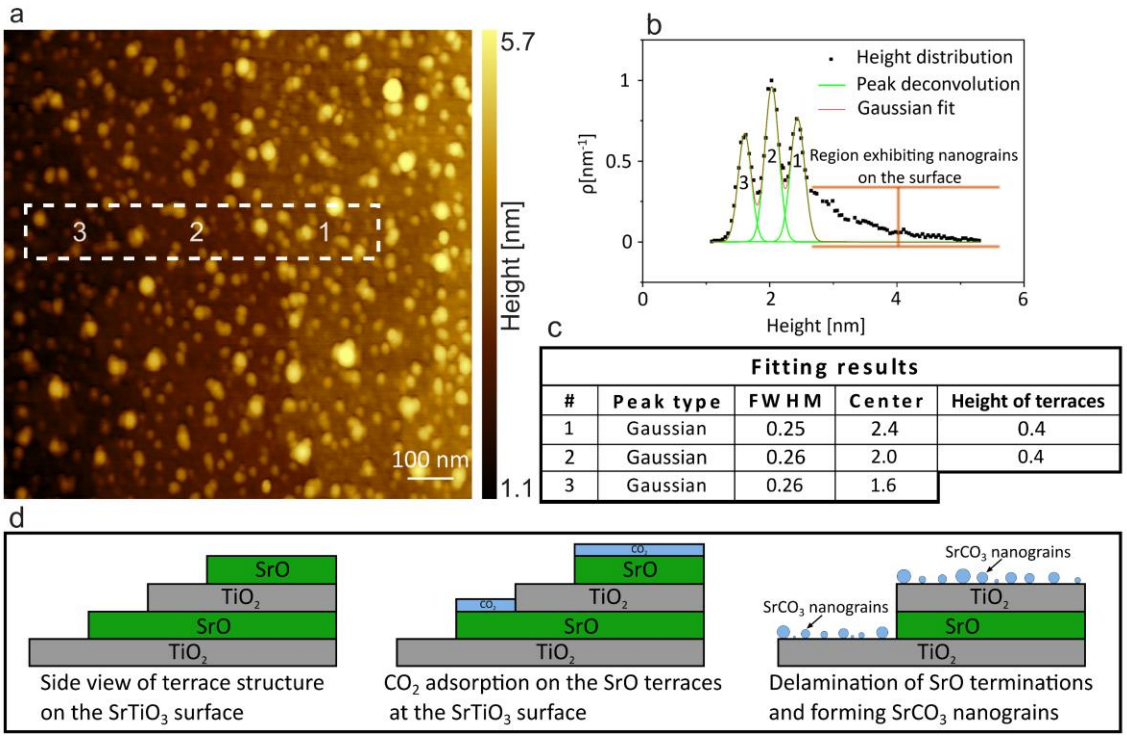

Fitting results

#	Peak type	FWHM	Center	Height of terraces
1	Gaussian	0.25	2.4	0.4
2	Gaussian	0.26	2.0	0.4
3	Gaussian	0.26	1.6	

Figure 6.6: Illustration of how carbonate adsorption alters $SrTiO_3$ surface morphology after sample aging . (a) Tapping-mode AFM topography image of the $SrTiO_3$ surface after 18 months, depicting nanograin formation within a 1 µm × 1 µm area. The white dotted rectangle highlights the region used for height distribution analysis. (b) Height distribution of the surface steps that fitted with a Gaussian function. (c) Table detailing the fitting results, confirming the presence of a single termination type on the surface with a height of 0.4 nm. (d) Schematic representation of the delamination process on the $SrTiO_3$ surface. CO_2 adsorption on the SrO terminations resulting in changing the binding energy between SrO and TiO_2 terminations, leading to the delamination of SrO termination and formation of $SrCO_3$ nanograins.

AFM scans of the sample before aging reveal that the volume of the SrO termination and carbonate molecules on the surface is approximately 1.5×10^{-4} µm^3 across the scan area. After aging, the volume of the nanograins is approximately 2.4×10^{-4} µm^3, which is consistent within

experimental uncertainties. Based on these observations, we suggest that CO_2 adsorption on the SrO termination reduces the binding energy between the SrO and TiO_2 layers. This decrease in binding energy subsequently causes the delamination of the SrO termination, leading to the formation of $SrCO_3$ nanograins over the TiO_2 terraces, as presented in the schematic illustration in Figure 6 (d).

To characterize these nanograins, TERS was performed to achieve high-resolution and chemically sensitive probing. Figure 6.7 (a) presents the topography scan obtained in tapping mode, clearly revealing the presence of nanograins on the $SrTiO_3$ substrate. The simultaneously obtained TERS map of the same region, presented in Figure 6.7 (b), shows the Raman intensity map over the 1071 cm^{-1} peak (map integrated between 1060 cm^{-1} and 1080 cm^{-1}), which increases specifically over the nanograins. The presence of the 1071 cm^{-1} peak exclusively over the nanograins indicates that they are composed of $SrCO_3$.

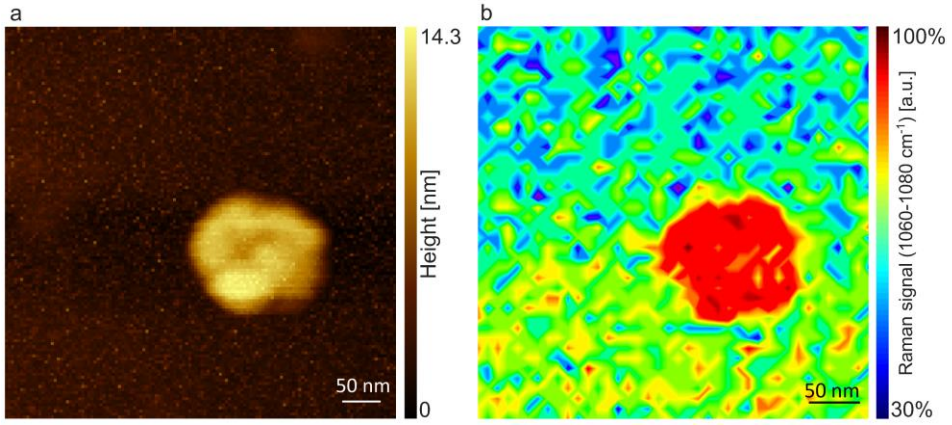

Figure 6.7: TERS measurement on an $SrCO_3$ nanograin formed by surface delamination . (a) Topography scan of a 400 nm × 400 nm region of an aged $SrTiO_3$ substrate, revealing agglomeration on the surface. (b) TERS map acquired in the same area as (a), with a resolution of 8 nm per pixel (25 × 25 pixels), showing a strong signal in the 1060–1080 cm^{-1} spectral range localized to the agglomeration, which is indicative of $SrCO_3$.

To increase the signal-to-noise ratio and delve into details, the near-field spectrum was averaged over 30 pixels on the nanograin as well as on the substrate, as illustrated in Figure 6.8. The averaged spectrum on the nanograin revealed two distinct peaks at 1071 cm^{-1} and 148 cm^{-1}. Upon consulting literature and the RRUFF database, these peaks are indeed associated with $SrCO_3$ [77,386]. The peak at 1071 cm^{-1} is attributed to the symmetric stretching vibration (v_1) of the carbonate ion (CO_3^{2-}), which is a high-frequency internal phonon mode characterized by A_{1g} symmetry according to group theory analysis [397,398]. The peak at 148 cm^{-1} corresponds to an internal phonon mode associated with the E_g mode, specifically the symmetric bending vibration

of the carbonate ions (CO_3^{2-}) [399]. These modes are commonly observed in the Raman spectra of carbonates and indicative of the presence of carbonate ions within the $SrCO_3$ structure.

Additionally, in the averaged near-field spectrum on the substrate, three distinct low-intensity peaks were observed at 683 cm^{-1}, 762 cm^{-1}, and 866 cm^{-1}. According to the previous research conducted in our group, these modes are indicative of surface phonon modes [335,400]. The capability of TERS to detect these modes, which are otherwise Raman-inactive due to the symmetry considerations in the bulk phase, highlights the technique ability to provide detailed insights into surface structural properties.

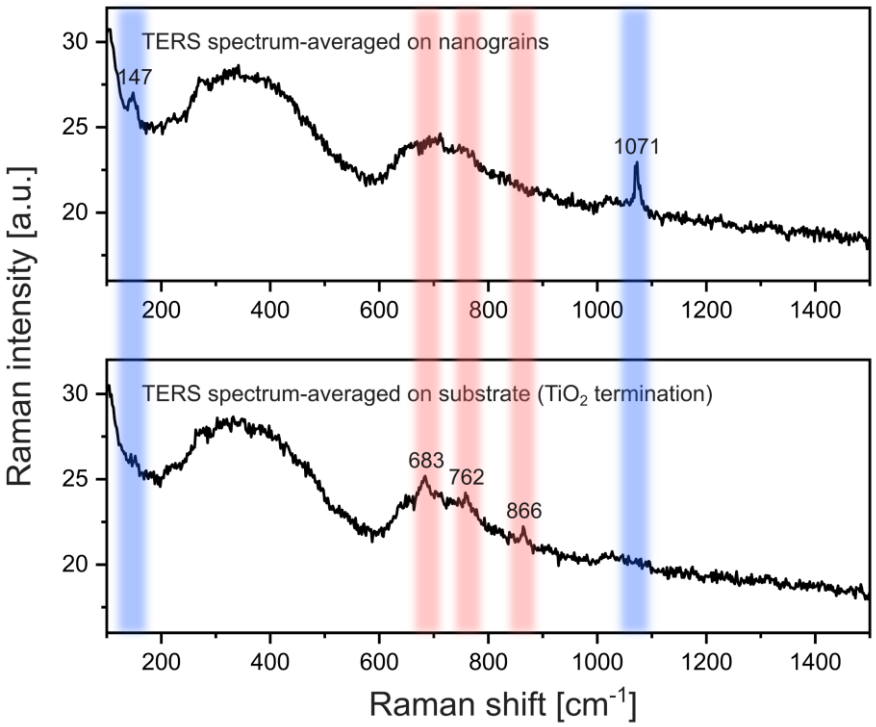

Figure 6.8: Comparison of the averaged near-field spectra on the nanograin (caused by delamination on SrO terminations) and the rest of the surface . The spectrum on the nanograin clearly shows peaks at 1071 and 183 cm^{-1} (highlighted in blue), which are characteristic signatures of $SrCO_3$. The spectrum on the rest of the surface displays peaks at 683, 762, and 866 cm^{-1} (highlighted in red), indicative of surface phonon modes on the TiO_2 surface. Both spectra include the far-field Raman signal from the $SrTiO_3$ sample, along with the plasmon-enhanced photoluminescence originating from the gold tip.

The mode at 683 cm^{-1} is associated with the Ti–O bonds stretching along the *c*-axis. This mode reflects the local symmetry and structural distortions present at the TiO_2 surface, which are not typically observed in the bulk material. The mode at 762 cm^{-1} corresponds to the antiphase rotational movement of the TiO_6 octahedra, a characteristic feature of surface phonon modes

influenced by surface reconstruction and relaxation phenomena. Lastly, the mode at 866 cm^{-1} is attributed to the stretching of Ti–O bonds along the *b*-axis, further indicating the presence of surface-specific vibrational dynamics.

These results confirm that the nanograins on the surface of the $SrTiO_3$ have $SrCO_3$ structure, and the surface terminations, initially a mixture of SrO and TiO_2, have transformed to solely TiO_2, as evidenced by the observed TiO_2 surface modes. Considering the results of the TERS measurements along with the AFM measurements, we conclude that the formation of those agglomerations is possible under the assumption that the binding energy of $SrCO_3$ on TiO_2-terminated $SrTiO_3$ is smaller in comparison to $SrCO_3$ on $SrCO_3$ surfaces. This leads to the observed reconstruction of the surface.

6.3.4 DFT calculation of binding energies

To verify the possibility that almost spherical $SrCO_3$ agglomerations can form spontaneously over an extended period, we calculated the binding energy of a $SrCO_3$ molecule on $SrCO_3$ and TiO_2-terminated $SrTiO_3$ for comparison. The results indicate higher binding energy between $SrCO_3$ and $SrCO_3$ in comparison to $SrCO_3$ on TiO_2-terminated $SrTiO_3$ under two considerations which are explained in the following. Thus, it is energetically more favorable to form $SrCO_3$ agglomerations instead of binding to $SrTiO_3$. For this purpose, we used the DFT code SIESTA with the Perdew-Burke-Ernzerhof (PBE) functional, TZVP basis sets, and pseudopotentials from PseudoDojo (standard PBE v0.4.1) [401–403]. For all calculations, periodic boundary conditions, a vacuum layer of 1.8 nm to separate the surface slabs, and dipole corrections were applied.

To account for the underlying bulk, we constrained the two bottom atomic layers of the $SrTiO_3$ slab, and for $SrCO_3$ we constrained the bottom within a range of half a primitive cell. To ensure convergence of the binding energies we considered various geometries. For a $SrCO_3$ molecule on a $SrCO_3$ surface, we calculated a binding energy of -6.47 eV with excellent convergence for regarding the geometry size (Table 6-3). The binding energy on a TiO_2-terminated $SrTiO_3$ does not converge. This was already reported for CO_2 on SrO-terminated $SrTiO_3$ which is very similar to our investigated system [208]. The binding energies vary between -6 eV and -8 eV. Thicker and larger slabs show higher binding energies, as shown in Table S1 in the supporting information.

We found two possible reasons for the lack of convergence. First, the binding state of the $SrCO_3$ differs depending on the surface TiO_2 surface area. When comparing the 2x2x3 with the 3x3x3 structure we see indeed a different binding state of the $SrCO_3$ molecule, as visualized in Figure 6.9. For the smaller geometry, only one of the $SrCO_3$ oxygen atoms binds to a surface titanium atom, the remaining atoms of the molecule stay close to the strontium atom (Figure 6.9 (a)). This is different for the 3x3x3 geometry where the $SrCO_3$ is almost flat and two oxygen atoms form bonds with two titanium surface atoms, occupying much more space in total (Figure 6.9 (b)). Another effect is the degree of freedom of the TiO_6 octahedra of $SrTiO_3$ which can tilt and rotate. The energy difference may therefore not relate to the surface but to the structure itself where different geometry sizes lead to slightly different boundary conditions and thus to different relaxation modes caused by the individual octahedra. This hypothesis is supported by our simulations where we only relaxed the top two TiO_2 surface layer including the $SrCO_3$ molecule. When adding further constraint slab layers, the binding energy converges since possible tilts and rotations are suppressed. This changes when using larger surfaces. Here convergence is not achieved because different surface areas can induce different relaxation modes. An overview of the binding energies for different supercell sizes is given in Table 6-4.

The increase of the binding energy for an increasing surface slab thickness and surface area would need more detailed investigation which is not within the scope of this work. However, we see that depending on the binding state of the $SrCO_3$ molecule and the relaxation mode the binding energy can be lower on a TiO_2-terminated $SrTiO_3$ surface in comparison to a $SrCO_3$ surface, especially considering that the change in binding energy may be related to different relaxation modes unrelated to the binding itself. Even smaller differences in binding energy can result in an increase of several magnitudes for a thermally activated process. In summary, the DFT calculations support our experimental observation of spontaneously forming spherical $SrCO_3$ agglomerations even though more detailed DFT studies are needed to fully explore the origin of the interactions between the surface and $SrCO_3$ molecule.

Table 6-3: Binding energies of a $SrCO_3$ molecule on a $SrCO_3$ surface for different geometry sizes.

Supercell size	Binding energy (eV)
2x2x1.5	-6.43
2x2x2.5	-6.47
3x3x1.5	-6.40

Table 6-4. Binding energies of a $SrCO_3$ molecule on a TiO_2-terminated $SrTiO_3$ surface for different geometry sizes.

Supercell size	Binding energy (eV)
2x2x2	-5.98
2x2x3	-6.29
2x2x4	-6.46
2x2x5	-6.60
3x3x2	-6.13
4x4x2	-6.63
3x3x3	-7.76
3x3x4	-8.05

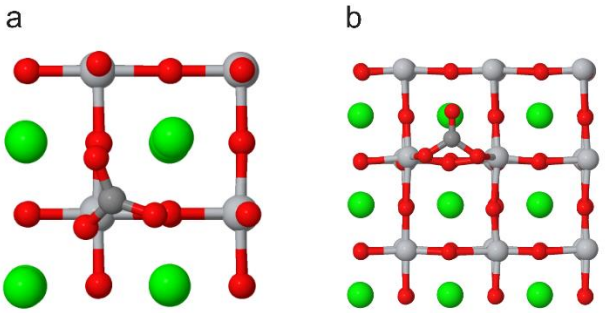

Figure 6.9: Comparison of a $SrCO_3$ molecule on a (a) 2x2x2 and (b) 3x3x3 SrO-terminated $SrTiO_3$ supercell. Structures were rendered with Jmol.

6.4 Conclusion

This research provides direct nanoscale evidence of selective CO_2 adsorption on SrO terminations of $SrTiO_3$ (100) crystal. Our theoretical investigations reveal that this adsorption process induces a reduction in the binding energy between SrO and TiO_2 terminations. High-resolution near-field imaging further confirms that this adsorption leads to delamination of the SrO terminations, forming the $SrCO_3$ nanograins on the surface. Consequently, the $SrTiO_3$ surface undergoes a transformation, leaving behind a single TiO_2 termination with $SrCO_3$ nanograins, in full agreement with the DFT calculations. This process represents a self-cleaning mechanism of the photocatalytically active strontium titanate (100) after CO_2 poisoning.

We arrived at this conclusion through a combination of experimental TERS and DFT simulations to investigate the surface properties of $SrTiO_3$ crystals. To obtain surfaces with both SrO and TiO_2

terminations the hydrothermal treatment process was optimized, as detailed in the supporting information. AFM measurements of the treated $SrTiO_3$ revealed two distinct steps with heights of 0.1 nm and 0.3 nm, deviating from the expected 0.2 nm step height for each SrO and TiO_2 terminations. This deviation arises from the selective monolayer adsorption, corresponding to the adsorption of molecules with an approximate size of 0.1 nm. A pronounced increase in the intensity of the peak at 1071 cm^{-1}, characteristic of $SrCO_3$, is observed in the near-field spectrum and imaging. This indicates that CO_2 preferentially adsorbs on SrO terraces, leading to the formation of $SrCO_3$, while adsorption on TiO_2 remains negligible. These experimental findings align with DFT simulations, which predict the same Raman peak associated with CO_2 adsorption on the SrO layer.

Additionally, our DFT calculations indicated a reduction in binding energy between SrO and TiO_2 terminations due to CO_2 adsorption. TERS measurements on aged $SrTiO_3$ surfaces further corroborate this, showing the presence of nanograins with Raman signatures at 1071 cm^{-1} and 148 cm^{-1}, characteristic of $SrCO_3$, distributed across the surface with Raman signatures at 683 cm^{-1}, 762 cm^{-1}, and 866 cm^{-1}, correspond to the surface phonon modes of the TiO_2 layer. Combining DFT calculations and TERS measurements, we conclude that CO_2 adsorption almost exclusively occurs on SrO terraces, altering the binding energy in the outer layers of SrO and TiO_2. Strontium carbonate adsorbates are however bound sufficiently strong leading to surface delamination and agglomeration, forming $SrCO_3$ islands on the TiO_2 layer. Our findings demonstrate the potent combination of TERS and DFT in unraveling nanoscale surface phenomena, providing a deeper understanding of interaction mechanisms on $SrTiO_3$ surfaces. This knowledge is crucial for optimizing surface quality and enhancing the functional longevity of $SrTiO_3$ in various applications, such as catalysis, carbon capture, and electronic devices.

6.5 Acknowledgments

A.R. acknowledges funding from a CFI infrastructure grant, an NSERC Discovery Grant (No. RGPIN-2024-06730), and two NSERC strategic partnership grants (Nos. 506289-2017 and 506953-17).

6.6 Conflict of Interest

The authors declare no conflict of interest.

6.7 Data Availability Statement

The data that support the findings of this study are available from the corresponding author upon reasonable request.

6.8 Supplementary information

Self-recovery of carbonate-contaminated strontium titanate (100) vicinal surfaces imaged by tip-enhanced Raman spectroscopy

Auto-régénération des surfaces vicinales (100) du titanate de strontium contaminées par des carbonates, révélée par spectroscopie Raman exaltée par effet de pointe

Mohammad Bakhtbidar,[1] Daniel Gueckelhorn,[1] Marivi Fernández-Serra,[2] Yon Leandro Leibas López,[1] Alexandre Merlen,[1,3] and Andreas Ruediger [1,*]

[1]EMT-INRS (Centre Énergie Matériaux Télécommunications, Institut National de la Recherche Scientifique), Varennes, QC H2X 1E3, Canada

[2]Institute for Advanced Computational Science, Stony Brook University, Stony Brook, NY 11794-5250, USA

[2]MAPIEM (Matériaux Polymères Interfaces Environnement Marin), Université de Toulon, 83130 La Garde, France

*andreas.ruediger@inrs.ca

6.8.1 Sample preparation

Commercially available $SrTiO_3$ single crystal substrates (10 × 10 × 0.5 mm, miscut angle < 0.5°, CrysTec GmbH) with one polished side were used as $SrTiO_3$ crystal sample. The topography of the as-received sample surface was characterized using an atomic force microscope, AFM (Smart SPM1000-AIST-NT Inc.) operating in tapping mode, as shown in Figure 6.10 (a). The height distribution over the region marked by the dashed line in the AFM scan is presented in Figure 6.10 (b), while the fitting results of the height distribution are displayed in Figure 6.10 (c). These results indicate a step height of 0.39 nm, confirming a uniform single termination across the surface. Additionally, the AFM scan reveals the presence of smooth terraces, free from adsorbates or environmental contamination. This demonstrates that the sample surface, prior to treatment and measurements, remains uncontaminated.

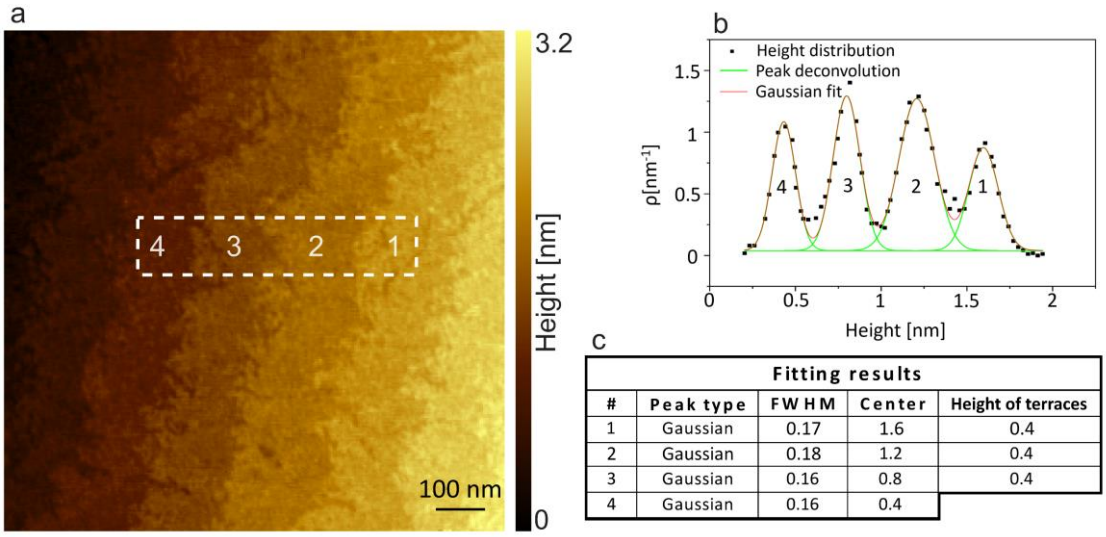

Fitting results				
#	Peak type	FWHM	Center	Height of terraces
1	Gaussian	0.17	1.6	0.4
2	Gaussian	0.18	1.2	0.4
3	Gaussian	0.16	0.8	0.4
4	Gaussian	0.16	0.4	

Figure 6.10: Topography of the as-received $SrTiO_3$ sample . (a) Tapping-mode AFM topography image of the $SrTiO_3$ surface as received, over the 1 μm × 1 μm area. (b) Height distribution over the surface terminations, fitted with a Gaussian function. (c) Table summarizing the fitting results, including the FWHM and center of the peaks, indicating single type termination (SrO or TiO_2) on the surface with heights of 0.4 nm.

To achieve a surface with both SrO and TiO_2 terminations, we perform a hydrothermal etching process followed by an annealing procedure. The experimental setup and further details on the hydrothermal etching process can be found in the literature published by our group [205]. After hydrothermal etching in deionized (DI) water with a resistivity greater than 10 MΩ·cm, the substrate undergoes a heating cycle under an oxygen flow of 100 sccm. The substrate is placed in an open furnace with an outlet of 0.5 cm in diameter and heated from room temperature to 1000 °C at a rate of 25 °C per minute. It is then maintained at 1000 °C for 30 minutes before being allowed to cool to room temperature over approximately 90 minutes, all while continuing in the oxygen flow.

The surface topography of the sample following treatment procedure is presented in Figure 6.11. A comparative analysis of the sample topography before and after treatment reveals that the process leads to the formation of sharper terraces relative to the untreated sample. The terrace heights are approximately 0.4 nm, which suggests the presence of a single-termination terrace.

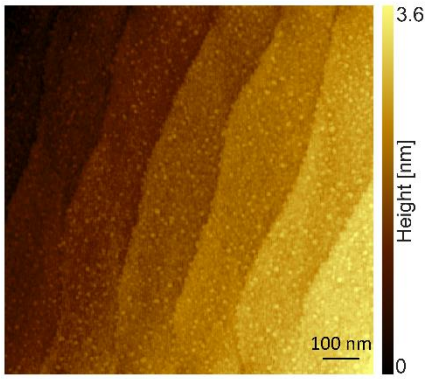

Figure 6.11: Tapping-mode AFM topography image of the $SrTiO_3$ surface after hydrothermal etching, annealing, and cooling in an oxygen flow , over the 1 μm × 1 μm area.

To achieve a surface with both TiO_2 and SrO terminations, the annealing conditions were modified by reducing the duration to 20 minutes and allowing the sample to cool in ambient air instead of an oxygen flow, thereby inducing oxygen deficiency.

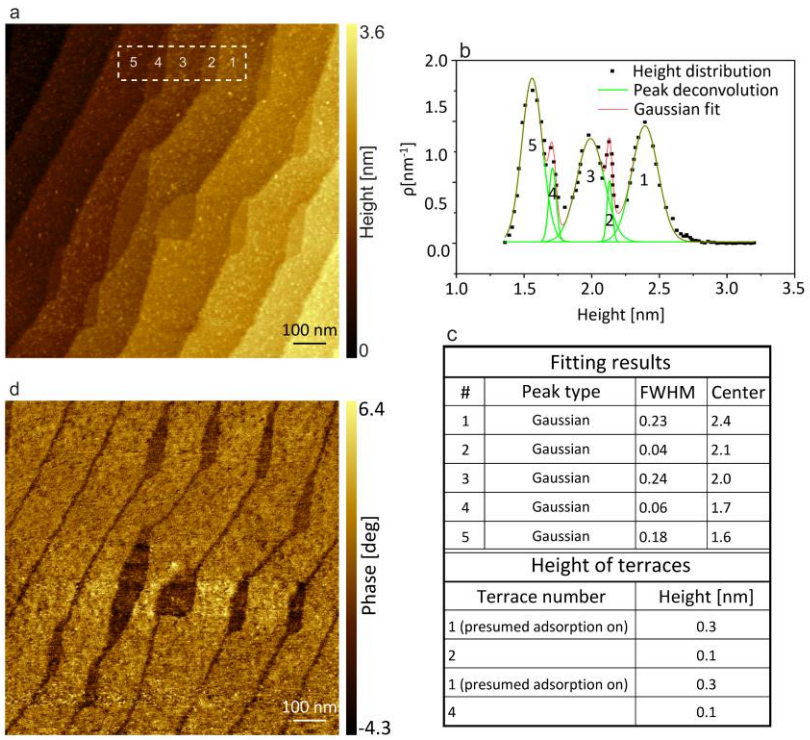

c

Fitting results			
#	Peak type	FWHM	Center
1	Gaussian	0.23	2.4
2	Gaussian	0.04	2.1
3	Gaussian	0.24	2.0
4	Gaussian	0.06	1.7
5	Gaussian	0.18	1.6

Height of terraces	
Terrace number	Height [nm]
1 (presumed adsorption on)	0.3
2	0.1
1 (presumed adsorption on)	0.3
4	0.1

Figure 6.12: Topography of the $SrTiO_3$ surface showing coexisting SrO and TiO_2 terminations . (a) Tapping-mode AFM topography image of the $SrTiO_3$ surface after hydrothermal treated and cooling in ambient condition, over the 1 μm × 1 μm area. The white dotted rectangle indicates the region used for height distribution analysis. (b) Height distribution over the surface terminations, fitted with a Gaussian function. (c) Table summarizing the fitting results, including the FWHM and center of the peaks, indicating two distinct terminations on the surface with heights of 0.1 nm and 0.3 nm. (d) Phase map illustrating two types of terminations with distinct chemical properties.

As shown in Figure 6.12, the treated surfaces exhibit two distinct terminations, the terraces with greater roughness display a height of approximately 0.3 nm, whereas the smoother terraces have a height of 0.1 nm. The phase map in Figure 6.12 (d), obtained from the same region, provides further validation of the coexistence of these terraces across the surface. By adjusting the annealing time, the ratio of these mixed terminations can be controlled, as demonstrated in Figure 6.2 of the manuscript.

6.8.2 DFT calculations

For the calculations, we used the DFT code SIESTA with the Perdew-Burke-Ernzerhof (PBE) functional, TZVP basis sets, and pseudopotentials from PseudoDojo (standard PBE v0.4.1) [401–403]. For all calculations, periodic boundary conditions, a vacuum layer of 1.8 nm to separate the surface slabs, and dipole corrections were applied. To consider the underlying bulk we constrain the two bottom atomic layers. The simulation geometry consists of a TiO_2-terminated $SrTiO_3$ slab with a $SrCO_3$ molecule on top. The binding energy of different supercell sizes was calculated. The results are shown in Table 6-5.

Table 6-5: Binding energies of a $SrCO_3$ molecule on a TiO_2-terminated $SrTiO_3$ surface for different geometry sizes.

Supercell size	Binding energy (eV)
2x2x2	-5.98
2x2x3	-6.29
2x2x4	-6.46
2x2x5	-6.60
3x3x2	-6.13
4x4x2	-6.63
3x3x3	-7.76
3x3x4	-8.05

7 CONCLUSION AND PERSPECTIVES

7.1 Investigation of monolayer carbonate adsorption and infrared-mode activation in $BaTiO_3$

In this study, TERS imaging of $BaTiO_3$ nanograins deposited on polycrystalline gold substrates demonstrated the technique's extraordinary sensitivity and selectivity at the nanoscale. Nanoparticles, synthesized by a microwave-assisted hydrothermal process, crystallized in the tetragonal phase and exhibited diameters ranging from 10 to 50 nm as confirmed by TEM analysis. Despite their ultrathin nature—sometimes only a few tens of atoms thick—the TERS platform achieved monolayer sensitivity and a lateral resolution of approximately 6.6 nm, enabling the chemical and structural analysis of individual nanograins. Importantly, the results revealed the activation of vibrational modes normally forbidden in Raman spectroscopy and traditionally only observable in the infrared spectroscopy. Such activation arises from the intense localized electric field gradients (~3×10^8 V/m) at the tip apex, which alter conventional selection rules and make otherwise silent modes visible.

The detection of carbonate-related peaks, including those associated with $BaCO_3$ layers originating from ambient CO_2 chemisorption, highlights the significant influence of surface chemistry on $BaTiO_3$ nanoparticles. These findings confirm that TERS can detect and map chemisorbed monolayers, revealing distortions in molecular bonding environments that remain invisible to far-field Raman. The amplified local fields, with a measured enhancement factor near 4.6×10^5 (corresponding to a field enhancement of ~26), further emphasize the method's capacity for probing surface phenomena with unprecedented sensitivity. Moreover, by simultaneously accessing Raman and infrared modes within a single measurement, TERS provides a dual spectroscopic perspective that is unattainable with conventional spectroscopy techniques, which lacks comparable spatial resolution. This ability to capture both Raman and IR information at the nanoscale offers a more comprehensive understanding of material vibrational dynamics, bonding environments, and symmetry breaking. In doing so, it opens new avenues for scientists in material characterization, providing unprecedented insight into nanoscale processes. These observations underscore TERS's unique capability to bridge structural analysis with chemical specificity, enabling the study of symmetry breaking, chemisorption, and IR-mode activation at the nanoscale. Such insights are crucial for advancing applications in heterogeneous catalysis, semiconductor device engineering, and corrosion science.

7.2 Tracking the superparaelectric limit in individual $BaTiO_3$ nanoparticles

High-resolution TERS was employed to investigate the size-dependent phase transition in $BaTiO_3$ nanoparticles, with particular focus on LSPR shifts and vibrational mode variations. Structural properties of the $BaTiO_3$ powders were first analyzed by bulk X-ray diffraction using a Bruker D8 Advance diffractometer with Cu Kα radiation (λ = 1.5406 Å), confirming tetragonal crystallinity and detecting carbonate contamination from atmospheric CO_2. However, as XRD provides information averaged over many nanoparticles, detailed insight into the structural and vibrational properties of individual nanograins requires complementary high-resolution techniques such as TERS. By comparing nanoparticles of 18 nm and 44 nm diameter, a direct correlation was established between size and the ferroelectric-to-paraelectric transition, demonstrating finite-size effects on ferroelectric stability.

The Raman bands at 306 cm^{-1} and 720 cm^{-1}, characteristic of tetragonal $BaTiO_3$, were strongly attenuated in the 18 nm particle and partially suppressed in regions of the 44 nm grain. These nanoscale signatures indicate that reduced particle dimensions intensify depolarization fields and surface energy, favoring transformation toward the cubic paraelectric phase. Near-field mapping further revealed a core–shell structure, consisting of a ferroelectric core encapsulated by a paraelectric shell, consistent with theoretical models of polarization gradient stabilization.

LSPR mapping simultaneously exposed dielectric changes associated with the phase transition: a ~7 nm red-shift in the gold luminescence peak, corresponding to a refractive index variation of ~0.11, was measured for the smaller nanoparticle. This result is in agreement with bulk $BaTiO_3$ data and confirms stabilization of the paraelectric phase at the nanoscale. Overall, these observations demonstrate that TERS enables direct correlation between crystallographic structure, dielectric response, and local polarization dynamics with nanoscale precision. Such insights not only advance the understanding of size-driven ferroelectric transitions but also highlight the broader potential of TERS for guiding applications in nanoelectronics, sensing, and energy-storage technologies.

7.3 Uncovering the self-cleaning effect on the (100) $SrTiO_3$ surface

Nanoscale investigations revealed that CO_2 preferentially adsorbs on SrO-terminated (100) surfaces of $SrTiO_3$. Complementary theoretical modeling showed that such adsorption weakens the binding between SrO and TiO_2 layers, while high-resolution near-field imaging confirmed that

this process promotes SrO layer delamination and the subsequent nucleation of $SrCO_3$ nanograins. Consequently, the original surface evolves into TiO_2 terraces decorated with $SrCO_3$ grains, consistent with DFT calculations. This process may act as a self-cleaning pathway for photocatalytically active $SrTiO_3$ (100) following CO_2 exposure.

These findings were established by combining TERS experiments with density functional theory. After optimized hydrothermal preparation, the surface presented both SrO and TiO_2 terminations. AFM measurements indicated step heights of 0.1 nm and 0.3 nm, differing from the expected 0.2 nm, which was attributed to selective monolayer adsorption. Near-field spectra exhibited a pronounced peak at 1071 cm^{-1}, characteristic of $SrCO_3$, localized on SrO terraces, whereas TiO_2 showed negligible adsorption. These experimental observations aligned with DFT predictions.

DFT calculations further indicated a reduced binding energy between SrO and TiO_2 layers after CO_2 uptake. TERS analysis of aged samples supported this scenario, revealing nanograins with $SrCO_3$ Raman features at 1071 and 148 cm^{-1}, along with TiO_2 phonon modes at 683, 762, and 866 cm^{-1}. Altogether, the integration of TERS and DFT demonstrates that CO_2 adsorption occurs primarily on SrO terraces, alters interlayer interactions, and drives the formation of $SrCO_3$ domains through delamination. These results underscore the effectiveness of combining near-field spectroscopy with theoretical modeling to unravel surface interactions at the nanoscale and to guide strategies for enhancing $SrTiO_3$ performance in catalysis, carbon capture, and electronic technologies.

Summarizing the outcomes from Chapters 4–6, four main conclusions emerge. First, TERS enabled characterization of surface adsorption on $BaTiO_3$, achieving monolayer sensitivity and revealing activation of infrared-only vibrational modes. Second, the finite-size effects in $BaTiO_3$ were probed, showing suppression of tetragonal Raman bands and correlated LSPR shifts that mark the nanoscale ferroelectric-to-paraelectric transition, thereby defining the superparaelectric limit in individual nanoparticles. Third, TERS localized CO_2 adsorption on $SrTiO_3$ (100) surfaces, demonstrating selective accumulation on SrO terminations. Fourth, high-resolution near-field mapping identified delamination and $SrCO_3$ nanograin formation, revealing how adsorption modifies interlayer binding energies. These insights demonstrate the capability of TERS to combine structural mapping with chemical specificity, to capture both Raman and infrared-active modes, and to resolve nanoscale processes that remain invisible to conventional techniques. This

underscores TERS's transformative role in advancing perovskite materials for catalysis, nanoelectronics, and energy technologies.

7.4 Future work and outlook

7.4.1 Improving tip fabrication

Improving probe fabrication remains a central challenge in TERS. Although electrochemical etching can yield sharp tips, the method is slow and subject to some variability. Future directions should prioritize automated etching with closed-loop feedback, in which current and voltage are monitored in real time so the process halts at the optimal geometry. This approach would produce more consistent apex radii and cone angles while reducing operator dependence. To further accelerate and standardize fabrication, subsequent steps such as tip alignment, cutting, and mounting should also be automated, increasing throughput and reproducibility. Silver-coated tips provide strong enhancement but are limited by oxidation; the development of Ag–Au alloy or core–shell designs may offer a balance of enhancement and durability. Advanced techniques such as focused ion beam milling or nanopatterning could be applied to create custom plasmonic tips with multipod or bow-tie shapes that intensify local fields. Finally, integrating tips directly onto quartz tuning forks or alternative resonators would improve mechanical stability and expand TERS applicability, including measurements in liquid environments.

7.4.2 Instrumental improvements

On the optical side, incorporating tunable lasers would enable resonance excitation tuned to different perovskite compositions and vibrational modes, moving excitation closer to plasmonic resonances at the tip apex. While supercontinuum sources with wavelength-selective filters can, in principle, cover the visible spectrum, their use remains challenging due to filter complexity and insertion losses. Employing high-NA objectives could further enhance field confinement, and improving the signal-to-noise ratio or boosting CCD photon counts would allow detection of weaker signals while suppressing etaloning artifacts. Adaptive optics could correct aberrations from the objective and sample, ensuring that the laser remains precisely focused on the tip apex. Finally, careful environmental control, including inert gas purging and temperature stabilization, will prolong silver tip lifetimes and reduce sample degradation during extended measurements.

7.4.1 Leveraging artificial intelligence and machine learning in TERS

The integration of artificial intelligence and machine learning can play a transformative role in TERS by improving signal processing, enabling real-time spectral fitting, and automatically removing noise. Advanced algorithms can also optimize scanning parameters on-the-fly, adaptively adjusting acquisition conditions to maximize sensitivity and resolution. Beyond denoising and fitting, machine learning models can detect subtle spectral features, classify vibrational signatures, and predict tip–sample interactions, thereby accelerating data interpretation and enhancing reproducibility. In addition, predictive models could suggest optimal laser power, integration time, or scanning speed before measurement, minimizing trial-and-error adjustments. Reinforcement learning and neural network approaches may also learn from large spectral datasets to forecast system performance, guide parameter tuning, and continually improve over time, making TERS experiments faster, more reliable, and more informative.

7.4.2 Expanding spectral reach

Future directions in TERS should also focus on expanding its spectral reach and coupling with other advanced materials. By exploiting the activation of infrared vibrational modes within TERS, researchers can simultaneously access Raman and IR information at the nanoscale, achieving insights that are normally inaccessible with either technique alone. This dual capability provides a deeper understanding of vibrational dynamics, symmetry breaking, and photon–phonon–polariton interactions in complex systems.

8 BIBLIOGRAPHY

1. E. A. R. Assirey, “Perovskite synthesis, properties and their related biochemical and industrial application,” *Saudi Pharmaceutical Journal*, 27 (6), 817–829, 2019, [doi:10.1016/j.jsps.2019.05.003].
2. N. Nuraje et al., “Perovskite ferroelectric nanomaterials,” *Nanoscale*, 5 (19), 8752–8780, 2013, [doi:10.1039/C3NR02543H].
3. B. Szafraniak et al., “Semiconducting metal oxides: $SrTiO_3$, $BaTiO_3$ and $BaSrTiO_3$ in gas-sensing applications: A review,” 2, *Coatings*, 11 (2), 185, 2021, [doi:10.3390/coatings11020185].
4. P. M. Bulemo et al., “Recent advances in ABO_3 perovskites: Their gas-sensing performance as resistive-type gas sensors,” *J. Korean Ceram. Soc.*, 57 (1), 24–39, 2020, [doi:10.1007/s43207-019-00003-1].
5. K. V. Sopiha et al., “Band gap modulation of $SrTiO_3$ upon CO_2 adsorption,” *Phys. Chem. Chem. Phys.*, 19 (25), 16629–16637, 2017, [doi:10.1039/C7CP01462G].
6. C. Lichtensteiger et al., “Ferroelectric size effects,” *in Physics of Ferroelectrics: A Modern Perspective* 105, pp. 305-338. Springer Berlin Heidelberg, 2007, [doi:10.1007/978-3-540-34591-6_7].
7. A. Roelofs et al., “Towards the limit of ferroelectric nanosized grains,” *Nanotechnology*, 14 (2), 250, 2003, [doi:10.1088/0957-4484/14/2/328].
8. D. D. Fong et al., “Ferroelectricity in ultrathin perovskite films,” *Science*, 304 (5677), 1650–1653, 2004, [doi:10.1126/science.1098252].
9. G. Binnig et al., “Scanning Tunneling Microscopy—from Birth to Adolescence (Nobel Lecture),” *Angewandte Chemie International Edition in English*, 26 (7), 606–614, 1987, [doi:10.1002/anie.198706061].
10. G. Binnig et al., “Atomic Force Microscope,” *Phys. Rev. Lett.*, 56 (9), 930–933, 1986, [doi:10.1103/PhysRevLett.56.930].
11. R. García et al., “Attractive and repulsive tip-sample interaction regimes in tapping-mode atomic force microscopy,” *Phys. Rev. B*, 60 (7), 4961–4967, 1999, [doi:10.1103/PhysRevB.60.4961].
12. J. Rychen et al., “A low-temperature dynamic mode scanning force microscope operating in high magnetic fields,” *Review of Scientific Instruments*, 70 (6), 2765–2768, 1999, [doi:10.1063/1.1149842].
13. J. Ojeda et al., “Fourier Transform Infrared Spectroscopy for Molecular Analysis of Microbial Cells,” *Methods in molecular biology (Clifton, N.J.)*, 881, 187–211, 2012, [doi:10.1007/978-1-61779-827-6_8].
14. C. N. Banwell, *Fundamentals of molecular spectroscopy*, 1994.
15. B. Dietzek et al., “Introduction to the Fundamentals of Raman Spectroscopy,” *in Confocal Raman Microscopy*, T. Dieing et al., Eds., pp. 21–42, 2011, [doi:10.1007/978-3-642-12522-5_2].
16. U. Kreibig et al., *Optical Properties of Metal Clusters*, 2013.

17. W. A. Murray et al., “Plasmonic Materials,” *Advanced Materials*, 19 (22), 3771–3782, 2007, [doi:10.1002/adma.200700678].

18. G. H. Chan et al., “Localized Surface Plasmon Resonance Spectroscopy of Triangular Aluminum Nanoparticles,” *J. Phys. Chem. C*, 112 (36), 13958–13963, 2008, [doi:10.1021/jp804088z].

19. A. Ziashahabi et al., “The Effects of Surface Oxidation and Interparticle Coupling on Surface Plasmon Resonance Properties of Aluminum Nanoparticles as a UV Plasmonic Material,” *Procedia Materials Science*, 11, 434–437, 2015, [doi:10.1016/j.mspro.2015.11.030].

20. S. K. Jha, “Deep-ultraviolet surface-enhanced Raman scattering and fluorescence using aluminum nanostructures,” PhD Thesis, ETH Zurich, 2013,.

21. J. L. Hammond et al., “Localized Surface Plasmon Resonance as a Biosensing Platform for Developing Countries,” 2, *Biosensors*, 4 (2), 172–188, 2014, [doi:10.3390/bios4020172].

22. J. M. Sweet, “Benjamin Franklin’s purse,” *Notes and Records of the Royal Society of London*, 9 (2), 308–309, 1997, [doi:10.1098/rsnr.1952.0018].

23. C. C. Neacsu et al., “Scanning-probe Raman spectroscopy with single-molecule sensitivity,” *Phys. Rev. B*, 73 (19), 193406, 2006, [doi:10.1103/PhysRevB.73.193406].

24. F. J. Adrian, “Charge transfer effects in surface-enhanced Raman scatteringa,” *The Journal of Chemical Physics*, 77 (11), 5302–5314, 1982,.

25. J. R. Lombardi et al., “Time-dependent picture of the charge-transfer contributions to surface enhanced Raman spectroscopy,” *The Journal of chemical physics*, 126 (24), 2007,.

26. A. Campion et al., “Surface-enhanced Raman scattering,” *Chemical society reviews*, 27 (4), 241–250, 1998,.

27. M. Sun et al., “Chemical mechanism of surface-enhanced resonance Raman scattering via charge transfer in pyridine–Ag_2 complex,” *J Raman Spectroscopy*, 39 (3), 402–408, 2008, [doi:10.1002/jrs.1839].

28. H. Xu et al., “Electromagnetic contributions to single-molecule sensitivity in surface-enhanced Raman scattering,” *Phys. Rev. E*, 62 (3), 4318–4324, 2000, [doi:10.1103/PhysRevE.62.4318].

29. D. Roy et al., “Novel methodology for estimating the enhancement factor for tip-enhanced Raman spectroscopy,” *Journal of Applied Physics*, 105 (1), 013530, 2009, [doi:10.1063/1.3056155].

30. B. Pettinger et al., “Tip-enhanced Raman spectroscopy (TERS) of malachite green isothiocyanate at Au(111): bleaching behavior under the influence of high electromagnetic fields,” *Journal of Raman Spectroscopy*, 36 (6–7), 541–550, 2005, [doi:10.1002/jrs.1332].

31. K. F. Domke, “Tip-enhanced Raman spectroscopy: Topographic and chemical information on the nanoscale,” PhD Thesis, 2006,.

32. C. N. R. Rao, “Transition Metal Oxides,” *Annual Review of Physical Chemistry*, 40 (Volume 40,), 291–326, 1989, [doi:10.1146/annurev.pc.40.100189.001451].

33. M. E. Lines et al., *Principles and Applications of Ferroelectrics and Related Materials*, 2001.

34. D. G. Schlom et al., “A Thin Film Approach to Engineering Functionality into Oxides,” *Journal of the American Ceramic Society*, 91 (8), 2429–2454, 2008, [doi:10.1111/j.1551-2916.2008.02556.x].

35. M. Dawber et al., “Physics of thin-film ferroelectric oxides,” *Rev. Mod. Phys.*, 77 (4), 1083–1130, 2005, [doi:10.1103/RevModPhys.77.1083].

36. R. E. Cohen, “Origin of ferroelectricity in perovskite oxides,” *Nature*, 358 (6382), 136–138, 1992, [doi:10.1038/358136a0].

37. B. Ravel et al., “Local structure and the phase transitions of $BaTiO_3$,” *Ferroelectrics*, 206 (1), 407–430, 1998, [doi:10.1080/00150199808009173].

38. Q. Zhang et al., “The ferroelectric and cubic phases in $BaTiO_3$ ferroelectrics are also antiferroelectric,” *Proceedings of the National Academy of Sciences*, 103 (40), 14695–14700, 2006, [doi:10.1073/pnas.0606612103].

39. Y. Li et al., “Significant increase of Curie temperature in nano-scale $BaTiO_3$,” *Applied Physics Letters*, 105 (18), 182901, 2014, [doi:10.1063/1.4901169].

40. N. Erdman et al., “The structure and chemistry of the TiO_2-rich surface of $SrTiO_3$ (001),” *Nature*, 419 (6902), 55–58, 2002, [doi:10.1038/nature01010].

41. D. M. Kienzle et al., “Vacant-Site Octahedral Tilings on $SrTiO_3$ (001), the $(\sqrt{13} \times \sqrt{13})$ *R*33.7° Surface, and Related Structures,” *Phys. Rev. Lett.*, 106 (17), 176102, 2011, [doi:10.1103/PhysRevLett.106.176102].

42. M. R. Castell, “Scanning tunneling microscopy of reconstructions on the $SrTiO_3$(001) surface,” *Surface Science*, 505, 1–13, 2002, [doi:10.1016/S0039-6028(02)01393-6].

43. J. Y. Li et al., “Domain switching in polycrystalline ferroelectric ceramics,” *Nature Mater*, 4 (10), 776–781, 2005, [doi:10.1038/nmat1485].

44. S. Schlag et al., “Size driven phase transition in nanocrystalline $BaTiO_3$,” *Solid State Communications*, 91 (11), 883–887, 1994, [doi:10.1016/0038-1098(94)90007-8].

45. R. J. D. Tilley, *Perovskites: Structure-Property Relationships*, 2016.

46. D. B. Mitzi, “Introduction: Perovskites,” *Chem. Rev.*, 119 (5), 3033–3035, 2019, [doi:10.1021/acs.chemrev.8b00800].

47. C. Moure et al., “Recent advances in perovskites: Processing and properties,” *Progress in Solid State Chemistry*, 43 (4), 123–148, 2015, [doi:10.1016/j.progsolidstchem.2015.09.001].

48. B. Aïssa et al., “Oxide and Organic–Inorganic Halide Perovskites with Plasmonics for Optoelectronic and Energy Applications: A Contributive Review,” 9, *Catalysts*, 11 (9), 1057, 2021, [doi:10.3390/catal11091057].

49. A. Janotti et al., “Effects of doping on the lattice parameter of $SrTiO_3$,” *Applied Physics Letters*, 100 (26), 262104, 2012, [doi:10.1063/1.4730998].

50. S. Saha et al., “Structural and optical properties of paraelectric $SrTiO_3$,” *J. Phys.: Condens. Matter*, 12 (14), 3325, 2000, [doi:10.1088/0953-8984/12/14/309].

51. Q. Wu et al., “Understanding the Interactions of CO_2 with Doped and Undoped $SrTiO_3$,” *ChemSusChem*, 9 (14), 1889–1897, 2016, [doi:10.1002/cssc.201600498].

52. C. Luo et al., “Photocatalytic CO_2 reduction over $SrTiO_3$: Correlation between surface structure and activity,” *Applied Surface Science*, 447, 627–635, 2018, [doi:10.1016/j.apsusc.2018.04.049].

53. G. C. Manika et al., “On the Ferroelectric to Paraelectric Structural Transition of $BaTiO_3$ Micro-/Nanoparticles and Their Epoxy Nanocomposites,” 11, *Molecules*, 25 (11), 2686, 2020, [doi:10.3390/molecules25112686].

54. M. B. Smith et al., “Crystal structure and the paraelectric-to-ferroelectric phase transition of nanoscale $BaTiO_3$,” *J. Am. Chem. Soc.*, 130 (22), 6955–6963, 2008, [doi:10.1021/ja0758436].

55. I. C. Amaechi, “Particle size effect on the photocatalytic kinetics of pyroelectric barium titanate particles.,” PhD Thesis, Doctorat en sciences de l’énergie et des matériaux, 2020,.

56. M. Sendova et al., “Temperature-dependent, micro-Raman spectroscopic study of barium titanate nanoparticles,” *Journal of Raman Spectroscopy*, 46 (1), 25–31, 2015, [doi:10.1002/jrs.4595].

57. H. Kalhori et al., “Catalytic Activity of $BaTiO_3$ Nanoparticles for Wastewater Treatment: Piezo- or Sono-Driven?,” *ACS Appl. Nano Mater.*, 6 (3), 1686–1695, 2023, [doi:10.1021/acsanm.2c04568].

58. S. W. Lu et al., “Characterization of carbonate on $BaTiO_3$ ceramic powders,” *Materials Research Bulletin*, 35 (8), 1303–1312, 2000, [doi:10.1016/S0025-5408(00)00331-7].

59. S. D. M. Brown, “Resonance Raman spectroscopy of single-walled carbon nanotubes,” Thesis, Massachusetts Institute of Technology, 2000,.

60. M. S. Dresselhaus et al., “Raman spectroscopy of carbon nanotubes,” *Physics Reports*, 409 (2), 47–99, 2005, [doi:10.1016/j.physrep.2004.10.006].

61. A. Kukovecz et al., “A detailed Raman study on thin single-wall carbon nanotubes prepared by the HiPCO process,” *Eur. Phys. J. B*, 28 (2), 223–230, 2002, [doi:10.1140/epjb/e2002-00224-8].

62. J. D. Baniecki et al., “Chemisorption of water and carbon dioxide on nanostructured $BaTiO_3$–$SrTiO_3$(001) surfaces,” *Journal of Applied Physics*, 106 (5), 054109, 2009, [doi:10.1063/1.3169654].

63. G. Rakotovelo et al., “Adsorption of CO, CO_2 and NO molecules on a $BaTiO_3$ (0 0 1) surface,” *Surface Science*, 603 (9), 1221–1228, 2009, [doi:10.1016/j.susc.2009.03.006].

64. C. Baeumer et al., “Carbonate formation lowers the electrocatalytic activity of perovskite oxides for water electrolysis,” *Journal of Materials Chemistry A*, 9 (35), 19940–19948, 2021,.

65. B. Boga et al., “Role of $SrCO_3$ on Photocatalytic Performance of $SrTiO_3$-$SrCO_3$ Composites,” *Catalysts*, 12 (9), 978, 2022,.

66. M. del C. B. López et al., “Characterization of barium titanate powders: barium carbonate identification,” *Journal of the American Ceramic Society*, 82 (7), 1777–1786, 1999,.

67. G. Kolhatkar et al., “Nanoscale investigation of materials, chemical reactions, and biological systems by tip enhanced Raman spectroscopy – a review,” *Journal of Materials Chemistry C*, 6 (6), 1307–1319, 2018, [doi:10.1039/C7TC05688E].

68. M. Moskovits, “Surface-enhanced spectroscopy,” *Rev. Mod. Phys.*, 57 (3), 783–826, 1985, [doi:10.1103/RevModPhys.57.783].

69. H.-J. Freund et al., “Surface chemistry of carbon dioxide,” *Surface Science Reports*, 25 (8), 225–273, 1996, [doi:10.1016/S0167-5729(96)00007-6].

70. N. Kumar et al., “Accurate measurement of enhancement factor in tip-enhanced Raman spectroscopy through elimination of far-field artefacts,” *Applied Physics Letters*, 104 (12), 123106, 2014, [doi:10.1063/1.4869184].

71. A. Hartschuh et al., “Near-field Raman spectroscopy using a sharp metal tip,” *Journal of microscopy*, 210 (3), 234–240, 2003,.

72. Y. Huang et al., “Shell-Isolated Tip-Enhanced Raman and Fluorescence Spectroscopy,” *Angewandte Chemie*, 130 (25), 7645–7649, 2018,.

73. E. J. Ayars et al., “Electric field gradient effects in Raman spectroscopy,” *Physical Review Letters*, 85 (19), 4180, 2000,.

74. W. J. Merz, “The electric and optical behavior of $BaTiO_3$ single-domain crystals,” *Phys. Rev.*, 76 (8), 1221–1225, 1949, [doi:10.1103/PhysRev.76.1221].

75. M. Veithen et al., “Temperature dependence of the electro-optic tensor and refractive indices of $BaTiO_3$ from first principles,” *Phys. Rev. B*, 71 (13), 132101, 2005, [doi:10.1103/PhysRevB.71.132101].

76. J. Zegenhagen et al., “Microscopic structure and structuring of perovskite surfaces and interfaces: $SrTiO_3$, $RBa_2Cu_3O_{7-\delta}$,” *Applied Physics A: Materials Science & Processing*, 67 (6), 711–722, 1998, [doi:10.1007/s003390050843].

77. J. Hong et al., “Water mediated growth of oriented single crystalline $SrCO_3$ nanorod arrays on strontium compounds,” *Sci Rep*, 11 (1), 3368, 2021, [doi:10.1038/s41598-021-82651-0].

78. M. R. Filip et al., “The geometric blueprint of perovskites,” *Proceedings of the National Academy of Sciences*, 115 (21), 5397–5402, 2018, [doi:10.1073/pnas.1719179115].

79. C. Rossel, “Perovskites: a class of materials with multiple functionalities and applications,” *EDP Sciences*, 49 (3), 10–14, 2018, [doi:10.1051/epn/2018301].

80. J. Xu et al., “Perovskites–Revisiting the venerable ABX_3 family with organic flexibility and new applications.”

81. Y. H. Kim et al., “Metal halide perovskite light emitters,” *National Academy of Sciences*, 113 (42), 11694–11702, 2016, [doi:10.1073/pnas.1607471113].

82. H. Koinuma, “Chemistry and electronics of oxides from carbon dioxide to perovskite,” *Elsevier BV*, 486 (1–2), 2–10, 2005, [doi:10.1016/j.tsf.2004.11.243].

83. Y. Jiang et al., “Optical bandgap tuning of ferroelectric semiconducting $BiFeO_3$-based oxide perovskites via chemical substitution for photovoltaics,” *American Institute of Physics*, 8 (12), 2018, [doi:10.1063/1.5053634].

84. R. J. H. Voorhoeve et al., “Perovskite oxides: materials science in catalysis,” *American Association for the Advancement of Science*, 195 (4281), 827–833, 1977, [doi:10.1126/science.195.4281.827].

85. L. Zhang et al., “Advances in the application of perovskite materials,” *Nano-Micro Lett.*, 15 (1), 177, 2023, [doi:10.1007/s40820-023-01140-3].

86. P. S. Dobal et al., “Phase transitions in $Ba_{1-x}Sr_xTiO_3$ cHigh-permittivity perovskite thin films for dynamic random-access memorieseramics,” *Taylor & Francis*, 29 (3–4), 1–10, 2002, [doi:10.1080/07315170214359].

87. A. I. Kingon et al., “High-permittivity perovskite thin films for dynamic random-access memories,” *Springer Nature*, 21 (7), 46–52, 1996, [doi:10.1557/s0883769400035910].

88. S. Sasikumar et al., “Electronic structure, optical and chemical bonding properties of strontium doped barium titanate,” *Elsevier BV*, 206, 163752–163752, 2019, [doi:10.1016/j.ijleo.2019.163752].

89. A. Pancotti et al., “Surface structure characterization of a (√5 × √5)-R26.6° reconstruction of strontium titanate (001) by X-ray photoelectron diffraction,” *Surface Science*, 715, 121937, 2022, [doi:10.1016/j.susc.2021.121937].

90. C.-W. Chang et al., “Nanoconfinement of metal oxide MgO and ZnO in zeolitic imidazolate framework ZIF-8 for CO_2 adsorption and regeneration,” *Journal of Hazardous Materials*, 400, 122974, 2020, [doi:10.1016/j.jhazmat.2020.122974].

91. N. D. Parkyns, “The surface properties of metal oxides. Part II. An infrared study of the adsorption of carbon dioxide on γ-alumina,” *J. Chem. Soc. A*, (0), 410–417, 1969, [doi:10.1039/J19690000410].

92. R. N. Smith et al., “Infra-red study of carbon-oxygen surface complexes,” *Trans. Faraday Soc.*, 62 (0), 2280–2286, 1966, [doi:10.1039/TF9666202280].

93. W. I. Stuart et al., “Adsorption of water and carbon dioxide on beryllium oxide,” *Trans. Faraday Soc.*, 61 (0), 2763–2771, 1965, [doi:10.1039/TF9656102763].

94. A. Rüdiger et al., “Nanosize ferroelectric oxides–tracking down the superparaelectric limit,” *Appl. Phys. A*, 80, 1247–1255, 2005, [doi:10.1007/s00339-004-3167-z].

95. D. Karpov et al., “Three-dimensional imaging of vortex structure in a ferroelectric nanoparticle driven by an electric field,” *Nat Commun*, 8 (1), 280, 2017, [doi:10.1038/s41467-017-00318-9].

96. P. A. P. Nascente, “Materials characterization by X-ray photoelectron spectroscopy,” *Journal of Molecular Catalysis A: Chemical*, 228 (1), 145–150, 2005, [doi:10.1016/j.molcata.2004.09.075].

97. H. Lipson, “Summarized proceedings of the fortieth anniversary celebrations of the discovery of X-ray diffraction - London, October 1952,” *Br. J. Appl. Phys.*, 4 (2), 33, 1953, [doi:10.1088/0508-3443/4/2/401].

98. J. M. Walls et al., *Surface Science Techniques*, 2013.

99. K. Urban, “The long road to visible atoms,” *German Research*, 30 (2), 13–15, 2008, [doi:10.1002/germ.200890023].

100. T. Mulvey, “Fifty years of high resolution electron microscopy,” *Phys. Bull.*, 34 (7), 274, 1983, [doi:10.1088/0031-9112/34/7/025].

101. J. E. Castle et al., “Applications of the scanning electron microscope to oxide surfaces,” *Anti-Corrosion Methods and Materials*, 13 (12), 6–11, 1966, [doi:10.1108/eb006753].

102. C. F. Quate, “Scanned probe microscopies,” *AIP Conference Proceedings*, 241 (1), 1–8, 1991, [doi:10.1063/1.41412].

103. K. E. Carr et al., “Scanning electron microscopy,” *Histopathology*, 6 (1), 3–24, 1982, [doi:10.1111/j.1365-2559.1982.tb02698.x].

104. G. LANDSBERG, “Eine neue Erscheinung bei der Lichtzerstreuung in Krystallen,” *Naturwissenschaften*, 16, 558, 1928,.

105. C. V. Raman et al., “A new type of secondary radiation,” *Nature*, 121 (3048), 501–502, 1928, [doi:10.1038/121501c0].

106. C. V. Raman, “A change of wave-length in light scattering,” *Nature*, 121 (3051), 619–619, 1928, [doi:10.1038/121619b0].

107. C. V. Raman et al., “The optical analogue of the Compton effectStimulated optical radiation in ruby,” *Nature*, 121 (3053), 711–711, 1928, [doi:10.1038/121711a0].

108. T. H. Maiman, “Stimulated optical radiation in ruby,” *Nature*, 187 (4736), 493–494, 1960, [doi:10.1038/187493a0].

109. E. H. Synge, “XXXVIII. *A suggested method for extending microscopic resolution into the ultra-microscopic region*,” *The London, Edinburgh, and Dublin Philosophical Magazine and Journal of Science*, 6 (35), 356–362, 1928, [doi:10.1080/14786440808564615].

110. E. A. Ash et al., “Super-resolution aperture scanning microscope,” *Nature*, 237 (5357), 510–512, 1972, [doi:10.1038/237510a0].

111. D. W. Pohl et al., “Scanning near-field optical microscopy (SNOM): Basic principles and some recent developments,” *in Scanning Microscopy Technologies and Applications* 0897, pp. 84–90, 1988, [doi:10.1117/12.944518].

112. M. Fleischmann et al., “Raman spectra of pyridine adsorbed at a silver electrode,” *Chemical Physics Letters*, 26 (2), 163–166, 1974, [doi:10.1016/0009-2614(74)85388-1].

113. J. Wessel, “Surface-enhanced optical microscopy,” *J. Opt. Soc. Am. B, JOSAB*, 2 (9), 1538–1541, 1985, [doi:10.1364/JOSAB.2.001538].

114. R. M. Stöckle et al., “Nanoscale chemical analysis by tip-enhanced Raman spectroscopy,” *Chemical Physics Letters*, 318 (1), 131–136, 2000, [doi:10.1016/S0009-2614(99)01451-7].

115. N. Hayazawa et al., “Metallized tip amplification of near-field Raman scattering,” *Optics Communications*, 183 (1), 333–336, 2000, [doi:10.1016/S0030-4018(00)00894-4].

116. R. Zhang et al., “Chemical mapping of a single molecule by plasmon-enhanced Raman scattering,” *Nature*, 498 (7452), 82–86, 2013, [doi:10.1038/nature12151].

117. S. Berweger et al., “Optical nanocrystallography with tip-enhanced phonon Raman spectroscopy,” *Nature Nanotech*, 4 (8), 496–499, 2009, [doi:10.1038/nnano.2009.190].

118. D. Courjon et al., *Le champ proche optique: théorie et applications*, 2001,.

119. H. Xie et al., “Enhanced Accuracy of Force Application for AFM Nanomanipulation Using Nonlinear Calibration of Optical Levers,” *IEEE Sensors Journal*, 8 (8), 1478–1485, 2008, [doi:10.1109/JSEN.2008.920722].

120. E. Meyer et al., “Introduction to Scanning Probe Microscopy,” *in Scanning Probe Microscopy: The Lab on a Tip*, E. Meyer et al., Eds., pp. 1–13, 2004, [doi:10.1007/978-3-662-09801-1_1].

121. R. García et al., “Dynamic atomic force microscopy methods,” *Surface Science Reports*, 47 (6), 197–301, 2002, [doi:10.1016/S0167-5729(02)00077-8].

122. T. Strahlendorff et al., “Tip wear and tip breakage in high-speed atomic force microscopes,” *Ultramicroscopy*, 201, 28–37, 2019, [doi:10.1016/j.ultramic.2019.03.013].

123. Y. Martin et al., “Atomic force microscope–force mapping and profiling on a sub 100-Å scale,” *Journal of Applied Physics*, 61 (10), 4723–4729, 1987, [doi:10.1063/1.338807].

124. T. R. Albrecht et al., “Frequency modulation detection using high-Q cantilevers for enhanced force microscope sensitivity,” *Journal of Applied Physics*, 69 (2), 668–673, 1991, [doi:10.1063/1.347347].

125. P. Günther et al., “Scanning near-field acoustic microscopy,” *Appl. Phys. B*, 48 (1), 89–92, 1989, [doi:10.1007/BF00694423].

126. K. Karrai et al., “Piezoelectric tip-sample distance control for near field optical microscopes,” *Applied Physics Letters*, 66 (14), 1842–1844, 1995, [doi:10.1063/1.113340].

127. F. J. Giessibl, “High-speed force sensor for force microscopy and profilometry utilizing a quartz tuning fork,” *Applied Physics Letters*, 73 (26), 3956–3958, 1998, [doi:10.1063/1.122948].

128. A. J. Stein, “A metrological atomic force microscope,” Thesis, Massachusetts Institute of Technology, 2002,.

129. B. Schrader, *Infrared and Raman Spectroscopy: Methods and Applications*, 2008,.

130. K. T. Schomacker et al., “Measurements of the absolute Raman cross sections of benzene,” *The Journal of Chemical Physics*, 85 (8), 4240–4247, 1986, [doi:10.1063/1.451795].

131. A. Hiraya et al., “Direct absorption spectra of jet-cooled benzene in 130–260 nm,” *The Journal of Chemical Physics*, 94 (12), 7700–7706, 1991, [doi:10.1063/1.460155].

132. A. Yildiz et al., “Kinesin Walks Hand-Over-Hand,” *Science*, 303 (5658), 676–678, 2004, [doi:10.1126/science.1093753].

133. U. Ch. Fischer et al., “Submicroscopic contact imaging with visible light by energy transfer,” *Applied Physics Letters*, 40 (3), 195–197, 1982, [doi:10.1063/1.93050].

134. D. W. Pohl et al., “Optical stethoscopy: Image recording with resolution λ/20,” *Applied Physics Letters*, 44, 651–653, 1984, [doi:10.1063/1.94865].

135. “Breaking the Diffraction Barrier: Optical Microscopy on a Nanometric Scale | Science,” <https://www.science.org/doi/abs/10.1126/science.251.5000.1468> (accessed 5 March 2025).

136. A. Harootunian et al., “Super-resolution fluorescence near-field scanning optical microscopy,” *Applied Physics Letters*, 49 (11), 674–676, 1986,.

137. S. Kirstein, “Scanning near-field optical microscopy,” *Current Opinion in Colloid & Interface Science*, 4 (4), 256–264, 1999, [doi:10.1016/S1359-0294(99)90005-5].

138. M. A. Paesler et al., “Near-Field Optics: Theory, Instrumentation, and Applications,” 1997.

139. P. Colomban et al., “On-site Raman identification and dating of ancient/modern stained glasses at the Sainte-Chapelle, Paris,” *Journal of Cultural Heritage*, 8 (3), 242–256, 2007, [doi:10.1016/j.culher.2007.04.002].

140. I. Freestone et al., “The Lycurgus Cup — A Roman nanotechnology,” *Gold Bull*, 40 (4), 270–277, 2007, [doi:10.1007/BF03215599].

141. M. Faraday, “X. The Bakerian Lecture. —Experimental relations of gold (and other metals) to light,” *Philosophical Transactions of the Royal Society of London*, 147, 145–181, 1997, [doi:10.1098/rstl.1857.0011].

142. G. Mie, “Contributions to the optics of turbid media, particularly of colloidal metal solutions,” pp. 377–445, 1976.

143. N. W. Ashcroft, “Solid State Physics,” *Thomson Learning*, 39, 1976.

144. P. B. Johnson et al., “Optical Constants of the Noble Metals,” *Phys. Rev. B*, 6 (12), 4370–4379, 1972, [doi:10.1103/PhysRevB.6.4370].

145. K. Kolwas et al., “Impact of the Interband Transitions in Gold and Silver on the Dynamics of Propagating and Localized Surface Plasmons,” *Nanomaterials (Basel)*, 10 (7), 1411, 2020, [doi:10.3390/nano10071411].

146. R. H. Ritchie, “Plasma Losses by Fast Electrons in Thin Films,” *Phys. Rev.*, 106 (5), 874–881, 1957, [doi:10.1103/PhysRev.106.874].

147. B. Hecht et al., “Local Excitation, Scattering, and Interference of Surface Plasmons,” *Phys. Rev. Lett.*, 77 (9), 1889–1892, 1996, [doi:10.1103/PhysRevLett.77.1889].

148. H. Ditlbacher et al., “Fluorescence imaging of surface plasmon fields,” *Applied physics letters*, 80 (3), 404–406, 2002,.

149. Z. Han et al., “Chapter 5 - Waveguiding with Surface Plasmon Polaritons,” *in Handbook of Surface Science* 4, N. V. Richardson et al., Eds., pp. 137–187, 2014, [doi:10.1016/B978-0-444-59526-3.00005-7].

150. L. M. Liz-Marzán et al., “Synthesis of Nanosized Gold−Silica Core−Shell Particles,” *Langmuir*, 12 (18), 4329–4335, 1996, [doi:10.1021/la9601871].

151. S. Xu et al., “Tetraurea calix[4]arenes with sulfur functions: synthesis, dimerization to capsules, and self-assembly on gold,” *Org. Biomol. Chem.*, 5 (3), 558–568, 2007, [doi:10.1039/B616358K].

152. J. C. M. Garnett et al., “VII. Colours in metal glasses, in metallic films, and in metallic solutions.—II,” *Philosophical Transactions of the Royal Society of London. Series A, Containing Papers of a Mathematical or Physical Character*, 205 (387–401), 237–288, 1997, [doi:10.1098/rsta.1906.0007].

153. J. Zhang et al., “Sample induced intensity variations of localized surface plasmon resonance in tip-enhanced Raman spectroscopy,” *Opt. Express*, 28 (18), 25998, 2020, [doi:10.1364/OE.403345].

154. D. L. Jeanmaire et al., “Surface raman spectroelectrochemistry: Part I. Heterocyclic, aromatic, and aliphatic amines adsorbed on the anodized silver electrode,” *Journal of Electroanalytical Chemistry and Interfacial Electrochemistry*, 84 (1), 1–20, 1977, [doi:10.1016/S0022-0728(77)80224-6].

155. M. G. Albrecht et al., “Anomalously intense Raman spectra of pyridine at a silver electrode,” *ACS Publications*, 1 May 2002, [doi:10.1021/ja00457a071] (accessed 23 March 2025).

156. K. Kneipp et al., Eds., *Surface-Enhanced Raman Scattering*, 2006, [doi:10.1007/3-540-33567-6].

157. M. Moskovits, “Surface roughness and the enhanced intensity of Raman scattering by molecules adsorbed on metals,” *The Journal of Chemical Physics*, 69 (9), 4159–4161, 1978, [doi:10.1063/1.437095].

158. K. Kneipp et al., “Single Molecule Detection Using Surface-Enhanced Raman Scattering (SERS),” *Phys. Rev. Lett.*, 78 (9), 1667–1670, 1997, [doi:10.1103/PhysRevLett.78.1667].

159. S. Nie et al., “Probing Single Molecules and Single Nanoparticles by Surface-Enhanced Raman Scattering,” *Science*, 275 (5303), 1102–1106, 1997, [doi:10.1126/science.275.5303.1102].

160. B. Pettinger et al., “Surface plasmon enhanced Raman scattering frequency and angular resonance of Raman scattered light from pyridine on Au, Ag and Cu electrodes,” *Surface Science*, 101 (1), 409–416, 1980, [doi:10.1016/0039-6028(80)90637-8].

161. D. A. Weitz et al., “Excitation spectra of surface-enhanced Raman scattering on silver-island films,” *Opt. Lett., OL*, 7 (4), 168–170, 1982, [doi:10.1364/OL.7.000168].

162. Jiang et al., “Single Molecule Raman Spectroscopy at the Junctions of Large Ag Nanocrystals,” *J. Phys. Chem. B*, 107 (37), 9964–9972, 2003, [doi:10.1021/jp034632u].

163. J. I. Gersten et al., “Theory of Enhance I Light Scattering from Molecules Adsorbed at the Metal-Solution Interface,” *Phys. Rev. Lett.*, 43 (2), 147–150, 1979, [doi:10.1103/PhysRevLett.43.147].

164. Y. Xie et al., “Adsorption and photon-driven charge transfer of pyridine on a cobalt electrode analyzed by surface enhanced Raman spectroscopy and relevant theories,” *Journal of Electroanalytical Chemistry*, 554, 417–425, 2003,.

165. E. Le Ru et al., *Principles of Surface-Enhanced Raman Spectroscopy: and related plasmonic effects*, 2008.

166. D. J. Masiello et al., “Many-body theory of surface-enhanced Raman scattering,” *Phys. Rev. A*, 78 (4), 042505, 2008, [doi:10.1103/PhysRevA.78.042505].

167. D. J. Masiello et al., “On the linear response and scattering of an interacting molecule-metal system,” *The Journal of chemical physics*, 132 (6), 2010.

168. E. H. Synge, “XXXVIII. A suggested method for extending microscopic resolution into the ultra-microscopic region,” *The London, Edinburgh, and Dublin Philosophical Magazine and Journal of Science*, 1928, [doi:10.1080/14786440808564615].

169. E. A. Ash et al., “Super-resolution aperture scanning microscope,” *Nature*, 237 (5357), 510–512, 1972.

170. E. Betzig et al., “Near-field diffraction by a slit: implications for superresolution microscopy,” *Appl. Opt., AO*, 25 (12), 1890–1900, 1986, [doi:10.1364/AO.25.001890].

171. M. Chaigneau, “Imagerie et spectroscopies en champ proche optique : de la nano-sonde à la caractérisation de matériaux,” phd thesis, Université de Nantes, 2007,.

172. F. De Fornel et al., “First images obtained in the near infrared spectrum with the photon scanning tunneling microscope,” *Optics Communications*, 102 (1), 1–5, 1993, [doi:10.1016/0030-4018(93)90462-E].

173. D. Courjon et al., “External and internal reflection near field microscopy: experiments and results,” *Appl. Opt., AO*, 29 (26), 3734–3740, 1990, [doi:10.1364/AO.29.003734].

174. J. Xu et al., “Determining structural and chemical heterogeneities of surface species at the single-bond limit,” *Science*, 371 (6531), 818–822, 2021, [doi:10.1126/science.abd1827].

175. M. Asghari-Khiavi et al., “Exploring the origin of tip-enhanced Raman scattering; preparation of efficient TERS probes with high yield,” *Journal of Raman Spectroscopy*, 43 (2), 173–180, 2012, [doi:10.1002/jrs.3021].

176. B.-S. Yeo et al., “Tip-enhanced Raman Spectroscopy – Its status, challenges and future directions,” *Chemical Physics Letters*, 472 (1), 1–13, 2009, [doi:10.1016/j.cplett.2009.02.023].

177. B. Ren et al., “Preparation of gold tips suitable for tip-enhanced Raman spectroscopy and light emission by electrochemical etching,” *Review of Scientific Instruments*, 75 (4), 837–841, 2004, [doi:10.1063/1.1688442].

178. O. E. Hüsser et al., “High-resolution deposition and etching of metals with a scanning electrochemical microscope,” *Journal of Vacuum Science & Technology B: Microelectronics Processing and Phenomena*, 6 (6), 1873–1876, 1988, [doi:10.1116/1.584191].

179. S.-Y. Ding et al., “Electromagnetic theories of surface-enhanced Raman spectroscopy,” *Chem. Soc. Rev.*, 46 (13), 4042–4076, 2017, [doi:10.1039/C7CS00238F].

180. J. Plathier et al., “Relation between plasmonic tip emission and electromagnetic enhancement evidenced in tip-enhanced Raman spectroscopy,” *Journal of Raman Spectroscopy*, 48 (12), 1863–1870, 2017, [doi:10.1002/jrs.5260].

181. M. Bakhtbidar et al., “Direct observation of carbonate chemisorption on barium titanate surfaces by tip-enhanced Raman spectroscopy,” *Advanced Materials Interfaces*, 11 (15), 2300993, 2024, [doi:10.1002/admi.202300993].

182. E. Heifets et al., “First-principles calculations for $SrTiO_3$(100) surface structure,” *Surface Science*, 513 (1), 211–220, 2002, [doi:10.1016/S0039-6028(02)01730-2].

183. T. Kubo et al., “Surface structure of $SrTiO_3$(100),” *Surface Science*, 542 (3), 177–191, 2003, [doi:10.1016/S0039-6028(03)00998-1].

184. J. Padilla et al., “Ab initio study of $SrTiO_3$ surfaces,” *Surface Science*, 418 (1), 64–70, 1998, [doi:10.1016/S0039-6028(98)00670-0].

185. J. Chang et al., “Atomically flat single-terminated $SrTiO_3$ (111) surface,” *Applied Physics Letters*, 92 (15), 152910, 2008, [doi:10.1063/1.2913005].

186. X. Li et al., “Water Adsorption and Dissociation on $BaTiO_3$ Single-Crystal Surfaces,” *J. Phys. Chem. C*, 118 (29), 15910–15918, 2014, [doi:10.1021/jp5051386].

187. J. D. Baniecki et al., “Chemisorption of water and carbon dioxide on nanostructured $BaTiO_3$–$SrTiO_3$(001) surfaces,” *Journal of Applied Physics*, 106 (5), 054109, 2009, [doi:10.1063/1.3169654].

188. C. He et al., “Unlocking the Potential of Halide Perovskites Through Doping,” *CCS Chemistry*, 5 (9), 1961–1972, 2023, [doi:10.31635/ccschem.023.202303019].

189. J. Zhao et al., “Screening Perovskites from ABO_3 Combinations Generated by Constraint Satisfaction Techniques Using Machine Learning,” *ACS Omega*, 7 (12), 10483–10491, 2022, [doi:10.1021/acsomega.2c00002].

190. N. Setter et al., “Ferroelectric thin films: Review of materials, properties, and applications,” *J. Appl. Phys.*, 100, 051606, 2006, [doi:10.1063/1.2336999].

191. V. Buscaglia et al., “$BaTiO_3$-Based Ceramics: Fundamentals, Properties and Applications,” *in Encyclopedia of Materials: Technical Ceramics and Glasses*, M. Pomeroy, Ed., pp. 311–344, 2021, [doi:10.1016/B978-0-12-803581-8.12132-0].

192. S. V. Kalinin, “Local potential and polarization screening on ferroelectric surfaces,” *Phys. Rev. B*, 63 (12), 2001, [doi:10.1103/PhysRevB.63.125411].

193. M. Setvin et al., “Polarity compensation mechanisms on the perovskite surface $KTaO_3$(001),” *Science*, 359 (6375), 572–575, 2018, [doi:10.1126/science.aar2287].

194. L. L. Rusevich et al., “The electronic properties of $SrTiO_3$-δ with oxygen vacancies or substitutions,” *Sci Rep*, 11 (1), 23341, 2021, [doi:10.1038/s41598-021-02751-9].

195. R. Kamel et al., “Structural and magnetic studies on perovskite rare-earth manganites (Nd1−xGdx)0.55Sr0.45MnO_3 (x=0, 0.1, 0.3 and 0.5): Observation of two-step magnetization and negative magnetization behavior,” *Journal of Magnetism and Magnetic Materials*, 426, 757–766, 2017, [doi:10.1016/j.jmmm.2016.10.129].

196. M. Kim et al., “Superconductivity in (Ba,K)SbO_3,” *Nat. Mater.*, 21 (6), 627–633, 2022, [doi:10.1038/s41563-022-01203-7].

197. J. T. Mefford et al., “Water electrolysis on La1−xSrxCoO_3−δ perovskite electrocatalysts,” *Nat Commun*, 7 (1), 11053, 2016, [doi:10.1038/ncomms11053].

198. S. Surendhar et al., “Enhancing the efficiency of gas sensing on perovskite $BaTiO_3$ nanoparticles using dynamic shock wave flow environment,” *Ceramics International*, 50 (13, Part B), 23710–23720, 2024, [doi:10.1016/j.ceramint.2024.04.094].

199. S. S. Patil et al., “La-Fe-O Perovskite Based Gas Sensors: Recent Advances and Future Challenges,” *ACS Omega*, 9 (28), 29994–30014, 2024, [doi:10.1021/acsomega.4c00334].

200. A. Hadj Youssef et al., “Symmetry-Forbidden-Mode Detection in $SrTiO_3$ Nanoislands with Tip-Enhanced Raman Spectroscopy,” *J. Phys. Chem. C*, 125 (11), 6200–6208, 2021, [doi:10.1021/acs.jpcc.0c10938].

201. D. Chapron et al., “Characterization of oxygen vacancies in $SrTiO_3$ by means of anelastic and Raman spectroscopy,” *Journal of Applied Physics*, 126 (15), 154101, 2019, [doi:10.1063/1.5115106].

202. M. Gaidi et al., “Microfabricated $SrTiO_3$ ridge waveguides,” *Applied Physics Letters*, 86 (22), 221106, 2005, [doi:10.1063/1.1942634].

203. E. J. Tarsa et al., “Growth-related stress and surface morphology in homoepitaxial $SrTiO_3$ films,” *Applied Physics Letters*, 68 (4), 490–492, 1996, [doi:10.1063/1.116376].

204. R. J. Kennedy et al., “The influence of lattice mismatch and film thickness on the growth of TiO_2 on $LaAlO_3$ and $SrTiO_3$ substrates,” *Journal of Crystal Growth*, 252 (1), 333–342, 2003, [doi:10.1016/S0022-0248(02)02514-9].

205. I. Velasco-Davalos et al., “Realization of single-termination $SrTiO_3$ (100) surfaces by a microwave-induced hydrothermal process,” *Applied Physics Letters*, 103 (20), 202905, 2013, [doi:10.1063/1.4831681].

206. K. Szot et al., “Surfaces of reduced and oxidized $SrTiO_3$ from atomic force microscopy,” *Phys. Rev. B*, 60 (8), 5909–5926, 1999, [doi:10.1103/PhysRevB.60.5909].

207. G. Koster et al., “Surface morphology determined by (0 0 1) single-crystal $SrTiO_3$ termination,” *Physica C: Superconductivity*, 339 (4), 215–230, 2000, [doi:10.1016/S0921-4534(00)00363-4].

208. K. V. Sopiha et al., “Band gap modulation of $SrTiO_3$ upon CO_2 adsorption,” *Physical Chemistry Chemical Physics*, 19 (25), 16629–16637, 2017, [doi:10.1039/C7CP01462G].

209. S. Carlotto et al., “Adsorption of CO and formation of carbonates at steps of pure and Co-doped $SrTiO_3$ surfaces by DFT calculations,” *Applied Surface Science*, 364, 522–527, 2016, [doi:10.1016/j.apsusc.2015.12.194].

210. U. Terranova et al., “Mechanisms of carbon dioxide reduction on strontium titanate perovskites,” *Journal of Materials Chemistry A*, 8 (18), 9392–9398, 2020, [doi:10.1039/D0TA01502D].

211. K. V. Sopiha et al., “Suppression of surfaces states at cubic perovskite (001) surfaces by CO_2 adsorption,” *Physical Chemistry Chemical Physics*, 20 (27), 18828–18836, 2018,.

212. K. V. Sopiha et al., “Suppression of surfaces states at cubic perovskite (001) surfaces by CO_2 adsorption,” *Phys. Chem. Chem. Phys.*, 20 (27), 18828–18836, 2018, [doi:10.1039/C8CP02535E].

213. K. Itoh et al., “Crystal structure of $BaTiO_3$ in the cubic phase,” *Ferroelectrics*, 63 (1), 29–37, 1985, [doi:10.1080/00150198508221381].

214. X. Xi, *Nanomaterial-based Biosensors for Detection of Salmonella Typhimurium and Avian Influenza Virus H5N1 in Poultry*, 2021,.

215. V. P. Pavlovic et al., “Raman Responses in Mechanically Activated 3,” *Journal of the American Ceramic Society*, 97 (2), 601–608, 2014, [doi:10.1111/jace.12423].

216. Y. Shiratori et al., “Raman scattering studies on nanocrystalline $BaTiO_3$ Part I—isolated particles and aggregates,” *Journal of Raman Spectroscopy*, 38 (10), 1288–1299, 2007, [doi:10.1002/jrs.1764].

217. F. Hao et al., “Ferroelectric and dielectric properties of sub-10 nm $BaTiO_3$ nanoparticles,” *Journal of Asian Ceramic Societies*, 13 (1), 107–115, 2025, [doi:10.1080/21870764.2025.2463162].

218. K. Aicher et al., “$BaTiO_3$ Nanoparticle Interfaces in Contact: Ferroelectricity Drives Tribochemically Induced Oxygen Radical Formation,” *Langmuir*, 40 (51), 26928–26935, 2024, [doi:10.1021/acs.langmuir.4c03390].

219. A. K. Kushwaha et al., “Surface-Induced effects in ferroelectric $BaTiO_3$ thin films,” *Surfaces and Interfaces*, 56, 105589, 2025, [doi:10.1016/j.surfin.2024.105589].

220. T. Hoshina et al., “Domain Size Effect on Dielectric Properties of Barium Titanate Ceramics,” *Jpn. J. Appl. Phys.*, 47 (9S), 7607, 2008, [doi:10.1143/JJAP.47.7607].

221. T. Hoshina et al., “Composite structure and size effect of barium titanate nanoparticles,” *Applied Physics Letters*, 93 (19), 192914, 2008, [doi:10.1063/1.3027067].

222. M. Nicklaus, *Tip-Enhanced Raman spectroscopy for nanoelectronics*, PhD thesis, 2014.

223. T.-X. Huang et al., “Tip-enhanced Raman spectroscopy: tip-related issues,” *Anal Bioanal Chem*, 407 (27), 8177–8195, 2015, [doi:10.1007/s00216-015-8968-8].

224. C. Blum et al., “Tip-enhanced Raman spectroscopy – an interlaboratory reproducibility and comparison study,” *Journal of Raman Spectroscopy*, 45 (1), 22–31, 2014, [doi:10.1002/jrs.4423].

225. T. L. Vasconcelos et al., “Optical nanoantennas for tip-enhanced Raman spectroscopy,” *IEEE Journal of Selected Topics in Quantum Electronics*, 27 (1), 1–11, 2021, [doi:10.1109/JSTQE.2020.3008526].

226. V. Poborchii et al., “Optimization of tip material and shape for near-UV TERS in Si structures,” *Journal of Raman Spectroscopy*, 40 (10), 1377–1385, 2009, [doi:10.1002/jrs.2417].

227. J. Stadler et al., “Tip-enhanced Raman spectroscopic imaging of patterned thiol monolayers,” *Beilstein J. Nanotechnol.*, 2 (1), 509–515, 2011, [doi:10.3762/bjnano.2.55].

228. C.-N. Lok et al., “Silver nanoparticles: partial oxidation and antibacterial activities,” *J Biol Inorg Chem*, 12 (4), 527–534, 2007, [doi:10.1007/s00775-007-0208-z].

229. L. Xue et al., “High-Resolution Chemical Identification of Polymer Blend Thin Films Using Tip-Enhanced Raman Mapping,” *Macromolecules*, 44 (8), 2852–2858, 2011, [doi:10.1021/ma101651r].

230. A. Taguchi et al., “Deep-UV tip-enhanced Raman scattering,” *Journal of Raman Spectroscopy*, 40 (9), 1324–1330, 2009, [doi:10.1002/jrs.2287].

231. J. D. Scherger et al., “Extending nanoscale spectroscopy with titanium nitride probes,” *Journal of Raman Spectroscopy*, 47 (11), 1332–1336, 2016, [doi:10.1002/jrs.4959].

232. J. D. Scherger et al., “Tunable, Liquid Resistant Tip Enhanced Raman Spectroscopy Probes: Toward Label-Free Nano-Resolved Imaging of Biological Systems,” *Langmuir*, 33 (31), 7818–7825, 2017, [doi:10.1021/acs.langmuir.7b01338].

233. A. Kharitonov et al., “Tunable optical materials for multi-resonant plasmonics: from TiN to TiON [Invited],” *Opt. Mater. Express, OME*, 10 (2), 513–531, 2020, [doi:10.1364/OME.382160].

234. M. J. Weber, *Handbook of Optical Materials*, 2018, [doi:10.1201/9781315219615].

235. G. Kolhatkar et al., “Effect of the gold crystallinity on the enhanced luminescence signal of scanning probe tips in apertureless near-field optical microscopy,” *Optics Express*, 25 (21), 25929–25937, 2017,.

236. J. J. Lingane, “Standard potentials of half-reactions involving + 1 and + 3 gold in chloride medium: Equilibrium constant of the reaction $AuCl_4^-$ + 2Au + $2Cl^-$ = $3AuCl_2^-$,” *Journal of Electroanalytical Chemistry (1959)*, 4 (6), 332–342, 1962, [doi:10.1016/0022-0728(62)80079-5].

237. S. S. Kharintsev et al., “Near-field optical taper antennas fabricated with a highly replicable ac electrochemical etching method,” *Nanotechnology*, 22 (2), 025202, 2010, [doi:10.1088/0957-4484/22/2/025202].

238. T. W. Huh et al., “Efficient fabrication of gold tips by electrochemical etching for tip-enhanced Raman spectroscopy,” *Int. J. Precis. Eng. Manuf.*, 18 (2), 221–226, 2017, [doi:10.1007/s12541-017-0028-1].

239. L. Billot et al., “Production of gold tips for tip-enhanced near-field optical microscopy and spectroscopy: analysis of the etching parameters,” 2, *Eur. Phys. J. Appl. Phys.*, 31 (2), 139–145, 2005, [doi:10.1051/epjap:2005049].

240. M. Lopes et al., “Fast and reliable fabrication of gold tips with sub-50 nm radius of curvature for tip-enhanced Raman spectroscopy,” *Review of Scientific Instruments*, 84 (7), 073702, 2013, [doi:10.1063/1.4812365].

241. A. Foti et al., “Low cost tips for tip-enhanced Raman spectroscopy fabricated by two-step electrochemical etching of 125 µm diameter gold wires,” *Beilstein J Nanotechnol*, 9, 2718–2729, 2018, [doi:10.3762/bjnano.9.254].

242. D. Hussain et al., “Optimizing the Quality Factor of Quartz Tuning Fork Force Sensor for Atomic Force Microscopy: Impact of Additional Mass and Mass Rebalance,” *IEEE Sensors Journal*, 17 (9), 2797–2806, 2017, [doi:10.1109/JSEN.2017.2677459].

243. A. Hartschuh et al., “High-Resolution Near-Field Raman Microscopy of Single-Walled Carbon Nanotubes,” *Phys. Rev. Lett.*, 90 (9), 095503, 2003, [doi:10.1103/PhysRevLett.90.095503].

244. N. Kumar et al., “Tip-enhanced Raman spectroscopy: principles and applications,” 1, *EPJ Techn Instrum*, 2 (1), 1–23, 2015, [doi:10.1140/epjti/s40485-015-0019-5].

245. A. Ferrari et al., “Determination of nanotubes properties by Raman spectroscopy,” *Philosophical Transactions of the Royal Society of London. Series A: Mathematical, Physical and Engineering Sciences*, 362 (1824), 2311–2336, 2004, [doi:10.1098/rsta.2004.1443].

246. H. Jaffe, “Piezoelectric Ceramics,” *Journal of the American Ceramic Society*, 41 (11), 494–498, 1958, [doi:10.1111/j.1151-2916.1958.tb12903.x].

247. K. Garrity et al., “Chemistry of Ferroelectric Surfaces,” *Advanced Materials*, 22 (26–27), 2969–2973, 2010, [doi:10.1002/adma.200903723].

248. I. C. Amaechi et al., “Catalytic Applications of Non-Centrosymmetric Oxide Nanomaterials,” *Angewandte Chemie International Edition*, 61 (43), e202207975, 2022, [doi:10.1002/anie.202207975].

249. J. Garra et al., “Defect-mediated adsorption of methanol and carbon dioxide on $BaTiO_3$(001),” *Journal of Vacuum Science & Technology A*, 27 (5), L13–L17, 2009, [doi:10.1116/1.3168563].

250. J. N. Domrzalski et al., “Surface functionalized barium titanate nanoparticles: a combined experimental and computational study,” *ECS Journal of Solid State Science and Technology*, 11 (6), 063006, 2022,.

251. P.-M. Deleuze et al., “Ferroelectric polarization switching induced from water adsorption in BaTiO 3 ultrathin films,” *Physical Review B*, 101 (7), 075410, 2020,.

252. F. Shao et al., “Tip-enhanced Raman spectroscopy: principles, practice, and applications to nanospectroscopic imaging of 2D materials,” *Anal Bioanal Chem*, 411 (1), 37–61, 2019, [doi:10.1007/s00216-018-1392-0].

253. M. Beccari et al., “Characterization of benzenethiolate self-assembled monolayer on Cu(100) by XPS and NEXAFS,” *Journal of Electron Spectroscopy and Related Phenomena*, 172 (1–3), 64–68, 2009, [doi:10.1016/j.elspec.2009.03.004].

254. M. Marsi et al., “ESCA Microscopy at ELETTRA: what it is like to perform spectromicroscopy experiments on a third generation synchrotron radiation source,” *Journal of electron spectroscopy and related phenomena*, 84 (1–3), 73–83, 1997.

255. P. M. Bertsch et al., “Applications of synchrotron-based X-ray microprobes,” *Chemical Reviews*, 101 (6), 1809–1842, 2001.

256. K. F. Domke et al., “Studying Surface Chemistry beyond the Diffraction Limit: 10 Years of TERS,” *ChemPhysChem*, 11 (7), 1365–1373, 2010, [doi:10.1002/cphc.200900975].

257. M. Moskovits, “Surface-enhanced Raman spectroscopy: a brief retrospective,” *Journal of Raman Spectroscopy*, 36 (6-7), 485–496, 2005.

258. M. Nicklaus et al., “Note: Tip enhanced Raman spectroscopy with objective scanner on opaque samples,” *Review of Scientific Instruments*, 83 (6), 066102, 2012, [doi:10.1063/1.4725528].

259. A. Jorio et al., “Symmetry-derived selection rules for plasmon-enhanced Raman scattering,” *Phys. Rev. B*, 95 (15), 155409, 2017, [doi:10.1103/PhysRevB.95.155409].

260. J. Stadler et al., “Developments in and practical guidelines for tip-enhanced Raman spectroscopy,” *Nanoscale*, 4 (6), 1856–1870, 2012.

261. A. B. Zrimsek et al., “Single-molecule chemistry with surface-and tip-enhanced Raman spectroscopy,” *Chemical reviews*, 117 (11), 7583–7613, 2017,.

262. B. Pettinger et al., “Surface-enhanced and STM-tip-enhanced Raman Spectroscopy at Metal Surfaces,” *Single Molecules*, 3 (5–6), 285–294, 2002, [doi:10.1002/1438-5171(200211)3:5/6<285::AID-SIMO285>3.0.CO;2-X].

263. L. R. McCourt et al., “A comparison of gold and silver nanocones and geometry optimisation for tip-enhanced microscopy,” *Journal of Raman Spectroscopy*, 51 (11), 2208–2216, 2020.

264. G. Kolhatkar et al., “Effect of the gold crystallinity on the enhanced luminescence signal of scanning probe tips in apertureless near-field optical microscopy,” *Opt. Express, OE*, 25 (21), 25929–25937, 2017, [doi:10.1364/OE.25.025929].

265. M. A. Young et al., “Plasmonic materials for surface-enhanced and tip-enhanced Raman spectroscopy,” *in Tip Enhancement*, pp. 1–39, 2007.

266. B. Pettinger et al., “Nanoscale Probing of Adsorbed Species by Tip-Enhanced Raman Spectroscopy,” *Phys. Rev. Lett.*, 92 (9), 096101, 2004, [doi:10.1103/PhysRevLett.92.096101].

267. Y. Fang et al., “Near field plasmonic gradient effects on high vacuum tip-enhanced Raman spectroscopy,” *Physical Chemistry Chemical Physics*, 17 (2), 783–794, 2015.

268. L. Meng et al., “Effect of electric field gradient on sub-nanometer spatial resolution of tip-enhanced Raman spectroscopy,” *Scientific reports*, 5 (1), 9240, 2015.

269. Z. Zhang et al., “Electric field gradient quadrupole Raman modes observed in plasmon-driven catalytic reactions revealed by HV-TERS,” *Nanoscale*, 5 (10), 4151–4155, 2013.

270. E. H. Morales et al., “On the relationship between surface reconstructions and step edge stability on $BaTiO_3$ (001),” *Surface science*, 609, 62–66, 2013,.

271. K. Momma et al., “VESTA 3 for three-dimensional visualization of crystal, volumetric and morphology data,” *Journal of Applied Crystallography*, 44 (6), 1272–1276, 2011, [doi:10.1107/S0021889811038970].

272. D. S. R. Rocabado et al., “Theoretical study of inorganic carbonaceous species reaction with the surfaces of $BaTiO_3$ (001),” *ECS Transactions*, 68 (1), 3177, 2015,.

273. K. V. Sopiha et al., “Suppression of surfaces states at cubic perovskite (001) surfaces by CO_2 adsorption,” *Physical Chemistry Chemical Physics*, 20 (27), 18828–18836, 2018, [doi:10.1039/c8cp02535e].

274. R. Böttcher et al., “Size effect in Mn^{2+}-doped $BaTiO_3$ nanopowders observed by electron paramagnetic resonance,” *Physical Review B*, 62 (3), 2085, 2000.

275. W. Sun, “Size effect in barium titanate powders synthesized by different hydrothermal methods,” *Journal of applied physics*, 100 (8), 2006, [doi:10.1063/1.2358005].

276. K. A. Chan et al., “Finding a needle in a chemical haystack: tip-enhanced Raman scattering for studying carbon nanotubes mixtures,” *Nanotechnology*, 21 (44), 445704, 2010.

277. D. Mehtani et al., “Tip-enhanced Raman spectroscopy with high contrast,” presented at Plasmonics: Metallic Nanostructures and Their Optical Properties III, 2005, 23–29, SPIE.

278. M. DiDomenico Jr et al., “Raman spectrum of single-domain $BaTiO_3$,” *Physical Review*, 174 (2), 522, 1968.

279. V. Dwij et al., “Revisiting 70 years of lattice dynamics of $BaTiO_3$: Combined first principle and experimental investigation,” *arXiv preprint arXiv:2012.12669*, 2020.

280. G. Pezzotti, “Raman spectroscopy of piezoelectrics,” *Journal of Applied Physics*, 113 (21), 8_1, 2013.

281. M. Sun et al., “Plasmon-driven selective reductions revealed by tip-enhanced Raman spectroscopy,” *Advanced Materials Interfaces*, 1 (5), 1300125, 2014.

282. M. Sun et al., “Plasmonic gradient effects on high vacuum tip-enhanced Raman spectroscopy,” *Advanced Optical Materials*, 2 (1), 74–80, 2014.

283. J. Ma et al., “Plexcitons, electric field gradient and electron–phonon coupling in tip-enhanced Raman spectroscopy (TERS),” *Nanoscale*, 13 (24), 10712–10725, 2021.

284. L. Meng et al., “Electromagnetic field gradient-enhanced Raman scattering in TERS configurations,” *The Journal of Physical Chemistry C*, 125 (10), 5684–5691, 2021.

285. A. D. Buckingham, “Permanent and induced molecular moments and long-range intermolecular forces,” *Advances in Chemical Physics*, 107–142, 1967.

286. J. K. Sass et al., “Electric field gradient effects on the spectroscopy of adsorbed molecules,” *The Journal of Physical Chemistry*, 85 (6), 621–623, 1981.

287. P. J. Feibelman, “Microscopic calculation of electromagnetic fields in refraction at a jellium-vacuum interface,” *Physical Review B*, 12 (4), 1319, 1975.

288. F. L. Pedrotti et al., *Introduction to optics*, 2017.

289. B. Pettinger et al., “Tip-enhanced Raman scattering: influence of the tip-surface geometry on optical resonance and enhancement,” *Surface Science*, 603 (10–12), 1335–1341, 2009.

290. P. Duran et al., “Heating-rate effect on the $BaTiO_3$ formation by thermal decomposition of metal citrate polymeric precursors,” *Solid State Ionics*, 141, 529–539, 2001.

291. Y. Gao et al., “Low-temperature synthesis of crystalline $BaTiO_3$ nanoparticles by one-step ‘organosol’-precipitation,” *Journal of Materials Chemistry*, 22 (34), 17573–17583, 2012.

292. S. Utara et al., “Ultrasonic assisted synthesis of $BaTiO_3$ nanoparticles at 25° C and atmospheric pressure,” *Ultrasonics Sonochemistry*, 41, 441–448, 2018,.

293. W.-S. Cho et al., “Stacking faults in $BaTiO_3$ particles synthesized from organic precursor,” *Journal of applied physics*, 81 (7), 3000–3002, 1997.

294. F. A. Miller et al., “Infrared spectra of inorganic ions in the cesium bromide region (700–300 cm^{-1}),” *Spectrochimica Acta*, 16 (1–2), 135–235, 1960.

295. G. Busca et al., “Solid-state and surface spectroscopic characterization of $BaTiO_3$ fine powders,” *Chemistry of materials*, 6 (7), 955–961, 1994.

296. P. Pasierb et al., “Structural properties of Li_2CO_3–$BaCO_3$ system derived from IR and Raman spectroscopy,” *Journal of molecular structure*, 596 (1–3), 151–156, 2001.

297. I. C. Amaechi et al., “Particle size effect on the photocatalytic kinetics of barium titanate powders,” *Catalysis Science & Technology*, 10 (18), 6274–6284, 2020, [doi:10.1039/D0CY01358G].

298. J. Plathier et al., “Note: Controlling the length of plasmonic tips obtained by pulsed electrochemical etching,” *Review of Scientific Instruments*, 89 (9), 096107, 2018, [doi:10.1063/1.5028052].

299. T. M. Shaw et al., “The properties of ferroelectric films at small dimensions,” *Annu. Rev. Mater. Sci.*, 30, 263–298, 2000, [doi:10.1146/annurev.matsci.30.1.263].

300. C. H. Ahn et al., “Ferroelectricity at the nanoscale: local polarization in oxide thin films and heterostructures,” *Science*, 303 (5657), 488–491, 2004, [doi:10.1126/science.1092508].

301. S. Chattopadhyay et al., “Size-induced diffuse phase transition in the nanocrystalline ferroelectric $PbTiO_3$,” *Phys. Rev. B*, 52 (18), 13177–13183, 1995, [doi:10.1103/PhysRevB.52.13177].

302. B. Meyer et al., “Ab initio study of $BaTiO_3$ and $PbTiO_3$ surfaces in external electric fields,” *Phys. Rev. B*, 63 (20), 205426, 2001, [doi:10.1103/PhysRevB.63.205426].

303. E. K. Akdogan et al., “Thermodynamic theory of intrinsic finite-size effects in $PbTiO_3$ nanocrystals. I. Nanoparticle size-dependent tetragonal phase stability,” *J. Appl. Phys.*, 101 (6), 2007, [doi:10.1063/1.2713081].

304. I. Ponomareva et al., “Modelling of nanoscale ferroelectrics from atomistic simulations,” *Current Opinion in Solid State and Materials Science*, 9 (3), 114–121, 2005, [doi:10.1016/j.cossms.2006.05.003].

305. C. Jeong et al., “Revealing the three-dimensional arrangement of polar topology in nanoparticles,” *Nat Commun*, 15 (1), 3887, 2024, [doi:10.1038/s41467-024-48082-x].

306. J. Rigor et al., “Plasmonic heating effects in tip-enhanced Raman spectroscopy (TERS),” *J. Phys. Chem. C*, 126 (32), 13986–13993, 2022, [doi:10.1021/acs.jpcc.2c03881].

307. P. Sedykh et al., “Size effects in fine barium titanate particles,” *Ferroelectrics*, 400 (1), 135–143, 2010, [doi:10.1080/00150193.2010.505514].

308. P. Chen et al., “Size-dependent infrared phonon modes and ferroelectric phase transition in $BiFeO_3$ nanoparticles,” *Nano Lett.*, 10 (11), 4526–4532, 2010, [doi:10.1021/nl102470f].

309. B. Jiang et al., “Size effects on ferroelectricity of ultrafine particles of $PbTiO_3$,” *Journal of Applied Physics*, 87 (7), 3462–3467, 2000, [doi:10.1063/1.372367].

310. M. J. Polking et al., “Controlled synthesis and size-dependent polarization domain structure of colloidal germanium telluride nanocrystals,” *J. Am. Chem. Soc.*, 133 (7), 2044–2047, 2011, [doi:10.1021/ja108309s].

311. L. J. McGilly et al., “Polarization closure in $PbZr_{(0.42)}Ti_{(0.58)}O_3$ nanodots,” *Nano Lett.*, 11 (10), 4490–4495, 2011, [doi:10.1021/nl2031103].

312. R. G. P. McQuaid et al., “Mesoscale flux-closure domain formation in single-crystal $BaTiO_3$,” *Nat Commun*, 2 (1), 404, 2011, [doi:10.1038/ncomms1413].

313. B. J. Rodriguez et al., “Vortex polarization states in nanoscale ferroelectric arrays,” *Nano Lett.*, 9 (3), 1127–1131, 2009, [doi:10.1021/nl8036646].

314. C.-L. Jia et al., “Direct observation of continuous electric dipole rotation in flux-closure domains in ferroelectric $Pb(Zr,Ti)O_3$,” *Science*, 331 (6023), 1420–1423, 2011, [doi:10.1126/science.1200605].

315. V. Skumryev et al., “Beating the superparamagnetic limit with exchange bias,” *Nature*, 423 (6942), 850–853, 2003, [doi:10.1038/nature01687].

316. D. Szwarcman et al., “The size-dependent ferroelectric phase transition in $BaTiO_3$ nanocrystals probed by surface plasmons,” *ACS Nano*, 5 (1), 507–515, 2011, [doi:10.1021/nn102385e].

317. A. Schilling et al., “Domains in ferroelectric nanodots,” *Nano Lett.*, 9 (9), 3359–3364, 2009, [doi:10.1021/nl901661a].

318. M. J. Polking et al., “Size-dependent polar ordering in colloidal GeTe nanocrystals,” *Nano Lett.*, 11 (3), 1147–1152, 2011, [doi:10.1021/nl104075v].

319. V. Buscaglia et al., “Grain size and grain boundary-related effects on the properties of nanocrystalline barium titanate ceramics,” *Journal of the European Ceramic Society*, 26 (14), 2889–2898, 2006, [doi:10.1016/j.jeurceramsoc.2006.02.005].

320. J. F. Lomax et al., “Size effects observed via the electrical response of $BaTiO_3$ nanoparticles in a cavity,” *J. Phys. Chem. C*, 116 (44), 23742–23748, 2012, [doi:10.1021/jp307218v].

321. M. J. Polking et al., “Ferroelectric order in individual nanometre-scale crystals,” *Nature Mater*, 11 (8), 700–709, 2012, [doi:10.1038/nmat3371].

322. L. W. Chang et al., “Size effects on thin film ferroelectrics: Experiments on isolated single crystal sheets,” *Applied Physics Letters*, 93 (13), 132904, 2008, [doi:10.1063/1.2990760].

323. L. J. McGilly et al., “Domain bundle boundaries in single crystal $BaTiO_3$ lamellae: Searching for naturally forming dipole flux-closure/quadrupole chains,” *Nano Lett.*, 10 (10), 4200–4205, 2010, [doi:10.1021/nl102566y].

324. M. M. Saad et al., “Investigating the effects of reduced size on the properties of ferroelectrics,” *IEEE Transactions on Ultrasonics, Ferroelectrics, and Frequency Control*, 53 (12), 2208–2225, 2006, [doi:10.1109/TUFFC.2006.168].

325. D. A. Tenne et al., “Raman spectroscopy of ferroelectric thin films and superlattices,” *Journal of the American Ceramic Society*, 91 (6), 1820–1834, 2008, [doi:10.1111/j.1551-2916.2008.02371.x].

326. A. M. Bratkovsky et al., “Smearing of phase transition due to a surface effect or a bulk inhomogeneity in ferroelectric nanostructures,” *Phys. Rev. Lett.*, 94 (10), 107601, 2005, [doi:10.1103/PhysRevLett.94.107601].

327. S. Li et al., “Size effects in nanostructured ferroelectrics,” *Physics Letters A*, 212 (6), 341–346, 1996, [doi:10.1016/0375-9601(96)00077-1].

328. R. Kretschmer et al., “Surface effects on phase transitions in ferroelectrics and dipolar magnets,” *Phys. Rev. B*, 20 (3), 1065–1076, 1979, [doi:10.1103/PhysRevB.20.1065].

329. T. Hidaka et al., “Formation and observation of 50 nm polarized domains in $PbZr_{1-x}Ti_xO_3$ thin film using scanning probe microscope,” *Applied Physics Letters*, 68 (17), 2358–2359, 1996, [doi:10.1063/1.115857].

330. T. Tybell et al., “Domain wall creep in epitaxial ferroelectric $Pb(Zr_{0.2}Ti_{0.8})O_3$ thin films,” *Phys. Rev. Lett.*, 89 (9), 097601, 2002, [doi:10.1103/PhysRevLett.89.097601].

331. S. V. Kalinin et al., “Nanoscale electromechanics of ferroelectric and biological systems: A new dimension in scanning probe microscopy,” *Annual Review of Materials Research*, 37 (Volume 37, 2007), 189–238, 2007, [doi:10.1146/annurev.matsci.37.052506.084323].

332. D. A. Bonnell et al., “Piezoresponse force microscopy: A window into electromechanical behavior at the nanoscale,” *MRS Bulletin*, 34 (9), 648–657, 2009, [doi:10.1557/mrs2009.176].

333. M. Kang et al., “Conformational heterogeneity of molecules physisorbed on a gold surface at room temperature,” *Nat Commun*, 13 (1), 4133, 2022, [doi:10.1038/s41467-022-31576-x].

334. J. Plathier et al., “Permittivity imaged at the nanoscale using tip-enhanced Raman spectroscopy,” *Nanoscale Horizons*, 2 (6), 365–369, 2017, [doi:10.1039/c7nh00075h].

335. A. Ruediger et al., “Detection of regions with reduced symmetry in crystal surfaces via tip-enhanced Raman spectroscopy,” *in Enhanced Spectroscopies and Nanoimaging 2022*, p. PC1220308, 2022, [doi:10.1117/12.2634220].

336. A. H. Youssef et al., “Topography-induced variations of localized surface plasmon resonance in tip-enhanced Raman configuration,” *Opt. Express*, 28 (9), 14161, 2020, [doi:10.1364/OE.389565].

337. G. Kolhatkar et al., “Composition variation in Al-based dilute nitride alloys using apertureless scanning near-field optical microscopy,” *Physical Chemistry Chemical Physics*, 18 (44), 30546–30553, 2016, [doi:10.1039/C6CP05063H].

338. P. R. West et al., “Searching for better plasmonic materials,” *Laser & Photonics Reviews*, 4 (6), 795–808, 2010, [doi:10.1002/lpor.200900055].

339. J. A. Faucheaux et al., “Plasmon resonances of semiconductor nanocrystals: Physical principles and new opportunities,” *J. Phys. Chem. Lett.*, 5 (6), 976–985, 2014, [doi:10.1021/jz500037k].

340. S. Ke et al., “Lorentz-type relationship of the temperature dependent dielectric permittivity in ferroelectrics with diffuse phase transition,” *Applied Physics Letters*, 93 (11), 112906, 2008, [doi:10.1063/1.2987733].

341. M. G. Harwood et al., “Curie point of barium titanate,” *Nature*, 160 (4054), 58–59, 1947, [doi:10.1038/160058a0].

342. S. Wada et al., “Change of macroscopic and microscopic symmetry of barium titanate single crystal around Curie temperature,” *Jpn. J. Appl. Phys.*, 37 (9S), 5385, 1998, [doi:10.1143/JJAP.37.5385].

343. D. Chahinez et al., “Modeling of the surface plasmon resonance tunability of silver/gold core–shell nanostructures,” *RSC Advances*, 8 (35), 19616–19626, 2018, [doi:10.1039/C8RA03261K].

344. M. M. Miller et al., “Sensitivity of metal nanoparticle surface plasmon resonance to the dielectric environment,” *J. Phys. Chem. B*, 109 (46), 21556–21565, 2005, [doi:10.1021/jp054227y].

345. S. Underwood et al., “Effect of the solution refractive index on the color of gold colloids,” *Langmuir*, 10 (10), 3427–3430, 1994, [doi:10.1021/la00022a011].

346. K. Ishikawa et al., “Surface relaxation in ferroelectric perovskites,” *Phys. Rev. B*, 60 (17), 11841–11845, 1999, [doi:10.1103/PhysRevB.60.11841].

347. S. Clemens et al., “Variable size and shape distribution of ferroelectric nanoislands by chemical mechanical polishing,” *Small*, 2 (4), 500–502, 2006, [doi:10.1002/smll.200500438].

348. S. Clemens et al., “Integration of ferroelectric lead titanate nanoislands for direct hysteresis measurements,” *Applied Physics Letters*, 87 (14), 142904, 2005, [doi:10.1063/1.2084322].

349. M. Nicklaus et al., “Direct observation of core–shell structures in individual lead titanate ferroelectric nanostructures by tip-enhanced refractive index mapping,” *Advanced Functional Materials*, 29 (2), 1806770, 2019, [doi:10.1002/adfm.201806770].

350. J. F. Scott, *Ferroelectric Memories*, 2000, [doi:10.1007/978-3-662-04307-3].

351. B. Sun et al., “ABO_3 multiferroic perovskite materials for memristive memory and neuromorphic computing,” *Nanoscale Horizons*, 6 (12), 939–970, 2021, [doi:10.1039/D1NH00292A].

352. M. Stengel et al., “Origin of the dielectric dead layer in nanoscale capacitors,” *Nature*, 443 (7112), 679–682, 2006, [doi:10.1038/nature05148].

353. K. Eisenbeiser et al., “Field effect transistors with $SrTiO_3$ gate dielectric on Si,” *Applied Physics Letters*, 76 (10), 1324–1326, 2000, [doi:10.1063/1.126023].

354. P. C. Joshi et al., “Structural and electrical characteristics of $SrTiO_3$ thin films for dynamic random access memory applications,” *Journal of Applied Physics*, 73 (11), 7627–7634, 1993, [doi:10.1063/1.353960].

355. K. Ahadi et al., “Enhancing superconductivity in $SrTiO_3$ films with strain,” *Science Advances*, 5 (4), eaaw0120, 2019, [doi:10.1126/sciadv.aaw0120].

356. J. J. Wu et al., “Catalytic ozonation of oxalic acid using $SrTiO_3$ catalyst,” *Ozone: Science & Engineering*, 33 (1), 74–79, 2011, [doi:10.1080/01919512.2011.536903].

357. S. Patial et al., “Tunable photocatalytic activity of $SrTiO_3$ for water splitting: Strategies and future scenario,” *Journal of Environmental Chemical Engineering*, 8 (3), 103791, 2020, [doi:10.1016/j.jece.2020.103791].

358. C. Luo et al., “Photocatalytic CO_2 reduction over $SrTiO_3$: Correlation between surface structure and activity,” *Applied Surface Science*, 447, 627–635, 2018, [doi:10.1016/j.apsusc.2018.04.049].

359. X. Wu et al., “Multifunctional photocatalysts of Pt-decorated 3DOM perovskite-type $SrTiO_3$ with enhanced CO_2 adsorption and photoelectron enrichment for selective CO_2 reduction with H_2O to CH_4,” *Journal of Catalysis*, 377, 309–321, 2019, [doi:10.1016/j.jcat.2019.07.037].

360. V. Sharma et al., “Cooperative Interactions between Surface Terminations Explain Photocatalytic Water Splitting Activity on $SrTiO_3$,” *PRX Energy*, 1 (2), 023002, 2022, [doi:10.1103/PRXEnergy.1.023002].

361. Q. Wu et al., “Understanding the Interactions of CO_2 with Doped and Undoped $SrTiO_3$,” *ChemSusChem*, 9 (14), 1889–1897, 2016, [doi:10.1002/cssc.201600498].

362. D. Kim et al., “Study of CO_2 adsorption properties on the $SrTiO_3$(001) surface with ambient pressure XPS,” *ACS Appl. Mater. Interfaces*, 16 (29), 38679–38689, 2024, [doi:10.1021/acsami.4c04729].

363. J. Balajka et al., “High-affinity adsorption leads to molecularly ordered interfaces on TiO_2 in air and solution,” *Science*, 361 (6404), 786–789, 2018, [doi:10.1126/science.aat6752].

364. J. Y. Park, “How titanium dioxide cleans itself,” *Science*, 361 (6404), 753–753, 2018, [doi:10.1126/science.aau6016].

365. E. Heifets et al., “Semi-empirical simulations of surface relaxation for perovskite titanates,” *Surface Science*, 462 (1), 19–35, 2000, [doi:10.1016/S0039-6028(00)00603-8].

366. J. Padilla et al., “Ab initio study of $SrTiO_3$ surfaces,” *Surface Science*, 418 (1), 64–70, 1998, [doi:10.1016/S0039-6028(98)00670-0].

367. B. Meyer et al., “Theory of $PbTiO_3$, $BaTiO_3$, and $SrTiO_3$ surfaces,” *Faraday Discuss.*, 114 (0), 395–405, 1999, [doi:10.1039/A903029H].

368. C. Cheng et al., “Structural relaxation and longitudinal dipole moment of $SrTiO_3$ surfaces,” *Phys. Rev. B*, 62 (15), 10409–10418, 2000, [doi:10.1103/PhysRevB.62.10409].

369. F. Corà et al., “QM investigations on perovskite-structured transition metal oxides: bulk, surfaces and interfaces,” *Faraday Discuss.*, 114 (0), 421–442, 1999, [doi:10.1039/A904517A].

370. V. Ravikumar et al., “Ferroelectric-Monolayer Reconstruction of the $SrTiO_3$ (100) Surface,” *Phys. Rev. Lett.*, 74 (6), 960–963, 1995, [doi:10.1103/PhysRevLett.74.960].

371. M. Kawasaki et al., “Atomic control of the $SrTiO_3$ crystal surface,” *Science*, 266 (5190), 1540–1542, 1994, [doi:10.1126/science.266.5190.1540].

372. P. A. W. van der Heide et al., “X-ray photoelectron spectroscopic and ion scattering study of the $SrTiO_3$ (001) surface,” *Surface Science*, 473 (1), 59–70, 2001, [doi:10.1016/S0039-6028(00)00954-7].

373. N. Bickel et al., “Ferroelectric relaxation of the $SrTiO_3$ (100) surface,” *Phys. Rev. Lett.*, 62 (17), 2009–2011, 1989, [doi:10.1103/PhysRevLett.62.2009].

374. T. Kubo et al., “Microscopic properties of the $SrTiO_3$ (100) surface,” *Appl Phys A*, 72 (S2), S277–S280, 2001, [doi:10.1007/s003390100662].

375. N. Ikemiya et al., “Surface structures of MgO (100) and $SrTiO_3$ (100) as revealed by atomic force microscopy,” *Journal of Crystal Growth*, 160 (1–2), 104–110, 1996, [doi:10.1016/0022-0248(95)00567-6].

376. J. Nie et al., “Control of step arrays on normal and vicinal $SrTiO_3$ (100) substrates,” *Jpn. J. Appl. Phys.*, 37 (9A), L1014, 1998, [doi:10.1143/JJAP.37.L1014].

377. A. Staykov et al., “Interaction of SrO-terminated $SrTiO_3$ surface with oxygen, carbon dioxide, and water,” *Journal of Materials Chemistry A*, 6 (45), 22662–22672, 2018, [doi:10.1039/C8TA05177A].

378. K. Szot et al., “Formation of micro-crystals on the (100) surface of $SrTiO_3$ at elevated temperatures,” *Surface Science*, 460 (1), 112–128, 2000, [doi:10.1016/S0039-6028(00)00522-7].

379. L. Langelüddecke et al., “Exploring the nanoscale: Fifteen years of tip-enhanced Raman spectroscopy,” *Appl Spectrosc*, 69 (12), 1357–1371, 2015, [doi:10.1366/15-08014].

380. C. T. Graefe et al., “Far-field super-resolution vibrational spectroscopy,” *Anal. Chem.*, 91 (14), 8723–8731, 2019, [doi:10.1021/acs.analchem.9b01731].

381. P. Verma, “Tip-enhanced Raman spectroscopy: Technique and recent advances,” *Chem. Rev.*, 117 (9), 6447–6466, 2017, [doi:10.1021/acs.chemrev.6b00821].

382. T. Deckert-Gaudig et al., “Tip-enhanced Raman spectroscopy – from early developments to recent advances,” *Chemical Society Reviews*, 46 (13), 4077–4110, 2017, [doi:10.1039/C7CS00209B].

383. M. D. Sonntag et al., “Single-molecule tip-enhanced Raman spectroscopy,” *J. Phys. Chem. C*, 116 (1), 478–483, 2012, [doi:10.1021/jp209982h].

384. F. Sánchez et al., “Tailored surfaces of perovskite oxide substrates for conducted growth of thin films,” *Chemical Society Reviews*, 43 (7), 2272–2285, 2014, [doi:10.1039/C3CS60434A].

385. R. Hess, *Blender Foundations: The Essential Guide to Learning Blender 2.5*, 2010, [doi:10.4324/9780240814315].

386. M. G. Brik, “First-principles calculations of structural, electronic, optical and elastic properties of magnesite $MgCO_3$ and calcite $CaCO_3$,” *Physica B: Condensed Matter*, 406 (4), 1004–1012, 2011, [doi:10.1016/j.physb.2010.12.049].

387. M. Kubo et al., “Molecular dynamics simulation on a layer-by-layer homoepitaxial growth process of $SrTiO_3$ (001),” *The Journal of Chemical Physics*, 109 (19), 8601–8606, 1998, [doi:10.1063/1.477525].

388. A. Hadj Youssef et al., “Giant step bunching on $SrTiO_3$ thin films grown epitaxially on vicinal MgO(100) surfaces,” *Applied Surface Science*, 570, 151266, 2021, [doi:10.1016/j.apsusc.2021.151266].

389. M. Dekermenjian et al., “Water Adsorption on MgO Surfaces: A Vibrational Analysis,” 8, *Crystals*, 13 (8), 1153, 2023, [doi:10.3390/cryst13081153].

390. “CRYSTAL23: A Program for Computational Solid State Physics and Chemistry | Journal of Chemical Theory and Computation,” *Journal of Chemical Theory and Computation* 19.20 (2022): 6891-6932.

391. J. P. Perdew et al., “Restoring the density-gradient expansion for exchange in solids and surfaces,” *Phys. Rev. Lett.*, 100 (13), 136406, 2008, [doi:10.1103/PhysRevLett.100.136406].

392. D. Vilela Oliveira et al., “BSSE-correction scheme for consistent gaussian basis sets of double- and triple-zeta valence with polarization quality for solid-state calculations,” *Journal of Computational Chemistry*, 40 (27), 2364–2376, 2019, [doi:10.1002/jcc.26013].

393. W. Pannhorst et al., “Zur Kristallstruktur von Strontianit, $SrCO_3$,” *Zeitschrift für Kristallographie - Crystalline Materials*, 131 (1–6), 455–459, 1970, [doi:10.1524/zkri.1970.131.16.455].

394. F. W. Lytle, “X-Ray diffractometry of low-temperature phase transformations in strontium titanate,” *Journal of Applied Physics*, 35 (7), 2212–2215, 1964, [doi:10.1063/1.1702820].

395. N. Biedermann et al., “High-pressure phase behavior of $SrCO_3$: An experimental and computational Raman scattering study,” *Phys Chem Minerals*, 44 (5), 335–343, 2017, [doi:10.1007/s00269-016-0861-2].

396. G. Beata et al., “CRYSPLOT: A new tool to visualize physical and chemical properties of molecules, polymers, surfaces, and crystalline solids,” *Journal of Computational Chemistry*, 40 (26), 2329–2338, 2019, [doi:10.1002/jcc.25858].

397. T. Nguyen-Thanh et al., “Lattice dynamics and elasticity of $SrCO_3$,” *Journal of Applied Crystallography*, 49 (6), 1982–1990, 2016, [doi:10.1107/S1600576716014205].

398. J. F. Alves et al., “Revisiting the Raman spectra of carbonate minerals,” 11, *Minerals*, 13 (11), 1358, 2023, [doi:10.3390/min13111358].

399. F. A. Rabuffetti et al., “Synthesis-dependent first-order Raman scattering in $SrTiO_3$ nanocubes at room temperature,” *Chem. Mater.*, 20 (17), 5628–5635, 2008, [doi:10.1021/cm801192t].

400. A. Hadj Youssef et al., “Symmetry-Forbidden-Mode Detection in $SrTiO_3$ Nanoislands with Tip-Enhanced Raman Spectroscopy,” *J. Phys. Chem. C*, 125 (11), 6200–6208, 2021, [doi:10.1021/acs.jpcc.0c10938].

401. M. J. van Setten et al., “The PseudoDojo: Training and grading a 85 element optimized norm-conserving pseudopotential table,” *Computer Physics Communications*, 226, 39–54, 2018, [doi:10.1016/j.cpc.2018.01.012].

402. A. García et al., “Siesta: Recent developments and applications,” *The Journal of Chemical Physics*, 152 (20), 204108, 2020, [doi:10.1063/5.0005077].

403. J. P. Perdew et al., “Generalized gradient approximation made simple,” *Phys. Rev. Lett.*, 77 (18), 3865–3868, 1996, [doi:10.1103/PhysRevLett.77.3865].